

Design, Construction, and Commissioning of an In-Core Materials Testing Facility for Slow Strain Rate Testing

by

Jeffrey R. O'Donnell

B.S. Engineering Physics
Rensselaer Polytechnic Institute
(1990)

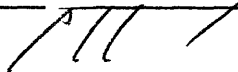
Submitted to the Department of Nuclear Engineering
in Partial Fulfillment of the Requirements for the Degree of

Doctor of Philosophy
at the
Massachusetts Institute of Technology

September 1994

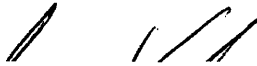
© Massachusetts Institute of Technology 1994. All rights reserved.

Signature of Author _____



Department of Nuclear Engineering
August 1994

Certified by _____



Otto K. Harling, Ph. D.
Professor of Nuclear Engineering
Director, Nuclear Reactor Laboratory
Thesis Supervisor

Certified by _____



Gordon Kohse, Ph. D.
Principal Research Scientist, Nuclear Reactor Laboratory
Thesis Supervisor

Accepted by _____

Allen F. Henry, Ph. D.
Chairman, Department Committee on Graduate Students

MASSACHUSETTS INSTITUTE

NOV 16 1994



Design, Construction, and Commissioning of an In-Core Materials Testing Facility for Slow Strain Rate Testing

by

Jeffrey R. O'Donnell

Submitted to the Department of Nuclear Engineering
on August 11, 1994 in partial fulfillment of
the requirements for the Degree of Doctor of Philosophy

Abstract

In the past several years a variety of austenitic stainless steel components in boiling water reactor (BWR) cores have failed by an intergranular cracking mechanism called irradiation assisted stress corrosion cracking (IASCC). Characteristics of such failures are that the component was exposed to a fast neutron fluence under tensile stress and in an oxidizing water environment.

A facility to study IASCC in typical BWR water and radiation environments was designed, built, and put into in-core service. This facility positions a pre-irradiated test specimen in the core of the MIT research reactor, circulates water with controlled temperature and chemistry past the specimen, and applies a tensile load to the specimen to maintain a constant slow strain rate until specimen failure. A DC potential drop (DCPD) technique was developed to measure specimen strain during in-core testing. Electrodes are incorporated to measure the specimen's electrochemical corrosion potential (ECP) under test, and for the initial analysis, while varying water chemistry, flow rate, in-core position, and reactor power level. A chemistry control system was designed and built to measure and control the water chemistry. Remote specimen handling tools and procedures were developed to allow the fracture surface to be analyzed by scanning electron microscopy (SEM). The facility and operating procedures were designed to minimize radiation exposure of personnel during facility operation and transfer to a hot cell for specimen removal and replacement. The facility's design also ensures that testing mishaps pose minimal risk to safe reactor operation.

Initial in-core tests, which measured the ECP of stainless steel in in-flux sections of the testing rig were completed successfully. These tests showed that the desired oxidizing environment can be established and monitored during in-core SSRT testing. Initial in-core SSRT testing has been demonstrated and a series of SSRT tests are presently underway. Results of these tests will be used to investigate the effects of neutron fluence and materials variables on IASCC.

Thesis Supervisor: Professor Otto K. Harling
Title: Professor of Nuclear Engineering
Director, Nuclear Reactor Laboratory

Thesis Supervisor: Dr. Gordon Kohse
Title: Principal Research Scientist

ACKNOWLEDGMENTS

I am especially grateful to my thesis advisors, Professor Otto Harling and Dr. Gordon Kohse, for their guidance and assistance throughout my work at MIT. I am grateful to Professor Harling in particular for providing me with the opportunity to attend MIT and work on a satisfying research project. Other project members whose assistance was essential to the successful completion of this work include Professor Ron Ballinger, Mr. Pete Stahle, Mr. Sunichi Suzuki, Mr. Kenro Takamori and Mr. Yoshihiko Tanaka. The efforts of Dr. Scott Mao and Mr. Y. Komori during the conceptual design phase of this project are also appreciated.

The help of individuals during the construction and testing phases of this project was crucial for the successful completion of this work. Undergraduate students who endured numerous long and difficult hours with me in the lab include Greg MacCandless, Juan Gonzales, Dorian Balch, Judy Leckman, and Joel Palacios. Theodore (TJ) Weber and Julian Guerra de la Torre were the most valuable players on the IASCC team for this past year which proved to be most challenging. TJ's and Julian's efforts were above and beyond my expectations of them. When situations arose requiring contingency measures, TJ and Julian consistently made themselves available. Every doctoral student should be lucky enough to have people like them to work with.

The assistance of the professionals at the MIT Nuclear Reactor Laboratory must not go unrecognized. Ernesto Cabello and Yakov Ostrovski provided valuable experience and help too numerous to list. The craftsman in the machine shop, Johnny Wasik and Ronny St. Jean, provided quality work and, when required, provided this work in a timely manner. The Reactor Radiation Protection Office, Fred McWilliams, Marcia Austin, Todd Date and Bruce Graber, provided many patient hours of consultation and guidance. I thank the Reactor Operations Office, Eddy Lau, Tom Newton, and the team of supervisors and reactor operators, for their help. The assistance of the reactor

maintenance staff for getting the facility into the reactor in working order was greatly appreciated. Paul Menadier and Yakov Ostrovski spent many long hours working on the electrical and interlock system. Ed Block helped with the initial design of the shielded transport cask and rig handling system. John "Chach" DiCiaccio spent many long days and evenings with me getting the rig handling system into working order. His efforts and skills were especially appreciated. I felt most confident when John was available to move the rig. Martin Morra and Hiu Au spent much time helping me with the metallurgical aspects of this thesis.

I thank Alexis Lewis for operating the SEM during the analysis of the irradiated specimens, Frank Warmsley for scanning the images into the computer, and Tom Fuller for his supervision while transporting these highly radioactive specimens to the SEM room for the analysis. I also thank Professor Tetsuo Shoji for offering his expertise during the SEM analysis of the fractured specimens.

I thank the Tokyo Electric Power Company (TEPCo) for funding a valuable and challenging research project. I also thank Professor Manson Benedict for providing me with funding for this past year through the Manson Benedict Fellowship.

I thank my parents, Robert and Graycie O'Donnell, for their constant assurance and support before and throughout my academic endeavor. Following six years of Naval service, poor high school grades still kept me from being admitted into an engineering school. My parents persuaded me to attend community college. They knew that with honest effort I could get good grades and would then be able to attend a "good" school. Seven years later I am writing my Ph.D. thesis at MIT; they were right.

Most important of all I thank my wife, Kathy. While I spent many long days and nights in the lab, she was at home taking care of our son alone. I owe her countless nights and weekends. I also owe my son, Michael, a lot of time. Mike, daddy will soon be home for dinner and to read to you much more frequently. I look forward to repaying these debts.

TABLE OF CONTENTS

ABSTRACT	2
ACKNOWLEDGMENTS	3
TABLE OF CONTENTS	5
LIST OF FIGURES	8
LIST OF TABLES	15
1. INTRODUCTION	17
1.1. Motivation	17
1.2. Background	18
1.3. Context	19
1.4. Organization of This Report	20
1.5. References	21
2. LITERATURE REVIEW	23
2.1. Corrosion, Electrochemical Corrosion Potential (ECP) and ECP Measurements	23
2.2. Stress Corrosion Cracking	36
2.3. The Slow Strain Rate Technique	44
2.4. Irradiation Assisted Stress Corrosion Cracking	48
2.5. References	62
3. EXPERIMENTAL FACILITY DESCRIPTION	67
3.1. Facility Overview	67
3.2. In-Core Tensile Rig	69
3.2.1. Load Train	69
3.2.2. Strain Measurement by DCPD	73
3.2.3. Loading Machine and Loading Machine Control	85
3.2.4. Test Specimen ECP Measurement	86
3.2.5. Autoclave	89
3.2.6. Thimble	90
3.2.7. Dummy Element	91
3.2.8. CO ₂ Thimble Atmosphere	92
3.3. In-Core ECP Mapping Rig	94
3.3.1. Rig Description	94
3.4. Water System	97
3.4.1. Main Recirculation Loop	97
3.4.2. Main Loop Heater and Heater Control	100
3.4.3. Charging System	103
3.4.4. Letdown System	105
3.4.5. Clean Up System	108
3.4.6. Bubbling System	110
3.4.7. Chemical Injection System	111
3.4.8. Pressurizer and Pressure Relief	112
3.4.9. Auxiliary Cooling Water System	113
3.4.10. Instrumentation and Interlocks	114

3.5	Data Acquisition	116
3.5.1.	In-Core ECP Mapping	117
3.5.2.	In-Core SSRT Testing.....	118
3.6.	Radioactive Rig Handling System	119
3.6.1.	Introduction	119
3.6.2.	Component Description	120
3.7.	Radioactive Specimen Handling and Post Test Analysis	124
3.7.1.	Preparing SSRT Specimens for In-Core SSRT Testing.....	124
3.7.2.	Preparing Fractured SSRT Specimens for SEM Analysis	125
3.8.	Facility Support.....	126
3.8.1.	Reactor Top Lid	126
3.8.2.	Experimental Platform	127
3.9.	References	127
4.	FUNCTIONAL CHARACTERISTICS OF THE FACILITY	128
4.1.	Main Loop Water Volume	129
4.2.	Reactivity Calculations.	130
4.3.	Main Loop Thermal-Hydraulic Characteristics.	131
4.4.	Shielding Requirements	133
4.4.1.	Shielding Requirements for Transport of In-Core Components	133
4.4.2.	Shielding Requirements for Transport of Pre-Irradiated Specimens	136
4.4.3.	Shielding Requirements for Post SSRT Fracture Surface Analysis by Scanning Electron Microscopy	137
4.4.4.	Shielding Requirements for Main Loop Water Volume	138
4.5.	Stress Analysis	138
4.5.1.	Thimble	141
4.5.2.	Autoclave	141
4.5.3.	Load Train.....	141
4.5.4.	Potential for Hydrogen Embrittlement of Titanium Sections	142
4.5.5.	Transfer Cask and Rig Handling Equipment	142
4.6.	References	143
5.	TESTING AND RESULTS	145
5.1.	Experimental Characterization.....	145
5.1.1.	Load Train Compliance Test.....	145
5.1.2.	Facility Thermal-Hydraulic Characterization	148
5.1.3.	Specimen Load-Thermal Stability Test	151
5.1.4.	DCPD/Strain Calibration	152
5.1.5.	ECP Electrode Verification and Rig Pre-Conditioning	156
5.1.6.	Out of Core High Temperature Tensile Tests	164
5.1.7.	Reactivity Testing	168
5.2.	In-core ECP Mapping	170
5.2.1.	Overview	170
5.2.2.	Test Description	171
5.2.3.	Results.....	173
5.2.4.	Discussion	183
5.3.	In-core Tensile Testing	188
5.2.1.	Overview	188
5.2.2.	Test Description	188
5.2.3.	Results and Fractography	192
5.2.4.	Discussion	219
5.4.	References	225

6. CONCLUSIONS.....	227
6.1. Conclusions of In-Core ECP Measurements	227
6.2. Conclusions of In-Core Tensile Tests	228
6.3. Recommendations for Future Work.....	229
APPENDIX A. DETAILED DRAWINGS	231
APPENDIX B. FUNCTIONAL CHARACTERISTICS OF THE FACILITY.....	247
B.1. Water Volume	247
B.2. Rig Worth.....	248
B.3. ECP Rig Worth	249
B.4. Fluid Flow Characteristics of the Main Loop	250
B.5. Titanium Mass of In-Core Rig	251
B.6. Main Loop Radiation Levels-SSRT Rig	252
B.7. Main Loop Radiation Levels-ECP Rig	253
APPENDIX C. OPERATING INSTRUCTIONS	254
C.1. Facility Startup Operations	254
C.1.1. Specimen Loading onto Load Train Grips	254
C.1.2. Assembling the Facility in its In-Core Test Position	257
C.1.3. Tensile Test Startup	265
C.2. Facility Shutdown Operations.....	267
C.2.1. Securing From a Tensile Test	267
C.2.2. Disassembling the Entire Testing Facility From the Reactor Top....	269
C.2.3. Removal of the Fractured Test Specimen	275
C.3. Other Facility Operations	276
C.3.1. Removal of the Load Train to the Hot Cell for Specimen Replacement and Immediate Re-Testing	276
C.3.2. Removing Dissolved Gases From the Charging Tank by Venting the Charging Tank	277
C.3.3. Adding Water to the Charging Tank	278
C.3.4. Adding Additional Gas to the Charging Tank	280
APPENDIX D. RESULTS FROM IN-CORE ECP MEASUREMENTS.....	281
APPENDIX E. MECHANICAL PROPERTIES TEST OF SPECIMEN 80.	286

LIST OF FIGURES

Figure 2.1.	Electrochemical reactions occurring during corrosion of iron in oxygenated water.	24
Figure 2.2.	Schematic of a circuit to measure the electrode potential of a metal specimen.	26
Figure 2.3.	Representation of transport and kinetic processes in electrode reactions.	28
Figure 2.4.	Electrode potential-current density behavior of a cathodically biased half-cell reaction showing regions of activation control, transport control, and the transition between the two polarization mechanisms.	29
Figure 2.5.	Polarization diagram for the oxidation of iron in oxygenated water.	31
Figure 2.6.	Polarization diagram for the same reaction illustrated in Figure 2.4. shown with increased oxygen concentration.	32
Figure 2.7.	Polarization diagram for the same reaction illustrated in Figure 2.4. shown with added transport control.	33
Figure 2.8.	Polarization diagram for a passivating metal.	34
Figure 2.9.	Polarization diagram for the recombination of H ₂ and O ₂ on a platinum surface. H ₂ is in stoichiometric excess of O ₂ . The exchange current density for the hydrogen reaction on platinum is higher than the recombination rate.	35
Figure 2.10.	Relationships between time-to-failure and applied stress commonly observed in SCC.	39
Figure 2.11.	Relationship between t _f and initial value of stress intensity factor (K).	40
Figure 2.12.	General relationship between stress corrosion crack velocity and stress intensity (K).	41
Figure 2.13.	Stress and computed strain rate over the duration of a CERT test.	46
Figure 2.14.	Typical stress-strain curves for SSRT tests conducted with and without SCC.	47
Figure 2.15.	Effects of radiation on SCC.	49
Figure 2.16.	Relationship between the severity of IASCC and fluence for irradiated type 304 stainless steel under slow strain rate conditions in water at 288°C containing different amounts of oxygen. From reference.	51

Figure 2.17.	Compositional profiles by dedicated STEM analysis across grain boundaries from a HP type 348 stainless steel irradiated to 3.4×10^{21} n/cm ²	52
Figure 2.18.	Effect of neutron fluence on the strength of annealed type 304 stainless steel irradiated of 370°C.	54
Figure 2.19.	Effect of fast neutron fluence under LWR conditions on mechanical properties at 288°C of types 304 and 304L stainless steel.	54
Figure 2.20.	Plot of calculated creep strain rates at 300°C in a fast neutron flux of 5×10^{13} n/cm ² s (E>1 MeV) as a function of stress.	57
Figure 2.21.	IASCC susceptibility as related to ECP.	59
Figure 2.22.	ECP as related to oxidant concentration.	60
Figure 3.1.	The IASCC In-Core Mechanical Testing Facility	70
Figure 3.2.	The in-core SSRT rig specimen and grips.	72
Figure 3.3.	Typical examples of resistance change with strain [2].	75
Figure 3.4.	The DCPD Current Loop.	84
Figure 3.5.	The Instron Loading Machine	87
Figure 3.6.	The Top of the Autoclave.	91
Figure 3.7.	The Thimble Atmosphere Control System.	93
Figure 3.8.	The IASCC In-Core ECP Rig.	96
Figure 3.9.	The IASCC Water Chemistry Control System	98
Figure 3.10.	Main Recirculation Loop	99
Figure 3.11.	Schematic Diagram of the Main Loop Heater Controller.	101
Figure 3.12.	Schematic Diagram for Wiring of Main Loop Heater.	102
Figure 3.13.	Charging System	103
Figure 3.14.	Letdown System.....	106
Figure 3.15.	Clean Up System.....	109
Figure 3.16.	Bubbling System	110
Figure 3.17.	Chemical Injection System	111

Figure 3.18.	Pressurizer and Pressure Relief System	113
Figure 3.19.	Auxiliary Cooling Water System	114
Figure 3.20.	Shielded "Clam Shell" Transport Cask	121
Figure 3.21.	The three ton crane shown lifting the IASCC thimble/autoclave and the shielded "clam shell" transport cask.....	123
Figure 4.1.	Activity of the rig which has in it the most radioactive pre-irradiated SSRT specimen over the course of the rig's lifetime.	136
Figure 5.1.	The rigid test specimen utilized in the load train compliance measurement.	146
Figure 5.2.	Plot of load train extension verses load as measured during the load train compliance test.	147
Figure 5.3.	Plot generated using specimen number 2005 in its first loading.	154
Figure 5.4.	Plot generated using specimen number 2022 in its first loading.	155
Figure 5.5.	Plot generated using specimen number 2022 in its second loading.....	155
Figure 5.6.	Ag/AgCl electrode in top electrode cluster.....	158
Figure 5.7.	Ag/AgCl electrode in bottom electrode cluster.....	158
Figure 5.8.	Stainless steel electrode in top electrode cluster.....	159
Figure 5.9.	Stainless steel electrode in bottom electrode cluster.....	159
Figure 5.10.	Platinum electrode in top electrode cluster.	160
Figure 5.11.	Platinum electrode in bottom electrode cluster.....	160
Figure 5.12.	Dissolved oxygen concentration in letdown line.	161
Figure 5.13.	Calculated ECP of stainless steel in both top and bottom electrode clusters.....	161
Figure 5.14.	Letdown line water conductivity.....	162
Figure 5.15.	Stress vs. strain plot of the two AJ9139 specimens tested. Specimen number 2012 was furnace sensitized. Both specimens were cold worked to 30% following any heat treatment.	165
Figure 5.16.	Fracture surface from specimen 2005.....	166
Figure 5.17.	Fracture surface from specimen 2012.....	166
Figure 5.18.	Intergranular and ductile fracture surfaces from specimen 2012.....	167

Figure 5.19.	In-core ECPs measured and letdown line oxygen levels for the first 10 days of in-core testing. Shaded areas at the bottom of the graph indicates reactor operation at 4.5 MW unless otherwise specified.	174
Figure 5.20.	In-core ECP and letdown line oxygen for in-core testing days 8 through 20.	175
Figure 5.21.	In-core ECP and letdown line oxygen and hydrogen for days 17 through 26. ECPs are converted to SHE using the in-core Ag/AgCl electrodes.	178
Figure 5.22.	Letdown line conductivity for in-core testing at position 1.	180
Figure 5.23.	In-core ECP and letdown line oxygen and hydrogen for in-core testing in position 2. ECPs are converted to SHE using the in-core Ag/Ag/Cl electrodes.	182
Figure 5.24.	Letdown line conductivity for in-core testing at position 2.	182
Figure 5.25.	Temperature in both electrode clusters, in-core ECP and letdown line dissolved oxygen recorded during the 200°C run.	186
Figure 5.26.	In-core ECP and letdown line oxygen and hydrogen for days 19 through 23. ECPs are converted to SHE using the in-core platinum electrodes.	186
Figure 5.27.	In-core ECP and letdown line oxygen and hydrogen for HWC runs in position 2. ECPs are converted to SHE using the in-core platinum electrodes.	187
Figure 5.28.	Stress strain curve for initial in-core tests.	193
Figure 5.29.	Strain and strain rate for testing of specimen 2021.	194
Figure 5.30.	Strain and strain rate for testing of specimen 2003.	195
Figure 5.31.	Strain and strain rate for testing of specimen 80.	196
Figure 5.32.	Strain and strain rate for testing of specimen 82.	197
Figure 5.33.	The fracture surface of specimen 2003. 97% of the surface was intergranular. A small ductile region appears at the top of the picture.	198
Figure 5.34.	The side of specimen 2003. The specimen's diameter is reduced by less than 5%.	198
Figure 5.35.	Ductile section of the fracture surface.	199
Figure 5.36.	Magnified image of small ductile sites.	199
Figure 5.37.	Intergranular fracture surface of specimen 2003.	200

Figure 5.38.	Magnified image of intergranular fracture surface.	200
Figure 5.39.	Side view of shear ductile fracture surface.	201
Figure 5.40.	Magnified image of shear ductile fracture surface.....	201
Figure 5.41.	Side of specimen 2003 away from the fracture surface. A small crack is seen in the center of the image.	202
Figure 5.42.	Magnified image of the crack illustrated in Figure 5.42.....	202
Figure 5.43.	Side of specimen 2003 away from the fracture surface. Several cracks are seen.....	203
Figure 5.44.	Magnified image of large crack in upper right side of Figure 5.44.	203
Figure 5.45.	One of several small cracks found on the side of the specimen away from the fracture surface.	204
Figure 5.46.	One of several small cracks found on the side of the specimen away from the fracture surface.	204
Figure 5.47.	Fracture surface of specimen 80. A small intergranular surface was found in the bottom edge of the fracture surface. The reduction in area was 65%.	205
Figure 5.48.	A magnified image of the ductile fracture surface of specimen 80.	205
Figure 5.49.	The top left quadrant of specimen 80's fracture surface.	206
Figure 5.50.	The bottom left quadrant of specimen 80's fracture surface. The intergranular surface is seen in the bottom of the image.	206
Figure 5.51.	The top right quadrant of specimen 80's fracture surface.	207
Figure 5.52.	The bottom right quadrant of specimen 80's fracture surface.	207
Figure 5.53.	Side image of the fracture surface of specimen 80.	208
Figure 5.54.	Typical blunted cracks found on the side of specimen 80 away from the fracture surface.	208
Figure 5.55.	Magnified image of blunted crack shown in figure 5.53. Note the small cracks emanating from the corners of the blunted crack.	209
Figure 5.56.	Image of side of specimen 80 away from the fracture surface showing slip bands, and small intergranular, transgranular and blunted cracks. ..	209
Figure 5.57.	Magnified image of transgranular cracks on the side of specimen 80....	210
Figure 5.58.	Fracture surface of specimen 82. 9% of the fracture surface was found to be intergranular. The reduction in area was 60%.	211

Figure 5.59.	Side view of specimen 82's fracture surface showing reduction in diameter and large blunted cracks.	211
Figure 5.60.	Top left quadrant of the fracture surface. Intergranular and transgranular surfaces are seen on the left side of this image.	212
Figure 5.61.	Bottom left quadrant of the fracture surface. An intergranular surface is seen at the bottom right corner of this image.	212
Figure 5.62.	Top right quadrant of the fracture surface.	213
Figure 5.63.	Bottom right quadrant of the fracture surface.	213
Figure 5.64.	A magnified image of the intergranular surface seen in Figure 5.60.	214
Figure 5.65.	Side view of the intergranular surface seen in Figure 5.63. Note the slip bands to the side of the intergranular surface, but no slip bands in line with the intergranular surface.	214
Figure 5.66.	Magnified view of the intergranular surface seen in Figure 5.59. The intergranular surface becomes transgranular and finally ductile.	215
Figure 5.67.	A large crack on the side of specimen 82 which became blunted. This crack is seen in the lower right side of the specimen's side in Figure 5.58.	215
Figure 5.68.	Cracks in the side of specimen 82.	216
Figure 5.69.	Intergranular, transgranular and blunted cracks on the side of specimen 80.	216
Figure 5.70.	Transgranular cracks emanating from the corner of a blunted crack.	217
Figure 5.71.	Cracks at what appears to be a grain triple point.	217
Figure 5.72.	Transgranular cracks.	218
Figure 5.73.	Cracks and blunted cracks.	218
Figure D.1.	Raw position 1 data for Ag/AgCl electrodes in the top and bottom clusters and reference autoclave.	281
Figure D.2.	Raw position 1 data for platinum electrodes in the top and bottom clusters and reference autoclave.	281
Figure D.3.	Raw position 1 data for stainless steel electrodes in the top and bottom clusters and reference autoclave.	282
Figure D.4.	Position 1 data for letdown line dissolved oxygen and hydrogen concentration.	282
Figure D.5.	Position 1 data for Temperature.	283

Figure D.6.	Raw position 2 data for Ag/AgCl electrodes in the top and bottom clusters and reference autoclave.	283
Figure D.7.	Raw position 2 data for platinum electrodes in the top and bottom clusters and reference autoclave.	284
Figure D.8.	Raw position 1 data for stainless steel electrodes in the top and bottom clusters and reference autoclave.	284
Figure D.9.	Position 2 data for letdown line dissolved oxygen and hydrogen concentration.	285
Figure D.10.	Position 1 data for Temperature.	285
Figure E.1.	Mechanical property test of specimen 80, alloy 304 irradiated to $0.8 \times 10^{21} \text{cm}^{-2}$ ($E > 1 \text{MeV}$).	286

LIST OF TABLES

Table 2.1.	Electrode potentials of some common reference electrodes.	27
Table 2.2.	Alloy/Environment Systems Exhibiting SCC [10].	38
Table 2.3.	IASCC Service Experience [19].	50
Table 2.4.	Strain rate as a function of applied constant load at 550°C under fast neutron irradiation [2].	55
Table 2.5.	Strain rate as a function of applied constant load at 300°C under fast neutron irradiation.	56
Table 2.6.	Strain rate as a function of applied constant load at 300°C under fast neutron flux of $1 \times 10^{14} \text{ n/cm}^2 \text{ s}$ ($E > 0.1 \text{ MeV}$).	56
Table 2.7.	Linear energy transfer (LET) and G-values for some radiation species [18].	58
Table 3.1.	Load Train Components.....	69
Table 3.2.	Clean up system valve line up for charging tank clean up.....	109
Table 3.3.	Temperatures monitored in the water system.	115
Table 3.4.	The ranges and accuracy's of letdown line instrumentation.	116
Table 3.5.	Data acquisition wire designation used for in-core ECP mapping.	118
Table 3.6.	Data acquisition wire designation during in-core SSRT testing.	119
Table 5.1.	Computation of load train stiffness.	148
Table 5.2.	Temperatures measured and the heat loss calculated using these temperatures for various charging rates.	150
Table 5.3.	Temperature excursion for several heater demands.	151
Table 5.4.	Temperature effects on specimen strain.....	152
Table 5.5.	Average values and associated errors for the parameters α and β determined during the DCPD calibration.....	155
Table 5.6.	Major Events in Pre-Filming.....	163
Table 5.7.	Measurement of the rig's reactivity addition in the fully flooded condition.....	168

Table 5.8.	Measurement of the rig's reactivity addition in the dry condition.	169
Table 5.9.	Measurement of the rig's reactivity addition in the 50% flooded condition.....	169
Table 5.10.	Parameters controlled during for in-core SSRT testing.	189
Table 5.11.	Letdown water chemistry during in-core SSRT testing.	192

1. INTRODUCTION

1.1. Motivation

Environmental degradation of structural materials is a large concern to the nuclear power industry. It is responsible for limiting power plant reliability and availability, and may become significant in nuclear reactor plant lifetime extension assessments. Failure of in-core structural components requires repair or replacement resulting in expensive power plant downtime. The cost of one day's electrical capacity lost by a typical large nuclear power station is estimated to be \$800,000 or more. Maintenance on in-core components is difficult because of high radiation levels. ALARA concerns prevail and nonstandard procedures must be developed. Disposing of failed radioactive components is becoming increasingly expensive because of the present low level waste storage environment, and waste handling presents additional personnel exposure concerns. Failure of structural components during operation may present reactor safety issues. Moreover, since the lifetime cost of a nuclear power plant includes an initial capital layout that is large when compared to the initial capital layout for construction of fossil powered electric generator plants, extending the lifetime of a nuclear power plant is very attractive. It is estimated that a life extension for one nuclear power station of 20 years could save the utility \$600 million or more [1,2]. Material performance qualification standards for use in extending power plant licenses can be expected.

The phenomena of materials degradation in a nuclear reactor are not completely understood. Fast neutron irradiation from the fission process interacting with material creates defects in the material's crystal lattice which can affect the mechanical performance of these materials. Reactor structural materials are typically iron or nickel based alloys containing chromium which imparts its general corrosion resistance in

typical light water reactor environments. The steels, however, are susceptible to localized forms of corrosion including environmentally assisted cracking (EAC).

EAC is the phenomena whereby a crack in a structural material can propagate under a tensile load significantly lower than the expected critical tensile load to cause failure. For EAC to occur a specific material/environment condition must be established. The costs to the nuclear power industry resulting from unscheduled plant shutdowns as a result of EAC are high. In 1990 alone the lost electrical generating capacity resulting from unscheduled plant shutdowns is estimated to be in excess of 1280 days with a cost estimated to be over \$300 million. Repairs and remedial actions made necessary because of EAC of reactor internal structural components have increased annual O&M and capital costs by an estimated \$1 billion [3]. EAC consists of several cracking mechanisms including stress corrosion cracking (SCC), hydrogen embrittlement, corrosion fatigue, and liquid metal embrittlement. When a solution-annealed stainless steel, exposed to neutron and gamma radiation, cracks intergranularly under tensile stress in an oxidizing water environment the cracking mechanism is called irradiation assisted stress corrosion cracking (IASCC).

1.2. Background

IASCC was first observed in the early 1960's. Solution-annealed 304 stainless steel was used as fuel cladding in early pressurized water reactors (PWR). High tensile stresses were present because of fuel swelling and therefore high tensile stresses were initially considered to be required for IASCC to occur. Since then, it has become apparent that lower stresses may cause cracking if the material is exposed to increased fast neutron fluences. In the 1970's, for example, cracking in creviced locations in instrument dry tubes and control blade handles and sheaths was observed with tensile stresses considered at that time to be lower than the minimum stress required for IASCC to occur. Similar failures have been reported in commercial and US Navy test

pressurized water reactors (PWR), and in steam generating, heavy water reactors (SGHWR), which indicates that the problem is generic to all water reactor types [4]. To date, IASCC in reactor internals has been discovered during routine inspections and therefore has not significantly affected plant availability. However, the implications of IASCC are significant, both in terms of repair and outage costs as well as in the potential for cracking in components, e.g. a boiling water reactor's (BWR) upper guide plate, which may be extremely difficult to repair.

1.3. Context

The Tokyo Electric Power Company (TEPCo) and the Electric Power Research Institute (EPRI) funded the IASCC project at the Massachusetts Institute of Technology (MIT) with a goal to advance the general understanding of IASCC. The scope of the MIT IASCC project is described in this section.

The MIT IASCC project focused on the intergranular cracking of austenitic stainless steels subjected to a fast neutron fluence. Several tasks were undertaken to meet the projects goals. A variety of material specimens were irradiated under highly controlled temperature and environmental conditions [5]. Irradiated TEM specimens were used for metallurgical evaluation. TEM analysis was used to characterize the irradiated microstructure. STEM analysis measured the degree of major element segregation. A computer code was developed to predict the degree of radiation induced segregation (RIS) of major austenitic stainless steel elements (chromium, Iron, and Nickel) [6,7]. The STEM analysis was used to benchmark the RIS code.

Efforts are being made to apply two electrochemical techniques to RIS characterization. While analytical electron microscopy provides a large amount of information about individual grain boundaries, electrochemical techniques have the potential to provide more global and average information on material damage. The two

electrochemical techniques undergoing evaluation are a modified electrochemical potentiokinetic repassivation (EPR) technique for grain boundary chromium depletion, and a fixed transpassive technique for impurity (Si, P) segregation [8].

Theoretical activities include the development of bulk water radiolysis and crevice chemistry models [9, 10]. Experimental activities include an in-core boiling coolant corrosion loop [11], an in-core slow strain rate tensile (SSRT) testing facility, and an in-core crack growth sensor facility [12].

The author of this thesis led the group which did the final design, constructed and placed into service an in-core SSRT facility, the centerpiece of the IASCC program. The facility was intended to be used to test the susceptibility of pre-irradiated specimens to IASCC in a variety of environments including normal BWR water chemistry (NWC) and hydrogen water chemistry (HWC), and various fast neutron and gamma fluxes by varying reactor power or sample location. Forthcoming results of testing performed utilizing this facility will be used to develop a model which can be used to determine the degree to which a nuclear reactor structural component is likely to fail by IASCC. Initial testing utilized tensile test specimens irradiated in the dry irradiation facility. These specimens have a nearly identical history to the TEM specimens used in other phases of the IASCC program.

1.4. Organization of this Report

This report is divided into 6 chapters. Chapter 1 contains an outline of the problem which this project addresses, and briefly describes the relation of the project to other efforts. Chapter 2 contains a literature review leading to a description of the state of the knowledge of IASCC. Chapter 3 contains a physical description of facility. Chapter 4 contains the functional characteristics of the facility. Chapter 5 includes results and testing performed using the facility for this thesis. This chapter is divided into 3 sections.

Section 5.1. describes the testing and results obtained in out-of-core testing and other tests leading to initial in-core testing. Section 5.2. covers in-core ECP measurements. Section 5.3. describes the in-core slow strain rate testing performed. Chapter 6 contains conclusions and recommendations for future experiments.

1.5. References

- [1] Bonk, G., Heiges, H., and Stancave, P., "BWR Life Extension Economics", ASME Conference on Plant Aging, 1987

- [2] Tiren, L. I., "Swedish Program on Plant Life Extension", JAIF International Conference on Water Chemistry in Nuclear Power Plants, Tokyo, 1988

- [3] Marston, T. U., and Jones, R. L., "Materials Degradation Problems in the Advanced Light Water Reactors" Proceedings of the Fifth International Conference on the Environmental Degradation of Materials in Nuclear Power Systems: Water Reactors, ANS, Monterey, CA, 1991

- [4] Andresen et al., "State of the Knowledge of Radiation Effects on Environmental Cracking in Light Water Reactor Core Materials: Proceedings of the Fourth International Conference on the Environmental Degradation of Materials in Nuclear Power Systems: Water Reactors, ANS, Houston, TX, 1990

- [5] Boerigter, S. T., "An Investigation of Neutron-Irradiation Induced Segregation in Austenitic Stainless Steels", Sc.D. Thesis, MIT, Cambridge, MA, 1992.

- [6] Mansoux, H., "Experimental Determination of Radiation Induced Segregation Susceptibility in Austenitic Stainless Steels", S.M. Thesis, MIT, Cambridge, MA, 1994.

- [7] Flores, C. D., "Evaluation of Radiation Induced Segregation in Fe-Ni-Cr Alloys", S.M. Thesis, MIT, Cambridge, MA, 1994.

- [8] MIT Nuclear Reactor Laboratory Staff, "Irradiation Assisted Stress Corrosion Cracking and BWR Chemistry Studies", Fifth Annual Report for the Period August, 1992-August, 1993 to Tokyo Electric Power Company and Electric Power Research Institute, Report No. MITNRL-055, 1993.
- [9] Chun J. H., "Modeling of BWR Water Chemistry", S.M. Thesis, MIT, Cambridge, MA, 1990.
- [10] Chun J. H., "Modeling of Crevice Chemistry", Sc.D. Thesis, MIT, Cambridge, MA, 1994.
- [11] Outwater, J. O., "Design, Construction, and Commissioning of an In-Pile BWR Coolant Chemistry Loop", Sc.D. Thesis, MIT, Cambridge, MA, 1991.
- [12] Vergara Aimone, J. A., "The Development of a Facility for the Evaluation of Environmentally Assisted Cracking of In-Core Structural Materials in Light Water Reactors", Ph.D. Thesis, MIT, Cambridge, MA, 1992.

2. LITERATURE REVIEW

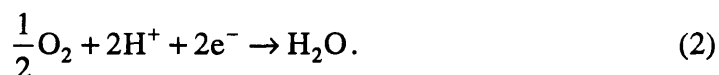
2.1. Corrosion, Electrochemical Corrosion Potential (ECP) and ECP Measurements

Corrosion may be defined as an unintentional attack on a material through reaction with the surrounding medium [1]. According to this definition materials other than metals may be subject to corrosion, but a description of the environmental degradation of metals independent of other materials is required. There is good reason for this. Since metals have a high electrical conductivity, their corrosion is normally of an electrochemical nature. The chemical deterioration of electrically non-conducting materials, such as plastics and ceramics, is governed by other physico-chemical principles [2]. For the purpose of this report only metals in aqueous environments are discussed.

Corrosion of metal typically takes the form of oxidation of metallic atoms to ionic species, for example the oxidation of iron



The results is a phase change, metallic Fe to ionic Fe. To conserve charge a corresponding reduction reaction must take place on the metallic surface, for example the reduction of oxygen



The reduction reaction can take place anywhere on the metallic surface since the electrons are free to conduct throughout the metal, its range, however, is usually limited by the conductivity of the water environment. A typical electrochemical corrosion reaction, which is made up of oxidation and reduction half-reactions, is illustrated in Figure 2.1.

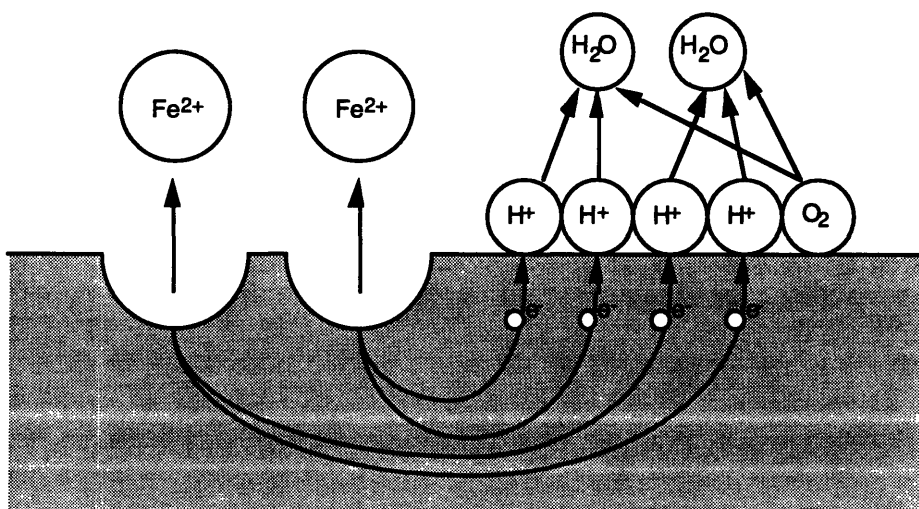


Figure 2.1. Electrochemical reactions occurring during corrosion of iron in oxygenated water.

There exists a change in Gibb's free energy (ΔG) corresponding to the electrochemical corrosion reaction. The free energy change for a chemical reaction at a temperature, T , is given by

$$\Delta G_T = \Delta G_T^0 + RT \ln \left[\prod_i (a_i)^{n_i} \right], \quad (3)$$

where:

- ΔG_T^0 is the standard free energy change for the reaction at the prescribed temperature
- a_i is the activity for species i in the chemical reaction
- n_i is the stoichiometric coefficient for species i in the chemical reaction
- R is the gas constant

This relation is useful as a criterion of corrosion for postulated corrosion reactions. Its main utility is that it allows one to determine if a particular environmental agent (dissolved species) or the solvent can interact chemically with the metallic structure to cause corrosion of the structure. If the computed free energy change is positive, it indicates that corrosion cannot occur by the postulated reaction. However, it does not

mean that it cannot occur due to the reaction of another environmental agent. For this reason, computations of this sort should include all constituents present in the environment. If the computed free energy change is negative, it indicates that corrosion by the postulated reaction is possible. The computation provides no information about the rate of the corrosion reaction.

Electrochemical reactions take place at the interface between a metal and a solution. An electric field exist across this metal-solution interface due to the nature of the reaction and the deposition of ionic and dipolar species on the solution side of the interface. Although this electric field is present, it cannot be measured directly. Instead, a relative measurement is made which provides useful information.

The circuit used in this measurement is shown in Figure 2.2. The electrode under investigation, the working electrode (WE), is connected to a second electrode, the reference electrode (RE), by means of a voltmeter. Since it is necessary to make these measurements in virtual absence of a current flowing in the circuit, the voltmeter should have a high input impedance (typically greater than $10^{10}\Omega$). In addition, it is usually necessary to make measurements over the range of $\pm 2.0V$ with an accuracy on the order of $\pm 1.0mV$.

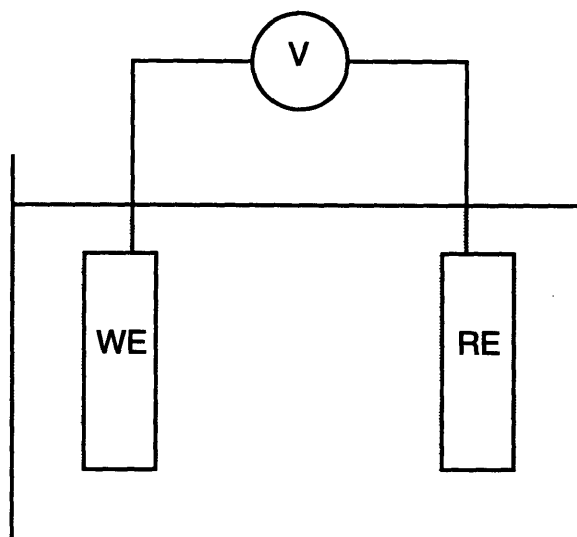


Figure 2.2. Schematic of a circuit to measure the electrode potential of a metal specimen.

The reference electrode should possess a stable, known electrical half-cell potential. Since all electrode potential measurements are relative, it is convenient to have a "universal reference point". By convention, the electrode potential of the hydrogen-hydrogen ion electrochemical reaction



is assumed to have a value of 0.000V when hydrogen gas is at unit fugacity (partial pressure of $\text{H}_2 = 1.0$ atm.) and the hydrogen ion is at unit activity (solution $\text{pH}=0$). This is called the standard hydrogen electrode (SHE). The electrode potentials of some common reference electrodes are given in Table 2.1.

Table 2.1. Electrode potentials of some common reference electrodes.

Name	Electrode Reaction	Electrode Potential (V vs. SHE)
Saturated Calomel	$2\text{Hg} + 2\text{Cl}^- \rightarrow \text{Hg}_2\text{Cl}_2 + 2\text{e}^-$	0.241
Saturated Copper-Copper Sulfate	$\text{Cu} \rightarrow \text{Cu}^{2+} + 2\text{e}^-$	0.298
Silver-Silver Chloride	$\text{Ag} + \text{Cl}^- \rightarrow \text{AgCl} + \text{e}^-$	0.234 (for 1.0 M KCl)

The half-cell potential of the working electrode (test specimen) shown in Figure 2.2. is the voltage measured on the voltmeter and is reported as x.xxxV vs. reference electrode. If it is required to convert the value of the electrode potential of the working electrode from one reference electrode scale to another, this is accomplished by

$$\phi_2 = \phi_1 + \phi_{1/2}, \quad (5)$$

where ϕ_2 is the working electrode half-cell potential relative to the second reference electrode (the desired quantity), ϕ_1 is the working electrode half-cell potential relative to the first reference electrode (measured quantity), and $\phi_{1/2}$ is the electrode half-cell potential of the first reference electrode relative to the second reference electrode.

The Nernst equation is derived using equation 3 to be

$$\phi_0 = \phi^0 + \frac{RT}{nF} \ln \left[\prod_i (a_i)^{n_i} \right], \quad (6)$$

where: F is Faraday's constant.

n is the number of equivalents in the chemical reaction.

and may be used to compute equilibrium half-cell potentials for electrochemical reactions. Activities and/or activity coefficients are not necessarily available for ionic species in most corrosive solutions. For these cases, the concentrations of the species are

used in place of the respective activities when computing equilibrium electrode potentials.

The transport of chemical species from the bulk of the solution to the metal/solution interface is required for the electrochemical reaction to be sustained. Figure 2.3. is a representation of the processes which constitute the entire electrochemical reaction.

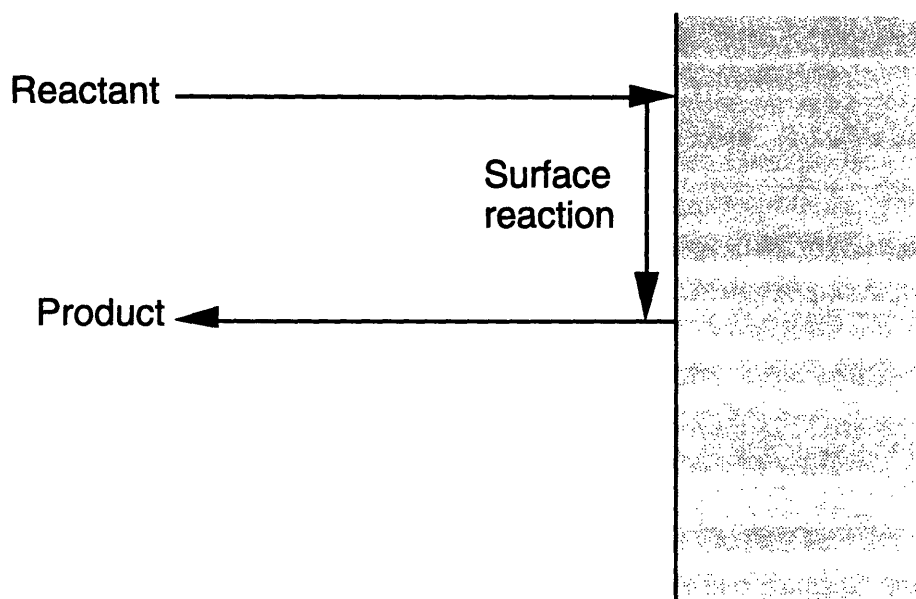


Figure 2.3. Representation of transport and kinetic processes in electrode reactions.

The three steps associated with electrochemical reactions are transport of the reactants to the interface, the electron transfer reaction, and transport of products from the interface. These steps are sequential, and therefore the overall rate of reaction is controlled by the slowest of the three steps. When the transport processes are capable of operating at high rates relative to the electron transfer reaction, the rate of the overall reaction can be described by the equations of electrode kinetics. These kinds of electrode reactions are said to be under activation control. On the other hand, when the electrode reaction is capable of operating at high rates relative to the transport processes, the rate of overall reaction can be described by equations of convective mass transport. These types

of electrode reactions are said to be under transport control. Figure 2.4. illustrates the polarization, or change in electrode potential, of an electrode operating under activation and transport control. The corrosion rate is proportional to current density.

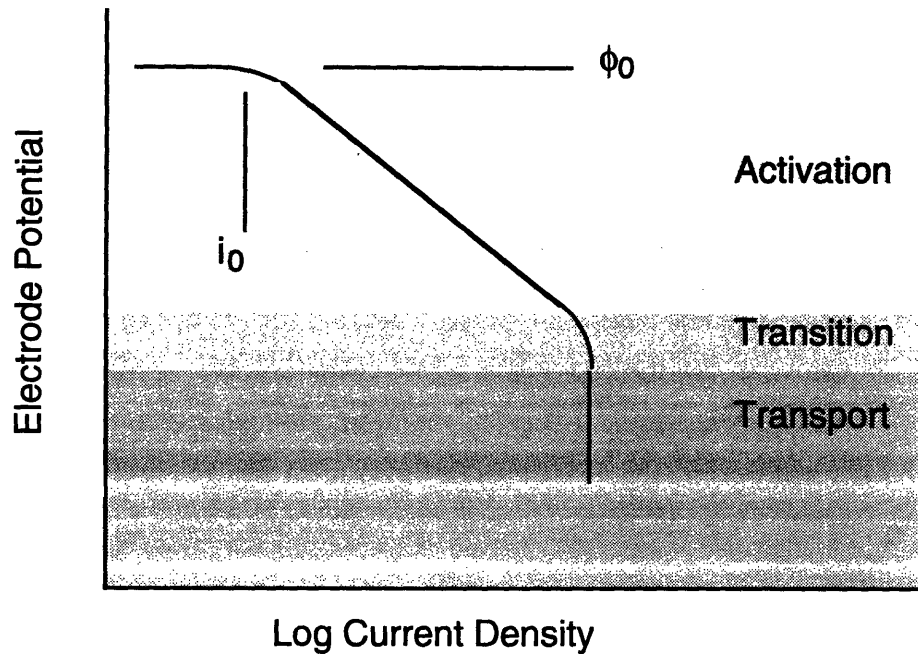


Figure 2.4. Electrode potential-current density behavior of a cathodically biased half-cell reaction showing regions of activation control, transport control, and the transition between the two polarization mechanisms.

In Figure 2.4. ϕ_0 is the equilibrium half-cell potential of the test specimen, or working electrode, with no corrosion present (current density is zero). This is the potential calculated using the Nernst relation (equation 6). As the reaction rate is increased the current density becomes greater than i_0 , and the potential begins to polarize under activation control. The current density labeled i_0 is known as the exchange current density. This is an important parameter because its value has a large effect on the corrosion potential and reaction rate. The exchange current density is different for each half cell reaction, and for the oxidation or reduction of species present in solution such as

oxygen and hydrogen it is dependent on the metal surface on which the reaction takes place on.

Structural components undergoing corrosion are usually not in contact with an external electrical circuit. Both the oxidation and reduction reactions take place on the same surface of the corroding component. Since the equilibrium half-cell potential of the oxidation and reduction reactions are different, the resulting measurable potential of the component is a mixed potential. This potential is known as the electrochemical corrosion potential (ECP). To develop an understanding of a component's ECP, charge conservation of the reactions taking place on the component's surface must be considered.

$$\sum_j i_j(\phi_{\text{corr}}) = 0, \quad (7)$$

where $i_j(\phi_{\text{corr}})$ is the current density of the j^{th} half-cell reaction at the component's ECP, ϕ_{corr} . Figure 2.5. illustrates the resultant ECP of an iron component in oxygenated water.

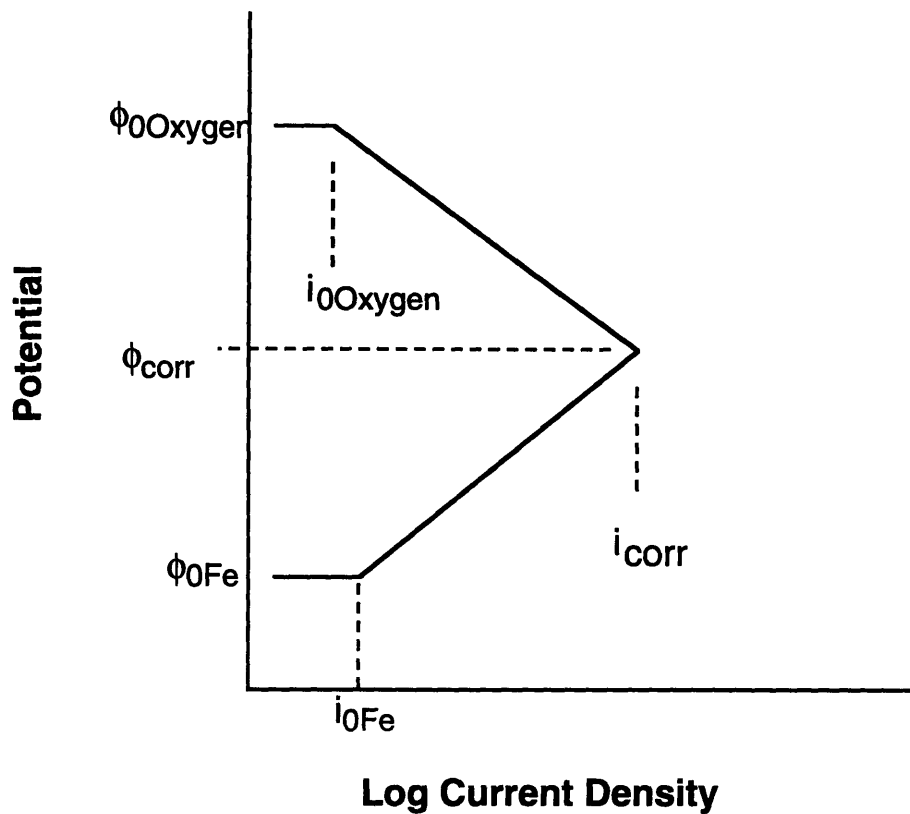


Figure 2.5. Polarization diagram for the oxidation of iron in oxygenated water.

The exchange current densities for the reduction of oxygen on iron and oxidation of iron are labeled $i_{0\text{Oxygen}}$ and $i_{0\text{Fe}}$ respectively. The resultant ECP and corrosion rate (i_{corr}) are also indicated.

Figure 2.6 illustrates the effects of increasing the oxidizer's concentration in the solution. In this example oxygen is the oxidizer. Increasing the concentration of oxygen increases the equilibrium half-cell potential of the reduction reaction. The Nernst relation, equation 6, can be used to verify this phenomena. The result is an increase in ECP and corrosion rate.

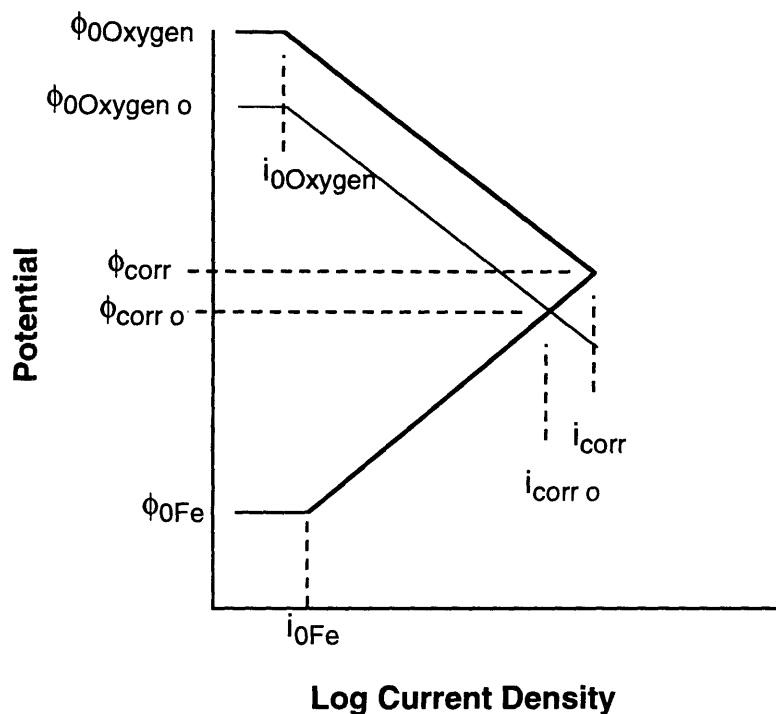


Figure 2.6. Polarization diagram for the same reaction illustrated in Figure 2.4. shown with increased oxygen concentration.

Figure 2.7. illustrates the effects of transport control on the ECP and corrosion rate. Transport of oxidizer, oxygen in this example, can be reduced by reducing the mixing of the solution, e.g., lowering the system's Reynolds number, etc. The result is a decrease in ECP and corrosion rate.

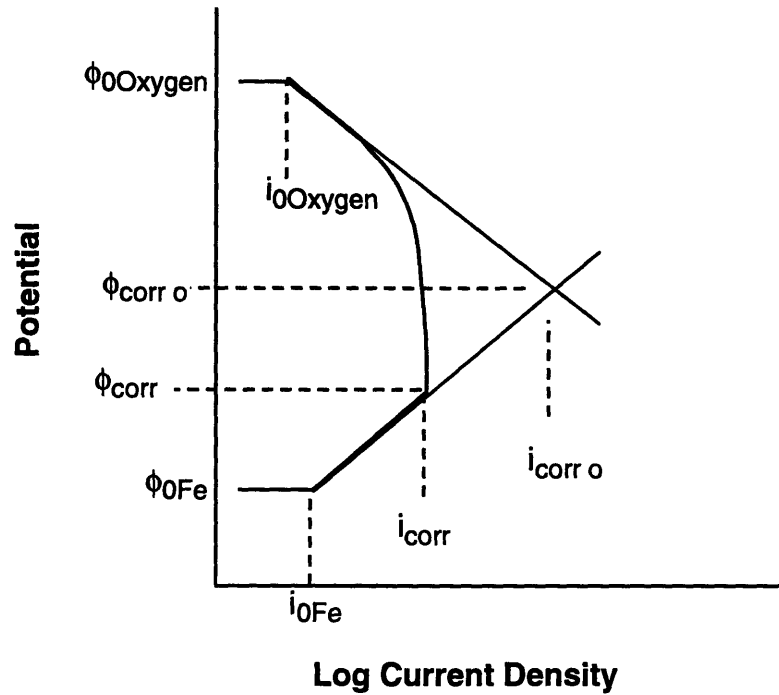


Figure 2.7. Polarization diagram for the same reaction illustrated in Figure 2.4. shown with added transport control.

Some metals passivate when polarized anodically. The result is a decrease in corrosion rate with increasing ECP. As ECP is increased above the passive regime the corrosion rate begins to increase in what is known as the transpassive regime. Passivity is illustrated in Figure 2.8.

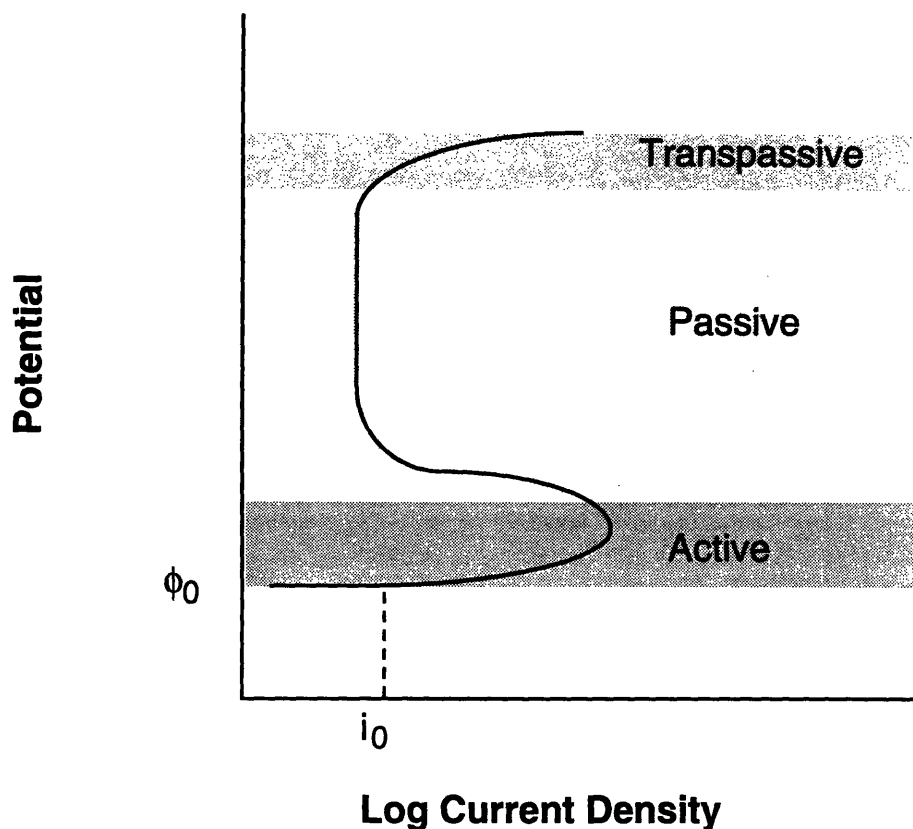


Figure 2.8. Polarization diagram for a passivating metal.

Aluminum, nickel, titanium, and stainless steel are examples of common metals which have a natural ability to resist corrosion by passivating. Although these metals are relatively immune to general corrosion while operating in the passive regime, they can be susceptible to localized forms of corrosion including stress corrosion cracking (SCC) [1]. In fact, the presence of a passive or corrosion film on a metallic surface is required for a material to be susceptible to SCC [5].

Noble metals such as platinum have an equilibrium half-cell potential for most aqueous environments higher than the equilibrium half-cell potential for the oxygen and hydrogen reactions in typical aqueous solutions. In these cases they do not corrode or form a corrosion film on their surface. For these reasons the exchange current densities for the oxygen and especially hydrogen reaction on platinum are high. In aqueous

environments containing both dissolved O_2 and H_2 , such as BWR recirculation and in-core water, the recombination of these two molecular species occurs readily on the surface of platinum. The polarization diagram for this reaction is illustrated in Figure 2.9. For environments with stoichiometric excess H_2 over the O_2 the ECP of the platinum electrode is the equilibrium half-cell potential for the hydrogen reaction which is fully predictable using the Nernst relation, equation 6. Platinum can be used as a reference electrode in nuclear power systems operating under HWC [6].

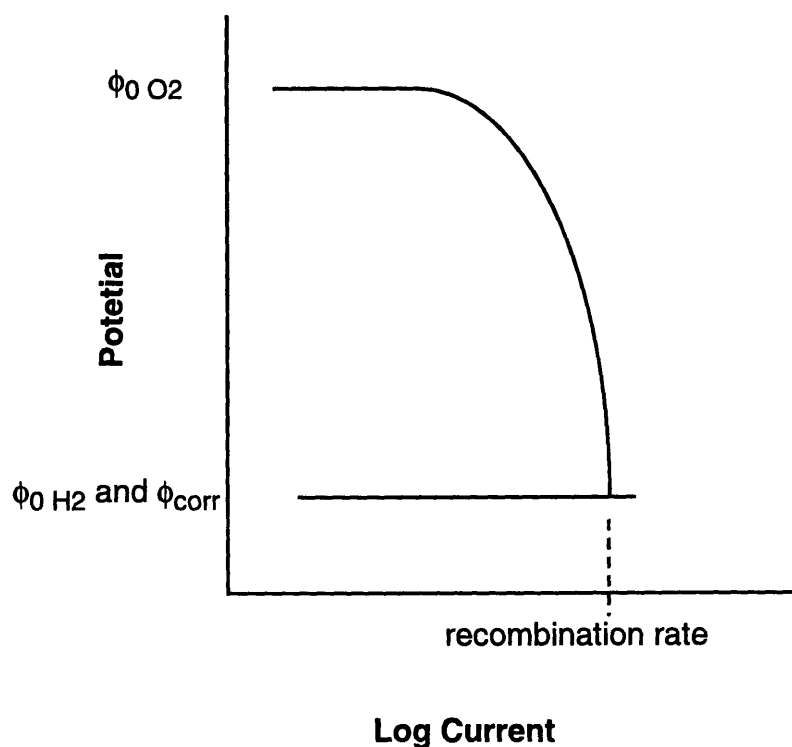


Figure 2.9. Polarization diagram for the recombination of H_2 and O_2 on a platinum surface. H_2 is in stoichiometric excess of O_2 . The exchange current density for the hydrogen reaction on platinum is higher than the recombination rate.

Methods for measuring electrode potentials (ECPs) have been described above. Although the procedure is relatively straightforward, ECP measurements in some environments can be non-trivial, e.g., the high temperature and radiation water environments in the in-core sections of a nuclear power reactor. The knowledge of the

ECP of structural materials in the in-core sections is important. H₂ gas is added to the feedwater of many BWR type nuclear reactors to suppress the ECP of the stainless steel components below -0.230V SHE. Below this potential intergranular SCC (IGSCC) and perhaps IASCC do not occur [7].

2.2. Stress Corrosion Cracking

Stress corrosion cracking (SCC) is the phenomena by which alloys fail by cracking when simultaneously stressed and exposed to certain environments. Failures occur at stress levels well below those which would cause failure in air. While application of the stress may be multi-axial, it is necessary for it to have a tensile component and cracking is usually in the plane perpendicular to it. SCC represents the most highly localized form of corrosion that is ever encountered.

SCC is a complicated phenomena. In order to gain some understanding of SCC, it is necessary to realize that three different disciplines are at work. These are physical metallurgy, electrochemistry and fracture mechanics.

Metallurgical variables which can affect material susceptibility to SCC include both point and line defect concentrations and locations in the crystalline lattice, precipitates in heat treatable alloys, concentration and types of impurity elements which can be both metallic and nonmetallic in nature. Other factors such as surface finish, residual cold work and metallurgical history (what was done to the alloy in bringing the component to its present shape) can also be important.

Texture should be considered. Grain size is important; an alloy generally becomes more susceptible with increasing grain size. Grain shape is also significant. After a manufacturing process during which grain growth occurs in one direction more than another, susceptibility in one direction of a component may be greater than another.

Plastic deformation increases the density of dislocations and these may play an important role in crack propagation. For heat treatable alloys that suffer from SCC, susceptibility is usually increased with increased strength. Finally the path may be transgranular or intergranular. In some alloys it is predominantly one, in others mixed, in still others the cracking mode may depend on the environment or the level of stress. Observations of crack path provide information about mechanisms since they indicate the relative importance of such factors as stress, chemistry and alloy composition.

Electrochemical reactions occur on the metal surfaces and the rates at which they occur affects the susceptibility of an alloy to SCC. The most important parameter is the ECP of the specimen. Changes in ECP will always affect stress corrosion reactions. Conductivity, pH, O₂ levels, solution composition and temperature are also important.

The manner in which the specimen is stressed may affect SCC susceptibility. A condition of plane strain, achieved when the specimen thickness is above a certain value which is related to its strength [8], may sometimes promote greater susceptibility than is observed in specimens below that thickness. The sharpness of cracks (notch root radius) is important. Blunt cracks can be expected to propagate less readily than sharp cracks. Crack or notch depth is important from the viewpoint of stress concentration. Loading mode is critical, being the relation between the directions of applied stress and the plane of cracking.

SCC is often described as a phenomena arising between an alloy and a specific environment. Failures of α -brass in aqueous ammonia, but not in sea water, is an often used example. Stainless steels fail in sea water, but not in aqueous ammonia. Table 2.2. lists some commonly observed types of failures. What needs to be explained is what property or action of a solution or corrodent is necessary to promote SCC. This will be attempted with a discussion of possible SCC mechanisms.

Table 2.2. Alloy/Environment Systems Exhibiting SCC [10].

Alloy	Environment
Mild Steel	Hot nitrate, hydroxide, and carbonate/bicarbonate solutions
High Strength Steels	Aqueous electrolytes, particularly when containing H ₂ S
Austenitic Stainless Steels	Hot chloride solutions, chloride contaminated steam
High Ni alloys	high purity steam
α-brass	aqueous ammonia
Al alloys	aqueous Cl ⁻ , Br ⁻ , and I ⁻ solutions
Titanium alloys	Aqueous Cl ⁻ , Br ⁻ , and I ⁻ solutions, organic liquids, N ₂ O ₄
Mg alloys	Aqueous Cl ⁻ /CrO ₄ ²⁻ solutions
Zr alloys	Aqueous Cl ⁻ solutions; organic liquids, I @ 350°C

Most SCC service failures occur from the influence of residual stresses. These arise during component manufacture and plant assembly, including welding. In laboratory work the stress is usually applied externally since it is then much easier to control and measure. The oldest and simplest test is to measure how long a specimen takes to break, the time to failure, t_f . Specimens are loaded in tension and surrounded by the solution or bent into a U-shape, clamped and then immersed. Typically, the value t_f varies as shown in Figure 2.10. Two observations are made. First, the t_f changes less markedly at stresses above a specified stress than below it. Secondly, it is not always clear whether a threshold stress exists below which SCC does not occur.

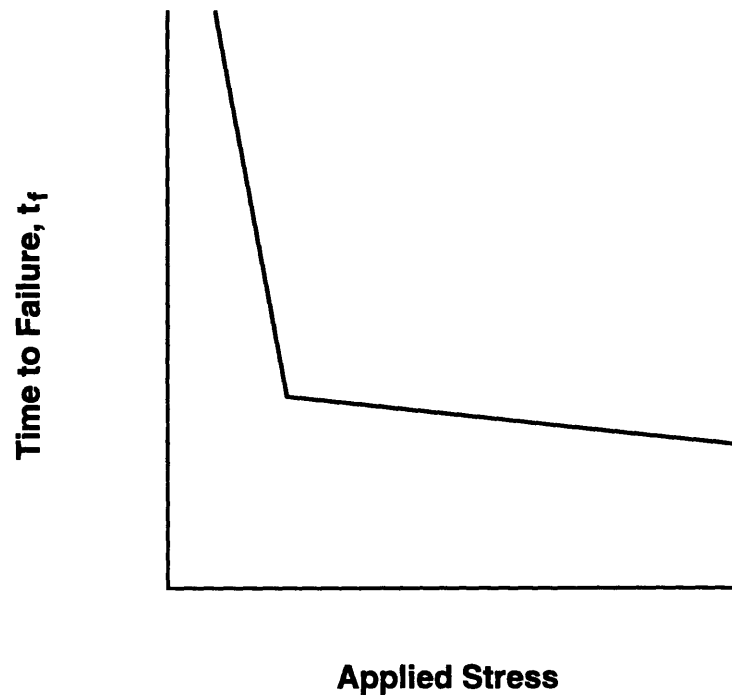


Figure 2.10. Relationships between time-to-failure and applied stress commonly observed in SCC.

In examining all the metallurgical and electrochemical variables that together determine susceptibility, the measurement of t_f is not altogether satisfactory since changes in t_f can arise from two different reasons. Time to failure is made up of two components, the time for the crack to initiate (t_i) and the time for it to propagate (t_p) so that

$$t_i + t_p = t_f. \quad (8)$$

Whether the effect of a changed variable on t_f arises from alterations to t_i or t_p may be of fundamental significance and it is therefore important under some circumstances to distinguish between the two. Engineering structures have numerous surface cracks and flaws arising from fabrication and assembly. If any of these is an incipient stress corrosion crack, t_i becomes unimportant. For this reason crack propagation has received the most attention.

Considerations such as this lead to the use of pre-cracked notched specimens [8]. Testing with this type of specimen takes into account the stress intensity, K , arising from the presence of a crack and applied load. When these specimens are tested, time to failure as a function of stress intensity generally behaves as illustrated in Figure 2.11. The appearance of a threshold stress intensity (K_{Isc}) is apparent. This value describes the stress intensity below which failure does not occur.

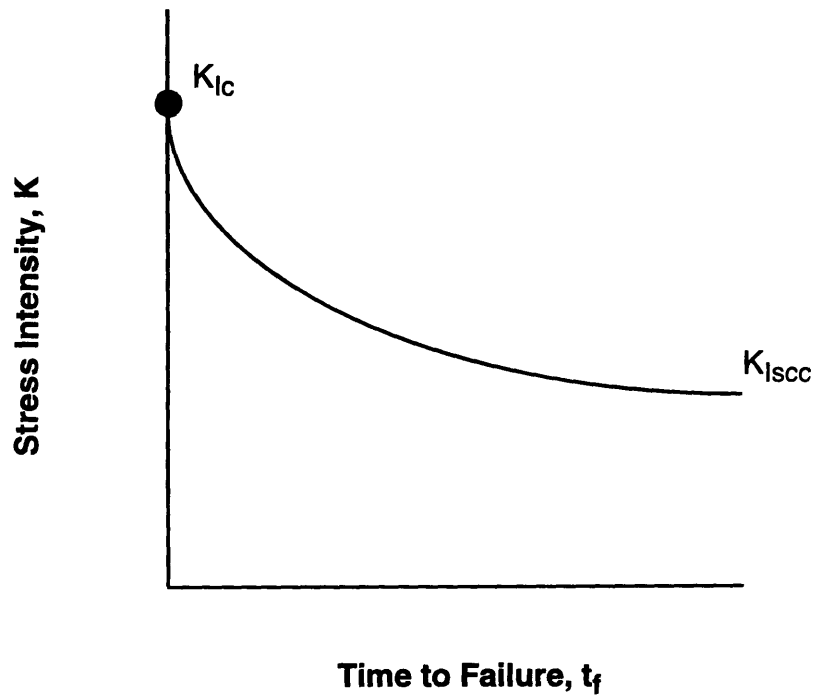


Figure 2.11. Relationship between t_f and initial value of stress intensity factor (K).

Since this test is mainly concerned with crack propagation, measuring crack velocity as a function of K is possible. Figure 2.12 shows the general relationship that exists between crack velocity and K . Three stages of cracking are observed. Stage I shows a logarithmic dependence of crack velocity on K . Stage II is sometimes called the plateau velocity and is generally interpreted as being caused by the chemical or electrochemical reaction at the crack tip being limited by diffusion of a critical reactant or product within the solution. This idea is supported by observations [9] that increasing the

solution viscosity lowers the plateau velocity. Stage III is rarely observed and arises mainly due to mechanical reasons.

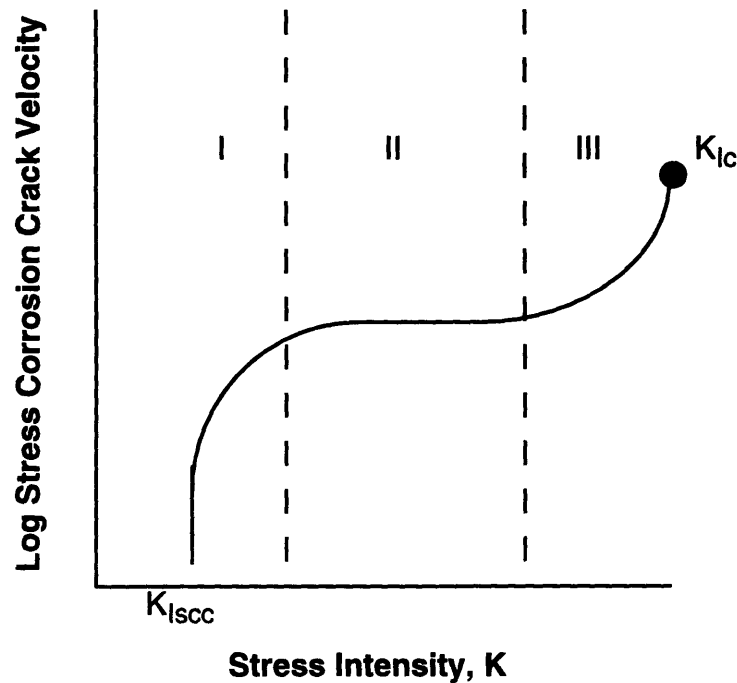


Figure 2.12. General relationship between stress corrosion crack velocity and stress intensity (K).

This type of experiment has been of considerable value. It has become possible to examine all the major variables, one at a time, for their effect on crack growth rate. As a result, it is possible to determine the effect of minute variations in composition, changes in heat treatment, electrochemical variables and changes in the aqueous species.

In many of the alloy systems shown in Table 2.2. the stable configuration of the alloy surface is that it is filmed. The possible mechanisms by which SCC occurs are those reactions between unfiled metals and the environment. Before considering these metal-environment mechanisms it is important to understand the method of film breakdown. Pitting is one method of film breakdown, but is not general to SCC systems. While pitting results in exposing unfiled metal to an aggressive environment it is not

limited to stressed materials like SSC. A more general method of film breakdown is film rupture due to metal surface strain. A slip system intercepting the metal-environment surface under stress results in localized strain at that point of the surface. A large strain breaks the brittle film and exposes metal to the environment where SCC mechanisms can take place [11].

Many researchers agree that an important mechanism for SCC systems is the rate at which the newly exposed metal repassivates, or forms a protective film. If repassivation is prompt the environment has too little time for SCC mechanisms to operate and no cracking can occur. If repassivation occurs slowly, sufficient time will exist for the environment to interact with the exposed metal surface and a crack can extend until the metal eventually repassivates. If very much time passes between film rupture and repassivation too much of the reaction may occur which can result in crack tip blunting or pitting. The film rupture-repassivation sequence occurs repeatedly during SCC until the component fails or conditions leading to SCC are removed, e.g., tensile stress is relieved or the environment is made benign [12].

The many mechanisms proposed for stress corrosion crack extension can be divided into two classes: mechanisms in which cracking proceeds by anodic dissolution of the crack tip material, and mechanisms in which cracking proceeds by mechanical methods [13]. Some proposed SCC models are as follows:

a) Crack propagation by the dissolution of bare metal due to film rupture provided by plastic strain or emerging dislocations at the crack tip. Since SCC takes place with material polarized anodically, corrosion of the exposed crack tip metal is easily conceived. The possible preferential corrosion of dislocations piled up at the crack tips as a result of plastic strain is also considered important. Minute compositional changes in a metal lattice occurring around dislocation pile-ups and

grain boundaries may cause significant directional differences in dissolution on an atomistic scale [10].

b) Crack propagation by the adsorption of surface active species at the crack tip which lowers chemical bonds and thus the surface energy. This mechanism supposes that the reaction between a species in the environment and the metal atoms at the crack tip can cause a redistribution of electrons in the orbits of the atoms so that the bond between them is weakened. The result is a reduction in surface energy which increases the propensity towards cracking under a tensile load [4].

c) Fracture of corrosion product films at the crack tip followed by their subsequent reformation.

d) Combinations of the above.

To minimize the incidence of occurrence of such a widespread type of failure, it is clearly important to know how to avoid SCC. The choices are simple, modifications to the material, environment, or stress as required.

Figures 2.10 and 2.11. shows that reducing the stress can reduce the possibilities of SCC failure. In practice this means that components must be stress relieved following cold work, welding, or any process from which significant residual stresses result. Design can help reduce operating stress levels. There are examples of tanks being operated containing liquids that cause SCC with residual and operating stresses controlled so that K_{Isc} is never exceeded [12]. These requirements are shown to affect both the design and plant engineer.

Modification of the environment, the use of inhibitors, or controlling the ECP of the metal out of the SCC operating range can reduce or even eliminate the tendency for

material failure by SCC. Removal of a damaging species in the environment, e.g., Cl⁻ for stainless steel components, significantly extends the component's lifetime. The use of inhibitors reduces the possibility of SCC. They can be dangerous, however, because if the ECP were to move back into the cracking range cracking can occur. Some inhibitors continue to work even when the ECP is in the cracking range, these inhibitors are commonly referred to as "safe" inhibitors. SCC failures can be eliminated by proper use of cathodic protection. Moving the ECP below the cracking range also lowers the corrosion rate. Care should be taken, however, to ensure that all components are protected and that the ECP is not allowed to return to the cracking region.

Thorough knowledge of a component's operating conditions, including stress state, temperature, and the aqueous environment it is to be operating in, is important in material selection. There exists large amounts of published data on alloy selection for various operating conditions. Care should be taken by the design engineer to ensure that all conditions are considered.

Stress corrosion cracking is a complicated subject. To appreciate the subtleties of this interaction requires both a metallurgical and electrochemical approach. To do accurate tests, potential control is necessary and the investigation of a range of potentials is always required. Commercial alloys are complicated. For example, they consist of impurity constituents that vary in concentration from one heat to another. These and other imperfections can cause cracking.

2.3. The Slow Strain Rate Technique

Most laboratory corrosion experiments try to collect significant amounts of data in short periods of time. This is often achieved by increasing the severity of the test. In SCC testing, environmental composition, temperature, or pressure can be altered to increase the aggressiveness of a test. The test specimen can be polarized galvanistically

or potentiostatically to stimulate the electrochemical reactions on the surface of the specimen, or its cracking susceptibility can be altered by changing its structure or composition. The slow strain rate technique (SSRT) is an accelerated test in that it facilitates cracking in circumstances where in constant load or strain tests cracking is not observed. SSRT tests have the additional advantage that tests are not stopped until the specimen breaks, either by SCC or ductile mechanisms. Constant load or strain tests can vary in length. If no results are obtained the test is usually halted after a period of time that may be arbitrary. Variation of the stopping time from laboratory to laboratory results in significant scatter.

SSRT testing makes use of a smooth tensile specimen strained in relatively stiff frame machines. The specimens are surrounded by the environment of interest then loaded in tension at a constant slow strain rate until fracture. The choice of strain rate is critical. If the strain rate is too high, ductile fracture by void coalescence would occur before the necessary electrochemical reactions could take place to promote SCC. It is also possible for the strain rate to be too low. In this case one can envision a strain rate being slow enough that even slow repassivation occurs rapidly with respect to film rupture. With most systems strain rates between 10^{-7} to 10^{-5} s^{-1} are found to promote SCC [14].

Some testing environments are too aggressive for many standard extensometers used for controlling specimen strain and strain rate. A reasonable alternative to constant strain rate is the constant extension rate technique (CERT) which makes use of a constant cross-head velocity. Cross-head displacement, and finally velocity, is measured by a linear variable differential transducer (LVDT) or extensometer at the loading machine cross-head. The cross-head displacement is the sum of extension of the testing machine and specimen. In the course of a CERT test the strain rate is not fixed. During elastic loading of the specimen the strain rate is constant. With the onset of plastic deformation

an increasing fraction of cross-head displacement goes into specimen strain and the strain rate increases. When necking occurs load drops and specimen strain becomes the sum of cross-head displacement and extension associated with loading rig strain release [16].

Figure 2.13. illustrates the computed strain rate over the duration of a CERT test.

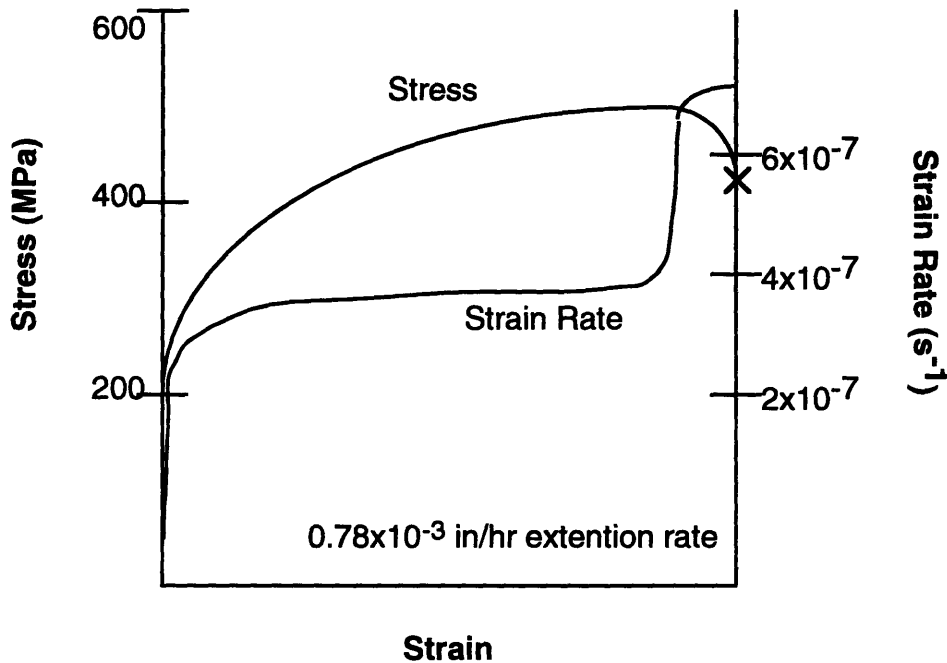


Figure 2.13. Stress and computed strain rate over the duration of a CERT test.

There are many readily measurable and quantifiable parameters that can be used in assessing results from SSRT tests. Comparing the stress-strain curves for 2 tests using similar materials, where one results in SCC and the other does not, provides significant information. In the test in which cracking occurs ultimate load and final strain are significantly lower than for the test in which no cracking occurs. This is illustrated in Figure 2.14.

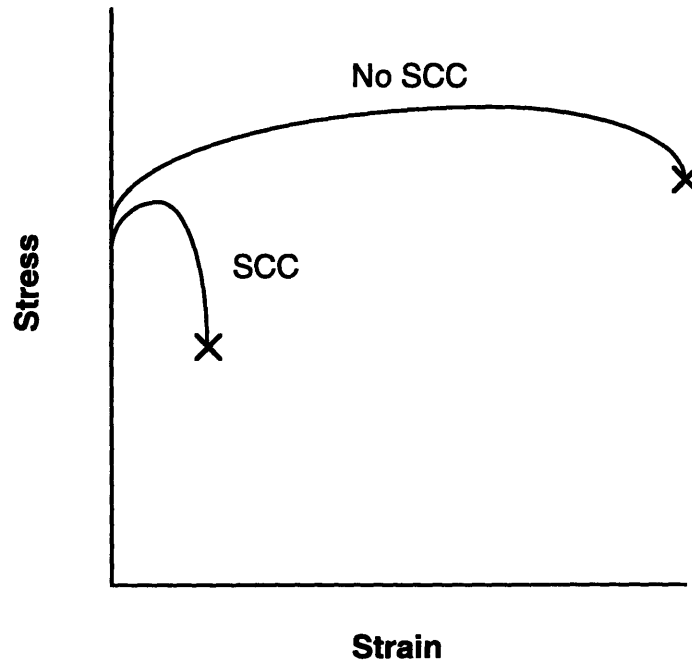


Figure 2.14. Typical stress-strain curves for SSRT tests conducted with and without SCC.

Other parameters that can be measured and are indicative of SCC susceptibility are time to failure, reduction in area, and area beneath the stress-strain curve.

Metallography should always be used to verify the presence or absence of SCC after SSRT testing [15]. Examination of the fracture surface provides quantifiable results. The fraction of the total fracture surface resulting from SCC can be measured; a high SCC percentage indicates a high degree of susceptibility. Secondary cracks provide information that is difficult to quantify. These are shallow surface flaws resulting from either a non-propagating surface phenomena which is not an indication of cracking susceptibility, or from testing in conditions near to SCC susceptibility.

The use of the SSRT in SCC testing has become widespread. The testing of laboratory specimens, even in tests with no SCC occurring, is usually completed within several days to 2 weeks. Testing of similar materials under slightly different conditions

(ECP, strain rate, solution specie concentration, etc.) to determine their effects on cracking susceptibility is incorporated into a test matrix. Results are usually easy to quantify, and more than one parameter can be used to verify SCC. Metallography of fracture surfaces verifies the fracture mechanism, SCC or ductile, and provides a convenient method of assigning a degree of susceptibility (%SCC).

2.4. Irradiation Assisted Stress Corrosion Cracking

Irradiation assisted stress corrosion cracking (IASCC) as a sub-category of SCC requires the simultaneous presence of three conditions: a susceptible material in a specific aggressive environment under tensile stress. Structural components of concern are located in the in-core or near core sections of light water reactors, BWR type reactor designs being the most likely for IASCC incidence. The fast neutron and gamma radiation play a significant role in IASCC in that a fast neutron fluence can make even solution annealed austenitic stainless steels susceptible to SCC in the oxidizing 288°C water present in the in-core and near core reactor sections. Moreover, the fast neutron and gamma radiation makes the initially benign water environment aggressive (oxidizing) by creating the oxidants O_2 and H_2O_2 . The effects of radiation on IASCC parameters are illustrated in Figure 2.15.

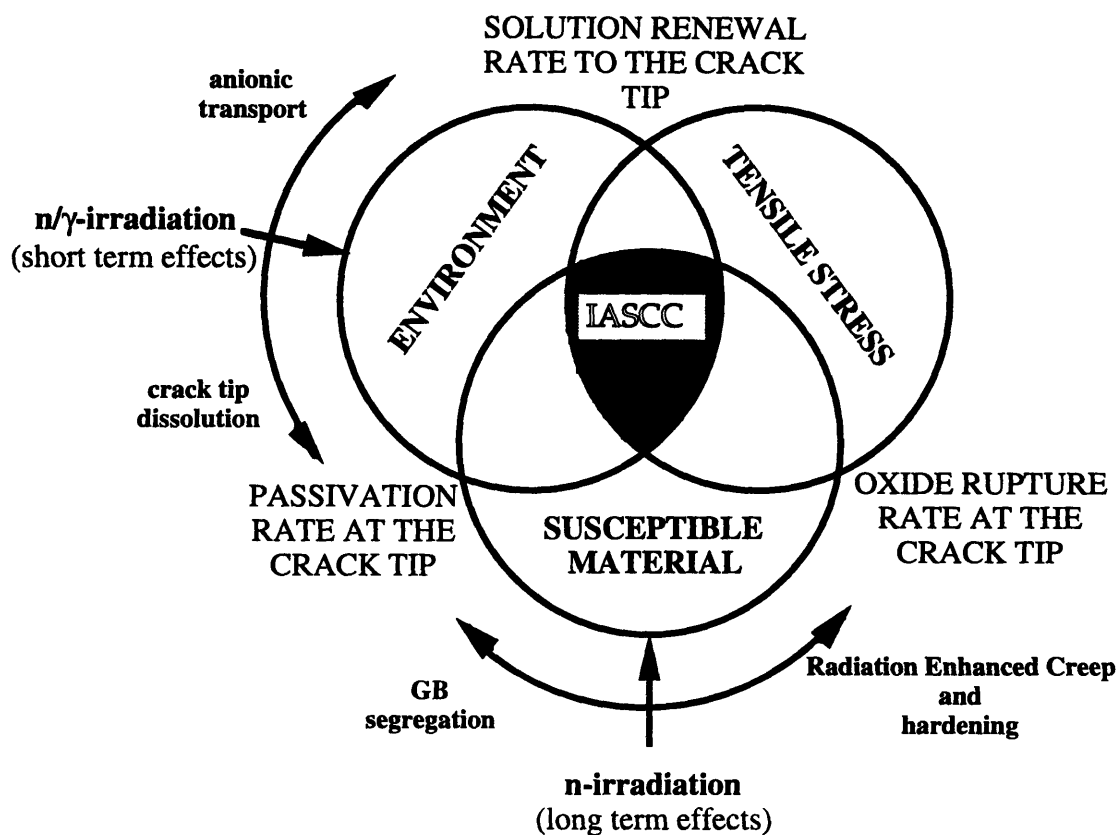


Figure 2.15. Effects of radiation on SCC [17].

The first reported instances of IASCC were in the early 1960's. Despite the use of non-sensitized stainless steels for use as in-core materials, intergranular stress corrosion cracking (IGSCC) of several stainless steel components has been reported for light water reactors or various designs. These failures are listed in Table 2.3.

A summary of trends and correlations noted in field data are as follows [18]:

1. All cracking is intergranular.
2. No intergranular cracking of solution annealed stainless steels is observed in components exposed to a fast neutron fluence less than about 3×10^{21} n/cm².
3. Cracking is observed in components even under relatively low tensile stresses if exposed to higher neutron fluxes.

4. Crevices accelerate cracking.
5. Grain-boundary carbides are not required for susceptibility.

Table 2.3. IASCC Service Experience [19].

Component	Material	Reactor Type	Sources of Stress
Fuel Cladding	304 SS	BWR	Fuel Swelling
Fuel Cladding	304 SS	PWR	Fuel Swelling
Fuel Cladding	20%Cr/25%Ni/Nb	AGR	Fuel Swelling
Fuel Cladding Ferrules	20%Cr/25%Ni/Nb	SGHWR	Fabrication
Neutron Source Holders	304 SS	BWR	Welding and Be Swelling
Instrument Dry Tubes	304 SS	BWR	Fabrication
Control Rod Absorber Tubes	304 SS	BWR	B ₄ C Swelling
Fuel Bundle Cap Screws	304 SS	BWR	Fabrication
Control Rod Follower Rivets	304 SS	BWR	Fabrication
Control Blade Handle	304 SS	BWR	B ₄ C Swelling
Control Blade Sheath	304 SS	BWR	Fabrication
Plate Type Control Blade	304 SS	BWR	Fabrication
Various Bolts *	A-286	PWR&BWR	Service
Steam Separator Dryer Bolts *	A-286	BWR	Service
Shroud Head Bolts *	600	BWR	Service
Various Bolts	x-750	PWR	Service
Guide Tube Support Pins	x-750	PWR	Service
Jet Pump Beams *	x-750	BWR	Service
Various Springs	x-750	BWR&PWR	Service
Various Springs	718	PWR	Service

* Cracking occurs away from high gamma and neutron fluxes.

IASCC represents the first time solution treated 304 was found to be susceptible to cracking in BWR reactor environments; exposure to a fast neutron fluence is responsible for susceptibility [20]. This is illustrated in Figure 2.16.

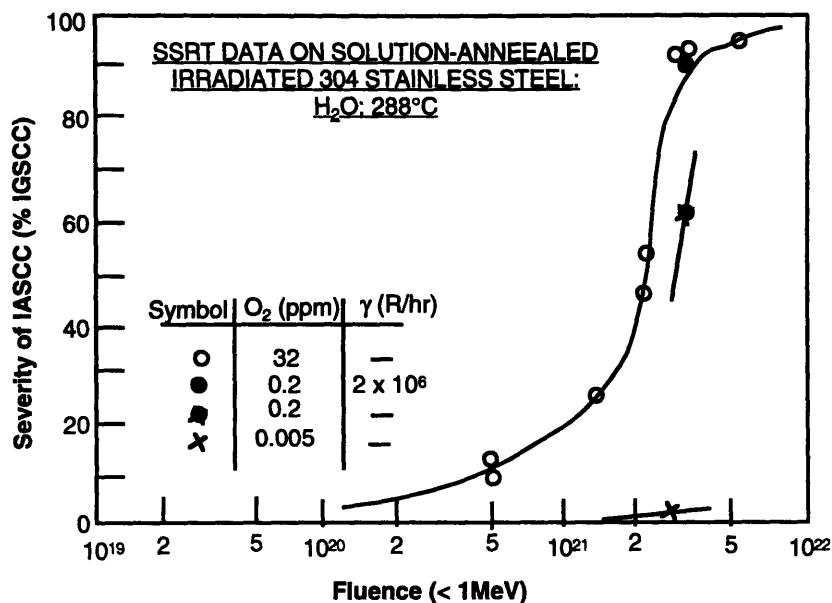


Figure 2.16. Relationship between the severity of IASCC and fluence for irradiated type 304 stainless steel under slow strain rate conditions in water at 288°C containing different amounts of oxygen. From reference [18].

A threshold fluence (of approximately 0.5×10^{21} n/cm²; $E > 1$ MeV) below which IASCC does not occur is apparent. The effects of radiation on material properties are numerous. Some of the effects that could increase cracking susceptibility include radiation induced segregation (RIS), radiation hardening, and radiation creep. Of these RIS has received the most attention. There is good reason for this. RIS is a persistent effect of radiation, its effects remain after the irradiation process ends. SSRT tests on pre-irradiated stainless steels conducted in hot cells using simulated BWR water chemistry reproduce the intergranular cracking found in IASCC. In addition, RIS produces grain boundary chemistry similar to that in furnace sensitized stainless steels. Following neutron irradiation, Cr and Fe concentrations are reduced while Ni, S, Si, and P concentrations are increased at the grain boundaries. No clear consensus has been reached regarding the effect of each constituent on IASCC susceptibility, some researchers attribute cracking to

the impurities (S, P, Si) [21], and others to the depletion of Cr [18]. RIS is illustrated in Figure 2.17.

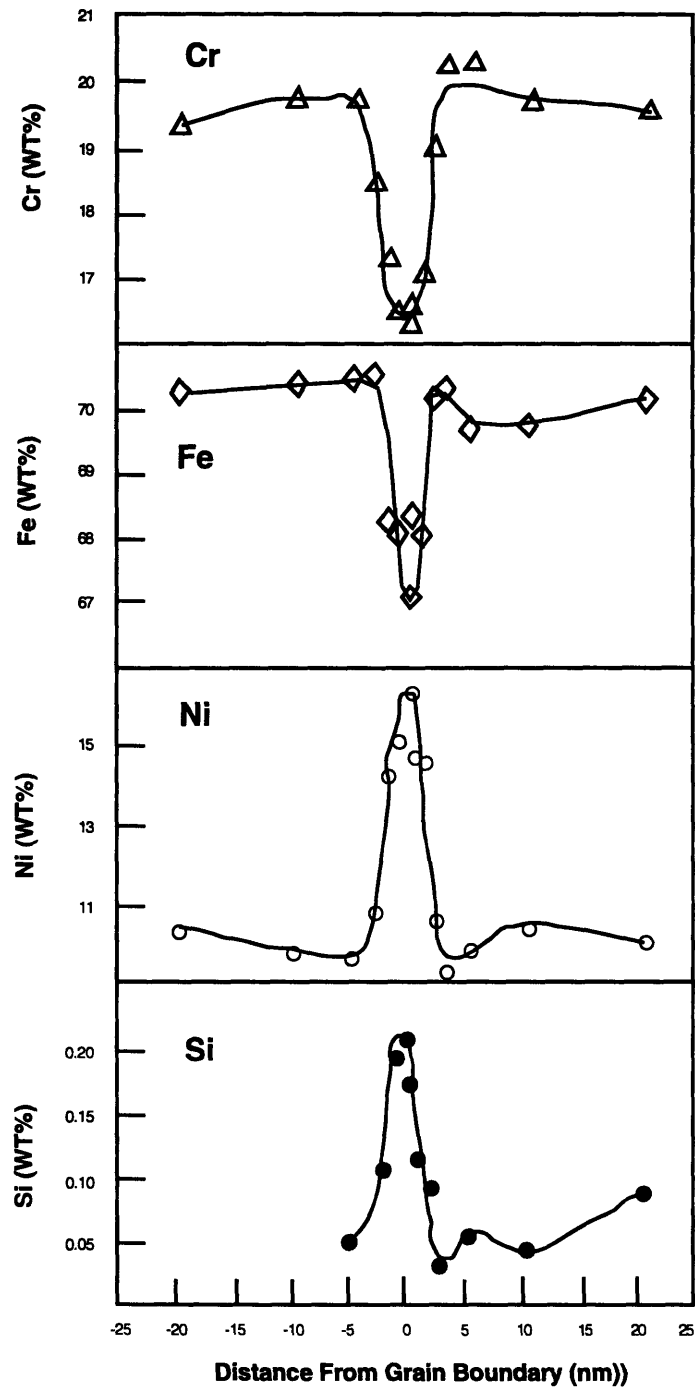


Figure 2.17. Compositional profiles by dedicated STEM analysis across grain boundaries from a HP type 348 stainless steel irradiated to 3.4×10^{21} n/cm² [18].

RIS is the result of diffusion of point defects created during the irradiation process. Fast neutrons interact with the nucleus of lattice atoms and some lattice atoms are "knocked" out of their lattice position. This results in a vacancy and interstitial or Frenkel Pair. Many of these pairs recombine and the defects are annihilated. If the knocked on atom is displaced a distance greater than three to five lattice spacings the likelihood of the pair recombining is reduced. At typical light water reactor operating temperatures the defects are mobile and they can diffuse throughout the metal lattice, the interstitial is more mobile than the vacancy. While defects diffuse in all directions, there is a net flux in the direction of defect sinks such as grain boundaries and dislocations. The vacancy diffuses by switching positions with neighboring lattice atoms. Given the choice, a vacancy will change positions preferentially with Cr or Fe over Ni. When a net flux of vacancies towards a grain boundary exists, a net flux of Cr and Fe atoms away from a grain boundary results. This phenomena is known as the inverse Kirkendall effect. Grain boundary concentration gradients of Cr, Fe, and Ni have been modeled [22] and confirmed by STEM microscopy [22, 23, 24]. Self interstitial atoms are associated with large misfit energies. These energies can be reduced if the self-interstitial bonds with solutes such as S, P, or Si. The solute-interstitial couple remain together as the interstitial diffuses towards a grain boundary resulting in a net flux of solutes towards the grain boundary. This phenomena is called solute-interstitial binding.

A second persistent radiation effect is radiation hardening. Significant data on radiation hardening of stainless steel exist [e.g. 25]. These data indicate an increase in yield strength, loss in ductility and a corresponding reduction in fracture toughness. Yield strength saturates at about 2 DPA. These effects are shown in Figures 2.18 and 2.19. The effect of radiation hardening on IASCC susceptibility is unclear. Harder materials are associated with higher crack tip stresses and strain rates [18]. Results of crack propagation models indicate that crack velocity, V , is related to crack tip strain rate, ϵ_{ct} , ($V = f(n) \epsilon_{ct}^n$) [26].

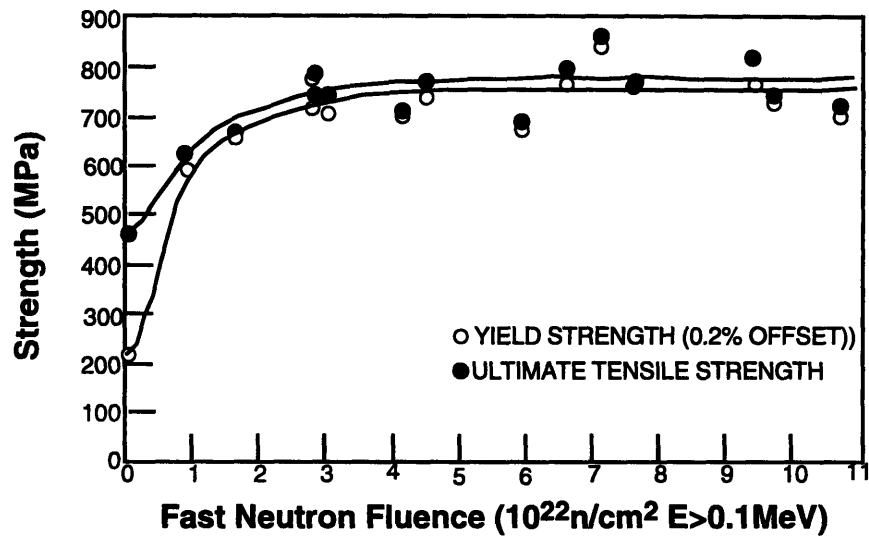


Figure 2.18. Effect of neutron fluence on the strength of annealed type 304 stainless steel irradiated of 370°C [25].

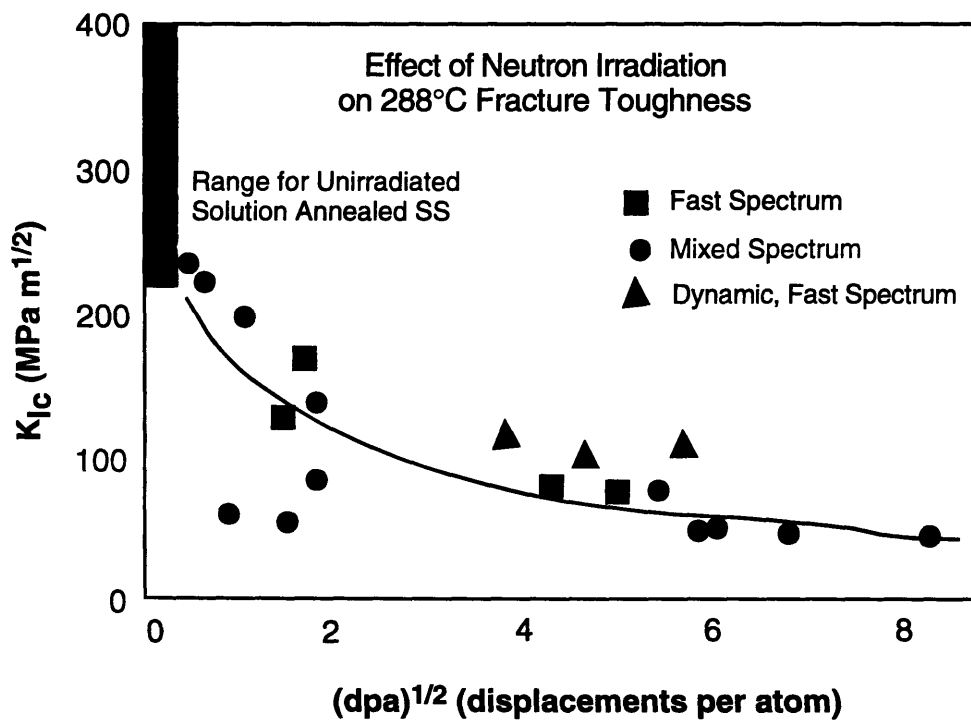


Figure 2.19. Effect of fast neutron fluence under LWR conditions on mechanical properties at 288°C of types 304 and 304L stainless steel [28].

Microscopy of pre-irradiated SSRT specimens shows dislocation channeling in which deformation is confined to sub-micron shear bands while the remaining matrix undergoes little or no deformation. Dislocation motion is made much easier if its path is free of obstacles. Dislocation density is increased during irradiation making dislocation movement increasingly difficult. It is possible for a dislocation to move through a narrow portion of a crystal lattice and as it does, clear or annihilate all potential obstacles in its path. This makes it easier for other dislocations to move in its wake. In this manner, slip is confined to a narrow band of slip planes free from defects. The result is intense shear bands which, if confined to the grain boundary regions and combined with effects of RIS, can increase SCC susceptibility [18].

A phenomena with potentially significant impact on IASCC is irradiation creep. Unlike irradiation hardening and radiation induced segregation (RIS), irradiation creep is a non-persistent effect; a fast neutron flux is required for it to operate. Irradiation enhanced creep, like thermal creep, is a time dependent strain resulting from a tensile stress. Large amounts of data exist regarding the effect of fast neutron fluence on creep, but most experiments were performed in fast breeder reactors which have higher fluxes and temperatures than LWRs. In an analysis by Wasilew et. al. [33], the in-flux activation energy for temperatures 300-550°C was determined to be 0.13 eV. Logunstev [34] provides the data in Table 2.4.

Table 2.4. Irradiation creep strain rate as a function of applied constant load at 550°C under fast neutron irradiation [2].

Stress (MPa)	Strain rate (s ⁻¹)
150	5x10 ⁻⁹
200	1.7x10 ⁻⁸
300	5x10 ⁻⁸
400	1.7x10 ⁻⁷

Using an activation energy of 0.13 eV, the data in Table 1 and the following relation

$$\dot{\epsilon}_2 = \dot{\epsilon}_1 \exp \left[\frac{Q}{k} \left(\frac{1}{T_1} - \frac{1}{T_2} \right) \right], \quad (10)$$

where:

- ϵ_1 is the strain rate at the known temperature
- ϵ_2 is the desired strain rate
- Q/k is the activation energy divided by Boltzmann's constant
- T_1 is the temperature of the known strain rate
- T_2 is the temperature at which the strain rate is desired.

irradiation enhanced creep strain rates at 300°C can be calculated. These are reported in Table 2.5.

Table 2.5. Irradiation creep strain rate as a function of applied constant load at 300°C under fast neutron irradiation.

Stress (MPa)	Strain rate (s-1)
150	2.25×10^{-9}
200	7.64×10^{-9}
300	2.25×10^{-8}
400	7.64×10^{-8}

Wasilew's analysis made use of data from experiments at EBR-II which had a fast neutron flux of about $10^{15} \text{ n/cm}^2 \text{ s}$. Garner [35] reports a linear relationship between steady state creep rate and fast neutron flux. Scaling strain rate from the flux of EBR-II to those typical of LWRs gives the strain rates in Table 2.6.

Table 2.6. Irradiation creep strain rate as a function of applied constant load at 300°C under fast neutron flux of $1 \times 10^{14} \text{ n/cm}^2 \text{ s}$ ($E > 0.1 \text{ MeV}$).

Stress (MPa)	Strain rate (s-1)
150	2.25×10^{-10}
200	7.64×10^{-10}
300	2.25×10^{-9}
400	7.64×10^{-9}

Figure 2.20. is a plot of these strain rates and an extrapolation to higher stresses.

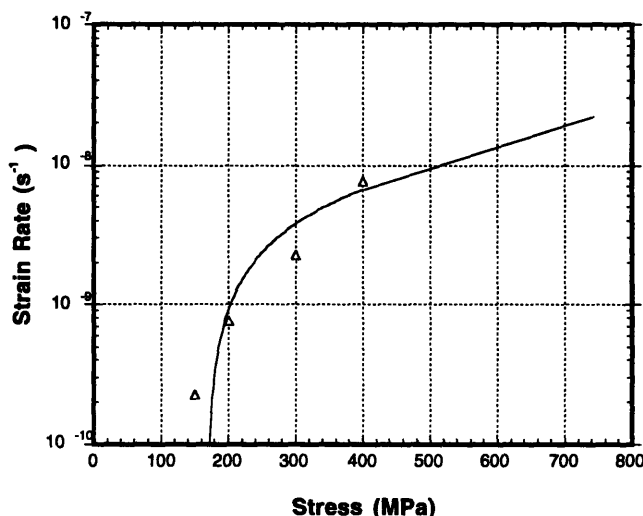


Figure 2.20. Plot of calculated irradiation creep strain rates at 300°C in a fast neutron flux of $5 \times 10^{13} \text{ n/cm}^2\text{s}$ ($E > 1 \text{ MeV}$) as a function of stress.

Kruglov [36] reports the steady state strain rate of a stainless steel specimen exposed to a fast neutron flux of $1 \times 10^{14} \text{ n/cm}^2\text{s}$ ($E > 0.1 \text{ MeV}$), at a temperature of 287 °C, under a tensile load of 301 MPa to be 1.4×10^{-9} . This is in good agreement with the results from the previous analysis.

Irradiation enhanced creep is a complex phenomena, because of this and the use of assumptions, misleading conclusions may arise from use of this analysis. These results do, however, suggest that irradiation enhanced creep may account for significant fractions of strain rate, especially the strain rate at a crack tip. The role that irradiation enhanced creep plays on IASCC susceptibility is unclear. More work in both the experimental and theoretical aspects of irradiation creep in power reactor environments is required for more quantifiable conclusions.

A specific aggressive environment is required for SCC. In the case of IASCC, ionizing radiation helps to create an oxidizing environment by increasing the amount of oxidizing species in the coolant through radiolysis [18]. Ionizing radiation interacts with the H₂O molecule creating a spectrum of radicals (e.g. e⁻aq, H⁺, H, H₂, O₂, OH, H₂O₂, HO₂). The concentrations of these species vary depending on decomposition and recombination rates, radiation flux and fluence, dissolved gases, and temperature [19].

Modeling of radiation water chemistry makes use of G-values assigned to all possible species for calculating the number of species produced per 100 eV energy absorbed by water. Production of these radicals is dependent upon the energy spectrum of the ionizing radiation. Table 2.7. lists the amount of energy deposited to the water medium per unit length (LET) for radiation and G values for several radiation produced species.

Table 2.7: Linear energy transfer (LET) and G-values for some radiation species [18].

Radiation Type	Radiation Mean LET (ev/nm)	e ⁻ aq	H ⁺	OH	H ₂	H ₂ O ₂	H	HO ₂
Fast n	40	0.93	0.93	1.09	0.88	0.99	0.5	0.04
γ	~0.01	2.7	2.7	2.86	0.43	0.61	0.61	0.03
mixed	n+γ	1.26	1.26	1.42	0.80	0.92	0.52	0.04
10 MeV H ⁺	13.5	1.46	1.46	1.52	0.70	0.90	0.64	0.04

Both gamma and fast neutron radiation are contributing factors to the water chemistry in a typical LWR, but fast neutrons provide the greatest effect. This is because the LET for fast neutrons is 40eV/nm, significantly larger than the LET for gamma radiation (~0.01 eV/nm). In addition, in power reactors, fast neutron fluxes (1.68x10⁹ Rad/hr) are typically higher than gamma fluxes (0.34x10⁹ Rad/hr). Thermal neutrons and beta particles play an insignificant role in radiation water chemistry [18].

The possible effects of radiolysis on IASCC susceptibility are numerous. Some of possible effects are: elevation of the ECP due to the increased concentration of oxidizing

species (H_2O_2 , O_2), damage to the material or protective film due to the presence of potentially harmful species (H_2O_2 , OH , HO_2 , e^-_{aq}), and increasing water conductivity due to the increased concentration of ionic species (H^+ , OH^- , NO_3^-). Radiation caused elevation of ECP has received the most attention. SSRT tests performed on notched pre-irradiated tensile specimens in 288°C water show a steep dependency of cracking on ECP in the vicinity of -100 to 0 VSHE. Figure 2.21 illustrates the relationship between susceptibility to intergranular SCC and ECP. ECP was measured in a separate autoclave on electrodes of similar materials. The SSRT tests were performed on notched specimens of commercial purity and high purity type 304 stainless steel pre-irradiated to various fluences. The tests were conducted in 288°C water (no irradiation present) using various concentrations of O_2 , H_2 , and H_2O_2 .

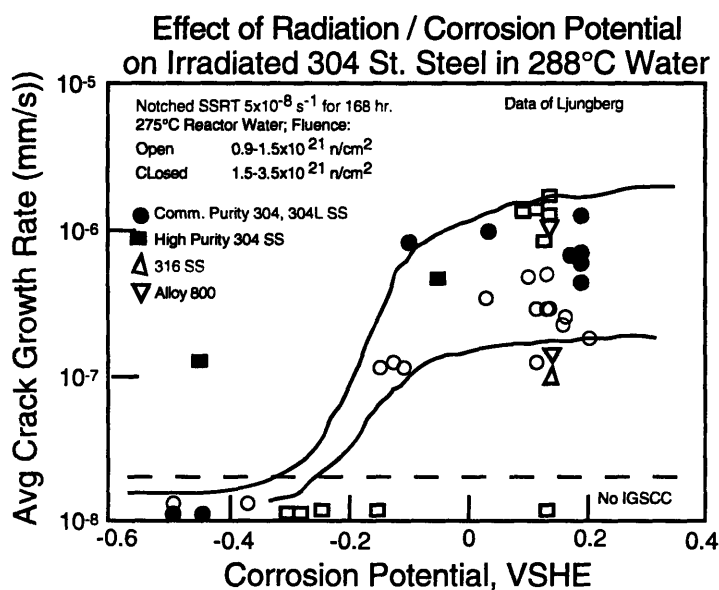


Figure 2.21. IASCC susceptibility as related to ECP [18].

Although large increases in oxidizing species result from radiolysis, the resulting increase in ECP is relatively small. This is due to the logarithmic dependence of ECP on the concentration of products and reactants described by the Nernst relation (equation 6). Figure 2.22. illustrates the dependence of ECP on oxidant concentration, in this case

dissolved O_2 . Kinetic and thermodynamic processes controlling ECPs are divided into three regions: (1) at higher oxygen concentrations a response of ~ 30 to 50 mV per decade is caused mostly by the change in oxygen concentration; (2) at very low oxygen concentrations the response is thermodynamic in nature and controlled by the hydrogen/water reaction; (3) between these two extremes a kinetically limited region exists where the potential changes rapidly from ~ 0 mVSHE to -500 mVSHE. The horizontal position of this slope is dependent on H_2 concentration and transport of O_2 in the solution to the metal solution interface.

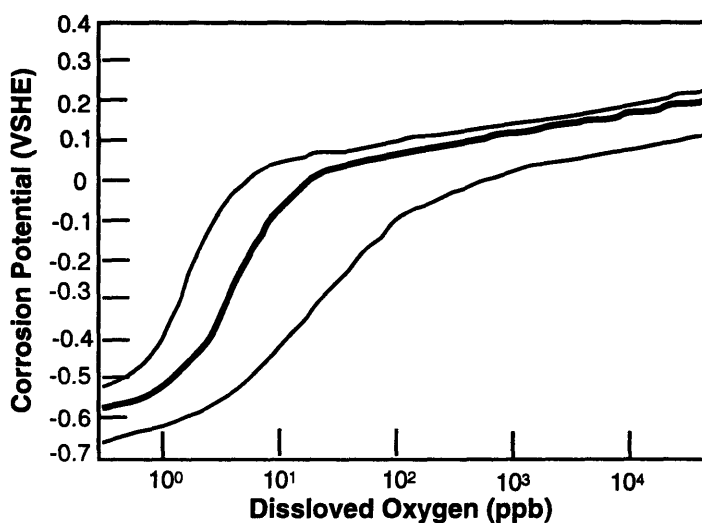


Figure 2.22. ECP as related to oxidant concentration.

Injecting H_2 into the feedwater in BWRs is successfully implemented to lower ECP in recirculation lines below the -230 mVSHE threshold potential for IGSCC of thermally sensitized stainless steels. This method of chemistry control is known as hydrogen water chemistry (HWC). Increasing the H_2 concentration affects the decomposition and recombination reactions of radiolytic species resulting in lower dissolved O_2 concentrations in letdown line water (typically less than 1 ppb for properly implemented HWC versus 200 ppb for NWC). Many researchers agree that there is a threshold ECP below which IASCC will not occur (for example Figure 2.21. and [18])

and proper implementation of HWC may be able to reduce in-core ECPs below this threshold. To verify this possibility theoretical modeling [30] and experimental measurements [31] of in-core ECPs have been performed. The ECP of in-core components for eight different BWR type nuclear reactors were calculated with varying concentrations of feedwater H_2 concentrations. Macdonald's mixed potential model (MPM) computed HWC to be not effective in lowering ECP of components located in mid-core or upper plenum sections of these reactors below the IGSCC threshold of -230mVSHE [30] with feedwater H_2 concentrations up to 2 ppm. Measurements of in-core ECP values using radiation qualified Ag/AgCl reference electrodes at the local power range monitors (LPRM) at J. K. Fitzpatrick BWR indicate that the ECP of components located in the lower plenum are reduced below -230mVSHE for H_2 feedwater concentrations greater than 1.1 ppm. Components located at the entrance to the upper plenum of the same reactor require a H_2 feedwater concentration greater than 2.7 ppm for the same results.

It is still unclear if fast neutron and gamma irradiation affects the ECP at the crack tip. The presence of radiation could raise the corrosion potential at the crack tip above that of the crack mouth since the solution in the crack is stagnant [18]. Measurements of growing crack-tip potentials in non-irradiated, hot-water environments show that the crack tip ECP remains low, approximately -0.5 VSHE for all bulk environment oxygen concentrations [28]. Recently, measurements have been made under irradiated conditions which show that only a small rise in ECP results from irradiation ($<0.05\text{ VSHE}$) [19]. Theoretical modeling of this work in progress [29], the results of this work will be valuable in determining the effect of irradiation on crack tip ECP.

While much has been learned about IASCC in recent years, much more knowledge is required before predictive models can be incorporated into reactor design and operation. Recent findings include the confirmation of a ECP below which IASCC

does not occur in out of core tests. This potential appears to be near the protection potential for IGSCC, -230mVSHE [32]. Further work is required in: obtaining consistent correlation between bulk and grain boundary chemistry and cracking susceptibility, determining the role of purely mechanical failure, and quantifying the non-persistent effects of irradiation, such as irradiation enhanced creep and presence of radicals, on IASCC susceptibility.

2.5 References

- [1] Fontana, M.G., Greene, N.D., Corrosion Engineering, McGraw-Hill Book Company, New York, NY, 1978.
- [2] Wranglen, G., An Introduction to Corrosion and Protection of Metals, Chapman Hall, New York, NY, 1985.
- [3] de Bethune, A. J., Licht, T. S., and Swendeman, N., Journal of the Electrochemical Society, 1959, Vol. 106, pg. 616.
- [4] Uhlig, H. H., and Revie, R. W., Corrosion and Corrosion Control. An Introduction to Corrosion Science and Engineering, John Wiley & Sons, New York, NY, 1985.
- [5] Diegle, R. B., and Boyd, W. K., "The Role of Film Rupture During Slow Strain-Rate Stress Corrosion Cracking Testing", Stress Corrosion Cracking-The Slow Strain Rate Technique, ASTM STP 665, G. M. Ugianski and J. H. Payer, Eds., American Society for Testing and Materials, 1979, pg. 26-46.
- [6] NWT Corporation, Corrosion Potential Measurement Source Book, EPRI NP-7142, Electric Power Research Institute, Palo Alto, CA, 1991.

- [7] BWR Water Chemistry Guidelines Committee, BWR Hydrogen Water Chemistry Guidelines:1987 Revision, EPRI NP-4947-SR, Electric Power Research Institute, Palo Alto, CA, 1987.
- [8] Brown, B.F., "Stress Corrosion Cracking in High Strength Steels and in Titanium and Aluminum Alloys", NRL, Washington, DC, 1972.
- [9] Scully, J.C., Editor, "The Theory of Stress Corrosion Cracking in Alloys", N.A.T.O. Brussels, 1971.
- [10] Scully, J. C., "Stress-Corrosion Cracking", Corrosion Chemistry, American Chemical Society, Washington, DC, 1979.
- [11] Engseth, P., and Scully, J. C., Corrosion Science, Vol. 15, pg 504, 1975.
- [12] Scully, J. C., Corrosion, Vol. 15, pg 505, 1975.
- [13] Latanison, R. M., Gastine, O. H., and Compeau, C. R., "Stress Corrosion Cracking and Hydrogen Embrittlement: Differences and Similarities", Proceeding of a Symposium in Environment Sensitive Fracture in Engineering Materials, AIME, 24-26 October, 1977.
- [14] Parkins, R. N., "Development of Strain-Rate Testing and Its Implications", Stress Corrosion Cracking-The Slow Strain Rate Technique, ASTM STP 665, G. M. Ugianski and J. H. Payer, Eds., American Society for Testing and Materials, 1979, pg. 5-25.
- [15] Payer, J. H., Berry, W. E., and Boyd, W. K., "Evaluation of Slow Strain-Rate Stress Corrosion Test Results", Stress Corrosion Cracking-The Slow Strain Rate Technique, ASTM STP 665, G. M. Ugianski and J. H. Payer, Eds., American Society for Testing and Materials, 1979, pg. 61-77.

- [16] Solomon, H. D., Povich, M. J., and Devine, T. M., "Slow Strain-Rate Testing in High Temperature Water", Stress Corrosion Cracking-The Slow Strain Rate Technique, ASTM STP 665, G. M. Ugianski and J. H. Payer, Eds., American Society for Testing and Materials, 1979, pg. 132-148.
- [17] Vergara-Aimone, J. A., "The Development of a Facility for the Evaluation of Environmentally Assisted Stress Corrosion Cracking of In-Core Structural Materials in Light Water Reactors", Ph.D. Thesis, MIT, Cambridge, MA, 1992.
- [18] Andresen, P. L., Ford, F. P., Murphy, S. M., Perks, J. M., "State of the knowledge of Radiation Effects on Environmental Cracking in Light Water Reactor Core Materials", Proceedings of the Fourth International Symposium on Environmental Degradation of Materials in Nuclear Power Systems, ANS, Jekyll Island, GA, August, 1989.
- [19] Was, G. S., and Andresen, P. L., "Irradiation Assisted Stress Corrosion Cracking in Austenitic Alloys", JOM, April, 1992.
- [20] Gordon, B. M., and Gordon, B. M., "Material Aspects of BWR Plant Life Extension", Nuclear Engineering and Design, 98, 1987.
- [21] Jacobs, A. J., Clausing, R. E., Miller, M. K., and Sheperd, C., "Influence of Grain Boundary Composition on the IASCC Susceptibility of Type 348 Stainless Steel", Proceedings of the Fifth International Symposium on Environmental Degradation of Materials in Nuclear Power Systems, ANS, Monterey, CA, August, 1991.
- [22] Boerigter, S. T., "An Investigation of Neutron-Irradiation Induced Segregation in Austenitic Stainless Steels", Sc.D. Thesis, MIT, Cambridge, MA, 1992.
- [23] Flores, C. D., "Evaluation of Radiation Induced Segregation in Fe-Ni-Cr Alloys", S.M. Thesis, MIT, Cambridge, MA, 1994.

- [24] Mansoux, H., "Experimental Determination of Radiation Induced Segregation Susceptibility in Austenitic Stainless Steels", S.M. Thesis, MIT, Cambridge, MA, 1994.
- [25] Bleiberg, M. L., and Bennett, J. W., Ed.s, Radiation Effects in Breeder Reactor Structural Materials, The Nuclear Metallurgy Committee of The Metallurgical Society of AIME, New York, NY, 1977.
- [26] Ford, F. P., Andresen, P. L., Solomon, H. D., Gordon, G. M., Ranganathan, S., Weinstein, D., and Pathania, R., "Applications of Water Chemistry Control, On-Line Monitoring, and Crack Growth Models for Improved BWR Materials Performance", Proceedings of the Fourth International Symposium on Environmental Degradation of Materials in Nuclear Power Systems, ANS, Jekyll Island, GA, August, 1989.
- [27] Straalsund, J. L., "Irradiation Creep in Breeder Reactors", in Radiation Effects in Breeder Reactor Structural Materials, The Nuclear Metallurgy Committee of The Metallurgical Society of AIME, New York, NY, 1977.
- [28] Jones, R. H., ed. Stress Corrosion Cracking, ASM International, Materials Park, Ohio, 1992.
- [29] Chun J. H., "Modeling of Crevice Chemistry", Sc.D. Thesis, MIT, Cambridge, MA, 1994.
- [30] Bertuch, A., Macdonald, D. D., Pang, J., Kriksunov, L., Arioka, K., "Modeling the Corrosion Behavior of the Heat Transport Circuits of Light Water Nuclear Reactors", in the Proceedings of the Fourth International Symposium on Environmental Degradation of Materials in Nuclear Power Systems, ANS, San Diego, CA, August, 1993.

[31] Indig, M. E., Goldstein, J. S., Jarvis, A. J., Pathania, R., "Electrochemical Response to Hydrogen Water Chemistry at the J. A. Fitzpatrick BWR", in the Proceedings of the Fourth International Symposium on Environmental Degradation of Materials in Nuclear Power Systems, ANS, San Diego, CA, August, 1993.

[32] Indig, M. E., Nelson, J. L., Wozadlo, G. P., "Investigation of the Protection Potential Against IASCC", Proceedings of the Fifth International Symposium on Environmental Degradation of Materials in Nuclear Power Systems, ANS, Monterey, CA, August, 1991.

[33] Wasilew, C., Erlich, K., and Bergmann, H. J., Influence of Irradiation on Material Properties: 13th International Symposium, Part II, ASTM STP 956, Philadelphia, PA, 1987

[34] Lognestev, Ye., N., Safonov, V. A., and Tyumentsev, S., Fiz. Metal. Metalloved., Vol 57, 1984.

[35] Garner, F. A., "Irradiation Performance of Cladding and Structural Steels in Liquid Metal Reactors", in Nuclear Materials, ed. Frost, B. R. T., Volume 10 of Materials Science and Technology, VCH, New York, NY, 1992.

[36] Kruglov, A. S., Bul'Kanov, M. E., Bykov, V. N., Pevchikh, Yu. M., Atomnaya Energiya, Vol. 48, pg 258-259, 1980.

3. EXPERIMENTAL FACILITY DESCRIPTION

3.1. Facility Overview

The centerpiece of the experimental facility is the in-pile "rig" which positions and loads a tensile test specimen in the MITR-II nuclear reactor core. The rig also acts as an autoclave for the high pressure and high temperature water at light water reactor (LWR) conditions. A modified Instron loading machine is positioned above the rig and loads the specimen in tension through the rig's load train. An electrical current is applied to the specimen and the voltage across the gage section of the specimen is measured. A computer monitors the potential drop, correlates the changing potential to a strain, and provides feedback to the loading machine for control. This method of strain measurement is called DC potential drop or DCPD. The CERT method of specimen loading can be used if required.

The main loop circulates controlled temperature and chemistry water past the specimen under test. Pure water is constantly being charged into the pressurized main loop by the charging system from the charging tank. Main loop chemistry control is provided by controlling the atmosphere within the charging tank and chemical addition through the chemical injection system. A back pressure regulator in the letdown line controls the system pressure. The high pressure side of the letdown line includes a reference autoclave which contains three electrodes; Ag/AgCl, platinum, and stainless steel. The low pressure side of the letdown line contains dissolved oxygen and hydrogen analyzers, a pH meter, two conductivity cells, sample points, demineralizers, and filters. Over temperature protection for the main loop is provided by the main heater controller. Over pressure protection is provided by an alarm and two relief valves. The amount of boiling in the in-core sections of the rig which may occur during postulated low pressure transients are minimized by a large auxiliary pressurizer. The water temperature in the auxiliary

pressurizer is maintained highest in the facility. Should pressure control be lost, pressure will drop until the saturation pressure for the water in the auxiliary pressurizer is reached. Pressurizer water will boil reducing the rate at which loop pressure drops, allowing time for the to cool and operators to begin taking corrective actions.

The rig is inserted into the reactor core through a reactor top lid designed and constructed to accommodate IASCC operations. The lid positions the rig and supports its weight and the weight of the Instron loading machine. The main loop and chemistry and pressurizer racks are located on an experimental platform adjacent to the reactor top. The chemistry and pressurizer racks contain all the valves, sensors, and other equipment which require status during normal operation. The IASCC experiment shares the platform with equipment for other in-core experiments.

A handling system has been designed and built to allow for ease of specimen removal and replacement while maintaining personnel exposures to radiation ALARA (as low as reasonable achievable). The specimens are removed and replaced remotely in the right hand hot cell within the reactor containment building. The DCPD sensing wires, when used, are attached to pre-irradiated test specimens in the hot cell. The procedure for moving the radioactive rig to and from the hot cell is similar to the procedure proven successful in moving the PCCL and BCCL loops. A "clam shell" type shielded transfer cask, similar to the one used to move the BCCL and PCCL loops but more robust, is used while moving the rig.

An in-core electrode rig which has two movable clusters of reference electrodes is used to map the electrochemical corrosion potential (ECP) of the autoclave in the in-core and above core areas. This in-core rig is used separately from the SSRT rig, but makes use of the SSRT rig's thimble, autoclave, and water chemistry control systems. The in-core ECP map, especially the ECP near the location of SSRT specimen, is necessary to characterize the environment of the test specimen and for calibration of the SSRT rig's in-

core platinum electrode. This platinum electrode is used with the in-core rig to monitor the test specimen's ECP during tensile testing.

3.2. In-Core Tensile Rig

The in-core tensile rig is an autoclave with a load train penetrating the pressure boundary. The autoclave is surrounded by an aluminum thimble and dummy fuel element which provides an interface with the MITR-II reactor coolant and core. The in-core rig in the MITR reactor core is illustrated in Figure 3.1.

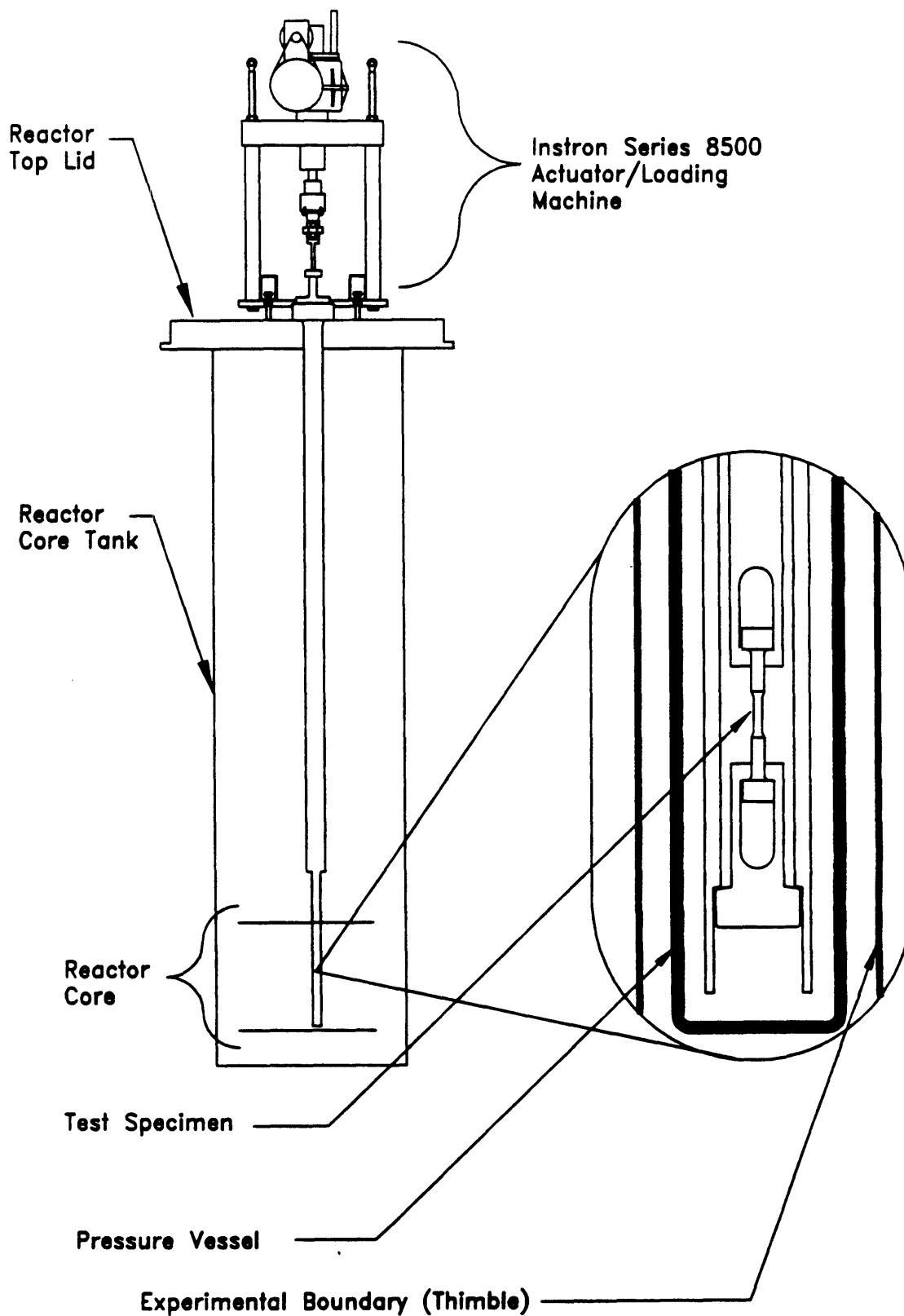
3.2.1. Load Train

The load train consists of the concentric pull rod and reaction tube. The pull rod is connected to and transmits the tensile load from the loading machine to the specimen. The reaction tube supports the compressive force exerted by loading the specimen. Each component consists of in-core and above core sections. The in-core sections are smaller in diameter because of the limited space within the core. The geometry and material composition of the pull rod and reaction tube are listed in Table 3.1. The in-core section of each is made of Ti 6Al-4V which does not become highly radioactive helping to minimize personnel radiation exposures during rig handling for specimen change-out.

Table 3.1. Load Train Components

Component	Material	Length (in.)	OD (in.)	ID (in.)
Lower Reaction Tube	Ti 6Al-4V	38.5	1.25"	0.875"
Upper Reaction Tube	316L SS	130.5	2.44"	1.25
Lower Pull Rod	Ti 6Al-4V	50.5	0.625"	0.312"
Upper Pull Rod	304L SS	127.53	0.75"	0.38"
Pull Rod Sleeve	Ti 6Al-4V	2.5	1.00	.312
Lower Grip Holder	Ti 6Al-4V	2.75	1.25	-
Lower Grip	Ti 6Al-4V	2.94	-	-

Figure 3.1. The IASCC In-Core Mechanical Testing Facility



The upper and lower pull rods are connected by the threaded pull rod sleeve. Four high density alumina spacers are positioned along the length of the pull rod to keep the pull rod and reaction tube from coming into electrical contact. This is required because the pull rod is used as a current path for the DCPD system.

The specimen is connected to the pull rod in tension by a grip machined into the bottom end of the lower pull rod. The bottom of the specimen is held by the lower grip. When the pull rod loads the specimen in tension the lower grip mates with the inside of the lower grip holder. The lower grip holder is threaded into the bottom of the lower reaction tube. When the pull rod is lowered the lower grip drops out of the lower grip holder and the specimen is lowered out of the reaction tube allowing access to the specimen for replacement. A titanium dowel keeps the lower grip and lower half of the broken specimen in the grip volume after fracture. The in-core section of the load train is illustrated in Figure 3.2. The load train is designed to place a tensile load of 1200 lbs on the test specimen. A rigid specimen was used to test load the load train and measure its compliance to 1500 lbs.

Leads for instrumentation are run within six rounded grooves cut along the length of the reaction tube. Four of these grooves are 3/32" wide and two are 1/8" wide. The platinum electrode makes use of one of the 1/8" grooves. A special "window" is cut through the reaction tube adjacent to the specimen for the platinum electrode to "see" the specimen.

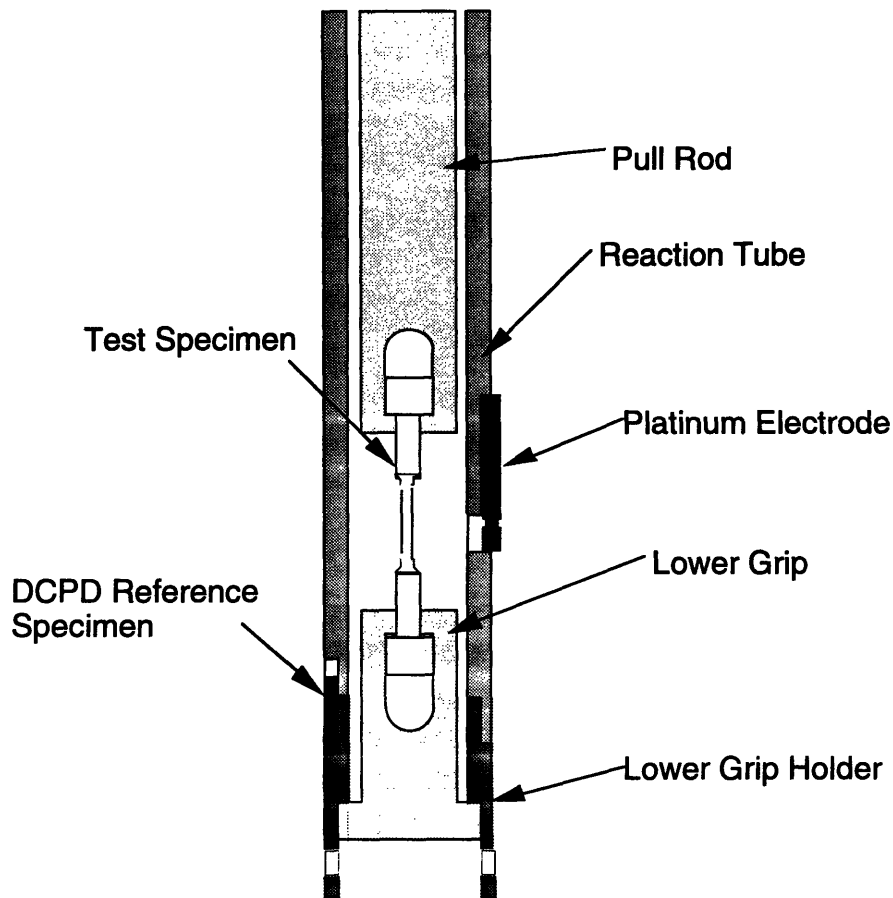


Figure 3.2. The in-core SSRT rig specimen and grips.

The DCPD current path and reference specimen sensing wires use the remaining 1/8" groove. An alumina sleeve with four bores is used as wire insulation. The outside diameter of the alumina sleeve is 0.11" and each bore is 0.028" in diameter. Four 0.020" wires are threaded the length of the sleeve. Two of these wires carry the DCPD current and are spot welded to the top of the reference specimen. The two other wires are attached to opposite ends of the reference specimen and are used to measure the potential generated by the DC current through the reference specimen. These wires are made of high purity nickel (99.6% Ni).

A slot for the DCPD reference specimen is machined into the bottom of the lower reaction tube within the 1/8" groove. The reference specimen fits snugly into the slot. The bottom head of the reference specimen is held in place by the counter-bored hole in the

lower reaction tube and by the upward force exerted on the lower grip holder by loading the specimen. The bottom head of the reference specimen is the only part of the reference specimen which comes in contact with the lower reaction tube. Water is allowed to flow past and around the reference specimen to ensure that it remains the same temperature as the SSRT test specimen.

The test specimen's two DCPD sensing wires use two of the four 3/32" grooves and are insulated by single bore alumina sleeves. Since these alumina sleeves are fragile, they are contained within a thin walled stainless steel tube with an outside diameter of 0.084 inches. The wires themselves are run within a thin walled (0.002 inch) stainless steel tube with an outside diameter of 0.032 inches. The alumina sleeves are located in the annulus between the two stainless tubes. The purpose of this last tube is to allow the wire to move up and down for specimen replacement and wire welding. The wires are threaded through the slots in the lower grip holder and lower grip to the specimen where they are attached to the specimen's shoulder sections on either side of the gauge section by spot welding. They are made from high purity nickel (99.8% Ni) and are 0.015 inches in diameter.

One of the remaining 3/32" grooves contains a dual junction sheathed thermocouple which monitors the water temperature near the specimen. The output of one junction goes to the heater controller for main loop temperature control, and the other goes to the facility's data acquisition system. The remaining groove is not used.

3.2.2. Strain Measurement by DCPD

The DC potential drop technique (DCPD) to measure strain makes use of the fact that certain metals exhibit a change of electrical resistance with change in strain. This resistance-strain phenomena was first reported by Lord Kelvin nearly 140 years ago (1856) [1]. Applications of this relation include strain gauge technology, an industry accepted

method of measuring material strain. A metal wire, with a known resistance-strain relation, is mounted to a loaded material specimen such that the wire and the specimen are strained equally. Because the metal wire, or strain gauge, can be much smaller than the material specimen being tested its presence has little effect on the test.

In strain gauge technology the resistance to strain relationship is referred to as either the strain sensitivity factor or gauge factor. Gauge factor is the term that has most recently become accepted by the industry and is defined as

$$G_f = \frac{\Delta R/R}{\Delta L/L}$$

where

G_f is the gauge factor

R is the resistance

L is the length

ΔR and ΔL are the changes in resistance and length respectively.

Unfortunately, the of the strain-resistance effect is not completely understood. Within certain limits, some materials exhibit a linear relationship between the change in resistance and the change in strain, while others show a variable relationship. These characteristics are illustrated in Figure 3.3. [2].

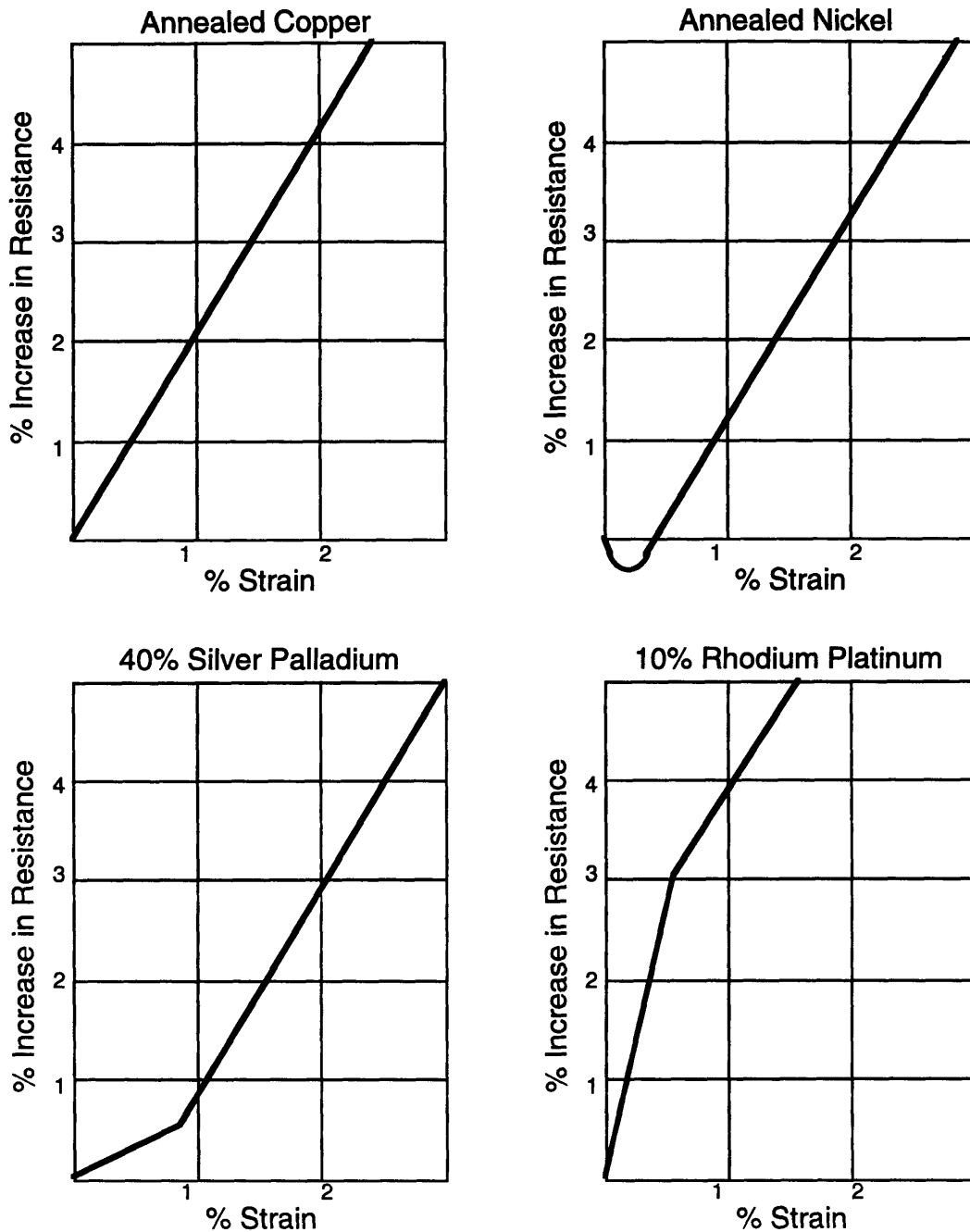


Figure 3.3. Typical examples of resistance change with strain [2].

The changes in dimensions resulting from strain can be expected to influence the resistance change, however the variation in gauge factor or different materials (e.g., -12.1 for nickel and +5.1 for 5% Iridium Platinum) indicates that this cannot be accounted for by

reason of dimensional change alone. The following analysis will help to explain the situation.

Let

$$R = \rho \frac{L}{A}$$

where ρ is resistivity

L is the length of the specimen

A is the area of cross section

By taking the natural log of both sides

$$\ln R = \ln \rho + \ln L - \ln A.$$

Differentiation gives

$$\frac{dR}{R} = \frac{d\rho}{\rho} + \frac{dL}{L} - \frac{dA}{A}.$$

Now, the volume

$$V = LA,$$

and

$$dV = V\varepsilon(1 - 2\nu),$$

neglecting higher order terms.

Where: V is volume

$\varepsilon = dL/L$ is the longitudinal strain

ν is Poisson's ration

By taking the natural log of the equation for volume and then differentiating, one can write

$$\frac{dV}{V} = \frac{dL}{L} + \frac{dA}{A}.$$

Introducing the value for dV above gives

$$\frac{dL}{L} (1 - 2\nu) = \frac{dL}{L} + \frac{dA}{A},$$

from which one finds that

$$\frac{dA}{A} = -2\nu \frac{dL}{L}.$$

Therefore

$$\frac{dR}{R} = \frac{d\rho}{\rho} + (1 + 2\nu) \frac{dL}{L}$$

and the gauge factor, G_f , is

$$G_f = \frac{dR/R}{dL/L} = \frac{d\rho/\rho}{dL/L} + (1 + 2\nu).$$

The quantity $(1+2\nu)$ represents the influence of dimensional change. Since Poisson's ratio is about 0.3 for most metals, the gauge factor would be about 1.6 if only dimensional change were involved. The results of experimental observation indicate that the ratio

$$\frac{d\rho/\rho}{dL/L}$$

must have considerable significance to account for large deviations of G_f from the value of 1.6.

In their study of resistance strain-characteristics of fine wires of various different materials, Jones and Maslen [2] point out that, with the exceptions of annealed copper and constantan, all the materials which they investigated showed at least one change in gauge factor as the strain was increased. Sometimes the change occurred abruptly and sometimes gradually; however, in all the materials which they examined the final gauge factor, which corresponds to plastic strain, reached a value of about 2.

For plastic strain volume is conserved so $\nu=1/2$ Consequently $(1+2\nu) = 2$. This suggests that for high strains,

$$\frac{d\rho/\rho}{dL/L} \approx 0$$

which means that $d\rho$ is approximately zero, or, that ρ , the resistivity, remains about constant when plastic deformation takes place.

The cause for the change in gauge factor as a material specimen is increasingly strained is the onset of plastic strain. When a small stress, such that strain is entirely elastic, is placed on a specimen the gauge factor is constant. As the stress is raised above the yield stress, plastic and elastic strains increase and the value of the gauge factor changes towards 2, the gauge factor associated with plastic strain for all materials.

The incremental strain that is elastic for increasing stress above yield depends on the ability of the material to harden. Determining the incremental total strain of a specimen loaded past yield by the change in resistance is not possible, either the elastic or plastic strain must be known. For the IASCC in-core SSRT testing facility elastic strain is calculated by using the load on the test specimen as measured by the load cell, the

specimen's geometry, and the material's elastic modulus. That is,

$$\epsilon^e = \frac{P}{EA}$$

where ϵ^e is the elastic strain
 P is the force on the specimen
 E is the elastic modulus for the material being tested
 A is the cross sectional area of the test specimen

The DCPD system used with the in-core SSRT testing facility uses the specimen itself as a strain gauge. As the specimen is strained its resistance changes. Using a calibration of resistance and strain for the material being tested then measuring the change in resistance and specimen load, total specimen strain is determined.

Because the resistance of the specimen is small, a large current (2-4 amps) is applied to the specimen and wires welded to either side of the gauge section of the specimen are used to measure the potential drop across the gauge section. By Ohm's law, the potential measured is equal to

$$V = I\rho \frac{L}{A}$$

where V is the potential drop
 I is the current through the specimen
 ρ is the specimen's resistivity
 L is the length of the specimen's gauge section
 A is the cross sectional area of the specimen.

Any change in potential caused by a change in current is compensated by dividing the measured potential across the specimen's gauge section by the potential across the reference specimen which is made of austenitic stainless steel (316L), one of the materials

scheduled for in-core SSRT testing. This reference specimen is electrically connected in series with the test specimen so that each has the same applied current. This compensation is expressed as

$$\frac{V}{V_r} = \frac{I\rho L/A}{I\rho_r L_r/A_r} = \frac{\rho L A_r}{\rho_r L_r A},$$

where V_r is the potential across the reference specimen
 L_r is the length of the reference specimen
 A_r is the cross sectional area of the reference specimen
 ρ_r is the resistivity of the reference specimen.

This compensation also corrects for changes in measured potential due to changes in material resistivity caused by temperature variations. Both specimens are located physically close to each other and should be similarly heated (by radiation) and cooled (by the main loop water).

The ratio is normalized by dividing by the initial values of potential drop across the specimen's gauge section (V_0) and the reference specimen (V_{r0}) to get the normalized potential (V_n)

$$V_n = \frac{V/V_0}{V_r/V_{r0}} = \frac{\rho L A_0}{\rho_0 L_0 A},$$

or

$$V_n = \frac{\rho}{\rho_0} \exp[(1 + 2\nu)\epsilon].$$

The normalized potential must be broken into elastic and plastic components:

$$\frac{V}{V_0} = 1 + \Delta V_n^e + \Delta V_n^p$$

neglecting higher order terms where ΔV^e is the change in the normalized potential due to elastic strain and ΔV^p is the change in the normalized potential due to plastic strain.

For elastic strain only

$$1 + \Delta V_n^e = \frac{\rho}{\rho_0} \exp[(1 + 2\nu)\epsilon^e].$$

For small elastic strain

$$\Delta V_n^e = \frac{\rho}{\rho_0} [1 + (1 + 2\nu)\epsilon^e] - 1$$

$$\Delta V_n^e = \alpha \epsilon^e$$

$$\alpha = 3.$$

Repeating for plastic strain only

$$1 + \Delta V_n^p = \frac{\rho'}{\rho_0} \exp[(1 + 2\nu)\epsilon^p].$$

For small plastic strain

$$\Delta V_n^p = \frac{\rho}{\rho_0} [1 + (1 + 2\nu)\epsilon^p] - 1.$$

For $\nu = 0.5$ and no change in resistivity during plastic strain

$$\Delta V_n^p = \beta \epsilon^p$$

$$\beta = 2.$$

These values were verified experimentally during the DCPD calibration.

The total true strain is equal to

$$\varepsilon = \varepsilon^e + \varepsilon^p,$$

$$\varepsilon = \frac{\Delta V_n^e}{\alpha} + \frac{\Delta V_n^p}{\beta},$$

and using load to calculate the elastic strain

$$\frac{P}{EA} = \frac{\Delta V_n^e}{\alpha}.$$

The total strain is then

$$\varepsilon = \frac{P}{EA} + \frac{\Delta V_n^p}{\beta},$$

and finally

$$\varepsilon = \frac{P}{EA} + \frac{1}{\beta} \left(V_n - \frac{\alpha P}{EA} - 1 \right).$$

Total strain is calculated using two inputs, the normalized potential (V_n) and the specimen load (P). This method of strain measurement has proven successful during all SSRT tests done out of core. The technique can measure strain with an accuracy of $\pm 10\%$.

The DCPD system has been shown to be a feasible way to measure strain in previous laboratory tests [3], and more recently with this testing facility.

Figure 3.4 is a schematic of the DCPD current loop which consists of a Sorensen SRL 10-25 VDC power supply, a polarity switching board (HP69736A Timer/Pacer card, HP69776A Interrupt card, Douglas-Randall DC relays), an integrating digital multimeter, an HP computer, and the in-core rig (SSRT specimen, reference specimen, pull rod, and wires and insulators).

The DCPD current path includes the pull rod, test specimen, lower grip and lower grip holder, reference specimen, and nickel wires which run up the reaction tube and is powered by the Sorensen power supply. Two pairs of probes provide input to the integrating digital multimeter card for measuring the potential drop across the gage section of both the test specimen and the reference specimen. To cancel any thermoelectric potential error caused by the probes and any thermal gradient that may be present, a DC relay board is used to switch the direction of current flow through the rig. Relay timing is set by the Timer/Pacer card, and is nominally set to change every 11 seconds.

The reference specimen is mounted in the outside wall of the lower reaction tube in the same axial position as the test specimen. This is important because both the reference specimen and the SSRT test specimen must receive similar radiation heating. Cooling is also important. The SSRT test specimen is well cooled by the main loop water, and the reference specimen must be cooled similarly. For this reason the reference specimen uses no ceramic insulation, and must be positioned so as to avoid shorts to the reaction tube

Before the slow strain rate test is started the test specimen is loaded by the Instron loading machine in load control to a predetermined load. The pre-load is nominally set to 157 lbs, which corresponds to a stress of 20 ksi. At this time three readings of the potential across the test and reference specimen are taken and averaged. These values become the initial potentials used to normalize the potentials measured during testing.

The sequence for each reading, for the initial readings and readings taken during the test, begins when the DC current polarity is switched. At this time a 2 second delay allows the current and potentials to stabilize. The potentials across the test and reference specimen are measured 6 times and the potential across each specimen is averaged. Eleven seconds after the current direction is switched, it is switched again. After another 2 second delay 6 potentials across each specimen are again measured and averaged. The two average potentials across each specimen are added, the sum associated with the test specimen is

divided by the sum associated with the reference specimen, and finally this ratio is normalized by using the initial potentials. The two sums and the normalized potential are recorded to disk and the normalized potential and load are displayed in real time every 22 seconds.

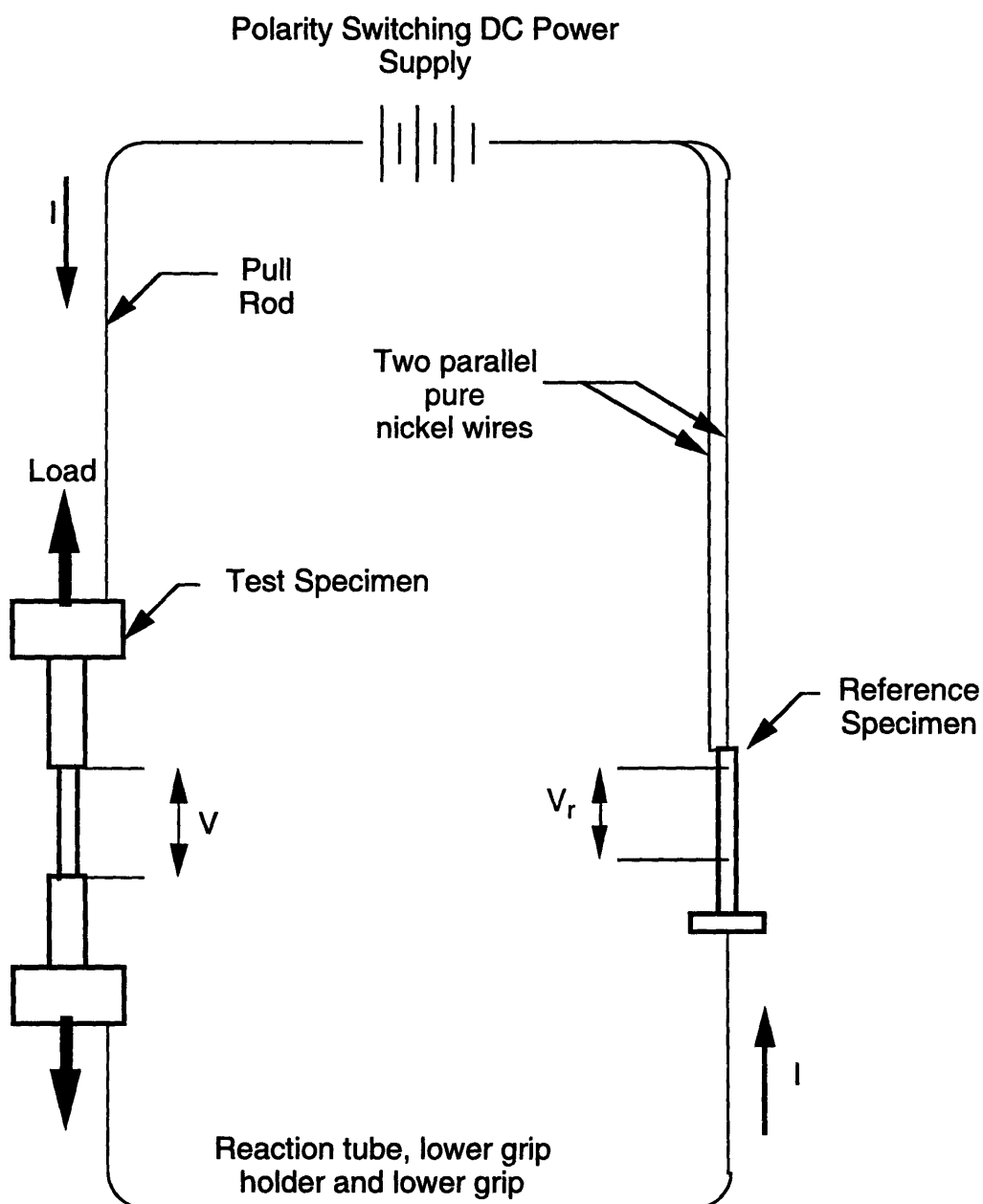


Figure 3.4. The DCPD Current Loop.

3.2.3. Loading Machine and Loading Machine Control

The loading machine provides a controllable tensile force on the SSRT test specimen to achieve a constant slow strain rate of $5 \times 10^{-7} \text{ s}^{-1}$. The loading machine is a standard Instron series 8500 electro-mechanical test system. This system was chosen because it includes all the features required to run tensile tests in a commercially available package.

The Instron actuator was attached to the platen, inverted, and mounted on the loading machine support. The loading machine support was made to allow easy removal and realignment of the loading machine on the MITR-II reactor top lid and in-core testing rig between tests. Once a new specimen is installed in the rig and the rig is in the reactor the actuator must be accurately aligned before it can be connected to the pull rod. The actuator is guided into position automatically about the rig's upper flange by a taper machined into the support's lower plate. The top of the pull rod has a removable 2-1/2 inch male pipe thread head and is connected to a 2-1/2 inch pipe nipple by a pipe union. The union is used to disconnect the pull rod from the loading machine for specimen changing. The pipe nipple is threaded into a pipe flange which is connected to the load cell. The pipe flange is electrically insulated from the load cell by a G10 spacer and insulating bolts. This is necessary since the pull rod is used as a current path for the DCPD system. The load cell provides indication of specimen load and control for the machine while in load control mode. The top side of the load cell is connected to the Instron loading machine actuator. The loading machine is illustrated in Figure 3.5.

Although the loading machine is rated for 20,000 lbs and the load cell is rated for 5000 lbs, only a fraction of this load will ever be needed for the tests initially scheduled. The specimens scheduled for testing have a small cross sectional area (0.0078 in^2). The

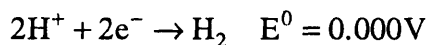
ultimate tensile load for the hardest specimen tested to date (304SS cold rolled to 30%) was 1100 lbs.

The main loop digital pressure transducer provides a feedback signal to the loading machine for pressure compensation. This is necessary because the main loop pressure affects the load measured by the load cell. Increasing loop pressure places an increasing compressive load on the load cell through the pull rod as it penetrates the pressure boundary. For example, the main loop is normally pressurized to 1750 psi, if there is no load on the specimen the load cell would have a compressive load of 772 lbs

3.2.4. Test Specimen ECP Measurement

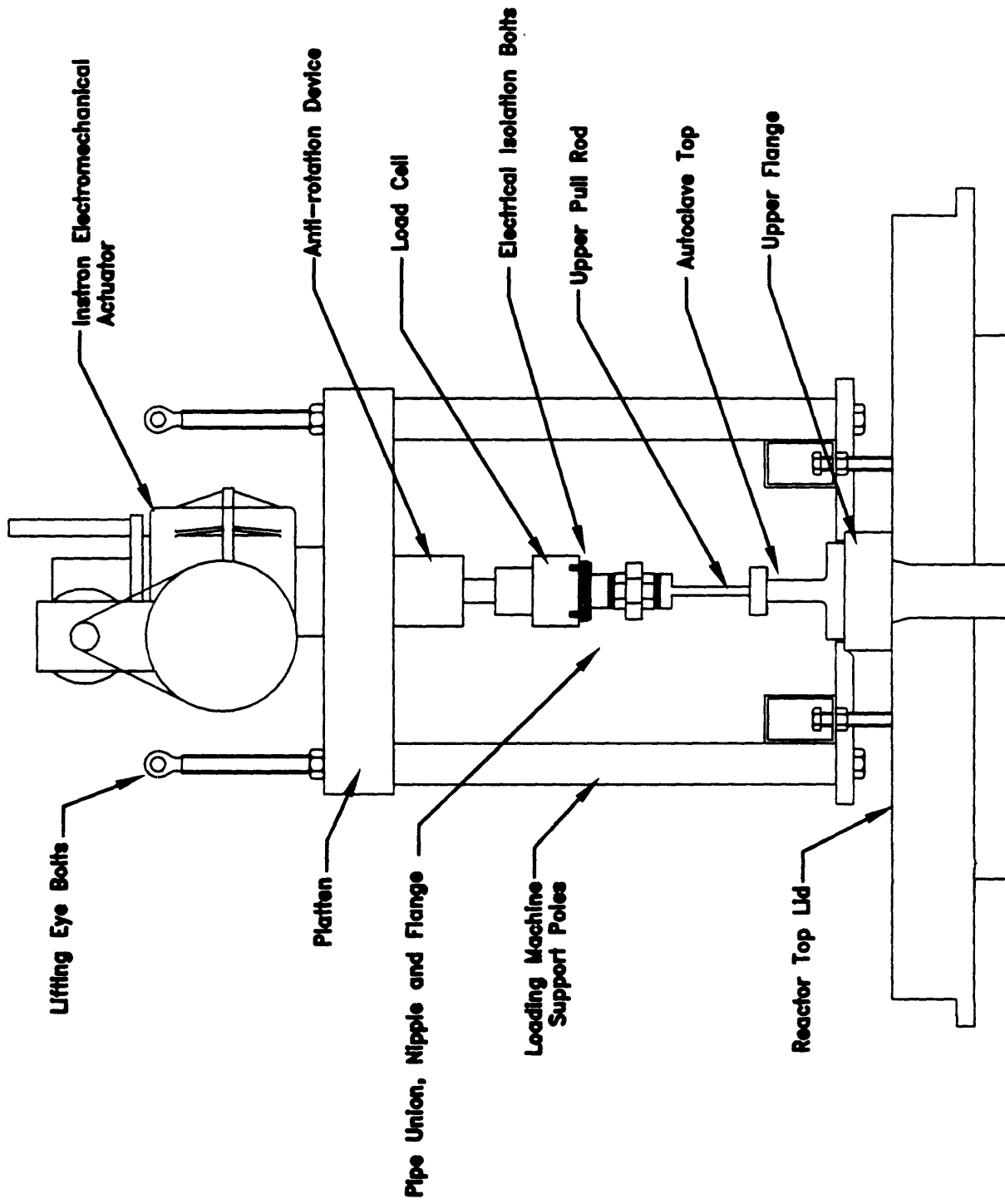
A platinum electrode is mounted in a window in the outer wall of the lower reaction tube adjacent to the test specimen. A high impedance voltmeter measures the potential between the platinum electrode and the rig and transmits the reading to the facility's data acquisition system. This potential is used to monitor the electrochemical potential (ECP) of the loaded test specimen.

Platinum is used as a reference electrode to measure the corrosion potential of a material specimen in an aqueous environment when sufficient hydrogen is present. The high exchange current density associated with platinum allows recombination reactions to take place when very small concentrations are present. The half reaction



readily takes place on the surface of the platinum. When sufficient H_2 is present in the

Figure 3.5. The Instron Loading Machine



environment such that any other species reacting by electrochemical means on the platinum surface do not polarize platinum, the potential is predictable using the Nernst relation

$$E = E^0 - \frac{RT}{nF} \ln \frac{P_{H_2}}{(H^+)^2},$$

where E is the potential of platinum vs. standard hydrogen electrode (SHE)

E^0 is the standard potential (defined to be 0.00V for the H_2 reaction)

R is the gas constant

T is the absolute temperature of the water

n is the number of equivalents associated with the reaction

F is Faraday's constant

P_{H_2} is the partial pressure of H_2 in the environment

(H^+) is the concentration of H^+ in the environment

and the platinum can be used as a reference electrode.

If the amount of H_2 in the environment is not high enough to prevent polarization, the potential of platinum will vary from the potential predicted by the Nernst relation. The potential on the electrode, however, will remain representative of the electrochemical nature of the environment. Any variation in the potential will reflect a change in the environment.

Scheduled in-core SSRT testing is to take place in normal water chemistry (NWC) which contains insufficient H_2 to prevent polarization of platinum. The potential of the platinum electrode will be the sum the effects of recombination of radiolytic H_2 , O_2 , H_2O_2 , and radicals.

A calibration of the potential of the platinum electrode against the rig was made during the ECP mapping procedures for varying reactor power levels, O_2 and H_2 concentrations, charging rates, and main loop flow rates. The potential of the platinum

electrode referenced to the rig during ECP mapping was measured to be -90mV with the reactor at full power, and +25mV with the reactor shutdown for baseline operating conditions. Moreover, many transients were carried out during in-core ECP mapping and the platinum electrode was sensitive to all changes.

3.2.5. Autoclave

The autoclave acts as a pressure barrier for the high pressure high temperature water. It is designed to contain 3200 psi water at 300°C. All tests presently scheduled are to be conducted at 1750 psi and 280°C.

The major components of the autoclave are the upper and lower containment tube, autoclave top, and various seals. As is the case for the lower pull rod and reaction tube, the lower containment tube is made of Ti 6Al-4V. The two sections of the containment tube are connected by a flange and 12 bolts with self-locking nuts. A Ni coated alloy 718 C-ring seal maintains the joint leak tight.

The weight of the upper and lower containment tubes is supported by the upper flange which is in turn supported by the reactor top lid. The autoclave top bolts to the upper flange. An O-ring between the upper containment tube and the autoclave top makes the seal. The O-ring is internally vented so that the internal pressure helps make the seal, and is made of Ni coated alloy 321 stainless steel.

The instrumentation lines which use the grooves machined in the reaction tube pass through the pressure barrier through feed-throughs in the autoclave top. There are six holes in the autoclave top, one per reaction tube groove. The feed-throughs for the six bare DCPD wires require the use of Viton® seals which must be maintained below 200°C. For this reason, standoffs are used for each DCPD feed-through. The two feed-throughs for the test specimen wires have cooling jackets on their standoff to provide additional cooling. This is required because these feed-throughs must be taken apart and re-made for each test.

The pull rod penetrates the pressure boundary through the autoclave top. A dynamic sealing ring made of Ekonol® filled TFE ensures that there is minimal coolant leakage and that the pull rod and autoclave top do not come into electrical contact. The entire seal consists of one seal backed up by a split backing ring pair made of Ekonol® filled TFE and a final backup ring made of Rulon®. The seal is supported by a packing nut which threads on to the neck of the autoclave top. The neck of the autoclave top is cooled by auxiliary cooling water. The top of the autoclave is illustrated in Figure 3.6.

The main loop water flow path through the rig begins with water entering the rig from the main loop supply line, through the autoclave top, and down to the bottom of the rig through the annulus between the containment and reaction tubes. Beneath the specimen the water changes direction and flows up through the lower grip holder and lower grip, past the test specimen, and to the top through the annulus between the reaction tube and pull rod. The water then exits the rig through the autoclave top and into the main loop return line.

3.2.6. Thimble

The thimble is made of Al 6061-T6 and is the only part of the in-pile rig which comes into contact with the MITR-II reactor coolant. It has a round cross section and is designed to withstand an internal pressure of 1500 psi. The autoclave fits within the thimble and the annulus between the autoclave and thimble is filled with flowing CO₂ gas. This gas gap provides thermal insulation preventing excessive heat loss and consequent reactor coolant boiling. An alumina spacer attached to the bottom of the lower containment tube ensures that the containment tube never comes into direct contact with the thimble. An aluminum slug fills the void between the bottom of the autoclave and the thimble.

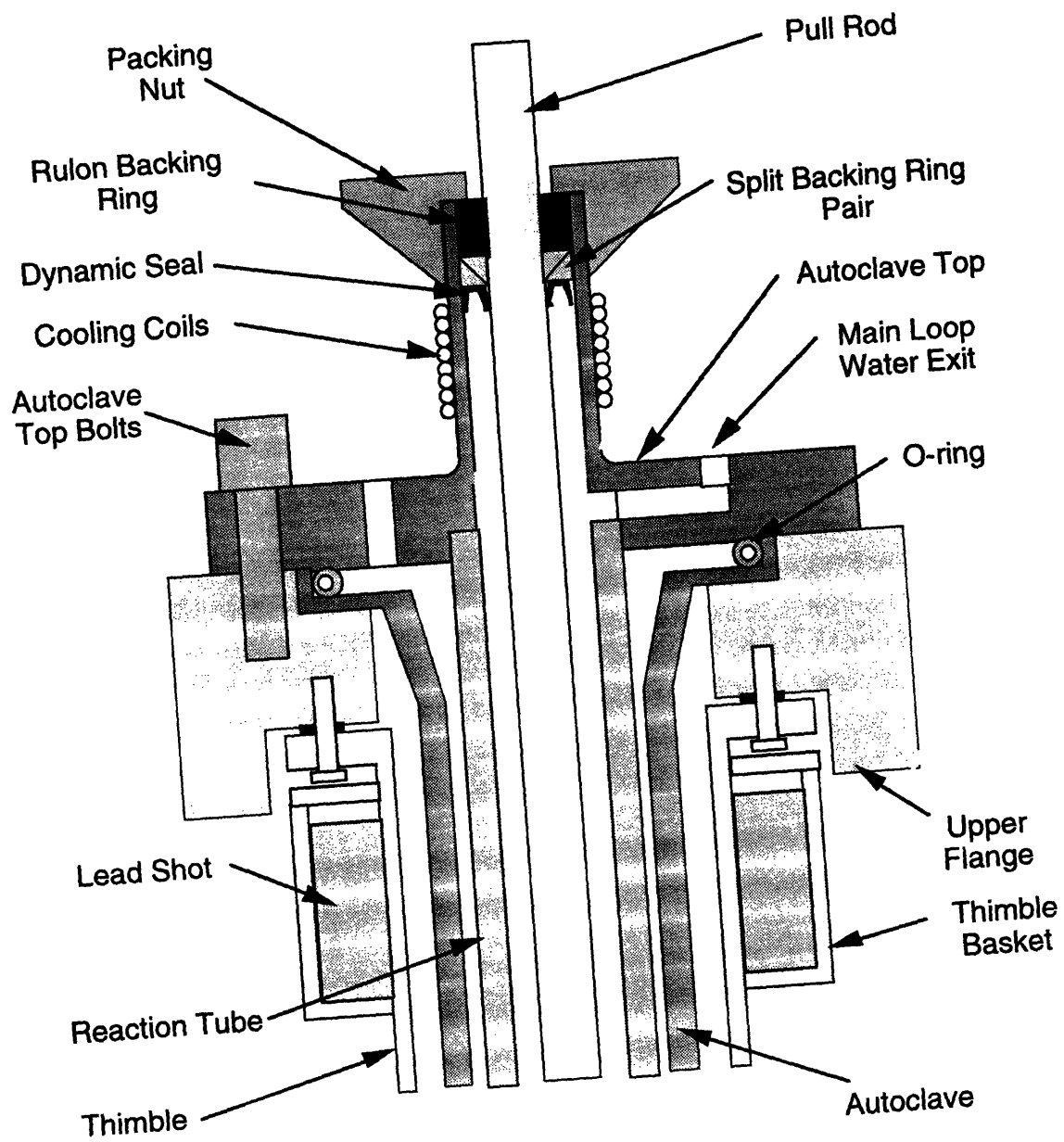


Figure 3.6. The Top of the Autoclave.

3.2.7. Dummy Element

The dummy fuel element provides the interface between the MITR-II reactor core and the in-core rig. It is made of Al 6061-T6 and is identical to the dummy element in use for PCCL and BCCL operations, including the method of handling, except that it has a

round rather than elliptical hole. All in-core testing presently scheduled with the IASCC in-core rig will be done in in-core position B3.

A shielding collar filled with lead shot is attached just below the thimble top flange. This collar fits within the step in the reactor top lid's test plug and supports the weight of the thimble. The bottom of this collar makes the reactor vessel atmosphere seal. Additional shielding for the gap between the thimble and autoclave is provided by a stainless steel collar located in the gap just above the reactor core. It is 12 inches long and is stepped and has four holes to allow steam to escape to the top without building up a large back pressure in the event of a lower containment tube rupture.

3.2.8. CO₂ Thimble Atmosphere

Flowing CO₂ fills the annulus between the thimble and the autoclave providing thermal insulation between the high temperature autoclave (280°C) and the relatively cool (50°C) MITR reactor coolant. Annulus pressure is maintained at 15 psi so that if a leak occurs minimal reactor water will enter the thimble. The humidity of the gas exiting the annulus is monitored to detect a thimble or autoclave leak. If the humidity reaches 90% an alarm will sound in the control room to warn experimenters. During normal operation thimble humidity is less than 15%. The entrance and exit ports for CO₂ to the thimble are on the upper flange. A rupture disk on the entrance line is designed to break at 80 psi. The entrance port is a large 3/4" hole so as to avoid a large back pressure in the event of a containment tube rupture.

The system consists of two liquefied CO₂ tanks plumbed to a dual tank regulator, one tank is in service at a time while the other tank is kept in reserve. When the pressure in the in-service tank drops to 300 psi an alarm sounds in the reactor control room to alert experimenters. If no action is taken the regulator automatically puts the reserve tank in service when pressure reaches 100 psi.

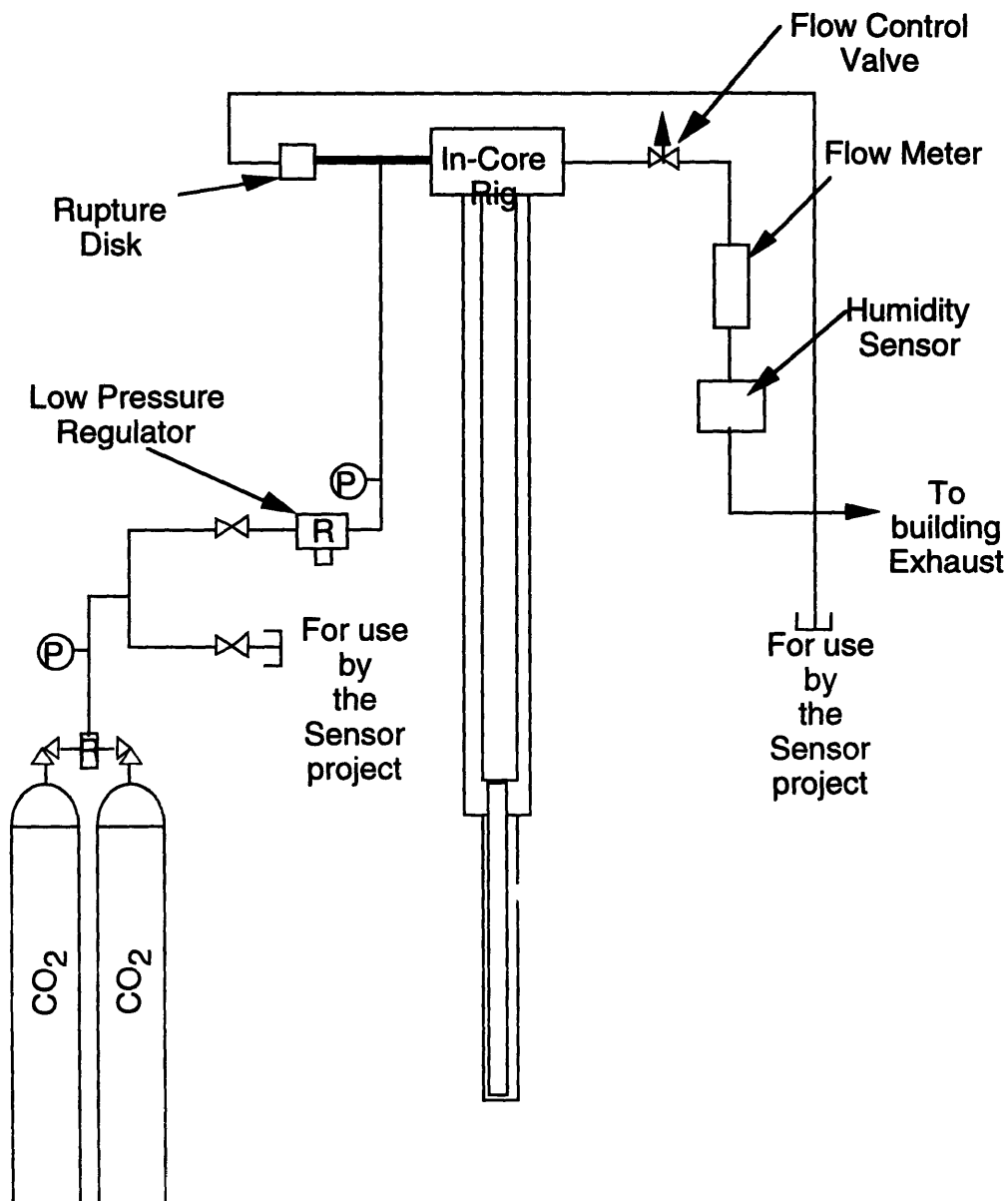


Figure 3.7. The Thimble Atmosphere Control System.

The regulator provides CO₂ at 80 psi to the reactor top for use by the IASCC in-core rig. Pressure is further reduced to 15 psi before entering the thimble.

An 1/8" aluminum tube extends through the exit port in the upper flange, down the annulus between the autoclave and the thimble to the containment tube flange. CO₂ exits the thimble through this tube, flows through a throttle valve, past the humidity sensor, and

to the containment building ventilation exhaust. A schematic of the CO₂ gas control system is shown in Figure 3.7.

3.3. In-Core ECP Mapping Rig

An in-core electrode rig was developed to study the effects of fast neutron and gamma radiation on the electrochemical corrosion potential (ECP) of stainless steel in high purity, 288°C water. The facility intended to measure the ECP of stainless steel and its sensitivity to varying parameters such as neutron and gamma dose rate and flow rate under both normal and hydrogen water chemistry conditions. These measurements will characterize the in-core facility used for slow strain rate testing (SSRT) of a variety of materials. Space constraints permit only a platinum electrode to be used during SSRT and the pre-characterization will be relied upon to calibrate the response of the rig, particularly under normal boiling water reactor chemistry (NWC). In addition, the data obtained is directly relevant to understanding in-core ECP in commercial BWRs. The water chemistry conditions and radiation dose rates of the rig are similar to those in commercial plants and the rig data can be used to benchmark radiolysis and ECP codes.

3.3.1. Rig Description

The testing facility consists of an in-core rig and water chemistry control system. The in-core rig is inserted into the MITR-II core through the reactor top lid and contains six electrodes in two electrode clusters. The water chemistry is controllable. Experiments under NWC and hydrogen water chemistry (HWC) are complete.

The in-core rig consists of an autoclave and electrode fixture. The autoclave is inserted into the MITR-II reactor core and contains the high temperature and pressure water; it is the same autoclave used for in-core SSRT testing. The electrode fixture positions six General Electric radiation qualified electrodes in two clusters in the in-core section of the autoclave. The fixture also guides the water to the bottom of the in-core

autoclave, up past both electrode clusters, and out of the rig. Each cluster consists of Ag/AgCl reference, platinum and stainless steel electrodes, and a dual junction thermocouple. The clusters are axially spaced 9 inches apart. Both the autoclave and electrode fixture are built in two sections; in-core and above core sections. The in-core sections are constructed of Ti 6Al-4V for optimum chemistry control and to minimize personnel radiation exposure during radioactive rig handling. The above core sections are made of stainless steel. The in-core rig is illustrated in Figure 3.8.

The electrodes are vertically movable to allow axial ECP mapping. In-core testing was completed using two positions. In position number 1 the bottom cluster was located in the center of the reactor core, and the top cluster was located 3 inches below the top of the core. In position number 2 both electrode clusters were moved up 9 inches from position 1 so that the bottom cluster was located 3 inches below, and cluster number two was located 6 inches above. Having both electrode clusters in the same axial core position for different tests provided internal verification of results and a means to minimize any calibration offset.

The water chemistry control system was the same water system used for in-core SSRT testing and consists of a recirculation circuit and water clean up system. The recirculation circuit, or main loop, pumps the high pressure and temperature water through a heater and the in-core rig, and back again. Clean water is continuously being added to the loop at a rate variable to a maximum of six main loop water inventory replenishments per hour. Letdown water passes through an external reference autoclave which contains an external reference Ag/AgCl and platinum and stainless steel electrodes. Downstream of the reference autoclave the water is cooled, de-pressurized, and sent to chemistry monitoring sensors. Chemistry monitoring includes dissolved oxygen, dissolved hydrogen, conductivity, and pH sensors. Letdown water chemistry is representative of main loop water chemistry. Main loop water temperature is controlled by varying the electric power

to the main loop heater, thermocouples located in either electrode cluster can be used for water temperature control as well as data acquisition.

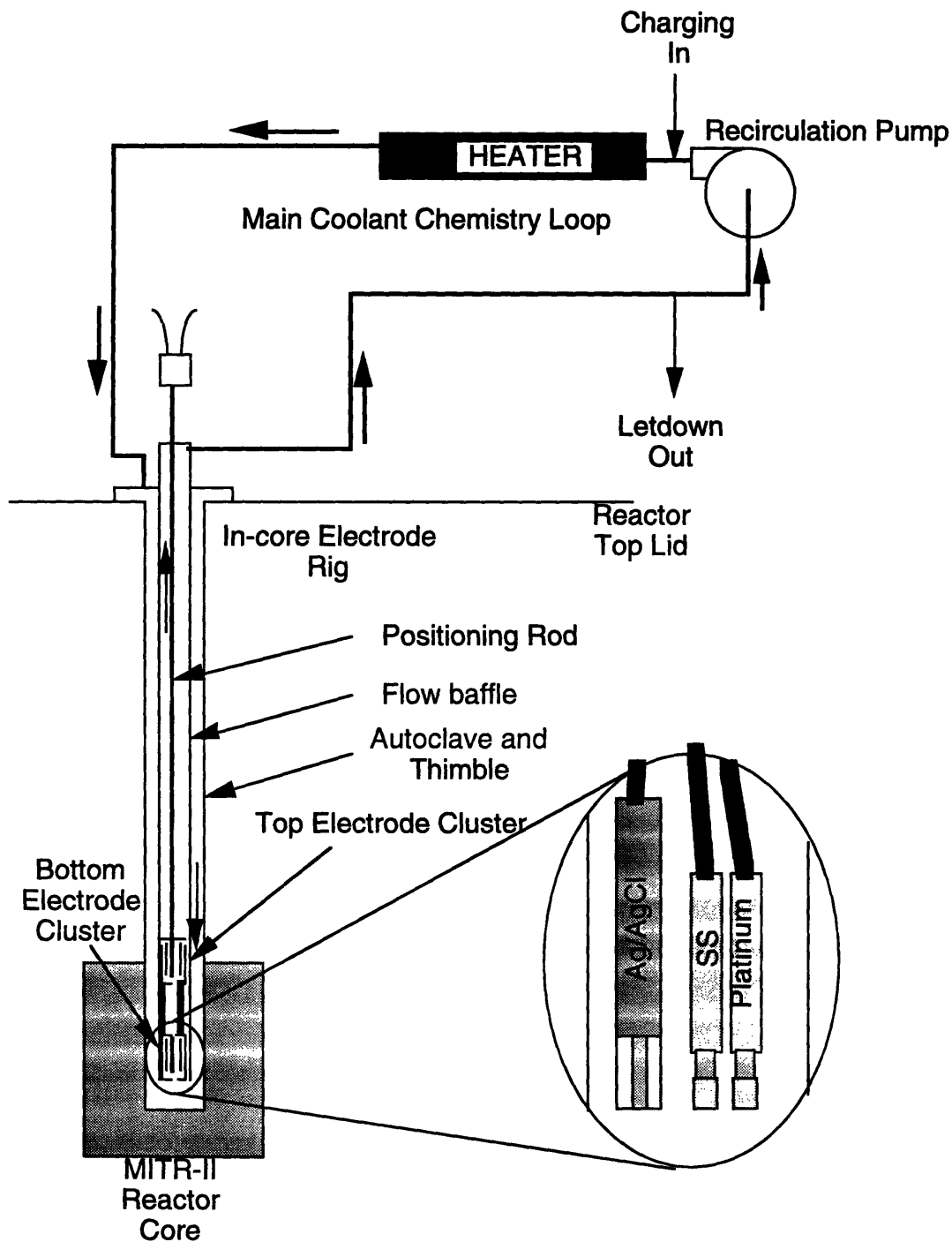


Figure 3.8. The IASCC In-Core ECP Rig.

3.4. WATER SYSTEM

Figure 3.9. is a schematic of the entire water system. For ease of operation and discussion the system is divided into functional subsystems. These are the main recirculation loop, charging system, letdown system, clean up system, bubbling system, pressurizer and pressure relief system, and chemical injection system.

3.4.1. Main Recirculation Loop

The main loop circulates controlled temperature and chemistry water past the specimen under test. The principal focus is on the concentrations of radiolysis products (dissolved H_2 , O_2 , H_2O_2 , and radicals), and the resulting electrochemical corrosion potential (ECP) of stainless steel. The ability to verify the desired chemical conditions at the test specimen is required. The ability to alter the chemical conditions as necessary is desired.

Components of the main loop include the main loop heater, main loop recirculation pump, 3/4" OD tubing, and fittings. A thermocouple adjacent to the loaded test specimen monitors the coolant temperature and provides input to the main heater controller and data acquisition. The main heater controller provides indication of the specimen temperature and automatic control of electrical power to the main heater.

A schematic diagram of the main loop and its connections to support lines is shown in Figure 3.10. Main loop water flow path begins as water leaves the in-pile rig through the autoclave top and into the main loop return line where it flows directly to the recirculation pump. The water exits the pump, flows through the main heater, through the main loop supply line, and enters the in-pile rig through the autoclave top. All tubing, except the tubing used inside the main loop heater, is seamless type 316L SS 3/4" outside

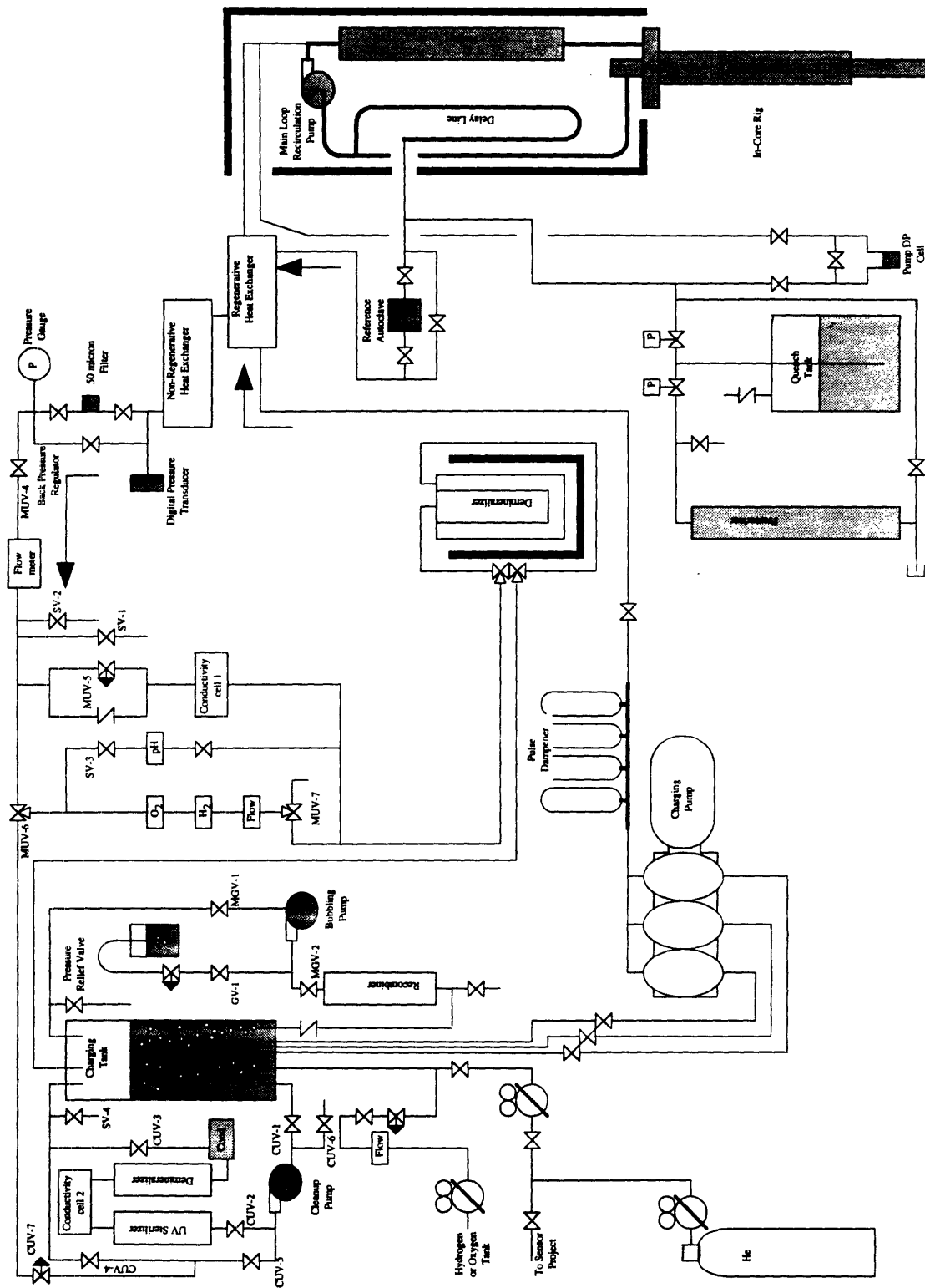


Figure 3.9. The IASCC Water Chemistry Control System

diameter with a wall thickness of 0.083". The design flow rate of the main loop is 5 gpm. All main loop fittings are Parker 37° flare fittings.

The main loop recirculation pump is an Autoclave Engineers MagnePump with the motor magnetically coupled to the pump head impeller. An identical pump has been generally reliable during all PCCL and the most recent BCCL campaign. The 120V, 3Ø motor is powered by a MagneTek GPD 503 pump controller which allows for main loop flow rate control by varying output frequency. This pump controller also provides electrical isolation for the pump's reactive load allowing an inverter type uninterruptable power supply (UPS) to be used for pump power. Cooling for the recirculation pump is provided by the auxiliary cooling water system.

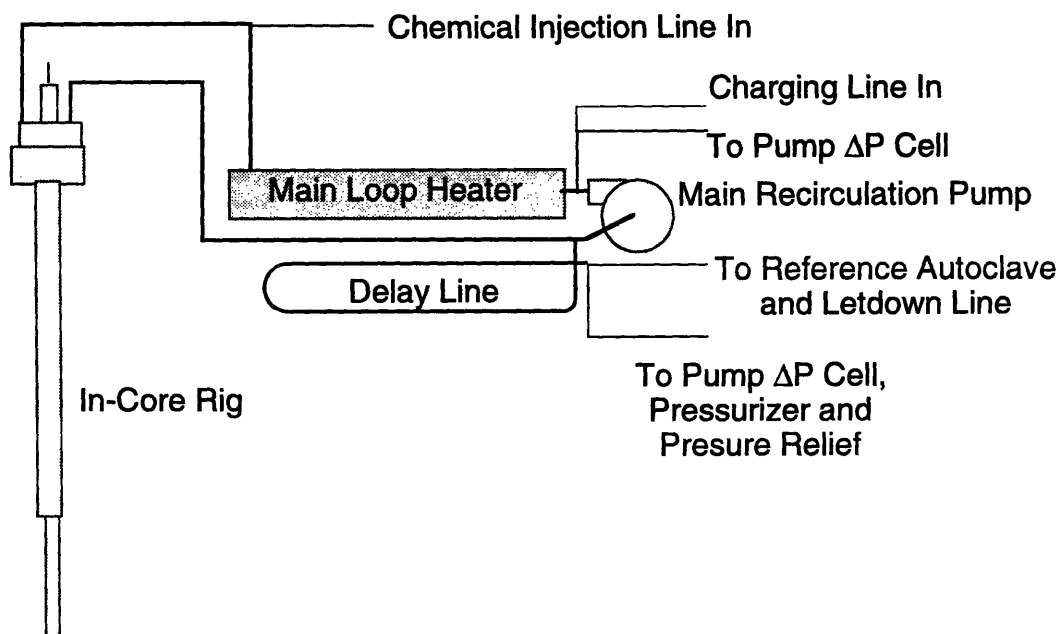


Figure 3.10. Main Recirculation Loop

Two inches of lead sheet covers the heater, main loop recirculation pump, and associated main loop tubing. Four layers of 1/2" lead sheet lie on the reactor top decking beneath the main loop recirculation pump and heater. A steel frame supports the weight of

the four layers of 1/2" lead sheet on each side and above the main loop. Additional shielding is provided by stacked lead bricks.

Attached to the main loop return line immediately upstream of the recirculation pump is the letdown line and pressurizer line tap. The first 12 feet of the letdown line is 10 feet of 3/4" OD tubing, identical to the tubing used in the main loop. This length, referred to from here on as the delay line, is physically located within the shielded volume. It acts as a one minute holding volume allowing the N-16 activity in the letdown water to decay prior to the coolant entering the unshielded sections of the letdown line (the half-life of N-16 is 7.1 s). The differential pressure across the length of the delay line is less than 1×10^{-3} psi at a charging rate of 600 cc/min and therefore does not affect pump differential pressure readings.

Immediately downstream of the recirculation pump is the charging line tap. Downstream of the heater, but before the in-pile rig, is the tap for the chemical injection pump. H_2O_2 or ionic species may be injected to the main loop water via the chemical addition pump for testing the effects of different additives on IASCC. Since H_2O_2 is not stable in 300°C water it must be added to the main loop close to where the water enters the in-pile rig to be of consequence near the test specimen. The main loop recirculation pump ΔP cell taps to both sides of the pump.

3.4.2. Main Loop Heater and Heater Control

The main loop water temperature adjacent to the test specimen is controlled by varying the electric power to the main loop heater. The heater is rated to 24 kW to make up for the nearly 10 kW of heat losses present in the loop with the reactor shutdown. Power for the heater is 480V, 3 ϕ , and is controlled by the main heater controller. A schematic of the heater controller is shown in Figure 3.11.

The heater controller has eight built in relays which automatically turn heater power off when required. If the heater power trips off automatically the controller must be manually reset. The following conditions will activate a heater trip: loop water temperature at the specimen greater than 290°C, loop water temperature at the heater outlet greater than 290°C, heater lead bath temperature greater than 370°C, main loop pressure less than 1650 psi, main loop pressure greater than 1950 psi, low charging tank level, low auxiliary cooling water flow, and loop water temperature at the specimen less than 260°C. The two high water temperature trips use entirely independent components. The low water temperature trip must be manually reset each time the system is started to allow heat up.

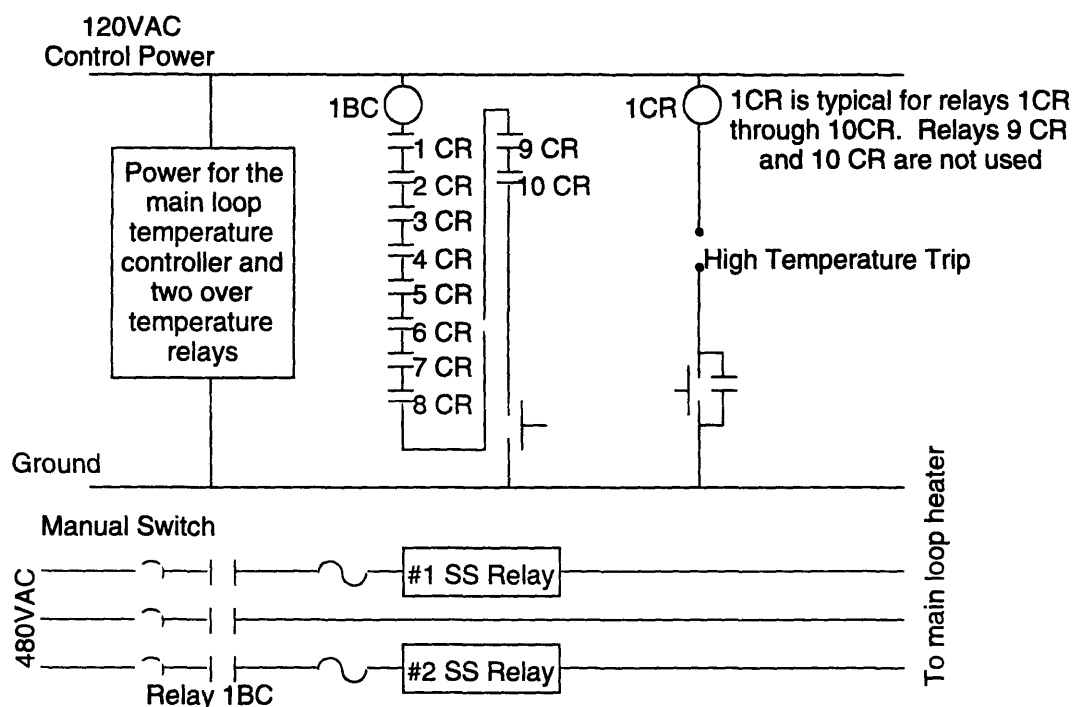


Figure 3.11. Schematic Diagram of the Main Loop Heater Controller.

The heater is a 4"X6"X68" rectangular steel tube filled with lead. Twelve Chromalox 3/4" NSL strip heaters, each rated for 2 kW, are clamped to the outside of the heater shell. Each strip heater is rated for 240V, so the strip heaters are connected as two parallel delta's with two strip heaters in series. A schematic of the heater wiring is shown in Figure 3.12. The water exiting the main loop recirculation pump enters the heater inlet

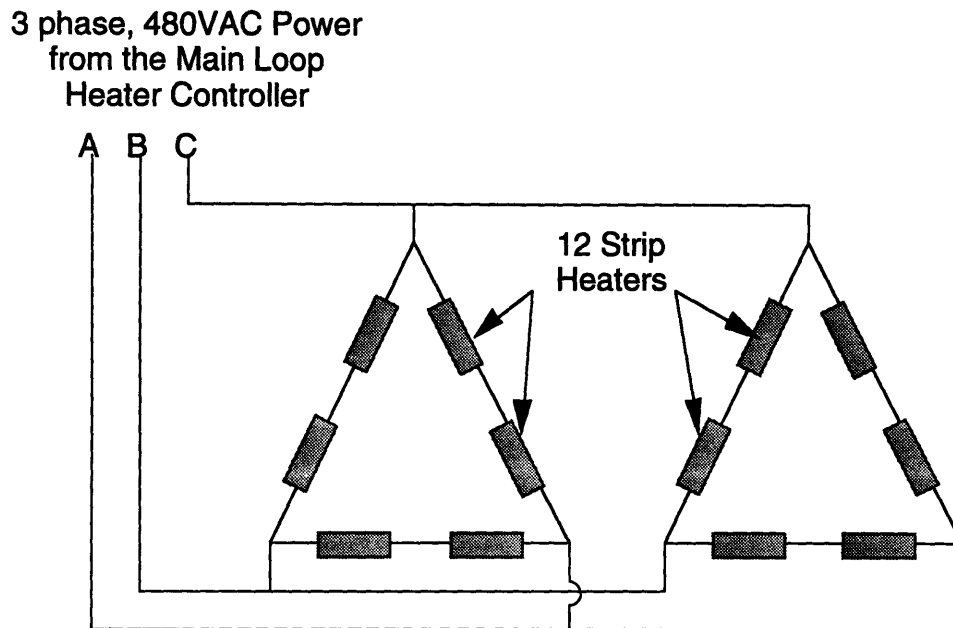


Figure 3.12. Schematic Diagram for Wiring of Main Loop Heater.

"Y" where it is divided into two parallel flow paths. These flow through the heater shell and lead bath. Once out of the lead bath, the water enters the outlet "Y" where the two flow paths recombine and the water enters the main loop supply line. The tubing used within the heater is seamless type 316L SS 5/8" OD with 0.083" wall thickness.

The lead acts as a heat transfer medium, it stores thermal energy, and provides shielding for personnel from the decay of radioactive N-16 present in the main loop water during reactor operation. The main loop heater rests on the reactor top platform next to the Sensor project's main loop heater. Both projects main loop return and letdown delay lines are located between the two heaters.

Completely encasing the heater, return line and delay line is two inches of ceramic fiber thermal insulation supported by an expanded aluminum shell. The thermal insulation about the heater reduces the strip heater's sheath temperature and improves its reliability and reduces overall power demand. A high temperature thermal compound is applied to each strip heater to increase its effective surface area in contact with the steel shell.

3.4.3. Charging System

The charging system provides makeup water from the charging tank with the desired chemistry and at a controllable flow rate to the main loop for main loop chemistry and pressure control.

The major components in the charging system include the charging tank, charging pump, regenerative heat exchanger, and a charging pump pulse dampener. The regenerative heat exchanger is located on the pressurizer rack, the remaining components are mounted on the chemistry control rack. A schematic diagram of the charging system is shown in Figure 3.13.

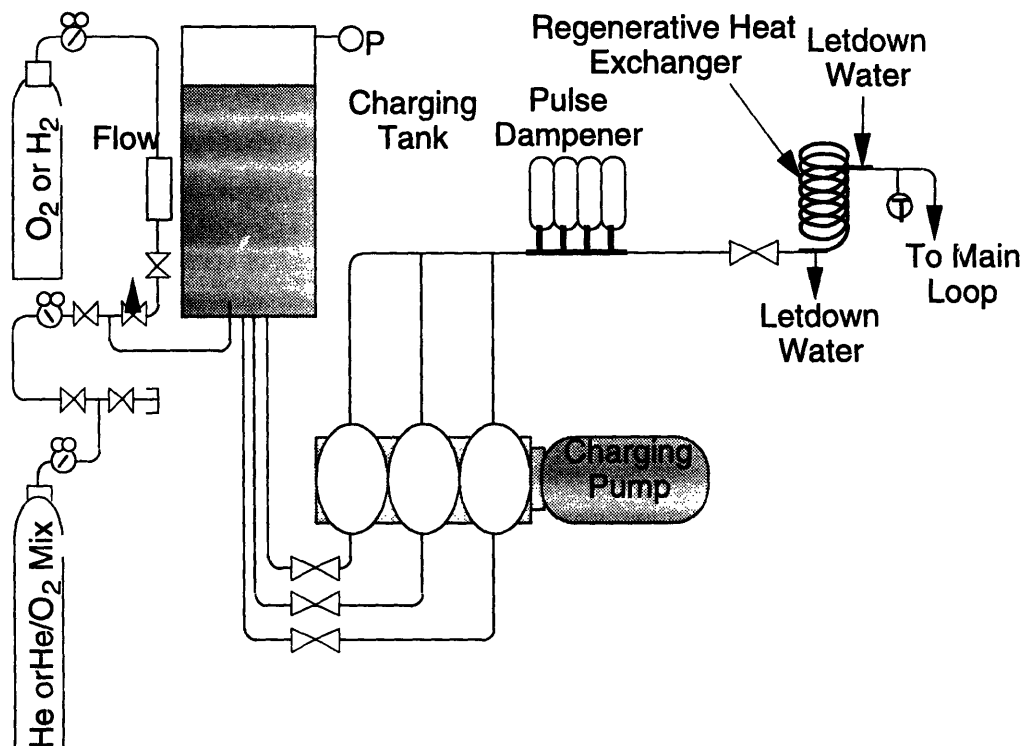


Figure 3.13. Charging System

Since the water in the main loop recirculates through the reactor core the concentration of radiolytic oxidizing species may increase to levels higher than desired. For this reason the capability to operate with a high loop water refresh rate is essential. The charging system was system was therefore designed to provide water to the main loop at a

rate equal to 600 cc/min. At this charging rate the main loop water inventory is refreshed every 10 minutes. This is similar to the water turnover time in a BWR.

The main loop charging pump is made by American Lewa (model EK-3), and is designed to charge water at room temperature to 2250 psi at 100-880 cc/min. Since main loop pressure affects the load on the specimen, the charging pump has a positive displacement diaphragm triplex pump head which minimizes pressure pulsations. A pulse dampener is also used to further limit the effects of pulsation on specimen load.

The charging tank has a 70 liter capacity and the water in the charging tank can have He or He/O₂ mix cover gas as required. Baseline conditions for scheduled in-core SSRT testing has the charging tank pressurized to 5 psi with 0.45%O₂ in He. At this pressure the charging tank O₂ concentration is 200 ppb. The high pressure He/O₂ tank is located on the reactor containment building floor adjacent to the thimble atmosphere CO₂ tanks. A regulator on the tank provides the gas at a pressure of 20 psi to the reactor top. On the chemistry rack the pressure is further reduced to 6.5 psi and supplied to the bottom of the charging tank. This last pressure regulator controls the pressure in the charging tank.

Additional gas can be added to the bottom of the charging tank through a flow meter, throttle valve, and isolation valve on the chemistry rack. O₂ is added for loop heat up and to accelerate establishing the oxidizing environment desired for in-core SSRT testing. This line was also used for the addition of H₂ to the charging tank for in-core ECP mapping using hydrogen water chemistry (HWC). For HWC studies the charging tank was pressurized with He gas.

The water in the charging tank is kept clean by continually pumping the water through the clean up system described in section 3.4.5 below. Water conductivity levels during in-core testing are normally less than 0.07 μS/cm.

3.4.4. Letdown System

The letdown system cools the water from the main loop, controls system pressure, provides letdown water at the operating temperature to the reference electrodes in the reference autoclave for electrochemical measurements, and directs the water from the main loop to the charging tank via the desired line for chemical analyses.

The letdown system consists of the following components: the delay line, reference autoclave and three electrodes, regenerative and non-regenerative heat exchangers, a back pressure regulator, various chemistry measurement sensors, and a demineralizer and filter. The reference autoclave and heat exchangers are located on the pressurizer rack, the remaining components are located on the chemistry control rack.

Figure 3.14. is a schematic of the letdown line. The water flows from the main loop at the upstream side of the main loop recirculation pump, through the shielded delay line and then to the reference autoclave. Downstream of the reference autoclave the water flows through the regenerative heat exchanger, non-regenerative heat exchanger, and to the chemistry control rack where the water pressure is reduced by the back pressure regulator. Water is then directed to one or more lines for chemical analysis, all water returns to the charging tank through the letdown line demineralizer.

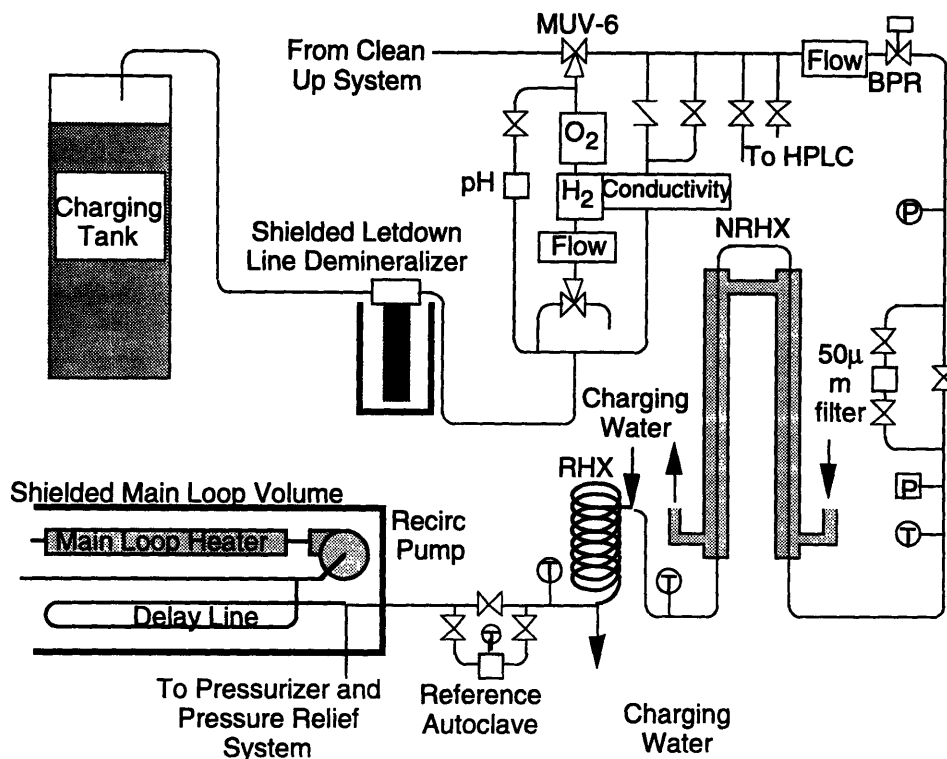


Figure 3.14. Letdown System

The reference autoclave is made of titanium and serves to hold Ag/AgCl, platinum and stainless steel electrodes. The water being tested is at the loop operating temperature and pressure. The electrochemical corrosion potentials (ECP) measured in the reference autoclave are recorded every minute to disk and displayed in real time by the data acquisition system. MUV-1, MUV-2, and MUV-3 are the reference autoclave's isolation and bypass valves. Normally all letdown water flows through the reference autoclave, but the reference autoclave may be bypassed for maintenance.

The regenerative heat exchanger increases the efficiency of the system by using the high temperature letdown water to heat the cold charging water before it enters the main loop. The non-regenerative heat exchanger ensures that the letdown water is cooled below 75°C to prevent damage to the back pressure regulator. The regenerative (RHX) and non-regenerative heat exchangers (NRHX) are counter flow tube in tube design with the letdown water flowing through the outer tube in the RHX, and through the inner tube in the

NRHX. The charging water flows through the inner tube in the RHX. Cooling of the NRHX is provided by the auxiliary cooling water system.

The back pressure regulator (MUV-4) controls the main loop pressure and has proven to be very reliable during all out of core and in-pile campaigns. Upstream of the back pressure regulator is a 50 μ m filter which removes solids that could cause the back pressure regulator to fail. This filter has isolation and bypass valves associated with it so that it can be changed without interrupting a test. A filter was successfully changed during in-core ECP mapping.

Downstream of the back pressure regulator the letdown water is directed through the letdown line flow rate meter, which provides indication of charging rate, then to one or more of several flow paths. These flow paths include: going directly to the letdown line demineralizer and charging tank (through MUV-5), to a sample tap for remote analysis (SV-1), to a sample line for on line ion chromatography analysis (SV-2), or via a three-way-valve to the chemistry measurement line (MUV-6 and MUV-7). Letdown water usually flows through the chemistry measurement line during in-core testing which has on line O₂ and H₂ sensors and a parallel line having a sensor for pH measurement. Water flow rate through the O₂ and H₂ sensors must be 150 cc/min so the chemistry measurement line includes a flow rate meter and a throttle valve. The three way valves allow the chemistry of the charging tank water to be measured in the chemistry measurement line. The conductivity of the letdown line water is monitored by a sensor located down stream of MUV-5. If, due to operator error, all lines downstream of the back pressure regulator are shut, an over pressure condition in the main loop may result. To avoid this, a spring loaded check valve (set to lift at 10 psi) acts as a relief valve around MUV-5.

All water entering the charging tank from the main loop passes through a demineralizer. This demineralizer minimizes the spread of radioactive corrosion products and ionic impurities to the charging water tank, and to the clean up, bubbling, and charging

systems. The letdown line demineralizer is located on the experimental platform floor away from the chemistry control and pressurizer racks and is shielded by two inches of stacked lead bricks to minimize experimenter exposure to radiation during in-core testing.

3.4.5. Clean Up System

The water being charged into the main loop must be kept as free of impurities as possible. To meet this need, the clean up system provides chemistry measurement capability (by on-line O₂ and H₂ sensors in the chemistry measurement line and a conductivity sensor in the clean up line) and clean up capability (ultraviolet sterilizer and demineralizer). A schematic diagram of the clean up system is shown in Figure 3.15.

The clean up system consists of the charging tank, clean up water pump, ultraviolet sterilizer, demineralizer, and several isolation valves. The demineralizer removes ionic impurities in the makeup tank water by ion exchange. The UV sterilizer decomposes organic matter and H₂O₂. All components are located in the chemistry control rack.

The system normally operates in charging tank clean up mode, with the clean up water pump providing flow from the bottom of the charging tank to the UV sterilizer, conductivity sensor, demineralizer, then back to the charging tank. The valve lineup for this mode of operation is shown in Table 3.2.

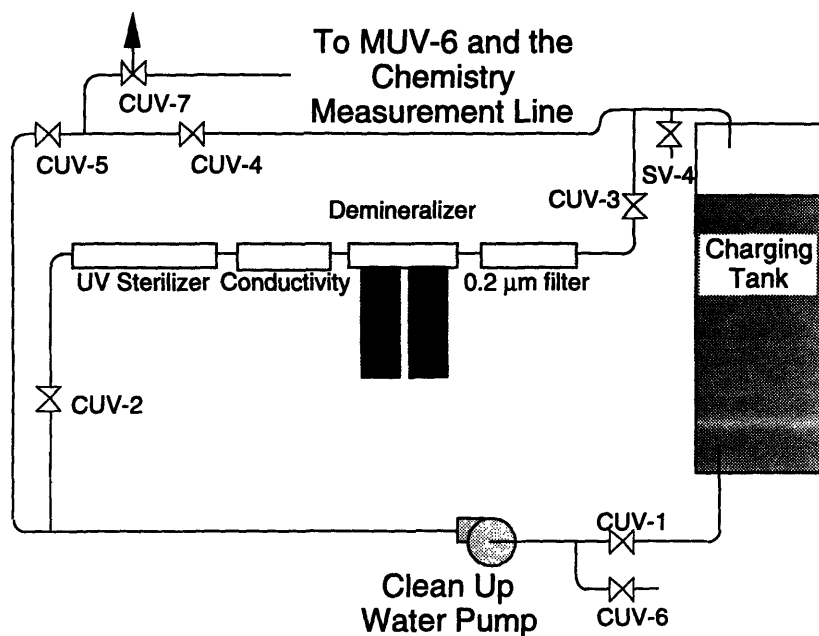


Figure 3.15. Clean Up System

Table 3.2. Clean up system valve line up for charging tank clean up.

Valve	Position
CUV-1	Open
CUV-2	Open
CUV-3	Open
CUV-4	Closed
CUV-5	Closed
CUV-6	Closed
CUV-7	Closed

The chemistry of the charging tank can be measured during charging tank clean up by opening CUV-5, throttling open CUV-7, and selecting the charging tank with MUV-6. Normally, the system operates in clean up mode with CUV-5 open, CUV-7 throttled open and MUV-6 selected to the letdown line. Throttle valves CUV-7 and MUV-5 are adjusted such that by changing the position of MUV-6 150 ml/min of water flows from either the charging tank or letdown line to the chemistry measurement line.

3.4.6. Bubbling System

The bubbling system maintains the dissolved gas concentration in the charging tank water at the desired levels. This is accomplished by recirculating the atmosphere at the top of the charging tank through a catalytic recombiner to the bottom of the charging tank. A throttled vent line allows for slow stripping of the charging tank atmosphere and addition of clean cover gas. Radiolytic H_2 and O_2 are recombined in the catalytic recombiner to form H_2O . Cover gas stripping helps the recombiner to maintain the charging tank O_2 and H_2 concentrations within desired control bands.

The bubbling system consists of the charging tank, bubbling pump, recombiner, gas stripping line and isolation and throttle valves. A schematic of the bubbling system is shown in Figure 3.16. The gas stripping line empties the used cover gas to the bottom of a vented bottle of water. The water prevents back diffusion of O_2 , CO_2 , etc. to the charging tank and provides visual indication of gas stripping rate.

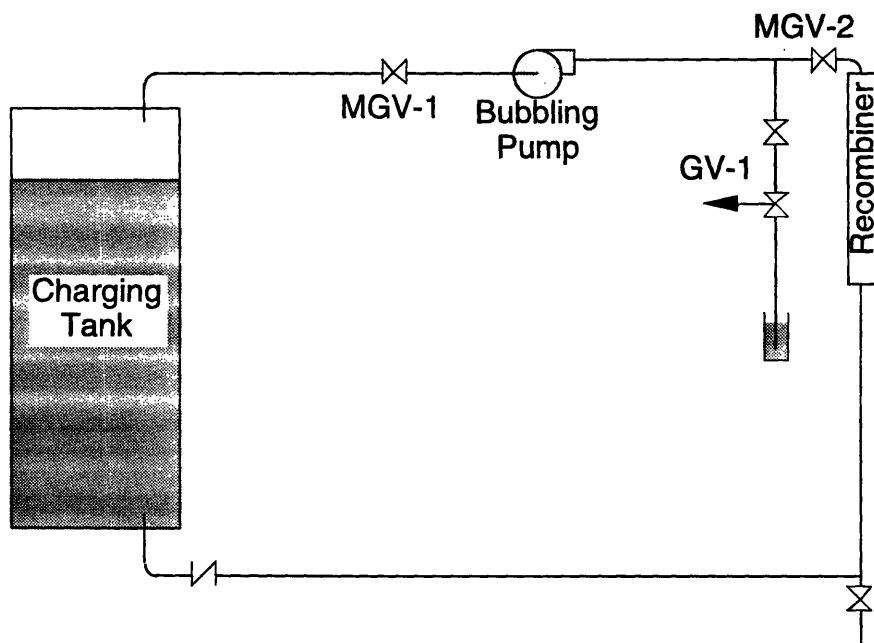


Figure 3.16. Bubbling System

3.4.7. Chemical Injection System

The chemical injection system provides the ability to add H_2O_2 and ionic species to study the effects of these additives on material cracking. The chemical injection system includes the chemical injection tank, chemical injection pump, flow meter, and valves. All components are mounted in the chemistry control rack. A schematic of the chemical injection system is shown in Figure 3.17.

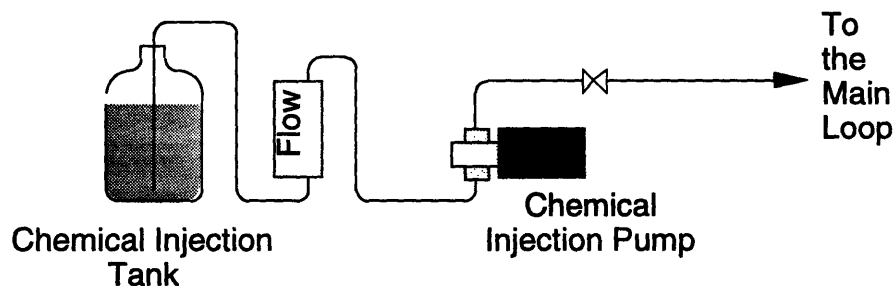


Figure 3.17. Chemical Injection System

The chemicals to be added to the main loop are measured and added to demineralized water in the chemical injection tank. The tank is connected to the suction of the chemical injection pump and the chemicals are injected to the main loop. The chemical injection system is connected to the main loop downstream of the main heater, immediately before the water enters the in-pile rig to minimize thermal decomposition of species such as H_2O_2 in the event that they are injected.

The chemical injection pump is a Milton Roy positive displacement plunger pump and is rated to pump water to pressures up to 2500 psi. The chemical injection system is identical to the chemical injection system used successfully for all BCCL campaigns.

The chemical injection system was not used for in-core ECP mapping or scheduled in-core SSRT testing since studying the effects of chemical additives on material cracking is not in the current test matrix. It is, however, in place in the chemistry control rack for use when necessary.

3.4.8. Pressurizer and Pressure Relief

The pressurizer minimizes boiling in the main loop in the event of a slow main loop leak or charging pump failure. It is attached to the main loop through the delay line and is located in the pressurizer rack. The pressurizer water temperature is maintained at 560 °F, which is hotter than the highest temperature anywhere in the main loop. In the event of a slow leak the pressure in the main loop and pressurizer will drop quickly until saturation pressure for the water in the pressurizer is reached. Pressurizer water will boil and the rate at which main loop pressure drops will decrease. The main loop heater trips off due to low system pressure before pressurizer boiling and main loop cooling begins.

The pressurizer is heated by two 2 kilowatt 120VAC tape heaters. The heaters are connected in series and are powered by the 220VAC output of the heater controller. A thermocouple located in the center of the pressurizer water volume measures the water temperature and sends a signal to the heater controller which is identical to the main loop heater controller. Figure 3.18. is a schematic of the pressurizer and pressurizer relief system.

The pressure relief system consists of two pressure relief valves and a quenching tank. All components are located in the pressurizer rack. Both relief valves are set to lift at 2500 psi which provides a large safety margin to the maximum design pressure of the autoclave (3200 psi). One relief valve is connected to the top of the pressurizer, the other is connected to the delay line. Each valve relieves water through a common header to the bottom of the 25 gallon quenching tank which is kept half full of water. The high pressure and high temperature water entering the quench tank from the relief valves initially flashes to steam, but will be condensed by the water. A spring loaded check valve, set to lift at 50 psi, acts as a relief valve for the quench tank and discharges to the containment building atmosphere.

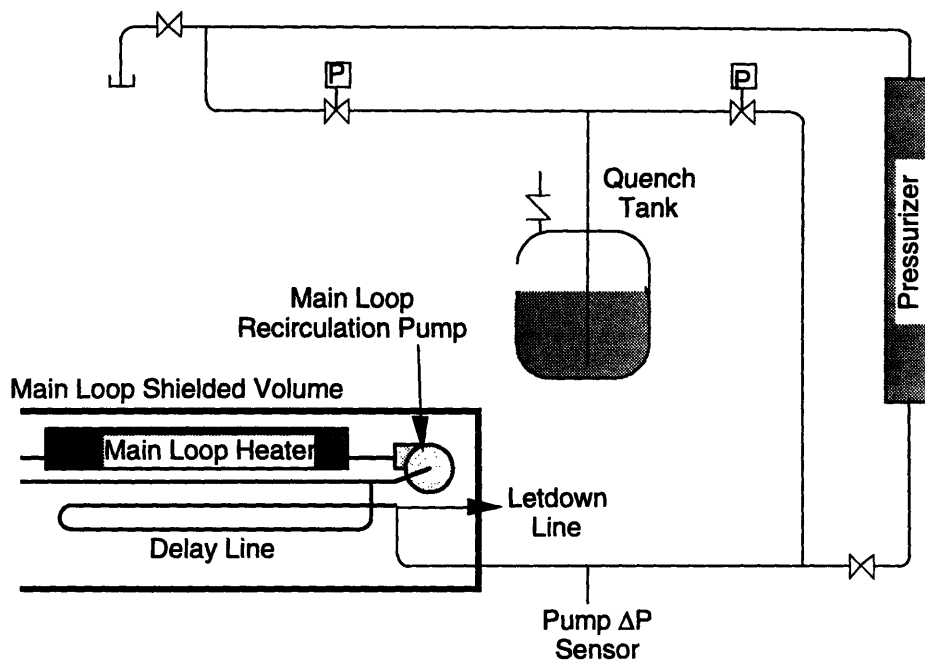


Figure 3.18. Pressurizer and Pressure Relief System

3.4.9. Auxiliary Cooling Water System

The auxiliary cooling water system provides cooling water to the experimental facilities as needed. The components that require cooling water are the main loop recirculation pump, non-regenerative heat exchanger, and cooling jackets for the fittings on the autoclave top including the dynamic seal and two test specimen DCPD wire feed-throughs.

The system also provides cooling water to the PCCL recirculation pump and the BCCL recirculation pump when operating in recirculation mode. Cooling water is pumped from the test tank to the component which requires cooling and back to the test tank. The test tank is cooled by pumping the test tank water to a heat exchanger in the equipment room where it is cooled by reactor secondary coolant and returned to the test tank. The test tank is located adjacent to the front mezzanine.

Cooling water is pumped to the experimental platform by the auxiliary cooling water pump located on the experimental platform. A flow switch provides an alarm and main loop heater trip when auxiliary cooling water flow rate drops below 2 gpm. The auxiliary cooling water system is illustrated in Figure 3.19.

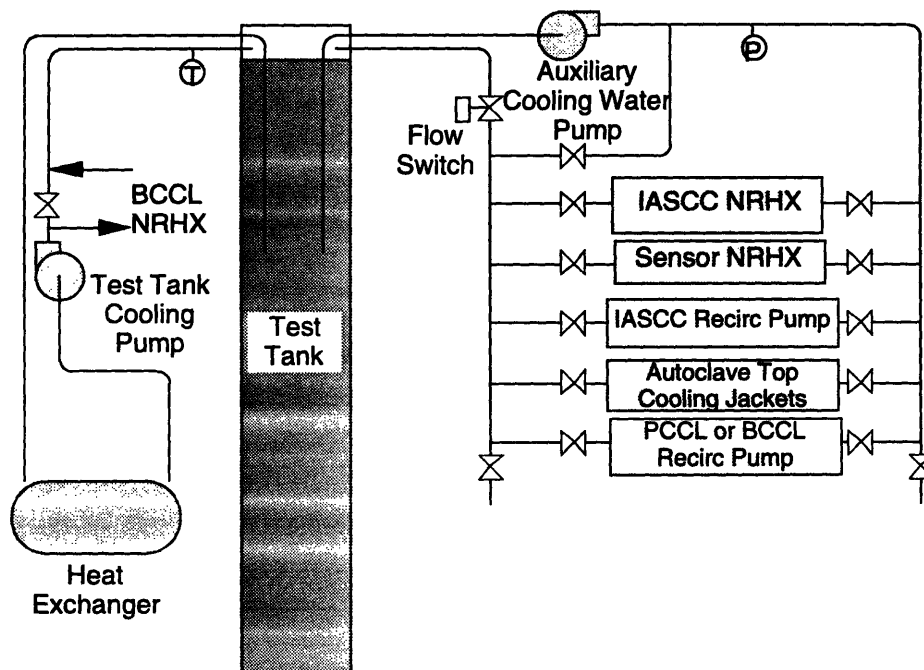


Figure 3.19. Auxiliary Cooling Water System

3.4.10. Instrumentation and Interlocks

Facility instrumentation includes main loop pressure, recirculation pump differential pressure, letdown line and charging tank water chemistry, and several temperatures. Main loop pressure is measured by two methods; a mechanical pressure gauge and a digital pressure transducer. Both indicate pressure locally on the chemistry rack. In addition, a 0-10V signal from the digital pressure transducer is used as input to the loading machine control for pressure compensation of specimen load, pressure indication in the reactor control room, and input to data acquisition. High and low pressure alarms and heater trips are provided by pressure switches in the letdown line located on the chemistry rack.

Pump differential pressure is measured by a Validyne Engineering transducer/transmitter and digital transducer indicator. The transducer/transmitter is mounted on the pressurizer rack, the transducer indicator is located on the chemistry rack and provides local indication of pump differential pressure in psi and a 0-10V signal for input to data acquisition. Data acquisition records the differential pressure and provides the alarm and heater trip if main loop flow is interrupted.

Table 3.3. lists the locations of temperatures measured and the output provided. All temperatures are measured by type K thermocouples. In-core temperature is measured by a sheathed thermocouple near the in-core test specimen. Pressurizer temperature is measured by a sheathed thermocouple located in the center of the pressurizer. All other thermocouples are spot welded to tubing or to the heater casing. Thermocouples 16, 17, 18, and 19 terminate at signal conditioners in the terminal panel on the reactor top. These four signal conditioners are used for impedance matching and allow the use of multiple recorders from one thermocouple.

Table 3.3. Temperatures monitored in the water system.

Output	No.	Name
Chemistry Rack Temperature Indicator	1	spare
Chemistry Rack Temperature Indicator	2	Heater Casing
Chemistry Rack Temperature Indicator	3	Heater Inlet
Chemistry Rack Temperature Indicator	4	Heater Outlet
Chemistry Rack Temperature Indicator	5	Reference Autoclave
Chemistry Rack Temperature Indicator	6	Charging Line RHX Outlet
Chemistry Rack Temperature Indicator	7	Letdown Line RHX Inlet
Chemistry Rack Temperature Indicator	8	Letdown Line NRHX Inlet
Chemistry Rack Temperature Indicator	9	Letdown Line BPR Inlet
Chemistry Rack Temperature Indicator	10	Spare
Heater Control	11	In-Core Temp
Heater Trip	12	Heater Outlet
Heater Trip	13	Heater Lead Bath
Heater Control	14	Pressurizer
Heater Trip	15	Pressurizer
D/A and Control Room Indication	16	In-Core Temp
D/A	17	spare
D/A	18	Heater Casing
D/A	19	Reference Autoclave

Table 3.4. summarizes the ranges and accuracies of letdown line instrumentation. All measurements from sensors in the letdown line except for pH are recorded to disk and displayed in real time by the data acquisition system.

Table 3.4. The ranges and accuracies of letdown line instrumentation

Parameter	Range	Accuracy
O ₂	0-100 ppb 0-1 ppm 0-10 ppm 0-100 ppm 1-1000 ppm	±1% of reading for all scales
H ₂	1-2 cc/kg 1-20 cc/kg 1-200 cc/kg	±2.5% of reading for all scales
Resistivity	0-20 MΩ-cm 0-2 MΩ-cm 0-0.2 MΩ-cm	±2% of full scale

Two DC voltages are provided by each Orbisphere oxygen and hydrogen analyzer. One signal is the voltage proportional to the oxygen or hydrogen concentration, the other signal identifies the scale of the reading. Three scales are available on the hydrogen analyzer, five scales are available on the oxygen analyzer.

Two level switches in the charging tank are used for indication of a slow water system leak. The first level switch trips when charging tank water inventory reaches 1/2 capacity (about 35 liters). This switch provides an alarm in the control room only. If charging tank water level were to reach the second level switch, 1/4 of charging tank capacity, the main loop heater trips off and a second alarm sounds in the control room.

3.5. Data Acquisition

The data acquisition system reads, records to disk and displays in real time facility parameters measured during testing. Parameters measured include specimen load, loading machine extension, DCPD, electrochemical potentials, pressures, differential pressures, chemistry, and temperatures.

3.5.1. In-core ECP Mapping

In-core ECP mapping made use of a Hewlett Packard 3488A switch control unit and Hewlett Packard 3478A multimeter controlled by a Hewlett Packard 9000 series computer. All instrumentation provided DC voltage signals to the data acquisition system. The data acquisition system read the voltages every 60 seconds and software written in-house converted the DC voltage measured to the value measured by the sensor. The value was recorded on disk and displayed on the CRT in real time.

All DC voltages were input to the data acquisition system at the terminal panel on the reactor top. Thermocouple was input from four signal conditioners in the terminal panel which provide a DC voltage proportional to temperature input by the thermocouples. In addition, the signal conditioners provided a DC voltage for indication of in-core temperature to the control room.

All wires input to the terminal panel are labeled for ease of installation and future modification. Table 3.5. lists the wire designation for each parameter read by data acquisition.

The data acquisition system provides an alarm to the control room and main loop heater trip for low main loop flow. This is determined by main loop recirculation pump differential pressure dropping below a preset limit.

Table 3.5. Data acquisition wire designation used for in-core ECP mapping.

Destination	Wire No.	Identification
Data Acquisition	1	Top Ag/AgCl Electrode
Data Acquisition	2	Top Pt Electrode
Data Acquisition	3	Top SS Electrode
Data Acquisition	4	Bottom Ag/AgCl Electrode
Data Acquisition	5	Bottom Pt Electrode
Data Acquisition	6	Bottom SS Electrode
Data Acquisition	7	Reference Autoclave Ag/AgCl Electrode
Data Acquisition	8	Reference Autoclave Pt Electrode
Data Acquisition	9	Reference Autoclave SS Electrode
Data Acquisition	10	O ₂ Measure
Data Acquisition	11	O ₂ Scale
Data Acquisition	12	H ₂ Measure
Data Acquisition	13	H ₂ Scale
Data Acquisition	14	Conductivity
Data Acquisition	15	Pressure
Data Acquisition	16	Pump ΔP
Data Acquisition	17	pH

3.5.2. In-core SSRT Testing

In-core SSRT testing made use of the same data acquisition system used for in-core ECP mapping for measurement of loop parameters with some modification. Table 3.6. lists the wire designation for each parameter read by data acquisition for in-core SSRT testing. A Hewlett Packard R/322 Controller was used to record load as measured by the load cell, loading machine extension, and DCPD (when used). Load and extension values were input directly to the computer from the Instron computer tower via a HP-IB interface. The DCPD system made use of a Hewlett Packard 6900 series multiprogrammer. Load, extension, and DCPD readings were taken every 22 seconds.

Table 3.6. Data acquisition wire designation during in-core SSRT testing.

Destination	Wire No.	Identification
Data Acquisition	1	In-core platinum Electrode
Data Acquisition	2	Specimen DCPD or Spare
Data Acquisition	3	Reference specimen DCPD or Spare
Data Acquisition	4	Spare
Data Acquisition	5	Spare
Data Acquisition	6	Spare
Data Acquisition	7	Reference Autoclave Ag/AgCl Electrode
Data Acquisition	8	Reference Autoclave Pt Electrode
Data Acquisition	9	Reference Autoclave SS Electrode
Data Acquisition	10	O ₂ Measure
Data Acquisition	11	O ₂ Scale
Data Acquisition	12	H ₂ Measure
Data Acquisition	13	H ₂ Scale
Data Acquisition	14	Conductivity
Data Acquisition	15	Pressure
Data Acquisition	16	Pump Δ P
Data Acquisition	17	pH

3.6. Radioactive Rig Handling System

3.6.1. Introduction

The radioactive rig handling system is utilized in removal of the radioactive slow strain rate tensile test (SSRT) rig from the MITR-II reactor to the shielded work area. The design considerations are existing containment facilities and personnel safety.

The transfer system is intended to shield personnel from the radioactive in-core sections of the IASCC test rig at all times during transfer. The design is similar to the design used for PCCL and BCCL loop handling. The handling system consists of the following components: the MITR reactor and reactor top lid, right hand hot cell, overhead crane, clam shell cask, lid plate and lead ring, and lifting beam.

The rig is removed from the reactor in two sections. The load train, which includes the autoclave top, reaction tube, pull rod, specimen and grips, is removed from the reactor as one section with the shielded clam shell cask to hot cell number 2 where specimen changing is done. Then the thimble, upper flange and autoclave are moved with the clam shell cask to their storage position adjacent to hot cell number 1. The clam shell cask provides shielding for the in-core section of the thimble and autoclave when in storage.

3.6.2. Component Description

The MITR-II reactor core tank holds and provides shielding for the SSRT test rig for the period between reactor shutdown and rig removal. During this period the short-lived radioactive nuclides will decay. Sc-46 is the only radioactive nuclide of concern because the in-core sections of the rig are made for the most part of Ti 6Al-4V and Al 6061. This radioactive nuclide is produced by an (n,p) reaction with Ti-46 and emits a 0.88 or 1.1 MeV gamma.

The rig will become highly radioactive after many uses. The activity of the rig after 100 effective full power days in the MITR-II reactor equivalent to testing 25 specimens is calculated to be 15.35 Ci.

The test specimens, having spent more than 220 effective full power days in the MITR-II reactor dry irradiation facility, are also highly radioactive. The activity of the most radioactive specimen, AJ9139 from capsule number 4, is estimated to be 0.35 Ci at time of use (decay of 2.5 years).

The clam shell cask shields the in-core portion of the SSRT test rig and test specimen during transfer. It is similar in design to the cask used for PCCL and BCCL loop handling. The cask provides 6.25 inches of lead shielding completely around and beneath the in-core section of the rig. The dose rate at 1 meter from the shielded rig is calculated to be less than 3 mR/hr during transfer when:

- The SSRT test rig has spent 100 effective full power days in the MITR-II reactor core.

- The most radioactive test specimen is being tested in the rig.

- The rig is allowed to decay for 2.5 days after shutdown (a weekend).

Figure 3.20. is an illustration of the clam shell cask. The cask stands 43 inches tall and shields up to 36 inches of the lower end of the rig. The cask has an outside diameter of 18.75 inches and an inside diameter of 5 inches. A 6.25 inch lead shutter slides into the lower section of the cask for bottom shielding. The cask weighs 4500 lbs.

The cask walls are concentric steel pipes. The external wall is 18.75 inch outside diameter piping with a wall thickness of 1/2 inch. The internal wall is 5.25 inch outside diameter steel piping with a wall thickness of 1/8 inch. The seam walls are 1/4 inch thick. The top and bottom are 1/2 inch steel plates.

Two 3/4 inch threaded rods are welded to the inside of the bottom plate of each shell of the cask. They extend through, and are welded to the top plate. Above the cask a crossbar connects the 2 rods on each shell. The crossbar is equipped with an eye for rigging and the over-head crane is used to lift and place the cask where it is needed. Each crossbar is positioned above the center of gravity of each shell of the cask (a radius of 6.4 inches) making it possible for the cask to be lifted while open. The maximum stress on each threaded rod is 3.1 ksi. The maximum stress on the crossbar is 2.0 ksi.

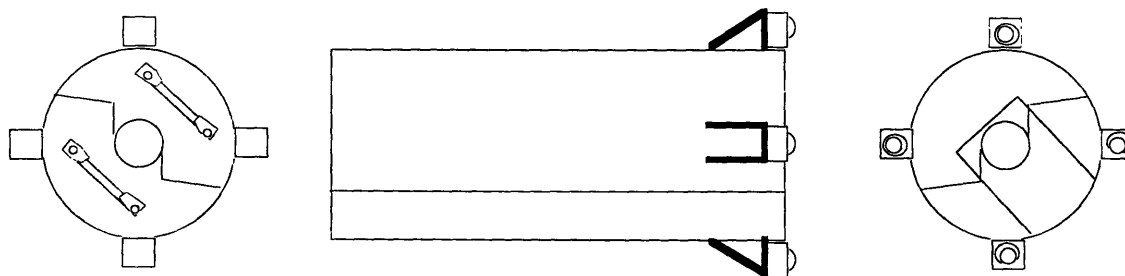


Figure 3.20. Shielded "Clam Shell" Transport Cask

The clam shell cask has four ball transfers as wheels, each ball transfer is rated for 2050 lbs. The advantage of this design is that it allows the cask to be moved into position, and opened and closed without the use of a crane. The existing cask used for loop transfer must be positioned by the overhead crane.

The seams of the cask are designed differently than the stepped design of the existing cask. This design is better because it incorporates a larger step and most of the seam is not parallel to the radius of the cask; the major direction of the radiation. Both ends of the seam, however, do lie in the same radial direction, thereby allowing the cask to close on an object with the largest possible diameter.

The lid plate sits on the reactor top lid and provides a flat surface of support for the cask four inches above the reactor top lid. The top of the IASCC SSRT test rig fits through the 13" hole in the plate. The plate is necessary in the removal of the load train. If no plate were used the upper flange would not allow the clam shell cask to close around the reaction tube. Beneath the plate is several inches of lead, provided by a large lead ring 4.5 inches tall, to shield the in-core portion of the SSRT test rig as it passes from the reactor to the cask. The platform is designed to be small enough to fit on the reactor top lid regardless of the in-core test position.

The lifting beam allows the 3 ton crane to lift the rig and clam shell cask simultaneously. This is illustrated in Figure 3.21. The lifting beam connects directly to the hook on the three ton crane. Four wire ropes for lifting hang from the lifting beam. The two outer most ropes hang from the lifting beam 6.4 inches from the center and are used to lift the clam shell cask. The two inner ropes hang from the lifting beam 4 inches from the center and are used to lift the rig.

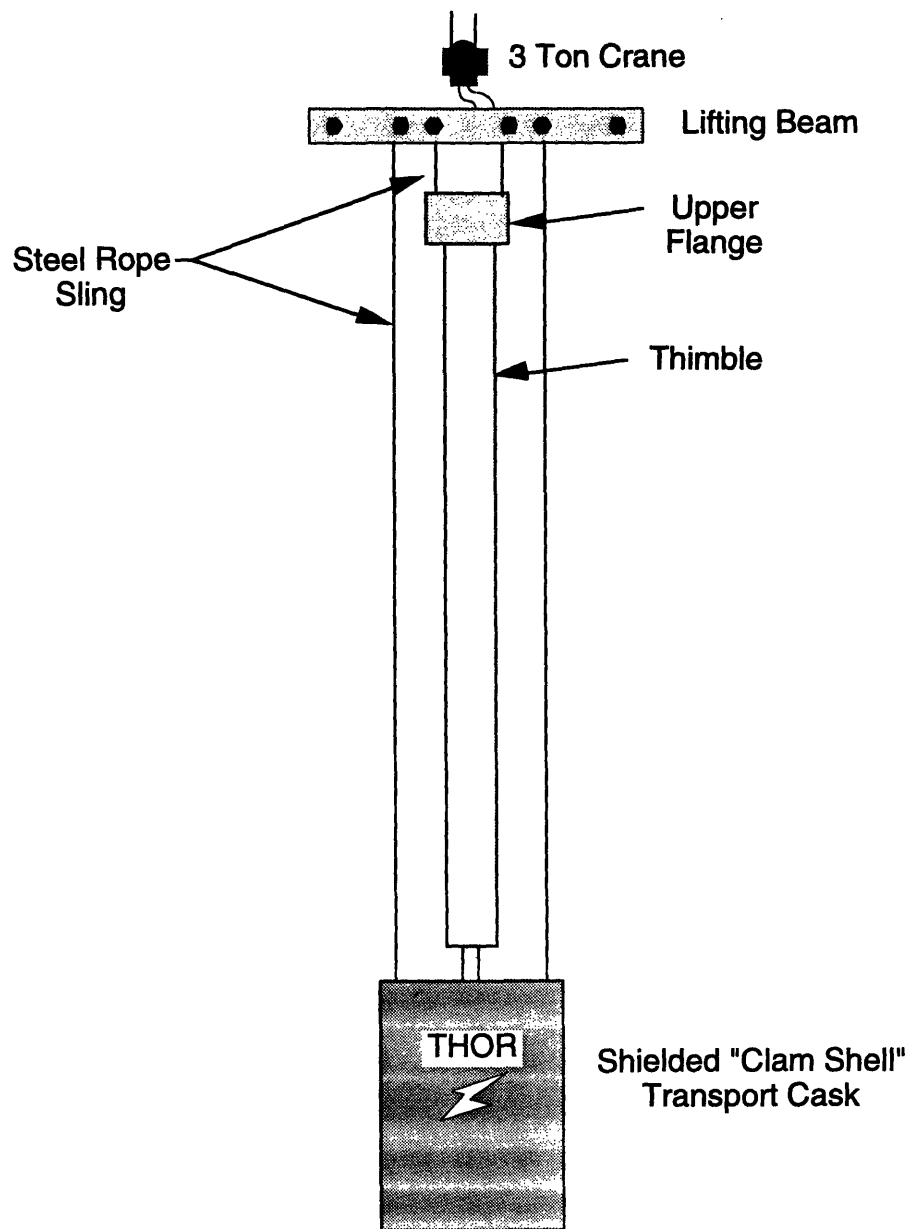


Figure 3.21. The three ton crane shown lifting the IASCC thimble/autoclave and the shielded "clam shell" transport cask.

The lifting beam has been specially designed to allow the top of the pull rod, which is the highest part of the rig, to be lifted as close as possible to the bottom of the crane's hook. This is important because the rig's length is just shorter than the clearance to the crane's highest position when over the reactor top lid. The lifting beam is rated for 3 tons;

it has been tested at twice the design weight, and a certificate of this test is on file. The clam shell cask lifting ropes have in-line turnbuckles for length adjustment.

The lifting ropes connect to the rig on either the autoclave top or the upper flange. To change the test specimen the load train is removed by connecting the lifting beam to the autoclave top. Two 3/8 inch holes are tapped in the top of the autoclave top for rigging eyebolts. These eyebolts are removed from the autoclave top when not in use.

The lifting beam is connected to the upper flange to remove the thimble and containment tube. On the top surface of the upper flange are two 3/8 inch tapped holes for rigging eyebolts, again the eyebolts are removed when not in use.

Hot cell number 2 is used for storing and working with the radioactive SSRT test rig. The hot cell is equipped with four 6 inch access holes in its top, through which the rig can be inserted. The port directly in front of the viewing window is used for specimen changing. A welding rig, specifically designed to spot weld the DCPD sensing wires to the pre-irradiated specimens, is positioned here.

A support bracket attached to the containment building wall above the hot cell is used to support the load train to allow the test specimen to be changed. A second support bracket attached to the containment building wall next to hot cell number 1 supports the thimble and autoclave when not in the reactor.

3.7. Radioactive Specimen Handling and Post Test Analysis

3.7.1. Preparing SSRT Specimens for In-Core SSRT Testing

64 SSRT specimens were irradiated in the MITR-II reactor core in the IASCC Dry Irradiation Facility. This facility and the materials irradiated are described in reference[4]. Specimens extraction of the from their aluminum holder following irradiation proved impossible without harming the specimens. The IASCC working group agreed to dissolve

the aluminum capsules using a 3N solution of NaOH. Prior to dissolution of capsules containing the pre-irradiated specimens tests were conducted on similar capsules containing specimens of the same materials. SEM examination of the surface of the specimens showed no etching. A black residue formed on part of the specimens which was removed by rubbing the surface with smooth cloth. A SSRT test of one specimen showed no indication of cracking through a strain of 16%. The test was conducted at room temperature in air with a 1N solution of NaSO₄ being supplied continuously by a wick.

The film on the irradiated specimens is removed in hot cell number 1 using 1 μm alumina powder on a piece of polishing cloth and the hot cell manipulators. The specimen is rinsed in an ultrasonic bath containing de ionized water in the hot box located in the back engineering lab. Following rinsing the specimen is transported to hot cell number 2 where it is stored until it is loaded into the in-core SSRT rig. Specimen transport makes use of a depleted uranium cask and high density concrete transport shield. The dose rate on the top surface of the transport cask with a AJ9139 specimen inside is about 1R/hr.

3.7.2. Preparing Fractured SSRT Specimens for SEM Analysis

Following in-core SSRT tests the two broken halves are carefully removed from the SSRT rig in hot cell number 2. The fractured specimen is transported to the hot box in the back engineering laboratory, one half at a time, using the depleted uranium cask and high density concrete shield. In the hot box the fractured specimen is loaded into the fixtured holder of the holder of the hydraulic specimen cutter which cuts the specimen on its shoulder section 1/16" above the gauge to shoulder section transition. This reduces the mass, and as a result, the activity of the fracture surface. It can then be placed in the shielded SEM specimen holder, which provides 2 inches of lead shielding, and transported to the SEM room for analysis in a second shielded radioactive material transport canister. MIT regulations require the radiation levels at the surface of the transport canister be less than 50mR/hr on contact and less than 10mR/hr at three feet.

When SEM analysis is complete both halves of the cut fractured SSRT specimen are returned to hot cell number 2, cataloged and placed into storage.

3.8. Facility Support

3.8.1. Reactor Top Lid

The Slow Strain Rate Tensile (SSRT) rig requires access to the reactor core through the reactor top lid. This capability did not exist with the former top lid. To meet these needs a new reactor lid was designed, manufactured, qualified for use and put into service. Several features, in addition to the through lid test facility, have been incorporated into the new lid. These include increased radiation shielding, four (4) inches of additional test space between the bottom of the lid and the top of the core tank water, and one additional small experiment penetration through the lid.

A two dimensional positioning of through-lid experiments, such as the IASCC in-core testing rig, has also been built into the lid. The positioning system will permit experiments such as the SSRT test rig to access any core position.

To accommodate the new reactor top lid the upper access shield ring was modified and the lid bearing was replaced. The previous reactor top lid was held down by nuts on threaded rods which extend through the upper access shield ring and lid. The new reactor top lid and upper access shield ring is held down by clamps on the outside of the upper access shield ring.

The gap between the reactor top lid and the upper access shield ring resulted in a radiation "halo" above the reactor top with the old top lid on and the reactor at full power. The new lid provides additional shielding to counter this phenomena.

3.8.2. Experimental Platform

The out-of-pile coolant/chemistry loops for the IASCC and Sensor projects require considerable floor space in addition to the previously existing space available on the reactor top. To accommodate the IASCC and Sensor project hardware a new semi-permanent platform extension was designed and built. The new facility extends out from the level of the reactor top a distance of 10 feet. It is of steel "H" beam construction. Beam connections are bolted to permit removal of all or part of the platform as necessary for reactor hall operations.

3.9. References

- [1] Murray, W. M., Stein, P. K., **Strain Gauge Techniques**, Massachusetts Institute of Technology, Cambridge, MA, 1958.
- [2] Jones, E., Maslen, K. R., **The Physical Characteristics of Wire Resistance Strain Gauges** Her Majesty's Stationery Office, London, 1952.
- [3] Lidar, P., "D. C. Potential Drop System Development", MIT Department of Nuclear Engineering, Cambridge, MA, 1991.
- [4] Boerigter, S. T., "An Investigation of Neutron-Irradiation Induced Segregation in Austenitic Stainless Steel", Sc.D. Thesis, MIT, MA, 1992.

4. FUNCTIONAL CHARACTERISTICS OF THE FACILITY

In-core experiments require documented, thorough analyses to ensure no violations of technical specifications, or harm to personnel or the reactor can result from the experiment, experimental procedures, or postulated accident scenarios. In working with radioactive materials ALARA concerns prevail. Procedures normally considered routine become non-trivial when extended to highly radioactive materials. Significant shielding, remote handling and well planned procedures aimed at minimizing the time experimenters spend in situations where high radiation dose rates exist are a must.

This chapter steps through some of the analyses performed to ensure safe operation of the facility for all aspects of operation. The main loop water volume calculation is described in section 4.1. Knowledge of the main loop water volume is important for determining the optimum main loop refresh (charging) rate, the radiation levels existing in the working areas from the reactor core during rig set-up and break-down, the main loop transport time and impact on safe reactor operation should an unplanned water volume change occur (reactivity impacts). The detailed reactivity analyses are described in section 4.2. Main loop thermal-hydraulic analyses, which includes the loop flow rate calculation, are described in section 4.3. Section 4.4. contains a description of the activation and shielding analyses used to establish the procedural requirements for facility transport to and from the reactor for specimen changing, handling of the highly radioactive pre-irradiated SSRT specimens before and after in-core SSRT, radioactive specimen analysis scanning electron microscopy, and the main loop volume which becomes significantly radioactive as the water passes through the high fast neutron flux in the MITR reactor core. Section 4.5. includes a description of the stress analyses required for qualification of the facility for in-core operation. This final section also contains a description of the analysis used for qualifying titanium as an in-core pressure vessel material.

While a description of the analyses are included in this chapter, the worksheets used for the analyses are included in Appendix B.

4.1. Main Loop Water Volume

Knowing the amount of water in the main loop was important in the design process for several reasons including water chemistry control, loop shielding requirements, determining radiation levels in accessible areas on the reactor top from reactor core radiation during rig transport, and reactivity analyses. Because the loop is a recirculation circuit the build up of radiolysis products (O_2 , H_2 , H_2O_2 , etc.) to unacceptable levels could not be ruled out. Based on radiolysis code calculations and experience with other loops, the design refresh rate for the loop was determined to be one main loop water volume every 10 minutes. The refresh rate of a typical BWR (~3 minutes) would have required an inordinately large and expensive charging pump.

The main loop including the SSRT rig contains 5470 ml water. A charging rate of 550 ml/min makes the refresh rate one loop inventory every 10 minutes. The main loop including the ECP rig contains 10,847 ml water. A charging rate of 1090 ml/min makes the refresh rate on loop inventory each minute. This high water volume was because of the larger ID in the upper reaction tube used during ECP mapping.

During rig transport procedures the thimble/autoclave is inserted into the reactor core before the load train is installed and taken out after the load train is removed. Care was taken in the design process so that when the load train was removed enough water remains in the autoclave to provide shielding for personnel from the high gamma and neutron flux present in the shutdown MITR-II reactor core.

Water level in the autoclave drops from the original level above the reactor top lid to a level 4.5 feet above the upper grid plate when the SSRT rig load train is removed. This water, the fact that not much time is spent working directly above the autoclave, plus

the small solid angle that exists at the top of the autoclave to the reactor core keeps personnel exposures to radiation to workable levels. The beam out of the top of the reactor is typically less than 100 mR/hr and is physically small.

The main loop water becomes radioactive as it passes through the reactor. The oxygen nucleus in the water molecule reacts with a fast neutron by (n,p) reaction to make N-16 ($t_{1/2}=7.1\text{s}$). Because of its short half-life, the concentration of N-16 in the main loop at the reactor top, and therefore the amount of shielding required for the main loop, is a strong function of the fraction of total loop transit time spent in the fast neutron flux and the time that the water takes to reach the reactor top. Knowing the total main loop water volume, the volume of the water within the in-core sections of the rig, and the water volume in the pull rod-reaction tube annulus is required. This discussion is continued in section 4.6. of this chapter.

The water in the in-core sections of the experimental facility moderates the neutron flux in the MITR-II reactor core. As a result, should the water volume or distribution vary during in-core testing reactor operation could be effected. Potential concerns include the removal of water from flooded in-core sections and their subsequent re-flooding, and the flooding of voids in the in-core sections. These two limiting scenarios are further addressed in the following section of this chapter.

4.2. Reactivity Calculations

This section describes the calculations performed regarding the reactivity insertion that would result after a sudden flooding of in-core regions. Three conditions were considered in this analysis. The first one assumes that the thimble loses its leak tightness and the annulus between the autoclave and thimble becomes instantaneously filled with the reactor coolant water, resulting in a reactivity insertion of $0.109\%\Delta K/K$ for SSRT testing and ECP mapping. The second condition assumes that the main loop water

is suddenly evaporated and instantaneously condensed inside the autoclave, resulting in a reactivity insertion of 0.191% $\Delta K/K$ for SSRT testing and 0.195% $\Delta K/K$ for ECP mapping. The last scenario assumed that these two events occur simultaneously, resulting in a reactivity insertion of 0.300% $\Delta K/K$ for SSRT testing and 0.304% $\Delta K/K$ for ECP mapping.

The limit for non-secured in-core experiments is 0.5% $\Delta K/K$ per experiment and 1.0 % $\Delta K/K$ for all in-core experiments. The MITR-II Technical Specifications define non-secured experiments as "Experiments where it is intended that the experiment should not move while the reactor is operating, but is held in place with less restraint than a secured experiment". The potential for water filling the void between the thimble and autoclave is considered non-secured since it is not intended to be filled. The thimble is pressurized to 15 psi so that a small thimble leak results in CO₂ leaking into the core tank. If any water gets into the thimble/autoclave annulus it will boil resulting in a high humidity alarm which warns personnel.

The main loop water in the autoclave is defined as non-secured since it is intended to remain single phase during reactor operation and in-core testing. The pressurizer is intended to ensure that main loop water remains in the liquid phase until the main loop heater shuts down on low pressure in the event of a large loop rupture.

4.3. Main Recirculation Thermal-Hydraulic Characteristics

Having an accurate value for main loop flow rate is important for shielding of main loop sections above the reactor top lid and predicting main loop water chemistry. O-16 reacts with a fast neutron by (n,p) reaction making N-16. N-16, in turn is unstable and decays with a half-life of 7.1 seconds emitting a high energy photon. While a slower loop flow rate will increase the water's residence time in-core, it will also increase the

time between when the water leaves the in-core sections of the rig until it passes through the reactor top lid.

Increasing the water residence time in-core increases the concentrations of radiolysis products in-core, but because of less mixing, transport of these species to the rig wall or specimen surface is reduced [4].

The main loop differential pressure for expected flow rates was calculated by summing the pressure drop caused by all main loop components using the following relation [3]:

$$\Delta p = \frac{v^2}{2v_f} \left[\sum_i K_i + f_i \frac{L_i}{D_i} \right]$$

Where: Δp is the differential pressure drop caused by the component

v is the fluid velocity

v_f is the specific volume of the fluid

K_i is the form coefficient

f_i is the friction factor associated with the component

L_i is the components length

D_i is the hydraulic diameter of the component

Using the measured pump differential pressure (of 13 psi) with the calculated mass flow rate gives a main loop flow rate of 12 gallons per minute (45.2 liters per minute).

The main heater must overcome main loop heat losses to the reactor core tank water, containment building atmosphere, and loop water refresh. The heat losses were calculated [4] and design heater capacity was doubled to allow for loop startup/heat up and a safety margin. Loop heating requirements were calculated to be about 10 kW with the reactor shutdown and 3.5 kW with the reactor operating at full power (4.5 MW). These values match actual heater demand; with the reactor at full power the heater runs at

12% of full power (24kW), and with the reactor shutdown the heater runs at 35% of full power.

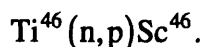
4.4. Shielding Requirements

4.4.1. Shielding Requirements for Transport of In-Core Components

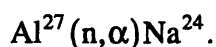
Transport of the radioactive testing rig to and from the reactor for specimen changing requires the use of a shielded transport cask. The shielding provided by the cask keeps personnel exposures to radiation during rig transfers ALARA (As Low As Reasonably Achievable). The previous chapter included a detailed description of the shielded clam shell cask. This section describes the calculations, assumptions, and constraints used in the design process.

Typical operational procedures have the reactor shutting down on a Friday after the conclusion of a tensile test; the rig is moved to the hot cell for specimen changing the following Monday. This 60 hour period allows short lived activation products to decay prior to rig transport, reducing the radiation exposure received by personnel in the area during the procedure.

Much of the in-core sections of the rig are, by design, made of the titanium based alloy Ti 6Al-4V. Titanium not only has superior corrosion properties in high temperature pure water to stainless steel, it does not become as highly radioactive as stainless steel after being exposed to a neutron fluence. Irradiated stainless steel contains significant amounts of Cr-51, Co-60, Fe-59 and other nuclides which do not decay over a two day period and would be of concern during in-core rig transfers. Ti 6Al-4V does not build up many long lived activation species. Al, V, and Ti all have half lives of 6 minutes or less. Since the rig is allowed to decay for more than 60 hours after the reactor is shutdown before it is transferred the largest concern is Sc-46 ($t_{1/2} = 83.8$ days), produced by the reaction



If conditions warrant, the rig could be moved 24 hours after the reactor is shutdown in which case Na-24 ($t_{1/2} = 15$ hours) becomes a radiological concern. Na-24 is produced by the reaction



The largest source for aluminum is the thimble.

Activation analyses were conducted using conservative assumptions. This was required since handling of the rig may be required after the reactor is shutdown for a period shorter than 60 hours. In addition, the in-core section of the rig contains a General Electric nuclear qualified platinum electrode which could become significantly radioactive and the degree to which it does is not accurately known. It contains Pt, stainless steel (Fe, Ni, Cr), and Co (the ceramic to metal braze is ~5% Co), the exact amount of each constituent is not known.

The assumptions used in calculating rig activity are:

- the rig has spent 100 full power days in-core, and has been allowed to decay for 60 hours (a weekend). 100 full power days is about equivalent to the in-core testing of 25 specimens.
- the only radioactive nuclide in the rig structures of significance is Sc-46.
- the most radioactive specimen has an activity of 0.35 Ci. This is derived from measurements of commercial purity 304 SS-heat AJ9139. The dose rates measured from AJ9139 TEM disks are more than 5 times higher than dose rates measured from TEM disks of the other materials scheduled for in-core SSRT testing [1] due to their high Cobalt content.

- the in-core sections of the rig are exposed to a thermal neutron flux equivalent to the peak thermal flux in the A ring of the MITR-II core. This is conservative since all in-core testing is to be done in in-core position B-3 which has a lower peak thermal neutron flux than exists in the A ring. Moreover, the majority of the mass of the in-core section of the rig is not in the peak thermal neutron flux.

The activity per gram of titanium was determined by the computer program "Activity" written and used by S. Boerigter to calculate the activity of the dry irradiation in the MITR-II reactor core [2]. The activity per gram of titanium after spending 100 full power days in the reactor is calculated to be 6.55 mCi/gm. The activity of the entire in-core rig (load train and thimble/autoclave) and most radioactive test specimen is calculated to be 10.25 Ci. The activity of the total rig over time is illustrated in Figure 4.1.

The rig, however, is never to be transported together, but as two sections; the load train and thimble/autoclave. The irradiated parts of the load train include the lower reaction tube, lower pull rod, lower grip, and test specimen. The irradiated parts of the thimble/autoclave include the lower containment tube, thimble, and aluminum slug. The calculated activities of the two sections after spending 100 full power days in-core are 5.71 Ci for the load train, and 4.54 Ci for the thimble/autoclave.

Using the higher of the two dose rates for calculating the required shielding during rig transport, 5.71 Ci, results in an unshielded dose rate of 5 R/hr at one meter. Adding the 6.25 inches of lead provided by the shielded clam shell cask reduces the dose rate on contact with the cask to 26 mR/hr.

After 4.75 full power days of operation the load train was removed using the clam shell cask, the measured dose rates on contact with the cask during transport were less than 1 mR/hr. The clam shell cask measured 3 mR/hr on contact during

thimble/autoclave transport. The thimble/autoclave had an additional 21.2 full power days from in-core ECP measurements. Dose rates on the clam shell cask during ECP rig transport to the spent fuel pool were less than 5 mR/hr. Experience to date indicates that exposures for a complete SSRT test cycle are less than 0.00015 person-mSv.

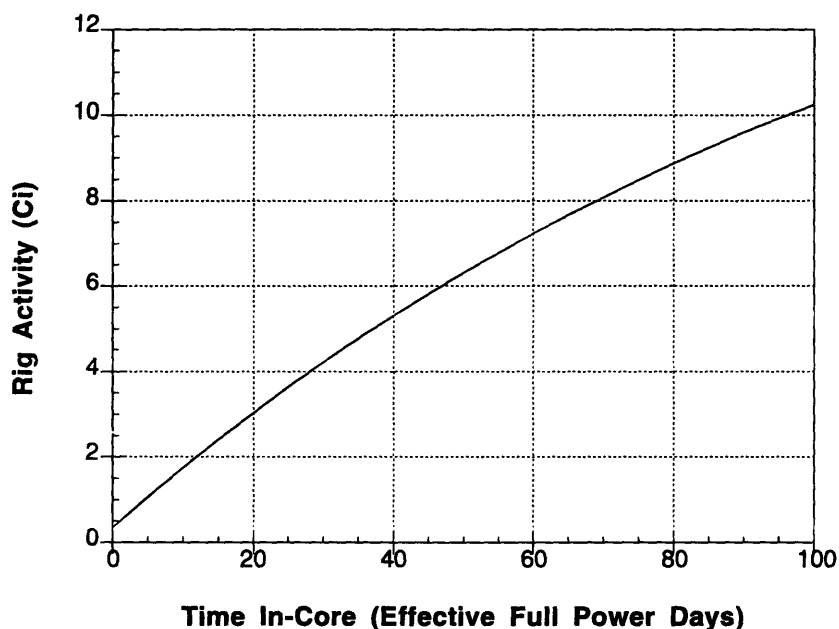


Figure 4.1. Activity of the rig which has in it the most radioactive pre-irradiated SSRT specimen over the course of the rig's lifetime.

4.4.2. Shielding Requirements for Transport of Pre-Irradiated Specimens

The pre-irradiated SSRT specimens need to be transported from hot cell number 1, where they were removed from the dry irradiation facility, to the hot box in the back engineering laboratory for cleaning and SSRT preparation. After cleaning, the specimens are then transported to hot cell number 2 where they are loaded into the SSRT testing rig.

After they have been fractured in the reactor core the specimens are returned to the hot box in the back engineering laboratory where they are cut in preparation for electron microscopy.

The specimens have been pre-irradiated and are highly radioactive. Of the four alloys to be subjected to in-core SSRT testing AJ9139 is the most radioactive. Each specimen weighs 10.5 grams, the AJ9319 specimens measure 350 mR/hr at 1 meter. The V945 specimens measure 45 mR/hr at 1 meter. Experience from radioactive STEM work [1] indicates that the activities of the remaining two alloys, K5 and K12, are lower than V945.

Shielding for transport between the hot cells and back engineering laboratory makes use of a depleted uranium transfer pig. This pig provides about 1.25 inches of depleted uranium as shielding which reduces dose rates by a factor of 20. The specimen is loaded into and removed from the pig in either the hot cell or hot box. The pig is transported between the two sites within a concrete transport cask, which provides an additional 2.5 inches of high density concrete as shielding which further reduces dose rates by a factor of 5.

4.4.3. Shielding Requirements for Post SSRT Fracture Surface Analysis by Scanning Electron Microscopy

Dose rates at the surface of a radioactive material transport container are limited by the MIT Radiation Protection Office to 50 mR/hr and 2 mR/hr at 3 feet from the surface of the container. To meet these requirements a fractured SSRT test specimen is cut to remove most of the unneeded mass in the hot box so that the fracture surface can be moved to the SEM room for SEM analysis. Experience indicates that the specimen cutter can remove most of the specimen mass, leaving less than 1 gram for transport and electron microscopy. The remaining specimen is shielded by about 4 inches of lead; 2

inches are provided by the lead collar on the SEM specimen holder and 2 inches are provided by lead in the transport container.

Dose rates at the operator's station at the electron microscope are limited to 5 mR/hr. The operator station is about 1 meter from the specimen stage. The 2 inches of lead shielding provided by the specimen holder reduces the dose rate by a factor of 10. Lead bricks are available in the SEM room for additional shielding if necessary.

4.4.4. Shielding Requirements for Main Loop Water Volume

The main loop water recirculating through the core of the MITR-II reactor becomes radioactive through the production of N-16. N-16 decays with a 7.1 second half-life emitting a high energy photon. The dose rate at the reactor top due to these photons were calculated for both the SSRT and ECP rigs; 12 mR/hr for the SSRT rig and 5 mR/hr for the ECP rig using 2 inches of lead as shielding. The difference is due to the difference in rig water volume, especially the volume between the upper reaction tube and upper pull rod. This volume is three times greater for the ECP rig allowing the water over 7 seconds to move from the in-core sections of the rig to the main loop tubing. Experience shows that 2 inches of lead lowers the radiation levels to between 10 and 15 mR/hr on the outside of the heater shield, and levels measured during SSRT rig operations are higher than the levels measured during ECP rig operations.

4.5. Stress Analysis

Pressure vessel design is based on ASME code Section III and Section VIII [5]. The simplified procedures of Division 1 of Section VIII are for the most part conservative for pressure vessels in conventional service and a detailed analysis of many pressure vessels constructed to the rules of Division 1 of Section VIII would show where the design could be optimized to conserve metal. However, it is recognized that the designer may be required to provide additional design considerations for pressure vessels to be

used in severe types of service such as vessels for highly cyclic types of operation, for services which require superior reliability, or for nuclear service where periodic inspection is usually difficult and sometimes impossible. The need for design rules for such vessels lead to the preparation of Section III and division 2 of Section III.

The rules most often used in stress analyses are the maximum stress theory, maximum shear stress theory, (Tresca criterion), and distortion energy theory (Mises criterion). It has been known for many years that both maximum shear stress theory and the distortion energy theory are superior to maximum stress theory in predicting both yield and fatigue failure in ductile materials. Section I and division 1 of Section VIII use maximum stress theory, by implication, but Section III, division 2 use maximum shear theory. Most experiments show that the distortion energy theory is more accurate than maximum shear stress theory, but shear stress theory was used for the rig's stress analyses because it was easier to apply and it offers some advantages in applying fatigue analyses.

The maximum shear stress at a point is defined as one-half of the algebraic difference between the largest and smallest of the three principal stresses. Thus, if the principal stresses are σ_1 , σ_2 , σ_3 , and $\sigma_1 > \sigma_2 > \sigma_3$, the maximum shear stress is $1/2 (\sigma_1 - \sigma_3)$. The maximum shear stress theory of failure states that yielding in a component occurs when the maximum shear stress reaches a value equal to the maximum shear stress at the yield point in uniaxial tension. In a uniaxial tensile test, at yield, $\sigma_1 = S_y$, σ_2 and $\sigma_3 = 0$; therefore the maximum shear stress is $1/2 S_y$. Therefore yielding in the component occurs when $1/2 (\sigma_1 - \sigma_3) = 1/2 S_y$.

In order to avoid mistakes the ASME codes define an additional term called "equivalent intensity of combined stress" or simply "stress intensity". The stress intensity, S_m , is defined as twice the maximum shear stress and is equal to the largest algebraic difference between any two of the three principal stresses. Thus the stress intensity is directly comparable to strength values found from tensile tests.

Different types of stress require different limits, and before establishing these limits it was necessary to choose the stress categories to which limits should be applied. The categories and sub-categories chosen were as follows:

A. Primary Stress

- (1) General primary membrane stress.
- (2) Local primary membrane stress.
- (3) Primary bending stress.

B. Secondary Stress

C. Peak Stress

Their chief characteristics may be defined as follows:

(a) Primary stress is a stress developed by the imposed loading which is necessary to satisfy the laws of equilibrium between external and internal forces and moments. The basic characteristic of a primary stress is that it is not self limiting. If a primary stress exceeds the yield strength of the material through the entire thickness, the prevention of failure is entirely dependent of the strain-hardening properties of the material. A typical example is stress due to internal or external pressure.

(b) Secondary stress is a stress developed by the self-constraint of a structure. It must satisfy an imposed strain pattern rather than being in equilibrium with an external load. The basic characteristic of a secondary stress is that it is self-limiting. Local yielding and minor distortions can satisfy the discontinuity conditions or thermal expansions which cause the stress to occur. Typical examples are thermal stresses and local bending stresses due to internal pressure at the shell discontinuities.

(c) Peak stress is the highest stress in the region under consideration. The basic characteristic of a peak stress is that it causes no significant distortion and is objectionable mostly as a possible source of fatigue failure. A typical example is stress concentrations due to local structural discontinuities such as a notch, small radius fillet, or hole.

The SSRT rig is composed of the thimble, autoclave, reaction tube, pull rod, and autoclave flanges. Detailed discussion and analyses are described in reference [6].

4.5.1. Thimble

The thimble is divided into two sections: in-core and above core sections. Both sections are made of Al 6061-T6. Design pressure is 1500 psi. Only primary stress was considered in the analyses.

4.5.2. Autoclave

The autoclave is the pressure boundary for the high pressure and temperature main loop water. It is designed for operation at 3200 psi at 300°C; operating pressure is 1750 psi. It is also divided into two sections: in-core and above core sections. The in-core section is made of Ti 6Al-4V and the above core section is made of 304L stainless steel. Between the two sections is a bolted flange with a C-ring seal. The above core section has a conical junction 2 inches above this flange.

Away from the structural discontinuities only primary stress is considered. In the areas near the structural discontinuities including the conical junction, flanges and flat bottom plate primary and secondary stresses are considered.

4.5.3. Load Train

The load train consists of the pull rod, lower grip, and reaction tube.

The reaction tube supports the compressive force exerted by loading the test specimen. It also serves as a separating wall between the inlet and outlet loop water flow. It is divided into two sections: above core and in-core sections. The in-core section is made of Ti 6Al-4V, the above core section is made of 316 stainless steel. Buckling caused by the compressive force was considered.

The pull rod is designed to transmit the tensile force generated at the loading machine to the test specimen at its in-core position. It is divided into two sections; in-core and above core sections. The in-core section is made of Ti 6Al-4V, the above core section is made of 304L stainless steel. The maximum load is 1200 lb. Only primary stresses were considered.

The lower grip transmits the tensile force at the bottom of the loaded test specimen to the bottom of the reaction tube. Its maximum load is 1200 lbs, primary and peak stresses were considered.

4.5.4. Potential for Hydrogen Embrittlement of Titanium Sections

The in-core sections of the pull rod, reaction tube, and autoclave were machined from Ti 6Al-4V bar stock. In-core space limitations demanded comparatively thin walls. This material was selected because of its excellent strength and corrosion resistance at high temperatures in aqueous environments, as well as because of its low neutron activation cross section. Because titanium alloys form hydrides which lower the materials fracture toughness, considering the potential for hydrogen embrittlement of these sections was necessary [7]. In this study very conservative assumptions were used and titanium was determined to not fail by the most limiting mechanism, delayed failure, after operating continuously for 356 days.

4.5.5. Transfer Cask and Rig Handling Equipment

The shielded rig handling system is used in transporting the radioactive rig between the reactor and hot cell. The equipment used includes the reactor building's 3 ton crane, the lifting beam, shielded clam shell cask, and numerous lifting eye bolts and slings.

The maximum load to be lifted by the 3 ton crane is 5000 lbs; the entire rig weighs 500 lbs and the shielded clam shell cask weighs 4500 lbs. The lifting beam is rated for lifting 3 tons suspended from its outer most lifting position. This position is to be used only for rigging the loading machine which weighs 1200 lbs. The clam shell cask uses the middle lifting position which is stronger than the outer most position. The lifting beam was test loaded with 6 tons, a certificate of its design and test load are on file in the MITR Reactor Operations Office.

The clam shell cask provides 6.5 inches of lead around the in-core sections of the rig. It has two rigging eyes bolted to the cask's four 3/4" threaded rods which extend through the top of the cask to the bottom plate. These rods are welded to both the bottom and top plates. The stress on each rod during cask rigging is calculated to be 3.1 ksi, a factor of 10 less than yield for the material. The maximum stress on the eyes during rigging is 2 ksi.

All slings, turnbuckles, and eyebolts used rated for the weight they are lifting with a safety factor of at least 2.

4.6. References

- [1] Mansoux, H., "Experimental Determination of Radiation Induced Segregation Susceptibility in Austenitic Stainless Steels", S.M. Thesis, MIT, Cambridge, MA, 1994.
- [2] Boerigter, S. T., "An Investigation of Neutron-Irradiation Induced Segregation in Austenitic Stainless Steels", Sc.D. Thesis, MIT, Cambridge, MA, 1992.
- [3] Todreas, N. E., and Kazimi, M. S, Nuclear Systems II, Elements of Thermal Hydraulic Design, Hemisphere Publishing Corporation, 1990.

- [4] Vergara Aimone, J. A., "The Development of a Facility for the Evaluation of Environmentally Assisted Cracking of In-Core Structural Materials in Light Water Reactors", Ph.D. Thesis, MIT, Cambridge, MA, 1992.
- [5] ASME Boiler and Pressure Vessel Code, Section III and VIII, American Society of Mechanical Engineers, 1988.
- [6] MIT Nuclear Reactor Laboratory Staff, "Irradiation Assisted Stress Corrosion Cracking and BWR Chemistry Studies", Second Annual Report for the Period September, 1989-November, 1990 to Tokyo Electric Power Company and Electric Power Research Institute, Report No. MITNRL-043, 1990.
- [7] O'Donnell, J. R., Takamori, K., Susceptibility of the Lower Containment Tube to Hydrogen Embrittlement, NRL-IASCC Technical Note, 1991.

5. TESTING AND RESULTS

This chapter contains a description of the tests conducted to qualify the facility for service and initial in-core studies. The results and discussions are also included.

5.1. Experimental Characterization

Initial tests were conducted out of core for three reasons:

- a. To verify that the facility was capable of performing as intended,
- b. To learn how the facility would behave under a variety of postulated scenarios prior to in-core testing,
- c. As an exercise for the experimenters in learning how best to operate and control the facility.

5.1.1. Load Train Compliance Test

The specimen is connected to the Instron loading machine through the highly compliant load train and accurate strain measurement using cross-head displacement measurement therefore requires further correction. Strain measurement using cross-head displacement is always necessary at high strains because the DCPD strain measurement technique provides accurate strain measurement only for small strains and with no cracking present. The potential drop measured across a strained specimen varies with crack nucleation and growth, localized strain or necking, and ductile void nucleation and growth in addition to elastic and plastic strain. The time during a slow strain rate test when the DCPD computed strain becomes unreliable, due to crack initiation and subsequent growth for example, must be determined to minimize strain measurement errors. This is done by computing strain using both the DCPD technique and compliance corrected loading machine extension, comparing the two computed strains, and signaling

the system when DCPD computed strain becomes unreliable for strain measurement as detected by the two strains diverging beyond a predetermined value.

Loading machine extension is the sum of the extensions of the test specimen and load train. The load train compliance test measures the load train extension as a function of load. Load train compliance can then be deducted from total extension to calculate specimen extension and finally strain.

For the load train compliance test a rigid specimen was machined to the dimensions of a typical SSRT test specimen irradiated in the Dry Irradiation facility [1] without the 0.100" diameter gauge section. It was made of high strength steel. Figure 5.1. is a construction drawing for the rigid test specimen.

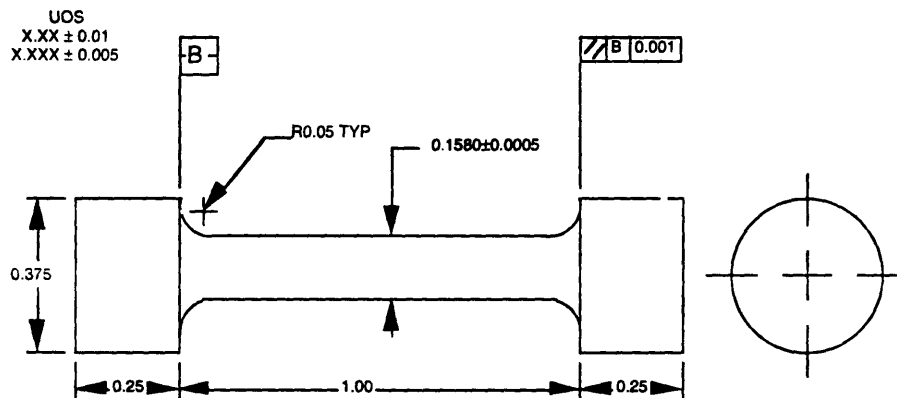


Figure 5.1. The rigid test specimen utilized in the load train compliance measurement.

This specimen was loaded in the grips of the load train, the load train was connected to the loading machine then pre-loaded to 50 lbs. Using a chart recorder to record the loading machine extension, which for this test is essentially load train extension, and specimen load, the specimen was loaded to 1500 lbs twice and subsequently unloaded to 50 lbs. The rigid specimen's extension is equal to the extension that would be present in the shoulder sections of a specimen designed for testing in this facility.

Figure 5.2. is the output of the compliance test.

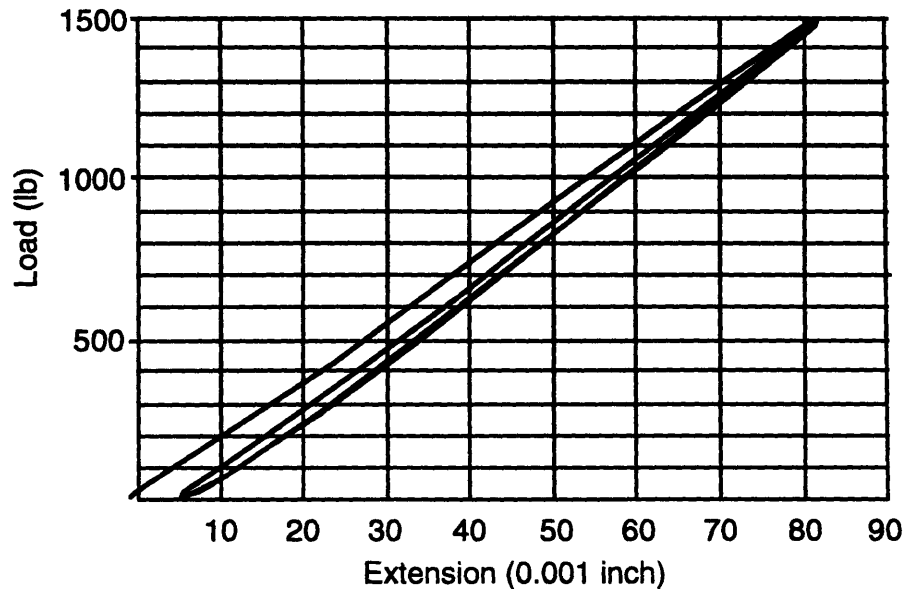


Figure 5.2. Plot of load train extension verses load as measured during the load train compliance test.

The two increasing load lines were used to determine the load to extension ratio (stiffness) of the load train by dividing each line into 10 segments of equal length, computing the change in load to change in extension ratio of each segment (stiffness), averaging them and computing the standard deviation. Segments 1 through 10 are for the first loading; segment 1 corresponds to the lowest load, segment 10 corresponds to the highest load. Segments 11 through 20 are for the second loading; segment 11 corresponds to the lowest load, segment 20 corresponds to the highest load. Table 5.1. lists the raw data and shows the average load train stiffness to be $19350 \pm 6.3\%$ lbs/in.

From Figure 5.2. it is apparent that the load train is more compliant for the first loading than the second. The load train has several threaded connections; some of these are made and unmade between each test. Upon loading the threads can become more tightly fastened and because no connections were undone between the two loadings an

increase in stiffness resulted for the second loading. The stiffness of the load train decreased slightly as the load was increased above 1000 lbs during the initial loading, but no decrease in stiffness was noted for the same high load during the second loading. This could be caused by the threaded connections mentioned previously, or by yielding and work hardening of the rigid specimen or load train.

Table 5.1. Computation of load train stiffness.

Segment Number	Stiffness (lb/in)
1	17800
2	18000
3	18500
4	19000
5	19100
6	19100
7	19100
8	19300
9	18500
10	17000
11	17600
12	18900
13	20300
14	20600
15	20700
16	20700
17	20700
18	20700
19	20700
20	20700
Average	19350
Standard Deviation	1218

A load train stiffness of 19000 lbs per inch is used for all slow strain testing done out of core and in-core.

5.1.2. Facility Thermal-Hydraulic Characterization

To develop an understanding of the temperature control and heating requirements for the main loop heater the facility was operated out of core with varying heater demands; varying heat load was accomplished by varying the charging rate. The heat loss in the main loop due to loop water inventory replenishment was determined for

several charging rates. Temperature stability was measured with and without heater demand transients.

To minimize the heat losses from the facility due to the required high charging rate, a regenerative heat exchanger makes use of the hot letdown water to heat the cold charging water. Calculations show the heat loss from the main loop due to loop water inventory replenishment to be the largest single loss in the facility (with a heater efficiency of 70% and a charging rate of 380 cc/min the heat losses are calculated to be 2.0 kW [2]). All heat losses must be made up by the main loop heater and therefore must be well characterized.

In addition to the heat supplied to the main loop by the main loop heater, nuclear heat is added to the in-core section of the main loop when the reactor is operated at power. The facility must be able to operate under all reactor power conditions, shutdown through full power, and during various reactor power transients. Vergara computes the heating requirements of the main loop heater with the reactor shutdown and at full power to be 10 kW and 3.5 kW respectively [2]. Experience gained through the operation of the dry irradiation shows that irradiation heating is variable for a constant reactor power level especially during the first three days after reactor startup due to the buildup of fission products and redistribution of power density [1]. The main loop heater must be able to not only maintain the loop at the desired temperature, but be able to minimize the temperature variance caused by a change in heater demand.

To characterize the thermal-hydraulic properties of the charging/letdown system, the loop was operated at 550°F with the in-core autoclave bypassed. Water flow was from the main loop recirculation pump to the heater and back to the pump. The following temperatures were recorded: charging tank water temperature, regenerative heat exchanger outlet on the charging line, regenerative heat exchanger inlet on the letdown side and regenerative heat exchanger outlet on the letdown side. The charging rate was

varied between 200 cc/min and 375 cc/min. Charging rates greater than 375cc/min were not possible due to the low maximum heater power available during out of core testing. Table 5.2. lists the temperatures measured and the heat loss due to loop water inventory replenishment at the various charging rates. Heat loss from the main loop due to loop water inventory replenishment is caused by the hot letdown water (550°F) being replaced by cold charging water (charging line RHX outlet). The heat loss was calculated using the following equation:

$$\dot{Q} = \dot{m} c_p (550 - T_{ch\ in}).$$

Where: \dot{Q} is the heat loss from the loop
 \dot{m} is the charging rate is mass per unit time
 c_p is the heat capacity of water at 525°F
 $T_{ch\ in}$ is the temperature of the water in the charging line at the outlet of the regenerative heat exchanger. The heat loss is very similar to the loss predicted by Vergara [2].

Table 5.2. Temperatures measured and the heat loss calculated using these temperatures for various charging rates.

Flow Rate (cc/min)	Charging tank (°F)	RHX out CH (°F)	RHX in LD (°F)	RHX out LD (°F)	Heat Loss From loop (watts)
200	75	407	505	125	1112
250	74.6	417	510	139.8	1293
325	75.2	416	515	152.5	1694
375	74.4	413	518	161.6	1998

A second test was conducted to test the ability of the heater to maintain loop temperature with varying heater demand. The loop was heated to 550°F and allowed to reach steady state with a charging rate of 200 cc/min. Heater power requirements were varied by varying the charging rate. Main loop temperature was monitored and the temperature excursion and the time taken to re-establish steady state was recorded. This was repeated using the charging rates listed in Table 5.3.

Table 5.3. Temperature excursion for several heater demands.

Initial Charging Rate (cc/min)	Final Charging Rate (cc/min)	Differential Power Requirement (watts)	Temperature Excursion (°F)	Time to re-establish steady state (min)
200	250	181	-5	10
250	325	401	-7	12
325	375	304	-4	8
375	200	-886	10	22
200	375	886	-12	36

The main loop heater was shown to have no problem controlling main loop temperature. At steady state the temperature variation is less than 0.5°F. As heater demand changes the heater responds quickly minimizing the temperature excursion and returning the system to steady state within about 40 minutes for the largest induced transient.

5.1.3. Specimen Load-Thermal Stability Test

Varying loop temperature causes the load train components to extend or contract. If either the pull rod or reaction tube expands or contracts more than the other a temperature excursion would affect specimen strain. The load train was designed to minimize these effects by using identical materials of similar lengths in both the pull rod and reaction tube. Because this compensation may not be perfect and serious ramifications on the ability of the facility to perform as intended would be the result of imperfect compensation, the effects of temperature variations on specimen strain were measured.

With the specimen loaded in the load train to a stress less than yield, the loading machine in position control and the loop pressurized and heated to 550°F, the loop temperature was varied to measure the effects of temperature on specimen strain. Changes in specimen strain were measured by measuring changes in specimen load. Table 5.4. lists the results of this test.

Table 5.4. Temperature effects on specimen strain.

Temperature (°F)	Time at Temperature (min)	Average Load (lbs)	Elastic Strain (%)
550	60	120±5	0.062±0.004%
560	30	120±5	0.062±0.004%
550	30	120±5	0.062±0.004%
540	30	120±5	0.062±0.004%
550	60	120±5	0.062±0.004%

The results indicate that no change in specimen strain results from a temperature variation of 10°F or less. Since all anticipated reactor transients except a reactor scram and main loop heater trip result in temperature excursions less than 10°F, the facility is expected to operated well with the heater and heater controller as built and tested.

5.1.4. DCPD/Strain Calibration

As discussed in chapter 3 of this thesis, the DC potential drop or DCPD technique was planned to be used with this facility to measure specimen strain for strain measurement and control for small strains. The DCPD technique measures the potentials across the specimen's gauge section and an unstrained reference specimen, and using the two potentials measured during the initial readings, calculates a normalized potential. This normalized potential is a function of elastic and plastic strain. The constants relating elastic and plastic strain to the normalized potential are α and β , such that:

$$\Delta V_n^e = \alpha \epsilon^e,$$

and

$$\Delta V_n^p = \beta \epsilon^p.$$

Where: ΔV_n^e is the change in normalized potential due to elastic strain
 ΔV_n^p is the change in normalized potential due to plastic strain
 ϵ^e is elastic strain
 ϵ^p is plastic strain

These relationships and the formula used for determining total strain from the normalized potential and measured load are derived in chapter 3. This section describes the tests used to determine the values of the constants α and β , and the associated error associated with measuring strain using the DCPD technique.

The length of the specimen's gauge section was measured, DCPD wires were spot welded on either side of the gauge section, the specimen was loaded into the grips of the load train, the grip section of the load train was flooded and the initial DCPD readings were taken. The specimen was slowly loaded until it had undergone some plastic deformation then unloaded while recording load and the normalized potential. The specimen was removed from the load train and the length of its gauge section was measured again. The amount of plastic strain incurred during the test was determined from the change in measured gauge section length. For each test the load verses the normalized potential was plotted. The parameter α was determined using the slopes of the loading and unloading lines in the load vs. normalized potential plot and the relation:

$$\alpha = \frac{EA}{\frac{dP}{dV_n}}$$

Where: P is load

E is the elastic modulus for stainless steel (28,000,000 psi was used for this test)

A is the cross section area of the specimen (0.00785 in²)

$\frac{dP}{dV_n}$ is the slope of load vs. the normalized potential for elastic strain

only. In most cases the unloading line was found to be the easier line to use.

The parameter β was determined using the change in normalized potential at 50 lbs and the change in gauge section length.

For this procedure the facility was not pressurized and tests were performed in room temperature water. Two specimens were used, a commercial purity 304 SS that had been 30% cold worked (specimen number 2005) and a 347L SS that had been solution annealed (specimen number 2022), each specimen was tested twice. The length of the specimen's gauge section were measured using a high resolution optical comparator. Shallow sharp notches were machined in each specimen's shoulder section on either side of its gauge section to help with measurement consistency. Each length was measured a minimum of 3 times and the average length computed and recorded as the measured length.

Figures 5.3. through 5.5. are the load vs normalized potential plots generated during the DCPD calibration procedure.

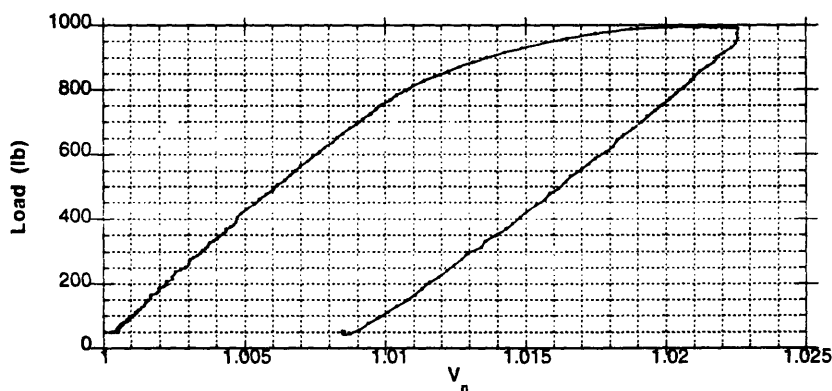


Figure 5.3. Plot generated using specimen number 2005 in its first loading.

Table 5.5. includes all the data measured and computed from the four DCDP calibration tests. The difference in the value for the elastic parameter (α) for the two materials is caused by the difference in initial condition of the two materials. Specimen 2005 was cold rolled to 30% which results in large residual elastic strains and affects the materials resistivity.

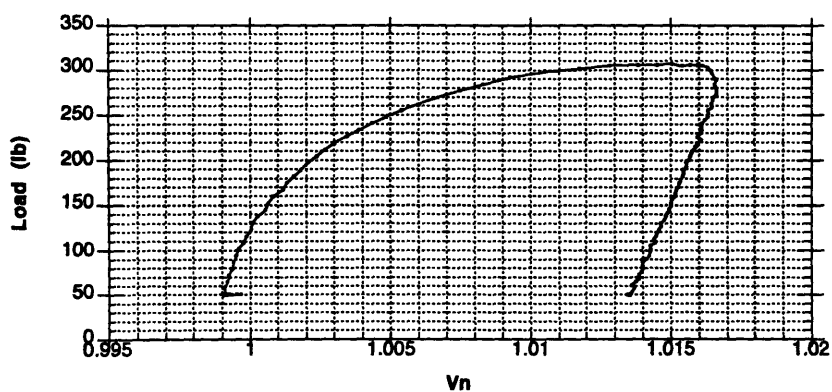


Figure 5.4. Plot generated using specimen number 2022 in its first loading.

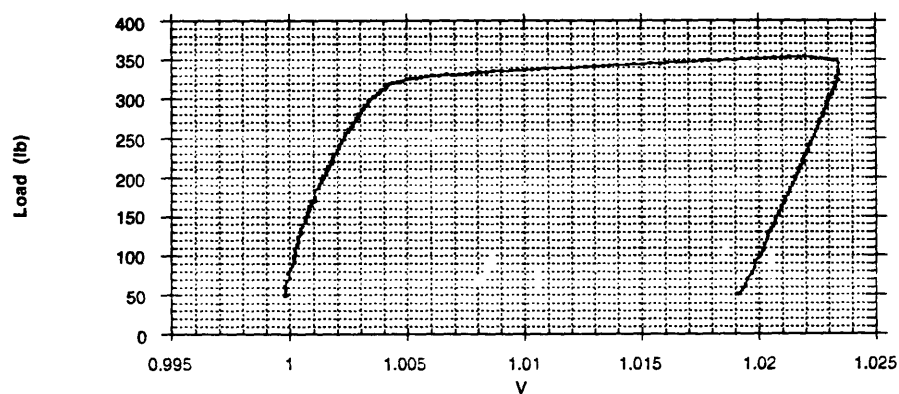


Figure 5.5. Plot generated using specimen number 2022 in its second loading.

Table 5.5. Average values and associated errors for the parameters α and β determined during the DCPD calibration.

Specimen	Test	$\frac{dP}{dV_n}$ (lb)	α	Plastic Strain Measured	ΔV_n	β
2005	1	737,500	0.298	0.387%	0.0084	2.17
2005	2	747,000	0.294	0.452%	0.0088	1.95
2022	1	652,200	0.337	0.83%	0.0142	1.71
2022	2	588,200	0.374	1.05%	0.0192	1.83
Average			0.326			1.92
Standard Deviation			0.038			0.20

5.1.5. ECP Electrode Verification and Rig Pre-Conditioning

An in-core electrode rig was developed to study the effects of fast neutron and gamma radiation on the electrochemical corrosion potential (ECP) of stainless steel in high purity, 288°C water. The facility is intended to measure the ECP of stainless steel and its sensitivity to varying parameters such as neutron and gamma dose rate, and flow rate under both normal and hydrogen water chemistry conditions. These measurements will characterize an in-core facility to be used for slow strain rate testing (SSRT) of a variety of materials. Space constraints permit only a platinum electrode to be used during SSRT and the pre-characterization will be relied upon to calibrate the response of the rig, particularly under normal boiling water reactor chemistry (NWC). In addition, the data obtained is directly relevant to understanding in-core ECP in commercial BWRs. The water chemistry conditions and radiation dose rates of the rig are similar to those in commercial plants and the rig data can be used to benchmark radiolysis and ECP codes.

The testing facility was constructed and run out-of-core at temperature and pressure for 20 days. The purpose of this test was twofold: 1) to pre-film the in-core rig surfaces and 2) to test the electrodes and chemistry monitoring equipment. Data was collected once per minute for each electrode (all electrodes measured relative to the autoclave structure using a high impedance digital voltmeter), letdown water conductivity, dissolved oxygen concentration, and recirculation pump differential pressure. Top and bottom stainless steel ECPs were corrected to standard hydrogen electrode (SHE) scale using the applicable Ag/AgCl reference electrode and the following equation:

$$E_{SS/SHE} = E_{SS/Rig} - \left[E_{Ag/AgCl/Rig} - (601.8 - 1.645(T - 25)) \right]$$

Potentials ($E_{SS/SHE}$, $E_{SS/Rig}$, $E_{Ag/AgCl/Rig}$) are measured in mV
 T is in-core electrode cluster temperature in degrees Celsius

Plots of the raw electrode data are illustrated in Figures 5.6 through 5.11. Plots of exit water dissolved oxygen, conductivity, and stainless steel ECP vs. SHE for both top and bottom electrode clusters are shown in Figures 5.12 through 5.14. Table 1 notes major events during the test. For the entire test the charging tank water conductivity was maintained at less than 0.08 $\mu\text{S}/\text{cm}$. All electrodes responded satisfactorily to water chemistry variations during the out-of-core test. ECP values measured were within the expected envelope. Note that the two clusters should have produced virtually identical results, and in fact, the differences in measured values do not exceed 70 mV. Apparent equilibrium values of ECP were generally established in approximately 10 hours.

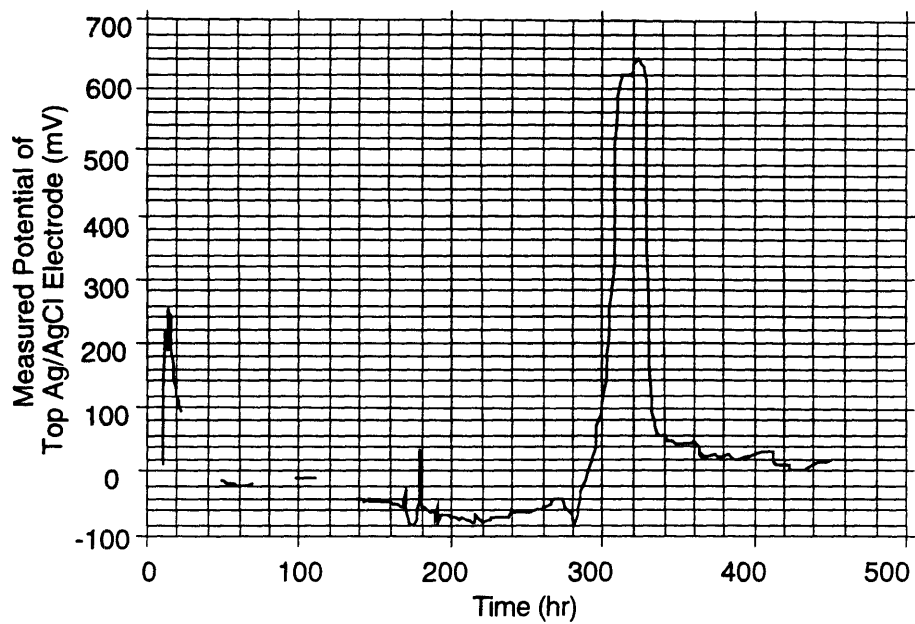


Figure 5.6. Ag/AgCl electrode in top electrode cluster.

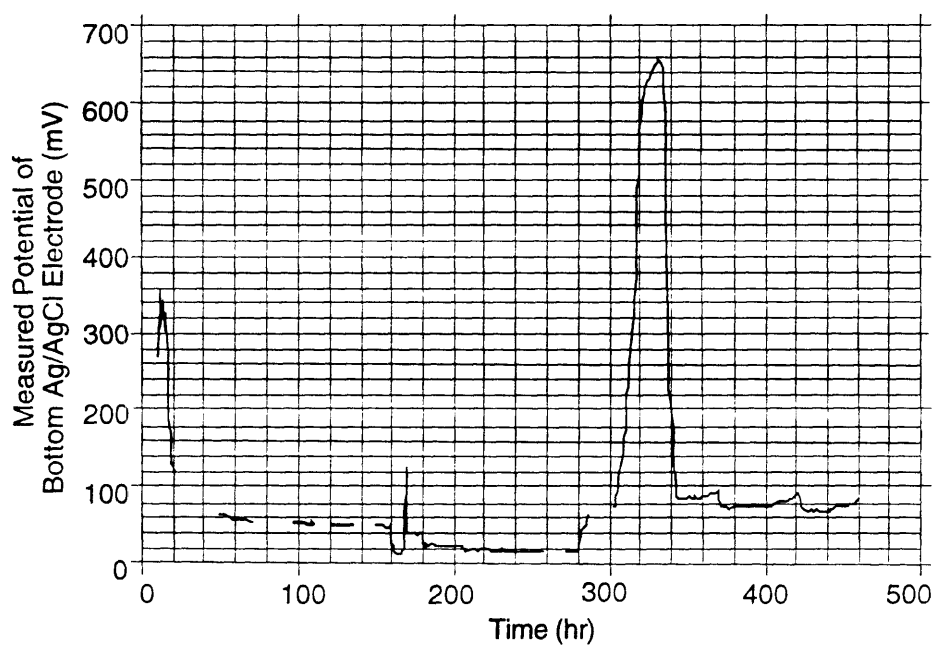


Figure 5.7. Ag/AgCl electrode in bottom electrode cluster.

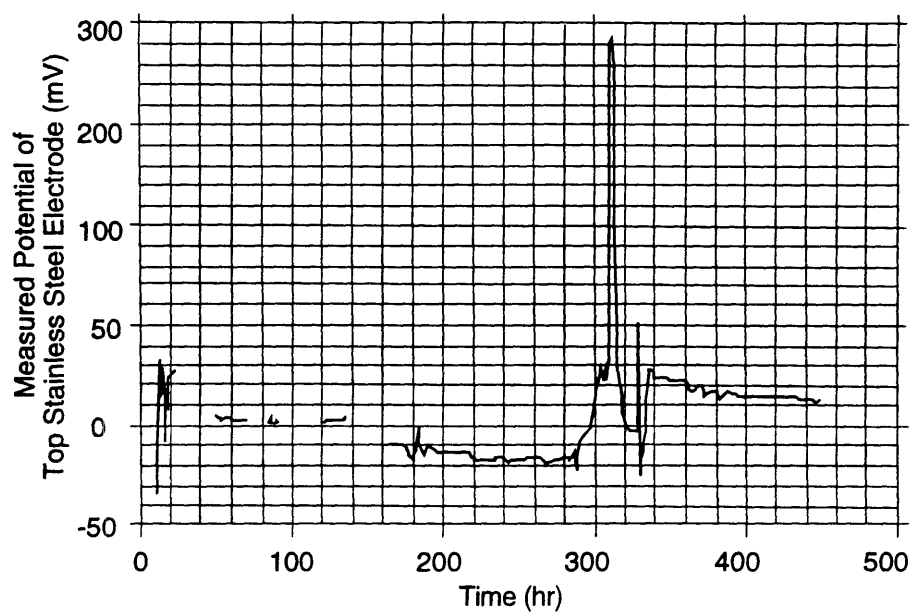


Figure 5.8. Stainless steel electrode in top electrode cluster.

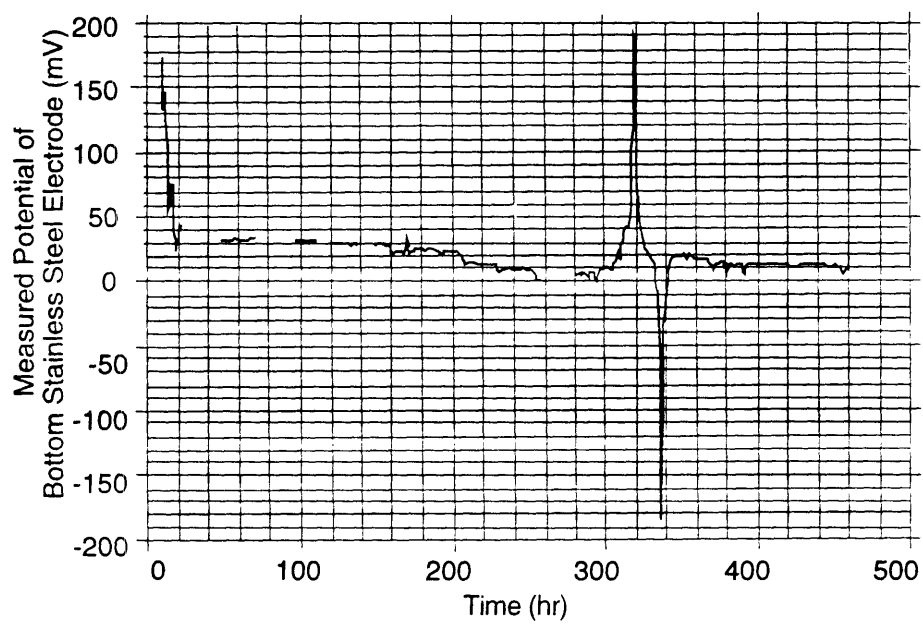


Figure 5.9. Stainless steel electrode in bottom electrode cluster.

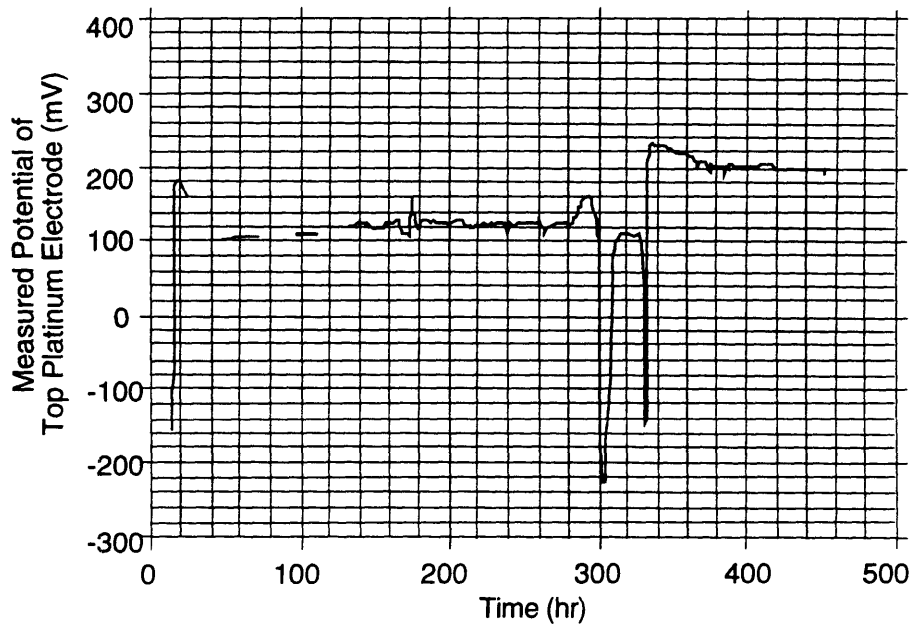


Figure 5.10. Platinum electrode in top electrode cluster.

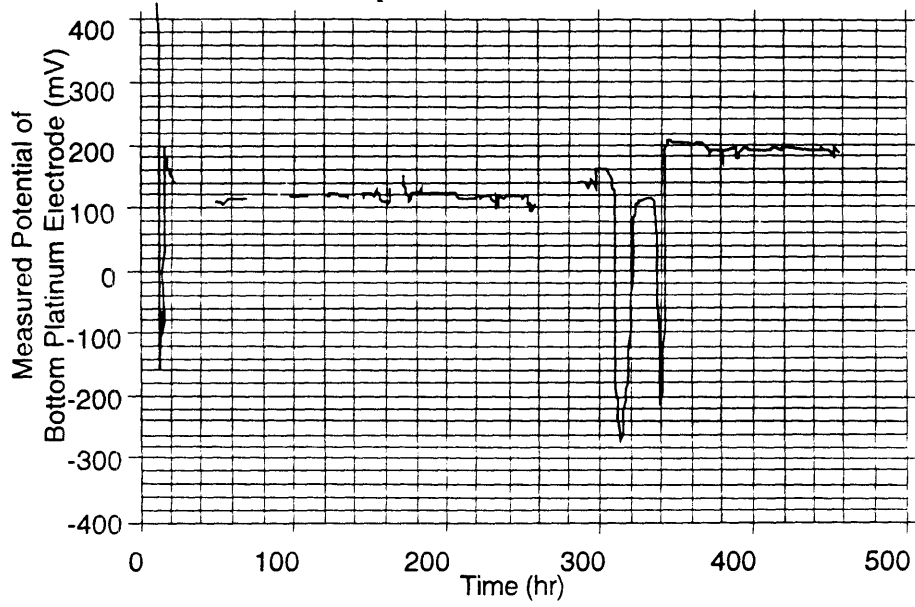


Figure 5.11. Platinum electrode in bottom electrode cluster.

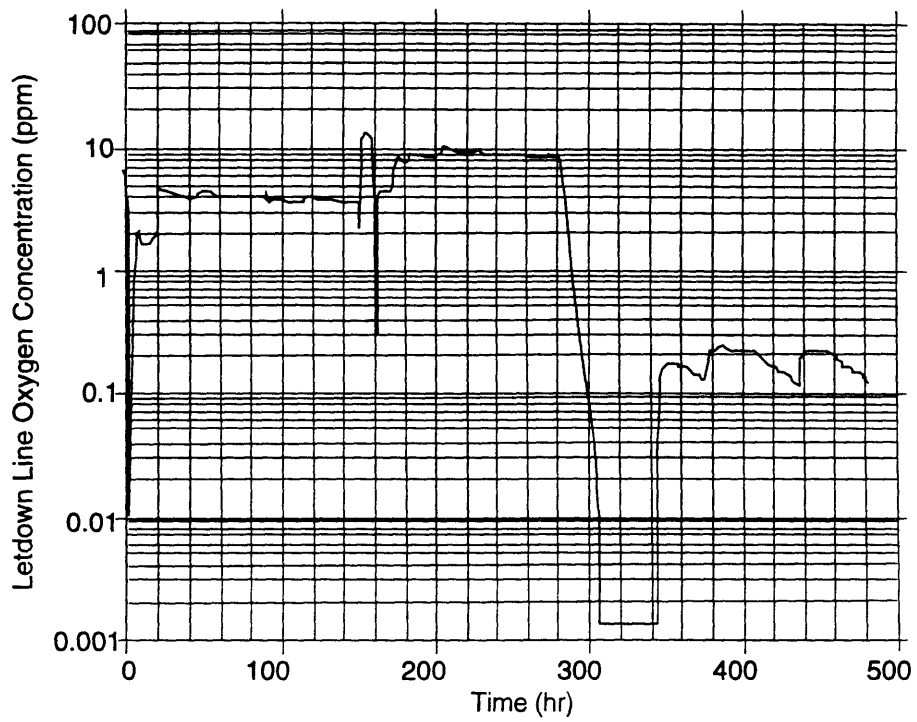


Figure 5.12. Dissolved oxygen concentration in letdown line.

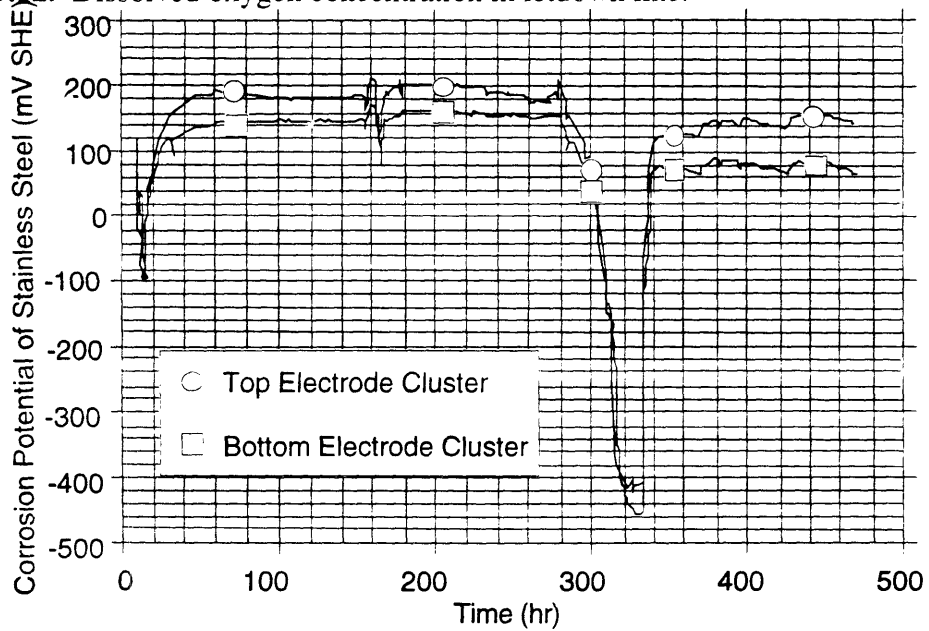


Figure 5.13. Calculated ECP of stainless steel in both top and bottom electrode clusters.

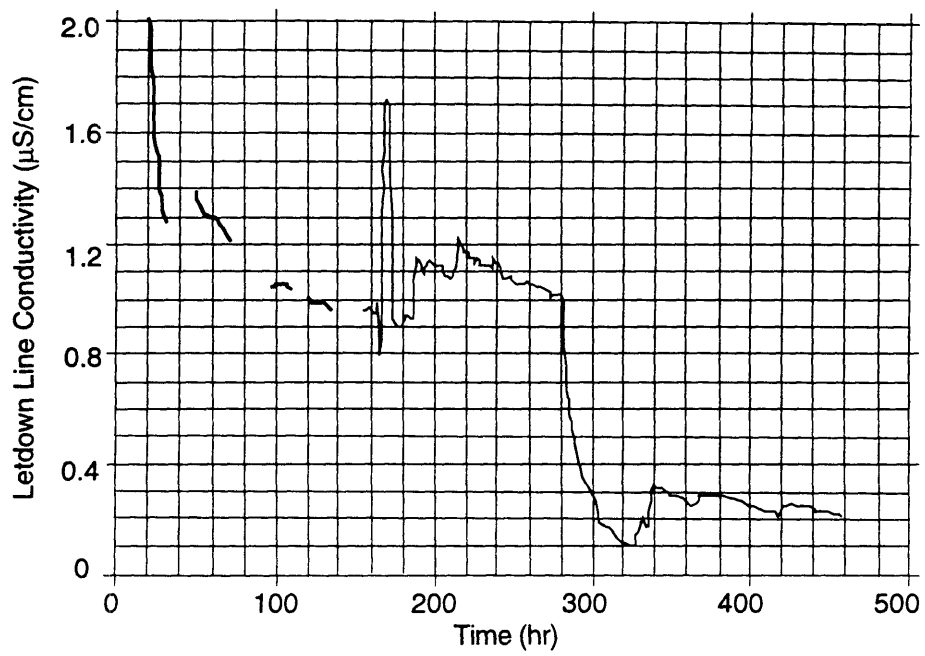


Figure 5.14. Letdown line water conductivity.

Table 5.6. Major Events in Pre-Filming

Time (hrs)	Description
10	Heaters Energized. Charging tank vented to air. Dissolved oxygen decreases in let-down due to consumption by rig.
15	Dissolved oxygen and ECP reach minimum. Oxygen is now entering the loop at the same rate as it is being consumed. Lowest ECP recorded is 30 mV(SHE). Lowest dissolved oxygen concentration recorded is 9 ppb.
15.5	Loop temperature reaches 288°C. Loop temperature will vary less than $\pm 3^\circ\text{C}$ for the remainder of the test.
50	Loop dissolved oxygen concentration reaches an approximate steady value of 5.5 ppm. Top and bottom ECP values are 190 and 130 mV(SHE) respectively.
155	Charging tank is pressurized with a He cover gas and vented to remove dissolved air.
156	Charging tank vent is closed and oxygen is added to the charging tank.
162	Charging tank is vented.
165.5	Charging tank vent is closed and oxygen is added.
170	Steady state oxygen and ECP values are attained. Dissolved oxygen concentration is 4.5 ppm. Top and bottom ECPs are 190 and 150 mV(SHE) respectively.
178	Added oxygen to the charging tank.
180	Steady state oxygen and ECP values are attained. Dissolved oxygen concentration is 12 ppm. Top and bottom ECPs are 200 and 155 mV(SHE) respectively.
208	Added oxygen to the charging tank.
210	Steady state oxygen and ECP values are attained. Dissolved oxygen concentration is 16 ppm. Top and bottom ECPs are 200 and 155 mV(SHE) respectively.
280	Charging tank is vented.
302	Dissolved oxygen concentration goes below 1 ppb.
313	Top and bottom ECPs reach minimum values of -430 and -455 mV(SHE).
315	Oxygen is added to the charging tank.
370	Oxygen is added to the charging tank.
425	Oxygen is added to the charging tank.
470	Test terminated.

5.1.6. Out of Core High Temperature Tensile Tests

Strain rate control using the DCPD technique was tested in high temperature and pressure water, similar to the environment that will exist during in-core tensile tests. The normalized potential (V_n) was found to have excessive noise for the control subroutine used. Much smoothing of the DCPD strain signal would be required to use the DCPD technique for strain rate control which would diminish the value of strain rate control. For this reason strain rate control using the DCPD technique was abandoned; the IASCC working group agreed that all tests were to be conducted using constant loading machine extension rate. The ability to varying the loading machine extension rate manually is maintained if additional control is required. The normalized potential will be monitored during slow strain rate testing since it provides valuable insight regarding the condition of the *in-situ* test specimen in real time.

To confirm that the in-core tensile test facility can load a specimen in tension at a slow strain rate in high temperature and pressure pure water, tensile tests were performed out of core before the rig became highly radioactive. Three tests were conducted, the first test loaded a 30% cold worked alloy 304 of commercial purity (heat AJ9139) at a constant extension rate of 18 mil/hr until failure. This extension rate corresponds to a strain rate of $1 \times 10^{-5} \text{ s}^{-1}$. The second test loaded a 30% cold worked alloy 304 of commercial purity (heat AJ9139), thermally sensitized at 650°C for 25 hr prior to cold rolling, using a constant extension rate of 0.78 mil/hr until failure. This extension rate corresponds to a strain rate of $4 \times 10^{-7} \text{ s}^{-1}$. The final out of core tensile test loaded a solution annealed alloy 316L using a constant extension rate of 0.78 mil/hr for 8 days. The final test specimen never fractured, the test was stopped because specimen failure was not imminent and the project's schedule required the test to be halted.

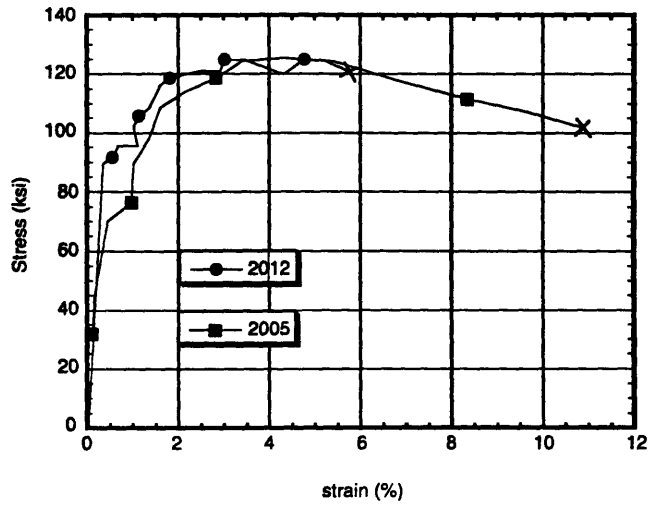


Figure 5.15. Stress vs. strain plot of the two AJ9139 specimens tested. Specimen number 2012 was furnace sensitized. Both specimens were cold worked to 30% following any heat treatment.

Figures 5.16. and 5.17 illustrate the fracture surface of the first two test specimens (numbers 2005 and 2012). 2005 showed no intergranular fracture and 18%. 2012 showed 12% intergranular fracture and no reduction in area.

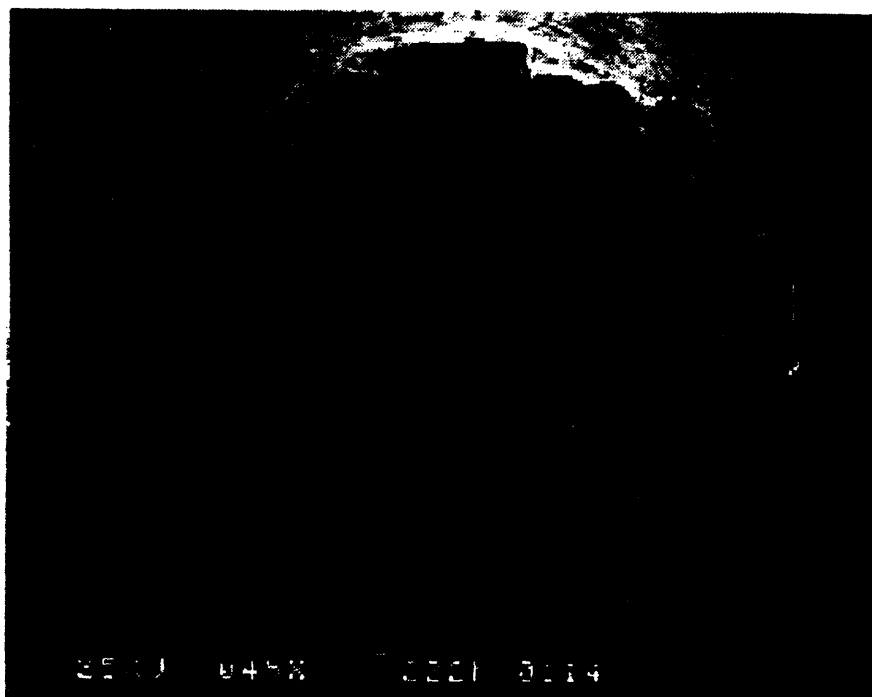


Figure 5.16. Fracture surface from specimen 2005.

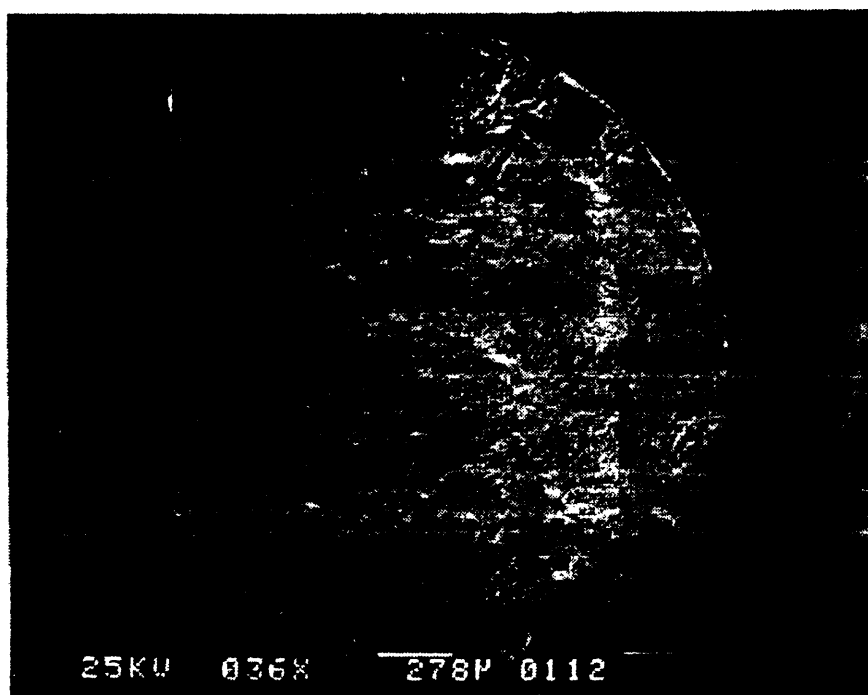


Figure 5.17. Fracture surface from specimen 2012.

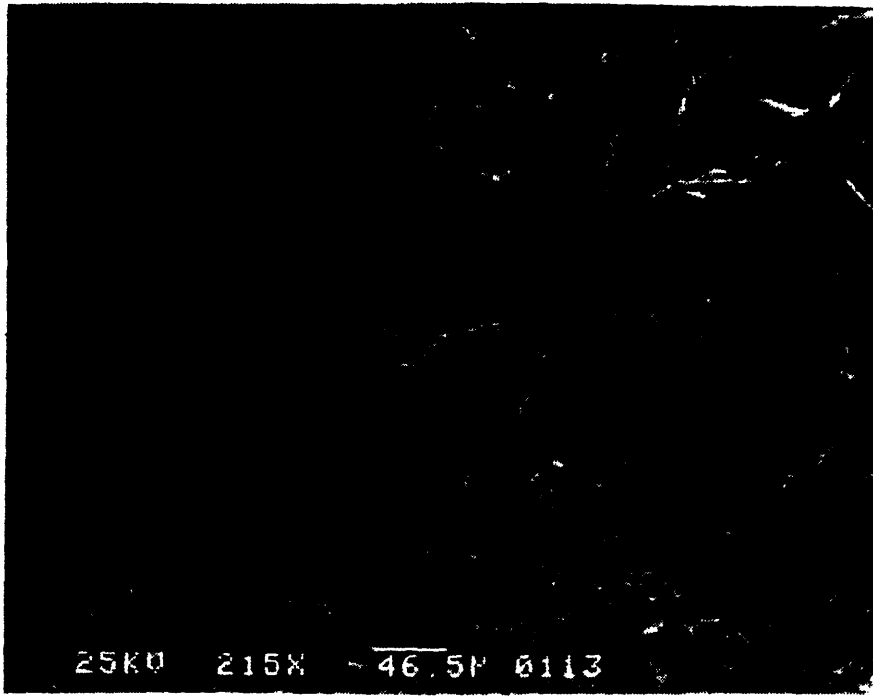


Figure 5.18. Intergranular and ductile fracture surfaces from specimen 2012.

5.1.7. Reactivity Testing

Reactivity worths of the IASCC in-core experiment in various loading conditions were measured. The reactivity worth of the in-core facility when the containment tube is flooded is measured to be $-443.6 \text{ m}\beta$. A transition from dry to flooded conditions of the experiment during reactor operation at criticality will result in positive reactivity insertion of $61.0 \text{ m}\beta$. This is equivalent to a change in reactivity of $0.048\% \Delta K/K$ which is significantly lower than the movable experiment reactivity limit of $0.20\% \Delta K/K$.

The reactivity measurements were done by first performing a baseline criticality without the installation of the facility in-core. The facility was then installed in the reactor core in flooded condition and a criticality measurement was made. Another criticality was also performed with insertion of a titanium and stainless steel mock-up of the in-core sections of the rig. This mock-up provided the same volumes and axial distribution of titanium and stainless steel present in the in-core sections of the rig. Portions of the mock-up were left dry to simulate a 50% flooded condition of the rig. Lastly, water was injected into the partial voids in the mock-up to simulate a completely flooded condition of the rig and another criticality was obtained. Reactor conditions at criticality for the various combinations were compared to obtain the reactivity worths of the in-core facility. Tables 5.7. through 5.9. list the parameters measured and test results.

Table 5.7. Measurement of the rig's reactivity addition in the fully flooded condition.

	Flooded Condition	Not Installed	Reactivity Difference ($\text{m}\beta$)
Shim Bank Height	0955	0880	-520
Reg Rod Height	0200	0403	40.9
Temperature ($^{\circ}\text{C}$)	32.25	26.95	35.5
Xenon	S/D 108 hrs	S/D 101 hrs	
Net Reactivity Change			-443.6

Table 5.8. Measurement of the rig's reactivity addition in the dry condition.

	Mock-up Half Flooded Condition	Not Installed	Reactivity Difference (m β)
Shim Bank Height	0960	0880	-570
Reg Rod Height	0165	0403	50.2
Temperature ($^{\circ}$ C)	28.6	26.95	8.3
Xenon	S/D > 101 hrs	S/D 101 hrs	
Net Reactivity Change			-511.3

Table 5.9. Measurement of the rig's reactivity addition in the 50% flooded condition.

	Mock-up Fully Flooded Condition	Dry Condition	Reactivity Difference (m β)
Shim Bank Height	0960	0960	0
Reg Rod Height	0200	0165	-9
Temperature ($^{\circ}$ C)	33.75	28.6	39.5
Xenon	S/D > 101 hrs	S/D > 101 hrs	
Net Reactivity Change			30.5

The reactivity insertion by removing all water present in the in-core sections of the rig, by linear extrapolation, is determined to be 61.0 m β .

5.2. In-Core ECP Mapping

5.2.1. Overview

An in-core electrode rig was developed to study the effects of fast neutron and gamma radiation on the electrochemical corrosion potential (ECP) of stainless steel in high purity, 288°C water. The facility measured the ECP of stainless steel and its sensitivity to varying parameters such as neutron and gamma dose rate, and flow rate under both normal and hydrogen water chemistry conditions. These measurements were used to characterize the in-core facility to be used for slow strain rate testing (SSRT) of a variety of materials. As discussed above, space constraints permit only a platinum electrode to be used during SSRT, the pre-characterization is relied upon to calibrate the response of the rig, particularly under normal boiling water reactor chemistry (NWC). In addition, the data obtained is directly relevant to understanding in-core ECP in commercial BWRs. The water chemistry conditions and radiation dose rates of the rig were similar to those in commercial plants and the rig data can be used to benchmark radiolysis and ECP codes.

A description of the testing facility is included in chapter 3. A description of the Ag/AgCl and platinum electrodes are given in reference [3]. A description of the facility's pre-film and out-of-core electrode verification are included in chapter 5.1. This section gives a summary and the results of in-core testing. A brief discussion and analysis of the results is included as well.

5.2.2. Test Description

The in-core ECP measurement facility allowed significant parameters to be varied while monitoring in-core and letdown water ECP, and letdown water chemistry. The following test matrix was used.

Run no. 1: Initial run. Determine an optimum loop refresh rate and charging tank chemical condition. The criteria is based obtaining ECP of in-core stainless steel components of about 200 mVSHE.

Run no. 2: Measurement of in-core ECP and letdown water chemistry at varying loop refresh rates.

Run no. 3: Measurement of in-core ECP and letdown water chemistry at several reactor power levels (i.e. varying neutron and gamma dose rates).

Run no. 4: Measurement of in-core ECP and letdown water chemistry at varying in-core water flow rates.

Run no. 5: Measurement of in-core ECP and letdown water chemistry at low main loop water temperature.

Run no. 6: Measurement of in-core ECP and letdown water chemistry under HWC. Reactor power levels and hydrogen concentrations were varied.

Runs 1 through 6 were performed first at electrode cluster position number 1. The electrode clusters were removed from the autoclave, a spacer made of solid titanium was placed in the bottom of the autoclave and the electrode clusters were re-installed in the autoclave at a position 9.25 inches higher than position number 1. In position number 2

the bottom electrode cluster was in the same axial position as was the top electrode cluster during testing in position number 1; the top electrode cluster was about 6 inches above reactor core.

Data was recorded to disk and displayed in real time every 71 seconds. The parameters recorded were test time, potentials measured by the six in-core electrodes, potentials measured by the 3 reference autoclave electrodes, dissolved oxygen and hydrogen, conductivity, and the temperatures of each electrode cluster, reference autoclave and heater casing. Recirc pump ΔP and main loop pressure were recorded to disk with each reading, but were not displayed in real time. All electrode potentials were measured with respect to ground. The ECP of the stainless steel electrodes were corrected to SHE by using

$$E_{SS/SHE} = E_{SS/Gnd} - E_{Ag/AgCl/Gnd} + E_{Ag/AgCl/SHE}.$$

Where: $E_{SS/SHE}$ is the ECP of stainless steel measured with respect to SHE
 $E_{SS/Gnd}$ is the measured stainless steel electrode potential
 $E_{Ag/AgCl/Gnd}$ is the measured Ag/AgCl electrode potential
 $E_{Ag/AgCl/SHE}$ is the correction for the Ag/AgCl electrode to SHE which is given by

$$E_{Ag/AgCl/SHE} = 601.8\text{mV} - 1.645\text{mV}(T - 25^\circ\text{C}).$$

For testing utilizing HWC the platinum electrodes were used in addition to the Ag/AgCl electrodes as a reference electrode. ECPs measured using the platinum electrode are converted to the SHE scale using the relation

$$E_{SS/SHE} = E_{SS/Gnd} - E_{Pt/Gnd} + E_{Pt/SHE}$$

Where: $E_{SS/SHE}$ is the ECP of stainless steel measured with respect to SHE
 $E_{SS/Gnd}$ is the measured stainless steel electrode potential
 $E_{Pt/Gnd}$ is the measured platinum electrode potential
 $E_{Pt/SHE}$ is the correction for the platinum electrode potential to SHE.

This correction makes use of the Nernst relation for the equilibrium potential for the hydrogen reaction which is

$$E_{Pt/SHE} = 1.985 \times 10^{-4} T \left[\text{pH} + \frac{1}{2} \log \frac{(H_2)}{1000K_{H_2}} \right]$$

Where: T is the temperature in °K
 (H_2) is the dissolved hydrogen concentration (ppb) in excess of stoichiometric O_2 .
 K_{H_2} is the hydrogen solubility coefficient (ppm/atm) and is

$$K_{H_2} = 1.24 \times 10^{-4} [T(^{\circ}F)]^2 - 9.307 \times 10^{-2} [T(^{\circ}F)] + 21.298 \quad [4].$$

5.2.3. Results

Testing in Position 1

The initial 8 days of in-core testing were utilized for determining the optimum operating conditions and verifying facility control methods. Operating temperature for the main loop was established to be 277°C. Equilibrium stainless steel ECP in both top and bottom electrode clusters were lower than those anticipated with charging tank chemistry controlled such that no oxygen was present in the charging water. To achieve the target ECP of 0 to +200mVSHE it was necessary to maintain a charging tank O_2

concentration of 200 ppb. Several charging tank O₂ concentrations were tried before deciding upon this value. A description of the system used to control charging tank chemistry is included in section 3.4.3. In-core stainless steel ECP and letdown line O₂ concentration for the initial 10 days of in-core testing are plotted in Figure 5.19.

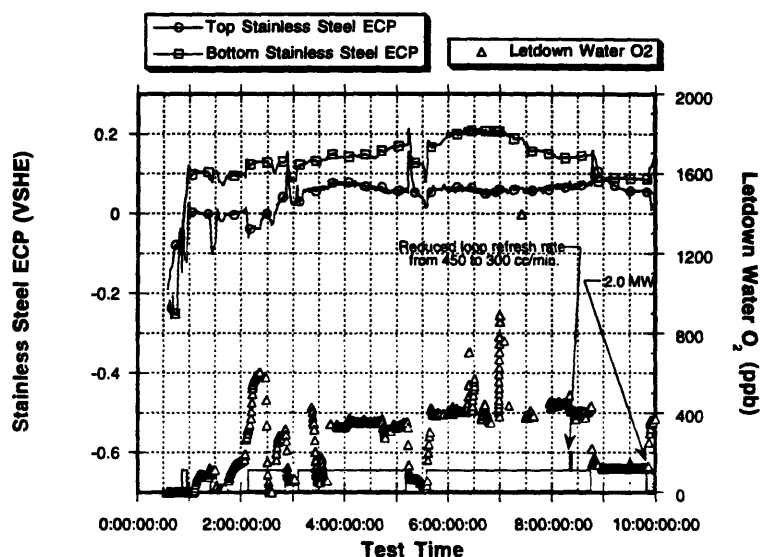


Figure 5.19. In-core ECPs measured and letdown line oxygen levels for the first 10 days of in-core testing. Shaded areas at the bottom of the graph indicates reactor operation at 4.5 MW unless otherwise specified.

On day 9 at 10:00AM (10:10:00:00) the charging rate was reduced from 450 to 300 cc/minute. As a result the letdown line oxygen decreased from 440 to 400 ppb. No changes in ECP or other parameters were noticed.

Figure 5.20 is the plot of stainless steel ECP for the period covering days 8 through 19; this period consisted of the majority of the studies utilizing NWC. Charging water chemistry for this testing period was 200 ± 20 ppb dissolved oxygen and $0.07 \mu\text{S/cm}$ conductivity unless noted otherwise. Reactor power transients occurred more frequently than planned which provided significant power transient data. A consistent result of

these transients was letdown oxygen concentration varying between 400 ± 30 ppb (4.5 MW reactor power) and 125 ± 15 ppb (reactor shutdown). In-core ECP measurements varied as well. Stainless steel ECP in the bottom electrode cluster varied between +140 and +160mVSHE for the reactor operating at 4.5 MW, except for the period 12:12:00:00 to 13:01:00:00 where an ECP of +240mVSHE was recorded. The ECP in the same electrode cluster with the reactor off was 70 ± 10 mVSHE. The ECP in the top electrode cluster varied between +65 and +80mVSHE with the reactor operating at 4.5 MW, and +55mVSHE with the reactor shutdown. The ECP recorded in the top electrode cluster required more time to reach steady state than was available for two of the low power transients, those transients were on days 13 and 14.

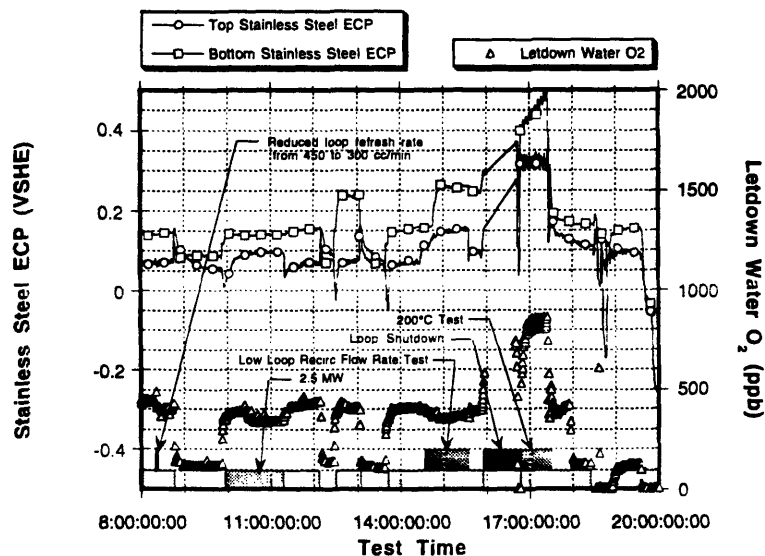


Figure 5.20. In-core ECP and letdown line oxygen for in-core testing days 8 through 20.

A 34 hour 1/2 power (2.5 MW reactor power) run was performed starting on days 10 through 12. During this test letdown oxygen concentration was 375 ± 10 ppb. Stainless steel ECP measured at the bottom electrode was 140mVSHE; stainless steel ECP measured at the top electrode cluster was 95mVSHE.

A 24 hour low Recirc flow rate with the reactor at full power run was performed on days 14 and 15. In this period the main loop Recirc pump frequency was reduced from 60 to 40hz in an eight hour period. No unexpected changes in thermal-hydraulic characteristics were noticed. Main loop heater power and heater casing temperature were unchanged. In addition, no noticeable temperature excursion occurred. Main loop heater ΔT increased from about 1°C to about 2°C. Recirc pump ΔP decreased from 13.5 to 6.5psi. This corresponds to a reduction in loop flow rate of about 70%, or from 12 to 8.4 gpm. In the initial 10 hours of this run letdown line oxygen concentration declined from 410 to 350ppb. In the following 6 hours letdown line oxygen increased to 375ppb and remained there to test completion. Stainless steel ECP measured in the top electrode cluster began to increase immediately after flow rate reduction from 60mVSHE to its final reading of 150mVSHE 16 hours later. Stainless steel ECP measured in the bottom electrode cluster increased six hours after test start from 160mVSHE to 260mVSHE. Measured ECP in this electrode cluster required four hours to stabilize.

On day 15 a 200°C main loop temperature run was attempted. During the cool-down an unisolable leak in the auxiliary cooling water system required facility shutdown and cool down. The shutdown lasted for 15 hours after which time testing resumed. The loop was heated to 200°C and the reactor was brought to full power and the 18 hour low temperature run was begun. In this period main loop temperature was not accurately controlled, temperature oscillated about 200°C with an amplitude of 7°C and a period of 1.6 hours. This was reflected in the letdown line dissolved oxygen and in-core ECP measurements. Steady state letdown line oxygen concentration was 830 ± 30 ppb. Steady state stainless steel ECP in the top electrode cluster was 320 ± 20 mVSHE. Steady state stainless steel ECP in the bottom electrode cluster was never achieved, it was increasing linearly through +500mVSHE when the test was ended and the loop heated to 277°C, normal operating the temperature.

On day 19 the charging tank oxygen was reduced to less than 8ppb. Letdown line dissolved oxygen concentration decreased from about 400 to 125ppb with reactor power at 4.5 MW. With the reactor shutdown letdown line dissolved oxygen was 8ppb. Stainless steel ECP was 165mVSHE in the bottom electrode cluster and 110mVSHE in the top electrode cluster. At 18:11:00:00 the Ag/AgCl reference electrode in the letdown line reference autoclave failed requiring it to be bypassed and isolated. Some oxygen was admitted into the charging tank. The charging tank was quickly vented and the charging tank dissolved oxygen concentration was returned to <8ppb within 2 hours. The reactor shutdown occurring on day 18 was not a complete shutdown. Power was reduced to 50kW for two hours. Three minutes after power was raised to 4.5 MW the reactor scrambled. The reactor was brought critical an hour and a half later and reached full power at 18:21:50:00. Equilibrium stainless steel ECP was never reached during this shutdown.

Figure 5.21 is a plot of stainless steel ECP and letdown line dissolved oxygen and hydrogen for days 17 through the end of in-core testing at electrode position 1, day 26. In this figure ECPs are converted to SHE scale using the in-core Ag/AgCl electrodes. Figure 5.26 illustrates stainless steel ECPs for the same time period but uses the platinum electrodes to convert the measurements to the SHE scale. Figure 5.26 will be discussed later; the subscripts Ag and Pt following units is used in the following discussion to help distinguish between the two readings.

At 19:14:00:00, with the reactor at 4.5 MW, hydrogen was admitted into the charging tank and charging tank dissolved hydrogen concentration was raised to 50ppb. Letdown line dissolved oxygen immediately lowered to <8ppb. Letdown line dissolved hydrogen concentration increased to 50ppb, the same concentration as the charging tank. Both in-core ECP measurements decreased. At 19:20:00:00 additional hydrogen was added to increase the charging tank and letdown line dissolved hydrogen concentrations

to 100ppb. Equilibrium stainless steel ECP was $-260\text{mVSHE}_{\text{Ag}}$ in the top electrode cluster and $-45\text{mVSHE}_{\text{Ag}}$ in the bottom electrode cluster. The reactor was shutdown for nine hours on day 20 during which time the equilibrium stainless steel ECP was $-275\text{mVSHE}_{\text{Ag}}$ in the top electrode cluster and $-350\text{mVSHE}_{\text{Ag}}$ in the bottom electrode cluster. After the reactor was brought to 4.5MW and steady state established steady state stainless steel ECP in both top and bottom electrode clusters were measured to be within 15mV of those before the shutdown.

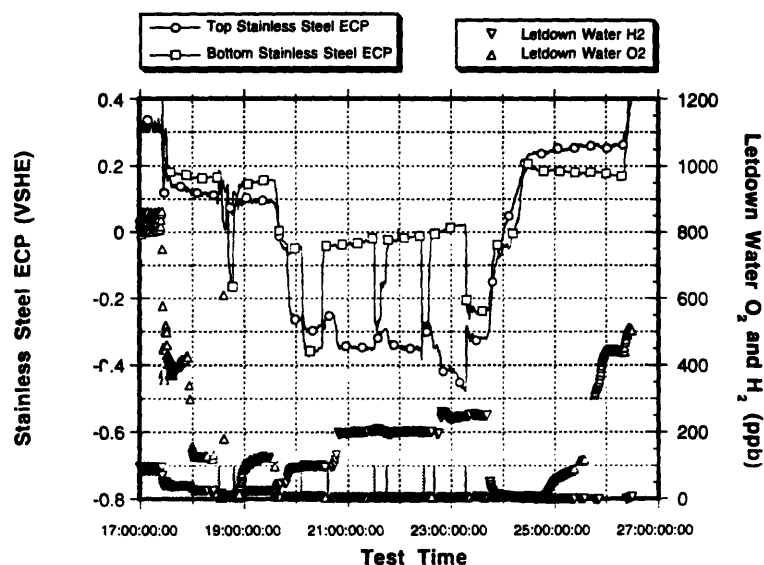


Figure 5.21. In-core ECP and letdown line oxygen and hydrogen for days 17 through 26. ECPs are converted to SHE using the in-core Ag/AgCl electrodes.

At 20:18:00:00 charging tank and letdown line dissolved hydrogen concentrations were increased from 100 to 200ppb. Equilibrium stainless steel ECP was $-350\text{mVSHE}_{\text{Ag}}$ in the top electrode cluster and $-30\text{mVSHE}_{\text{Ag}}$ in the bottom electrode cluster.

The reactor shutdown on day 21 was not a complete shutdown. Power was lowered from 4.5MW to 50kW at 21:12:00:00. At 21:15:00:00 reactor power was raised to 1MW. At 21:18:30:00 reactor power was returned to 4.5MW. Equilibrium stainless

steel ECP was never attained during this transient, however, during the power reduction to 50kW stainless steel ECP increased to about $-300\text{mVSHE}_{\text{Ag}}$ in the top electrode cluster and decreased to about $-290\text{mVSHE}_{\text{Ag}}$ in the bottom electrode cluster. When reactor power was raised to 1MW stainless steel ECP increased to about $-290\text{mVSHE}_{\text{Ag}}$ in the top electrode cluster and $-150\text{mVSHE}_{\text{Ag}}$ in the bottom electrode cluster. After reactor power was returned to 4.5MW equilibrium stainless steel ECPs were established in the top and bottom electrode clusters within 10mVSHE to what they had been prior to the reactor power transient.

On day 22 the reactor shutdown at 22:10:00:00. The reactor was brought critical and returned to 4.5 MW five hours later. During the transient equilibrium stainless steel ECP was $-300\text{mVSHE}_{\text{Ag}}$ in both the top and bottom electrode clusters. Following reactor return to 4.5MW equilibrium stainless steel ECP was $-345\text{mVSHE}_{\text{Ag}}$ in the top electrode cluster and $-10\text{mVSHE}_{\text{Ag}}$ in the bottom electrode cluster.

At 22:18:00:00 additional hydrogen was added to the charging tank to increase the charging tank and letdown line dissolved hydrogen concentrations to 200ppb. With reactor power at 4.5MW equilibrium stainless steel ECP was $-410\text{mVSHE}_{\text{Ag}}$ in the top electrode cluster and $+20\text{mVSHE}_{\text{Ag}}$ in the bottom electrode cluster. At 23:07:00:00 the reactor was shutdown. Equilibrium stainless steel ECP with the reactor shutdown was $-320\text{mVSHE}_{\text{Ag}}$ in the top electrode cluster and $-240\text{mVSHE}_{\text{Ag}}$ in the bottom electrode cluster.

At 23:17:00:00 hydrogen was vented from the charging tank and oxygen was added. Recorded in-core ECP measurements responded immediately to the added oxygen, The letdown line dissolved oxygen concentration did not indicate an increasing oxygen concentration until 24 hours later. Equilibrium stainless steel ECP was $+260\text{mVSHE}_{\text{Ag}}$ in the top electrode cluster and $+180\text{mVSHE}_{\text{Ag}}$ in the bottom electrode cluster. At 24:21:00:00 additional oxygen was added to the charging tank to increase the

letdown line dissolved oxygen concentration to 450ppb. Equilibrium stainless steel ECP was +280mVSHE_{Ag} in the top electrode cluster and +175mVSHE_{Ag} in the bottom electrode cluster. At 26:08:00:00 the facility was cooled down and shutdown.

Figure 5.21 is a plot of letdown line conductivity for the entire in-core test at position 1.

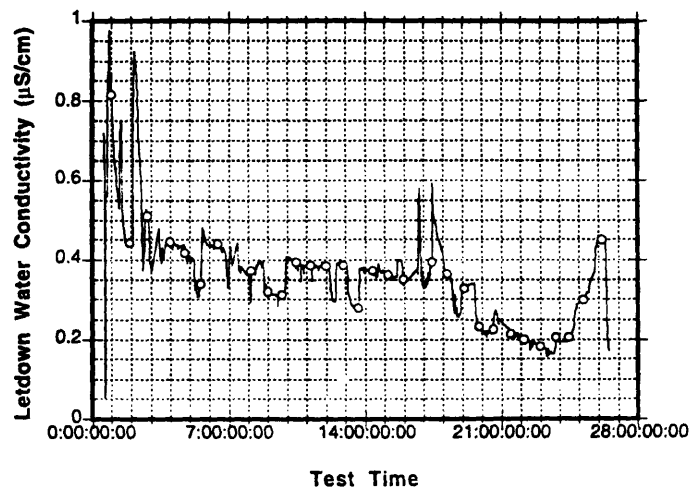


Figure 5.22. Letdown line conductivity for in-core testing at position 1.

Testing in Position 2

Stainless steel ECP in both the top and bottom electrode clusters and letdown line dissolved oxygen and hydrogen concentrations are plotted in figure 5.23. 200ppb charging tank oxygen concentration was established at 1:12:00:00 with reactor power at 4.5MW. Equilibrium stainless steel ECP was +290mVSHE in the top electrode cluster and 240mVSHE in the bottom electrode cluster. At 1:21:00:00 reactor power level was lowered to 2.5MW. Letdown line oxygen concentration decreased from 360 to 340ppb. Equilibrium stainless steel ECP was +300mVSHE in the top electrode cluster and

+220mVSHE in the bottom electrode cluster. Reactor power was returned to 4.5mW at 2:06:00:00. Letdown line dissolved oxygen concentration increased to 400ppb. Equilibrium stainless steel ECP returned to within 10mV of the value it had been before the power transient.

In Figure 5.24 ECPs are converted to SHE scale using the in-core Ag/AgCl electrodes. Figure 5.27. illustrates stainless steel ECPs for the same time period but uses the platinum electrodes to convert the measurements to the SHE scale. Figure 5.27. will be discussed later; the subscripts Ag and Pt following units are again used in the following description to help distinguish between the two readings.

At 3:12:00:00 oxygen in the charging tank was vented and hydrogen was added so that the charging tank and letdown line hydrogen concentration was 200ppb. Equilibrium stainless steel ECP was $-325\text{mVSHE}_{\text{Ag}}$ in the top electrode cluster and $-120\text{mVSHE}_{\text{Ag}}$ in the bottom electrode cluster. At 3:11:00:00 the reactor was shutdown. Equilibrium stainless steel ECP was $-210\text{mVSHE}_{\text{Ag}}$ in the top electrode cluster and $-400\text{mVSHE}_{\text{Ag}}$ in the bottom electrode cluster.

At 5:14:00:00 the facility was shutdown and cooled down.

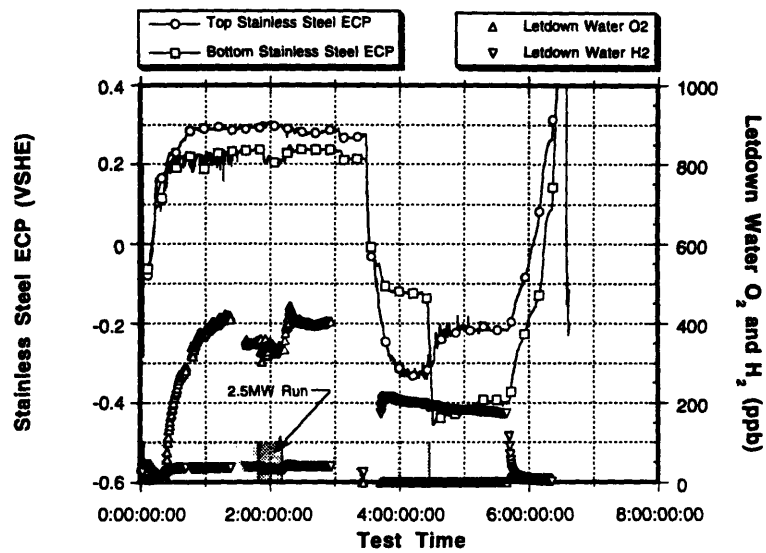


Figure 5.23. In-core ECP and letdown line oxygen and hydrogen for in-core testing in position 2. ECPs are converted to SHE using the in-core Ag/Ag/Cl electrodes.

Figure 5.24 is a plot of letdown line conductivity for the entire in-core test at position 1.

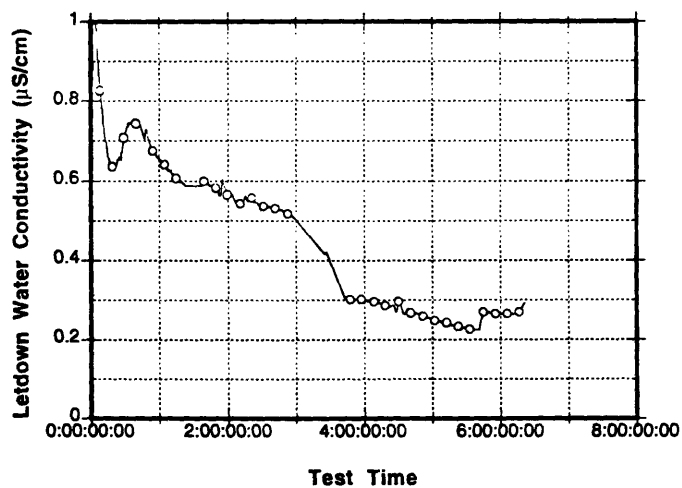


Figure 5.24. Letdown line conductivity for in-core testing at position 2.

5.2.4. Discussion

In-core SSRT testing requires the ECP of the stainless steel specimen under test to be in an environment similar to the environment existing in the in-core and above core sections of a typical BWR core operating under NWC. Typical ECP for these environments are 0 to +200mVSHE. These tests verify that the required potentials can be achieved in the peak flux region with the reactor on or off and letdown line oxygen concentration between 100 to 450ppb.

Equilibrium stainless steel ECP measurements using NWC in position 1 finds the potential in the bottom electrode cluster about 80mV higher than the top electrode cluster. The bottom electrode cluster is in the peak flux region of the MITR reactor core and the top electrode cluster is in the top section of the core. The integrated dose rate that the water had received was greater for the water in the top electrode cluster than the bottom. The actual potential difference is probably greater than 80mV. During the out of core electrode rig pre-film and electrode verification section described in 5.1.5 the top electrode cluster measured 70mV higher than the bottom electrode cluster. They should have been identical. For testing in position 2, stainless steel ECP in the top electrode cluster was between 50 to 90mV higher than the bottom electrode cluster. This result is consistent with results from out of core testing indicating that the ECP of stainless steel in the top sections of the reactor core are the same as those six inches above the core. In addition, measurements in position 1 with the reactor off shows that the ECP in the top electrode cluster is higher than the ECP in the bottom electrode cluster by the same amount. This could lead to the conclusion that radiation dose rate has a significant effect on ECP for in-core components. This finding is in agreement with results of Macdonald's Mixed Potential Model when it was used to calculate the ECP of stainless steel in several sections of eight commercial nuclear reactors [5]. For hydrogen concentrations less than 1ppm, 6 of the 8 modeled reactors had potentials in the mid-core sections higher than

potentials in the upper plenum. The potentials in the mid-core and upper plenum were similar and highly oxidizing in the remaining two cases.

The effects of integrated dose rate on ECP were observed in the reduced main loop flow rate run. Reducing the flow rate increases the dose received by the water and the resulting concentration of oxidizing radiolytic species as it passes through the in-core electrode clusters. Measured ECP increased by 80mV in top electrode cluster and 100mV in the bottom electrode cluster.

Letdown line oxygen concentrations were significantly higher for the run conducted with loop temperature reduced from 277 to 200°C. This is explained by the decreased recombination and decomposition rates at the reduced temperature; perhaps the most significant reaction being the decomposition of H_2O_2 . This also helps to explain the marked increase in in-core ECP measurements. Stainless steel ECP in the top electrode cluster increased by about 250mVSHE, from 70 to about 320mVSHE. Equilibrium stainless steel ECP was never reached in the bottom electrode cluster. The cause for this is unclear. Main loop temperature control was insufficient which resulted in non-steady state temperature for the extent of this run. This resulted from improper tuning of the heater controller for the loop heating requirements at the lower temperature. The temperature oscillation affected the behavior of letdown line dissolved oxygen and in-core ECP measurements which also oscillated. Temperature and its effects on in-core ECP measurements and letdown line dissolved oxygen are illustrated in Figure 5.25. The magnitude and relative phase difference between oxygen, ECP and temperature could be of use in bench marking the dynamic response of radiolysis and ECP models.

Testing using HWC showed that the Ag/AgCl electrodes were not adequate for use as reference electrodes for in-flux sections in reducing environments. Figures 5.26. and 5.27. are plots of stainless steel ECP using platinum as a reference electrode. The use of platinum as a reference electrode in environments where stoichiometric excess

hydrogen over oxygen exists is well established. There is much experimental evidence that in HWC environments the potential of platinum referenced to SHE is that predicted by the Nernst relation, even with significant concentrations of oxidizing species such as O_2 and H_2O_2 present [4, 6, 7]. Even when large uncertainties in local hydrogen concentrations exist, for example the hydrogen concentration in in-flux regions, only small errors in ECP measurements result. Changing the hydrogen concentration from 100 to 150 ppb shifts the potential of the platinum electrode by 9 mV. Comparing Figures 5.26 and 5.27 to Figures 5.21 and 5.23 the effects of dose rate on the Ag/AgCl electrodes are revealed. Figure 5.21 indicates that ECP cannot be reduced below the -230mVSHE threshold potential for IGSCC in the peak flux region for the concentrations of hydrogen used in these tests. Removing the high dose rates decreases the measured ECP to below the protection threshold and the ECP measured in the top electrode cluster by about 50mV. Figure 5.26 shows that ECP is below the -230mVSHE IGSCC threshold for in-flux sections when dissolved hydrogen concentrations are 200 and 250ppb. The ECPs measured in the top electrode cluster during HWC with the reactor on and off were similar using both the Ag/AgCl and platinum electrodes.

HWC ECP measurements in position 2 revealed similar results to position 1. The Ag/AgCl electrode in the bottom electrode cluster, which is now in the same axial position that the top electrode cluster had been in for testing in position 1, responded similarly to dose rate as it had during testing at position 1. The Ag/AgCl electrode in the top electrode cluster also responded similarly to the way that it had to changing dose rate as it had during testing in position 1. This suggests that the two electrodes responded differently to fast neutron flux during HWC operation. Both electrodes responded as expected during NWC operation.

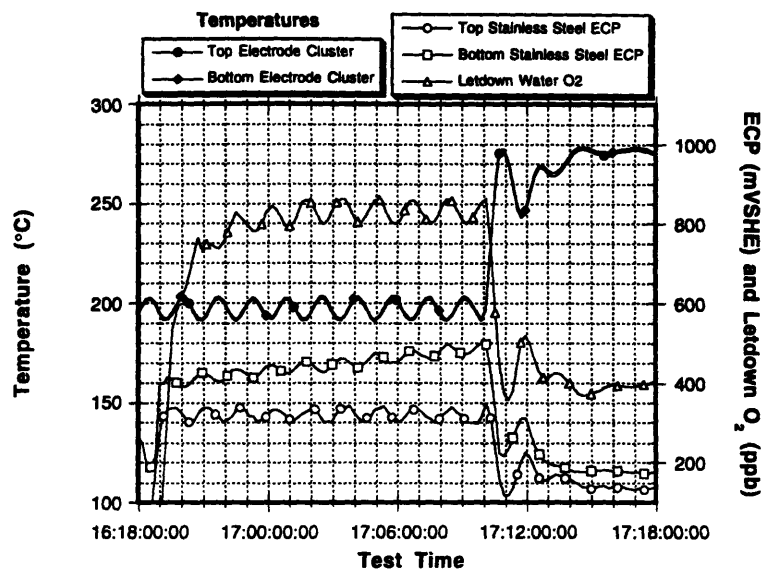


Figure 5.25. Temperature in both electrode clusters, in-core ECP and letdown line dissolved oxygen recorded during the 200°C run.

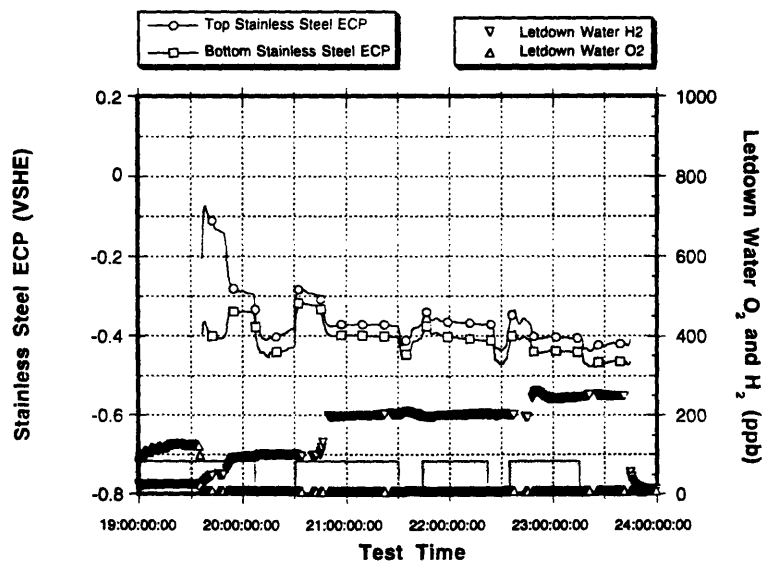


Figure 5.26. In-core ECP and letdown line oxygen and hydrogen for days 19 through 23. ECPs are converted to SHE using the in-core platinum electrodes.

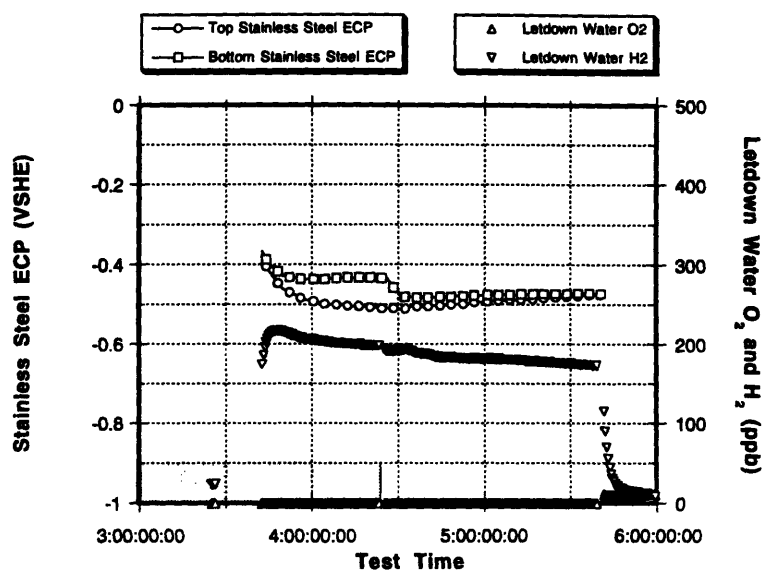


Figure 5.27. In-core ECP and letdown line oxygen and hydrogen for HWC runs in position 2. ECPs are converted to SHE using the in-core platinum electrodes.

Conductivity for the duration of in-core testing was higher than desired. Target conductivity was less than $0.2\mu\text{S}/\text{cm}$. Conductivity up to $1\mu\text{S}/\text{cm}$ [8] does not significantly impact ECP measurements (exception being conductivity due to Cu^{2+}), but does potentially impact the results of SSRT testing. For this reason an intense investigation was performed in an attempt to reduce coolant conductivity. A more detailed discussion of these investigations is included in the following section of this report, 5.3. These investigations showed that the high conductivity was not the result of transition metals (Fe^{2+} , Cr^{2+} , Ni^{2+} , Cu^{2+}) or the following anions: Cl^- , SO_4 , NO_3^- , F^- , CrO_4^{2-} or HCrO_4^- . Organic species are believed to be a major contributor to conductivity.

5.3. In-Core Tensile Testing

5.3.1. Overview

In-core SSRT testing was performed as a beginning of a study on the effects of fast neutron and gamma radiation on the IASCC susceptibility of austenitic stainless steels. The in-core radiation levels were $5 \times 10^{13} \text{ cm}^{-2}\text{s}^{-1}$ ($E > 1 \text{ MeV}$) for fast neutrons and $1 \times 10^9 \text{ R/hr}$ for gamma. Two non-irradiated specimens, one solution annealed and the other thermally sensitized, were tested in-core for facility shakedown and qualification purposes before testing of valuable pre-irradiated specimens. Complete results for two pre-irradiated specimens are included here. The results from further tests, which will contribute to a comprehensive understanding of the effects of fast neutron and gamma fluxes on IASCC susceptibility, will be included in future reports.

5.3.2. Test Description

The systems employed for chemical control and analyses and specimen loading control were described in chapter 3. The CERT testing method was employed for tests discussed in this section. The DCPD method of strain measurement and control was not used due to difficulties in handling the fine DCPD wire and ceramic insulators in the hot cell. This section describes the testing procedures followed for the in-core tensile tests.

Testing was performed at 277°C using NWC. Water chemistry was controlled so that exit water fell within the specifications listed in Table 5.10. An on-line high performance liquid chromatography (HPLC) system was added to the facility to enhance the existing chemistry monitoring capabilities. This was made necessary by the higher than desired exit water conductivity that persisted throughout in-core ECP measurements and SSRT testing.

Table 5.10. Parameters controlled during in-core SSRT testing.

Parameter	Control Band
dissolved oxygen	200-500 ppb
conductivity	as low as possible, typically <1 μ S/cm
Cl ⁻	<20 ppb
SO ₄ ²⁺	<20 ppb
F ⁻	<20 ppb
ECP (as measured by reference autoclave)	>0.000VSHE
Potential of in-core platinum vs. Gnd	50-150mV

Conditions were established and held for at least 24 hours prior to starting the tensile test to ensure that an adequate passive film had formed on the specimen's surface. After this 24 hour (minimum) soak, the specimen was pre-loaded to 138 MPa (20ksi) and the tensile test was started using the constant extension rate technique (CERT). The loading machine was run in position control using a ramp rate of 0.0198 mm/hr until specimen failure. Specimen load and loading machine extension were recorded to disk and displayed in real time every 22 seconds. Water chemistry parameters were recorded to disk and displayed in real time every 71 seconds.

In situations where it became necessary to pause the test the loading machine control mode was switched to load and specimen stress was lowered to the pre-load value of 138MPa. Events that made this necessary were reactor scrams and shutdowns, and loading machine control and data acquisition system difficulties. Testing was resumed by increasing the load in load control to a load corresponding to a stress less than or equal to the stress applied to the specimen when the test was paused, then switching the loading machine control mode to position and resuming the 0.0198 mm/hr ramp rate.

Testing of solution annealed alloy 347L and furnace sensitized alloy 304 specimens were conducted in-core prior to the testing of pre-irradiated specimens. These specimens were prepared from the same material stock and to the same physical specifications used in preparation of the pre-irradiated SSRT material specimens. The sensitized specimen was heated in a vacuum furnace at 650°C for 10 hours and air

cooled. Double loop EPR and Vicker's micro-hardness tests were conducted on a section removed from the button head of the specimen prior to in-core testing.

The irradiation of SSRT material specimens in an inert dry environment was described in reference [1]. These specimens were removed from their aluminum holders by dissolving the holder in a solution of 3N NaOH. Tests were conducted using similar holders and specimens to verify that holder dissolution had no effect on the material specimens. Specimens used for these tests were alloy 304, heat AJ9139, in both solution annealed and furnace sensitized conditions. Scanning electron microscopy analysis of the specimen surfaces following holder dissolution showed no indication of surface attack. A SSRT test was conducted on one specimen at room temperature in air with a 1N solution of NaSO₄ being supplied continuously by a wick. The stress vs. strain plot showed no indication of cracking through a strain of 16%.

Following in-core testing the fractured specimen was transported to the back engineering laboratory of the Nuclear Reactor Laboratory where it was prepared for SEM analysis. A small part of the specimen, which included the fracture surface, was cut from the rest of the specimen. This reduced the mass and total activity of material to be transported. The fracture surface was placed in a shielded SEM specimen holder. The shielded SEM specimen holder was placed into a shielded radioactive specimen transport canister and moved to the SEM room.

The following is a description of the specimens and testing procedures followed during the in-core testing campaign.

Specimen number 2021 (non-irradiated, solution annealed alloy 347L, heat K12)

The reactor was shutdown. The ramp rate used was 0.0198mm/hr for the initial 9 hours of testing then increased to 1.98mm/hr for the remainder of the test.

Specimen number 2003 (non-irradiated, sensitized alloy 304, heat AJ9139)

The EPR ratio for this specimen was 16.5, showing this specimen to be highly sensitized. The Vickers hardness number was 263. The reactor was operated at 4.2 MW. At the completion of this test the specimen appeared bent. Further investigations lead to the conclusion that the specimen was improperly positioned in the grips when load was first applied. Specimen loading procedures were modified for subsequent tests to prevent this from recurring.

Specimen number 80 (pre-irradiated to 0.8 DPA alloy 304, heat AJ9139)

Testing was done with the reactor operating at 4.0 MW. At 16% strain the main loop recirculation pump failed. The test was halted and the specimen pulled to failure at room temperature using a fast strain rate. The stress vs. strain curve shown in Figure 5.28 shows only the portion of the test conducted at a slow constant extension rate. All results are included in Appendix E.

Specimen Number 82 (pre-irradiated to 0.8 DPA alloy 304, heat AJ9139)

The reactor was operated at 4.0 MW. Testing was paused three times during the test. Prior to specimen yielding the reactor scrammed. Load was lowered from 420 MPa to 136 MPa and held there in load control until the reactor power was raised to 4.0 MW and temperature and chemistry conditions stabilized. To resume the test, load was raised to 420 MPa and the CERT test was restarted. The second pause occurred at a specimen strain of 4.5%. The loading machine was off for nearly 18 hours due to a problem with the loading machine control and data acquisition system. For this period load was nearly constant, 600 ± 20 MPa. The third and final pause occurred at a specimen strain of about 15%. A reactor shutdown was required. Specimen load was lowered and held at 136MPa. After reactor power was returned to 4.0 MW and all temperature and chemical

conditions stabilized, specimen stress was increased to 520 MPa and the CERT test was resumed.

5.3.3. Results and Fractography

Figure 5.28. shows the stress vs. strain curves for all in-core tests. These tests were performed under the mechanical and environmental conditions described above. Table 5.11. lists the actual loop exit water chemical conditions during in-core mechanical testing.

Specimens 80 and 82 were significantly hardened by the fast neutron irradiation. Each specimen's yield stress was 500 MPa. Testing of specimen number 80 was halted at 16% strain due to loss of main loop flow and therefore the end of this curve does not result in specimen failure. The non-irradiated specimens yielded at 180 MPa and hardened similarly for the first 8% strain. Specimen number 2003 failed much sooner since it was sensitized to a high degree by thermal treatment and was expected to crack. Specimen number 2021 was pulled at a fast strain rate and was not expected to crack.

Table 5.11. Letdown water chemistry during in-core SSRT testing.

Parameter	Measured Value
Conductivity ($\mu\text{S}/\text{cm}$)	0.6 - 0.8
Dissolved Oxygen (ppb)	250 - 500
Cl^- (ppb)	1.2 - 2.0
SO_4^{2-} and NO_3^- (ppb)	13 - 25
CrO_4^{2-} (ppb)	12 - 16
Cr (by ICP) (ppb)	< 5
F^- (ppb)	<0.5

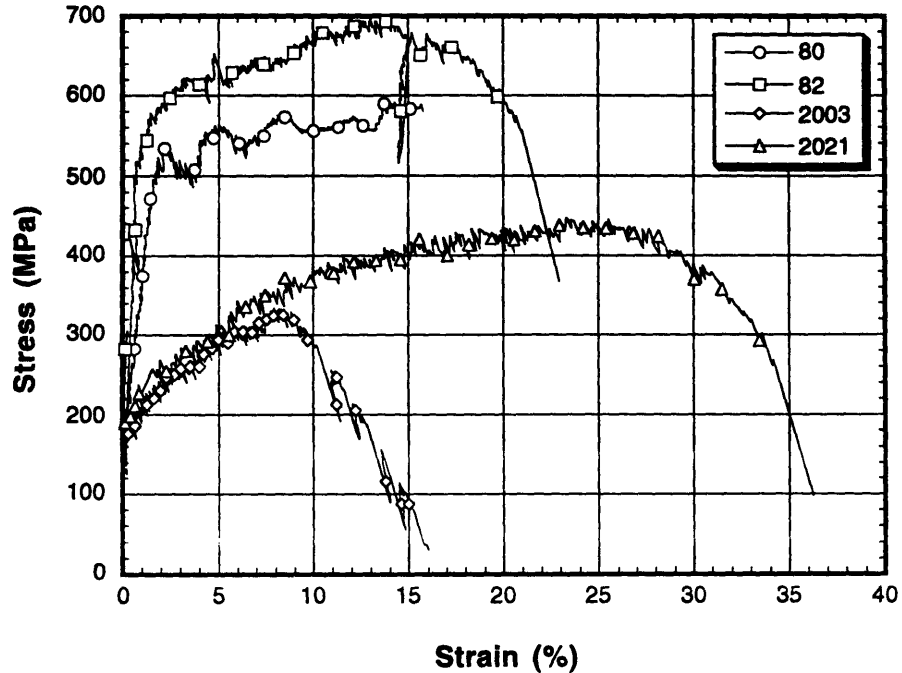


Figure 5.28. Stress strain curve for initial in-core tests. Specimen 2021 was non-irradiated alloy 347L loaded for the first 2% strain at a slow strain rate. The remainder of the test was performed at a strain rate 100x higher. Specimen 2003 was non-irradiated, furnace sensitized alloy 304. Specimens 80 and 82 were irradiated to $0.8 \times 10^{21} \text{ cm}^{-2}$ ($E > 1 \text{ MeV}$) alloy 304.

Figures 5.29 through 5.32. are plots of strain and strain rate for each of the above tests. Strain and strain rate were calculated using rig compliance.

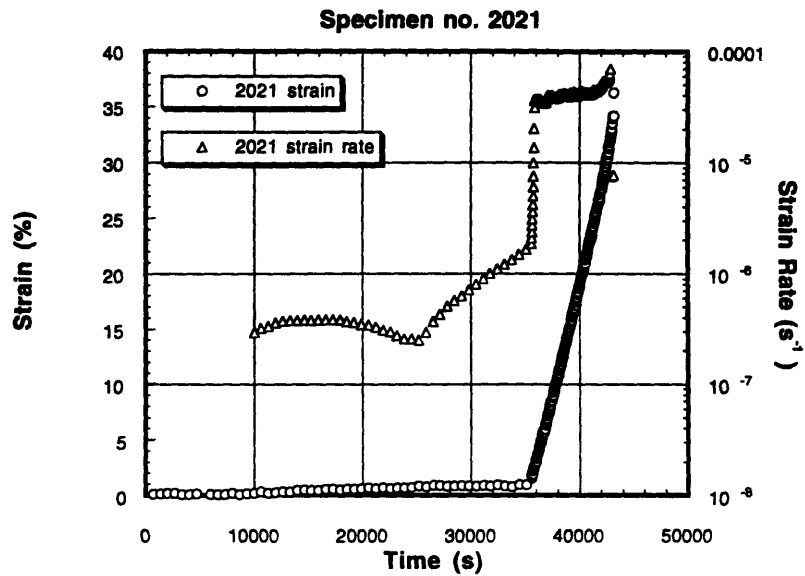


Figure 5.29. Strain and strain rate for testing of specimen 2021, non-irradiated alloy 347L.

The testing of specimen number 2021 was the shortest due to the high strain rate employed for the final portion of the test. The increase in loading machine extension rate from 0.0198 mm/hr to 1.98 mm/hr is clearly reflected in the strain rate as shown in Figure 5.29.

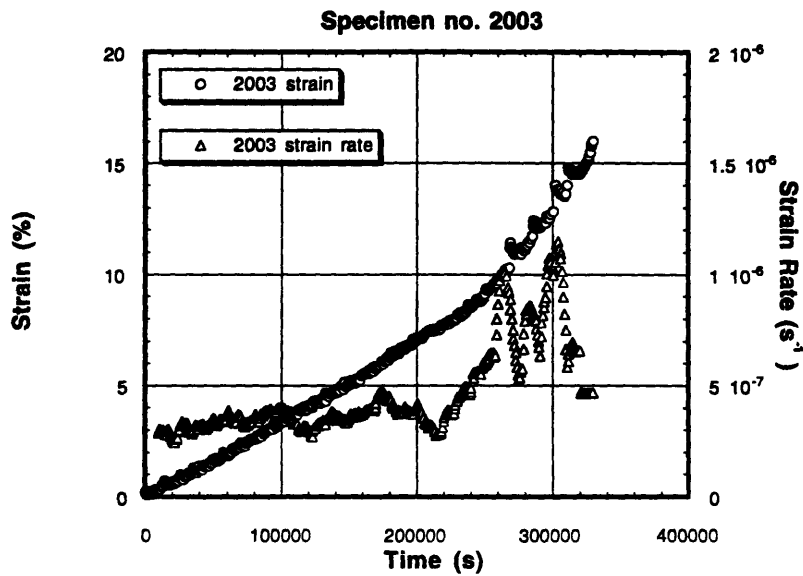


Figure 5.30. Strain and strain rate for in-core testing of specimen 2003, furnace sensitized alloy 304.

Testing of specimen 2003 is believed to be the first CERT test of an actively loaded tensile specimen positioned in the core of a critical nuclear reactor in high pressure, high temperature water. This test marked the initiation of in-core slow strain rate testing at the MIT Nuclear Reactor Laboratory. Strain rate was 3×10^{-7} to 4×10^{-7} through ultimate tensile stress. As specimen stress decreased the strain rate doubled. The large variations in strain rate near the end of testing resulted from specimen ratcheting.

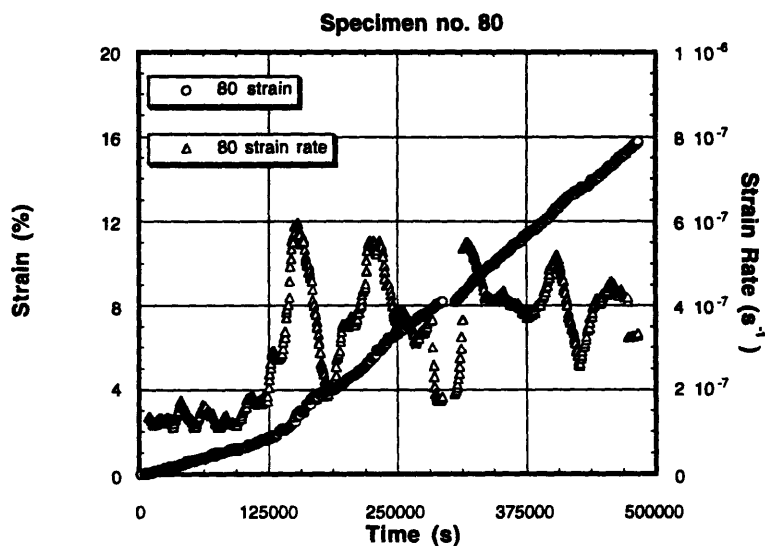


Figure 5.31. Strain and strain rate for in-core testing of specimen 80, alloy 304 irradiated to $0.8 \times 10^{21} \text{ cm}^{-2}$ ($E > 1 \text{ MeV}$).

Figure 5.31. illustrates the low constant strain rate associated with initial elastic loading of the specimen followed by a marked increase to a higher strain rate as the specimen hardens. The large deviations in strain rate that are observed after specimen yielding are due to the variations in stress which are shown in the stress vs. strain plot, Figure 5.28. Variations in stress, or specimen load, affect the extension of the rig and therefore specimen strain.

Strain and strain rate illustrated in Figure 5.32 are not smooth due to the many test pauses incurred while testing specimen number 82. While its stress vs. strain curve was smooth (Figure 5.28.), the strain rate used in testing specimen 82 was the least constant of all in-core tests carried out to this point of the testing program.

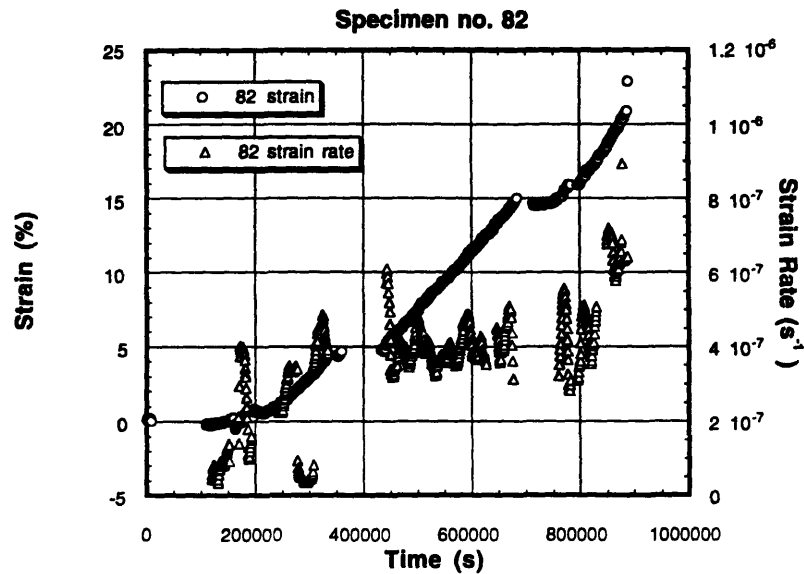


Figure 5.32. Strain and strain rate for in-core testing of specimen 82, alloy 304 irradiated to $0.8 \times 10^{21} \text{ cm}^{-2}$ ($E > 1 \text{ MeV}$).

Figures 5.33 through 5.73. are pictures taken during SEM analyses of the fractured specimens. Specimen 2003 is shown in Figures 5.33 through 5.46. The fracture surface of specimen 2003 was 97% intergranular and numerous large and small cracks were found on the specimen's sides. Specimen 80 is shown in Figures 5.47. through 5.57 and specimen 82 is shown in Figures 5.58 through 5.73. The fracture surface of specimen 80 was 3% intergranular, the fracture surface of specimen 80 was 9% intergranular. Intergranular and transgranular cracks and slip bands were found on both specimen's sides. Many of these cracks were seen to be blunted.

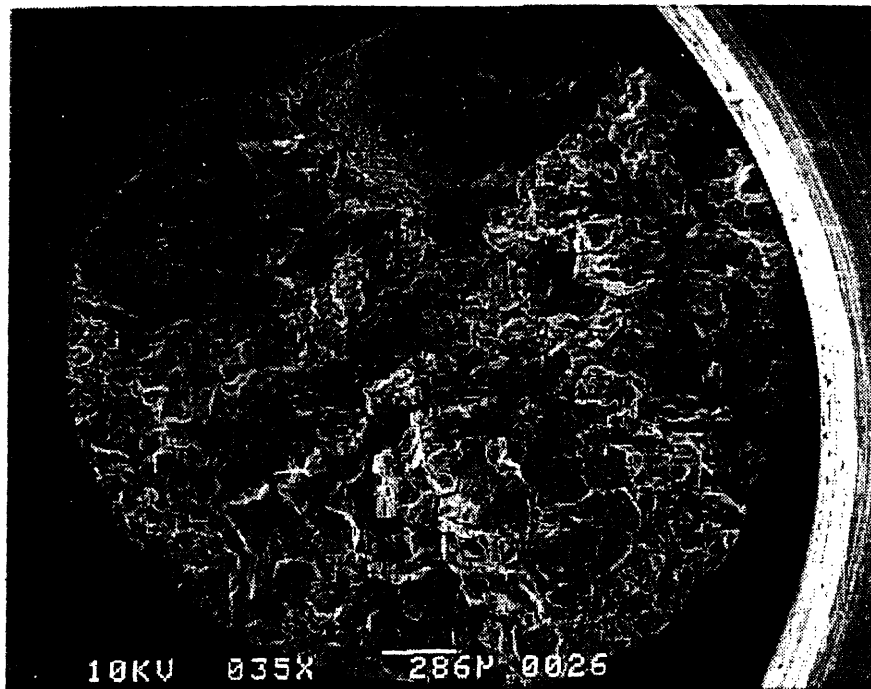


Figure 5.33. The fracture surface of specimen 2003, furnace sensitized alloy 304. 97% of the surface was intergranular. A small ductile region appears at the top of the picture.

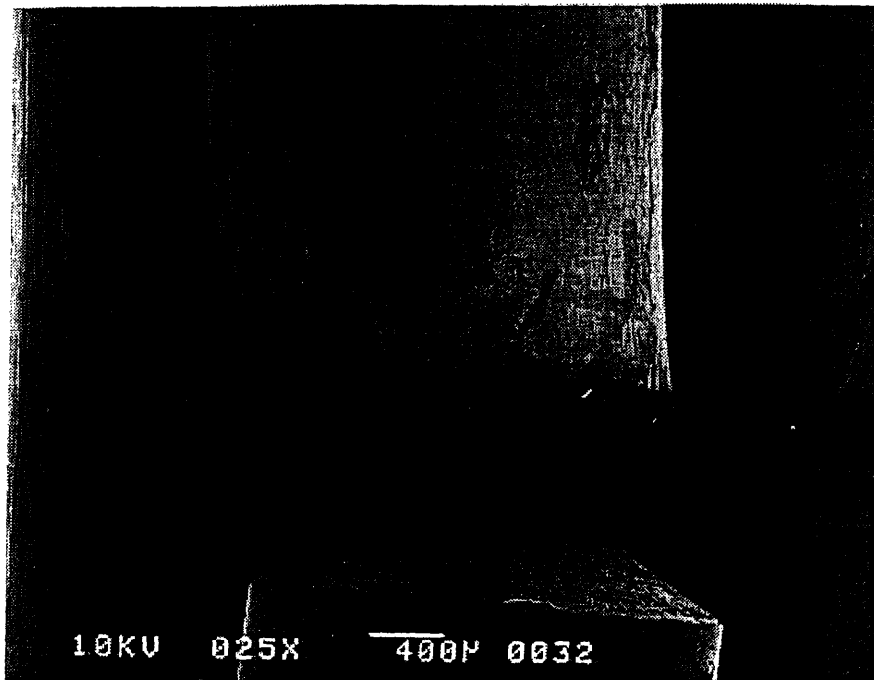


Figure 5.34. The side of specimen 2003, furnace sensitized alloy 304. The specimen's diameter is reduced by less than 5%. The cylindrical object in the lower part of the Figure is a drill blank used for diameter measurement calibration.



Figure 5.35. Ductile section of the fracture surface of specimen 2003, furnace sensitized alloy 304.

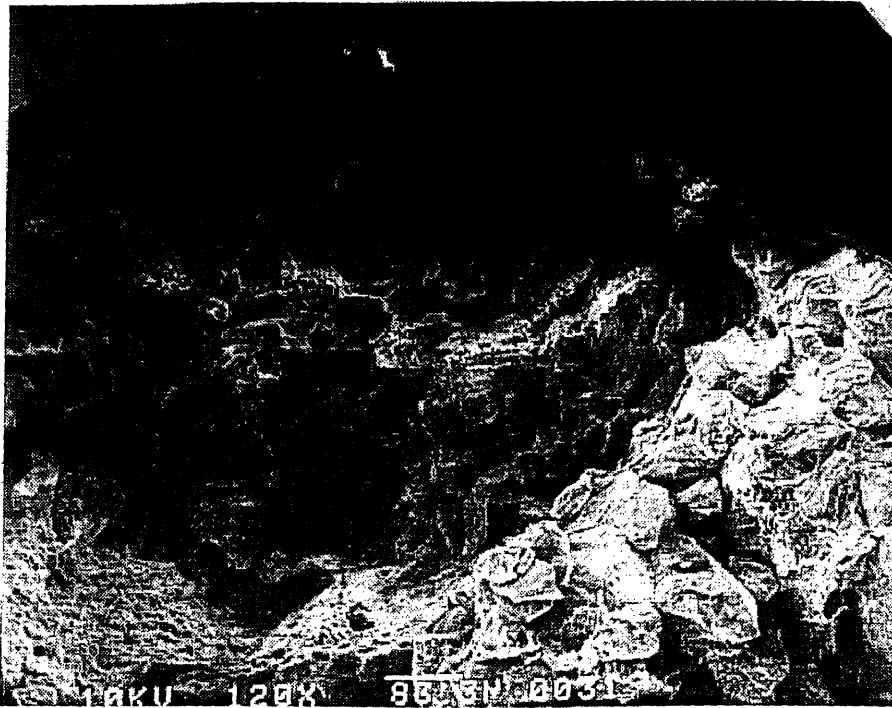


Figure 5.36. Magnified image of small ductile sites on the fracture surface of specimen 2003, furnace sensitized alloy 304.

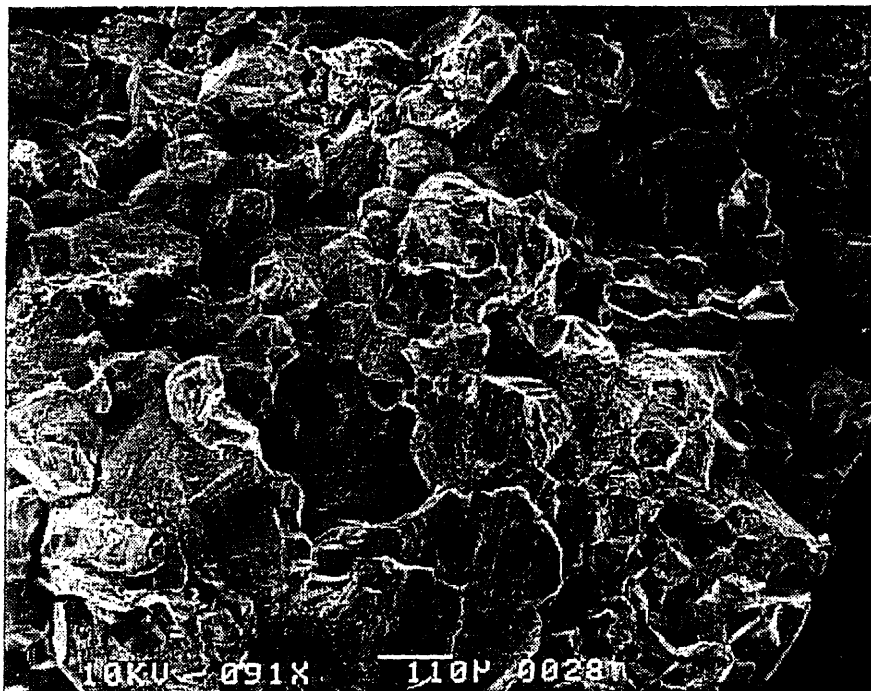


Figure 5.37. Intergranular fracture surface of specimen 2003, furnace sensitized alloy 304.

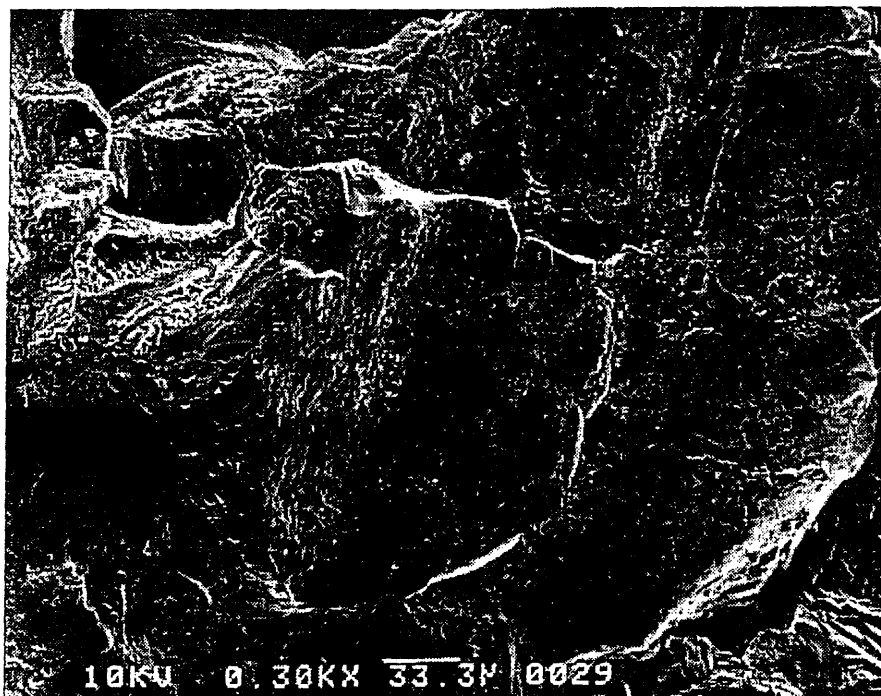


Figure 5.38. High magnification image of the intergranular fracture surface of specimen 2003, furnace sensitized alloy 304.

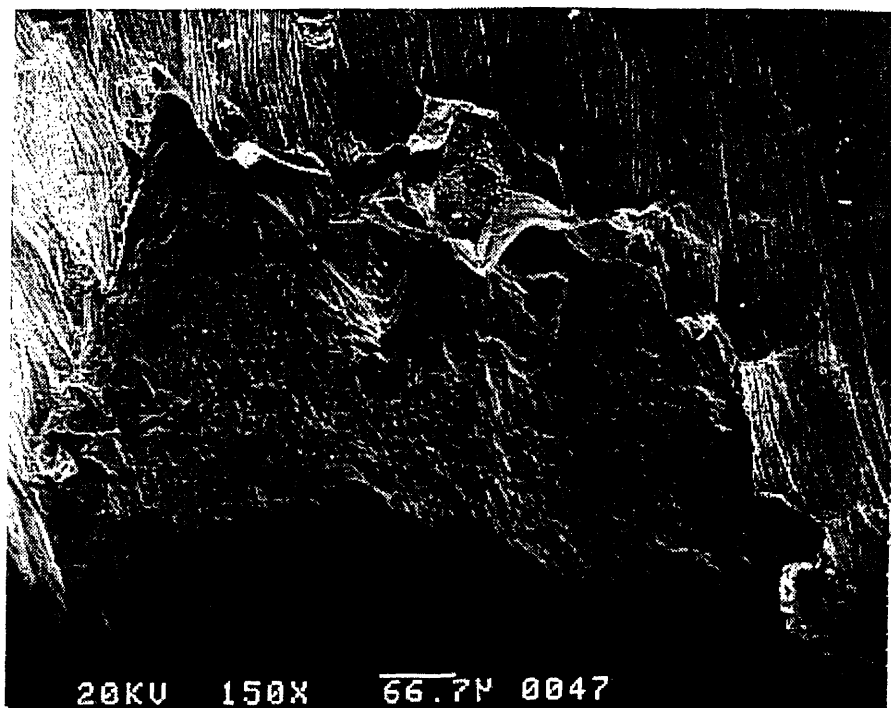


Figure 5.39. Side view of a shear ductile fracture surface on specimen 2003, furnace sensitized alloy 304.

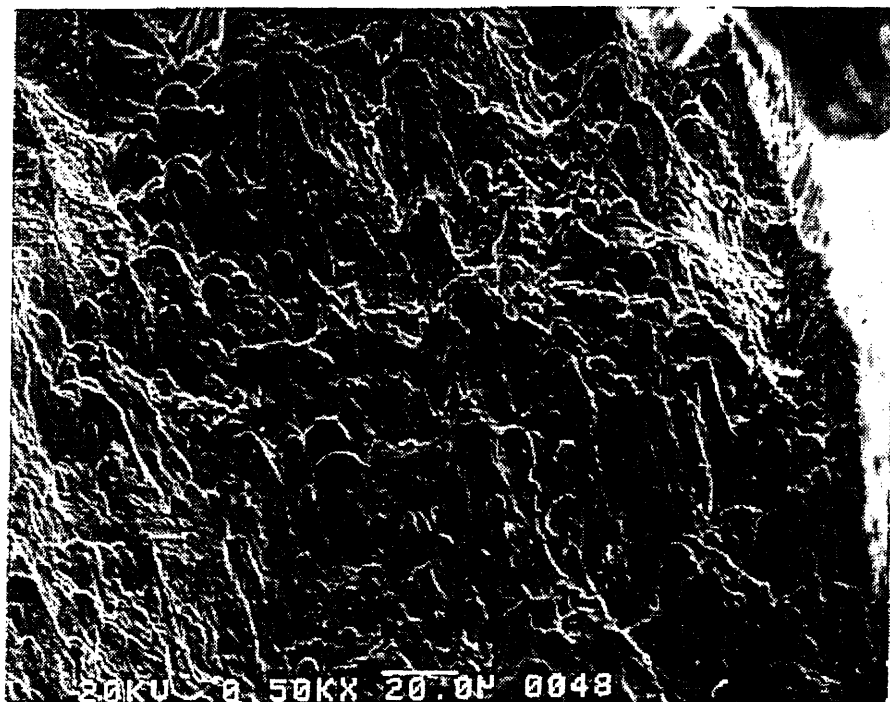


Figure 5.40. High magnification image of the shear ductile fracture surface shown above.

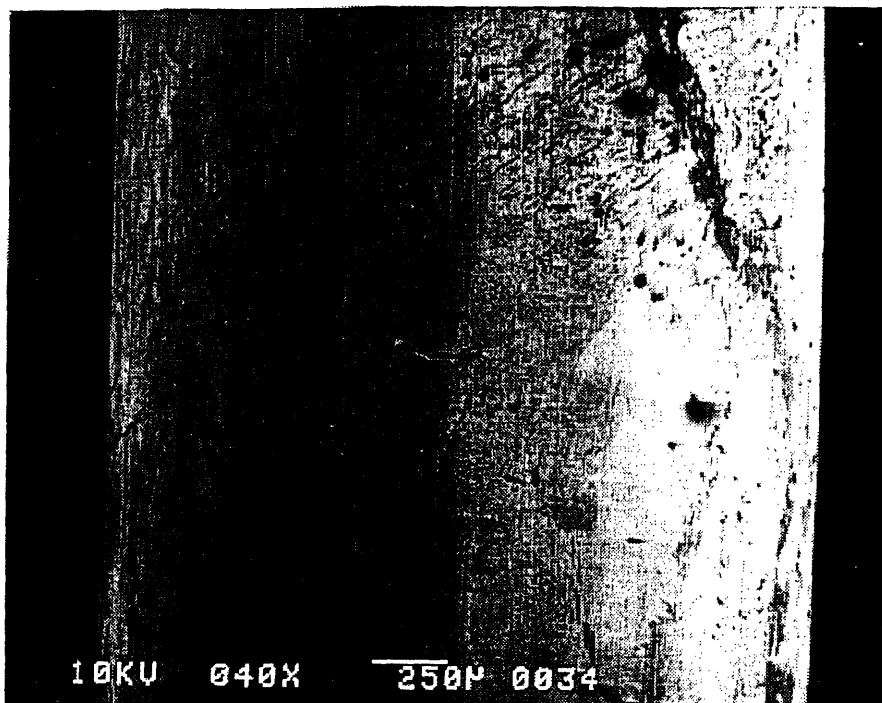


Figure 5.41. Side of specimen 2003, furnace sensitized alloy 304, away from the fracture surface. A small crack is seen in the center of the image.

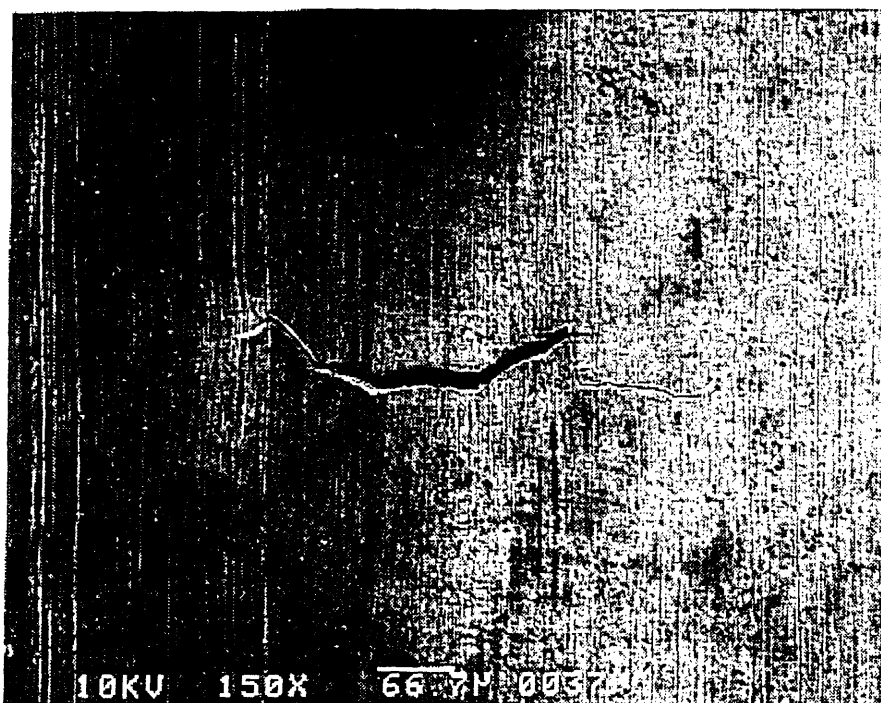


Figure 5.42. High magnification image of the crack illustrated in Figure 5.41.



Figure 5.43. Side of specimen 2003, furnace sensitized alloy 304, away from the fracture surface. Several cracks are seen.

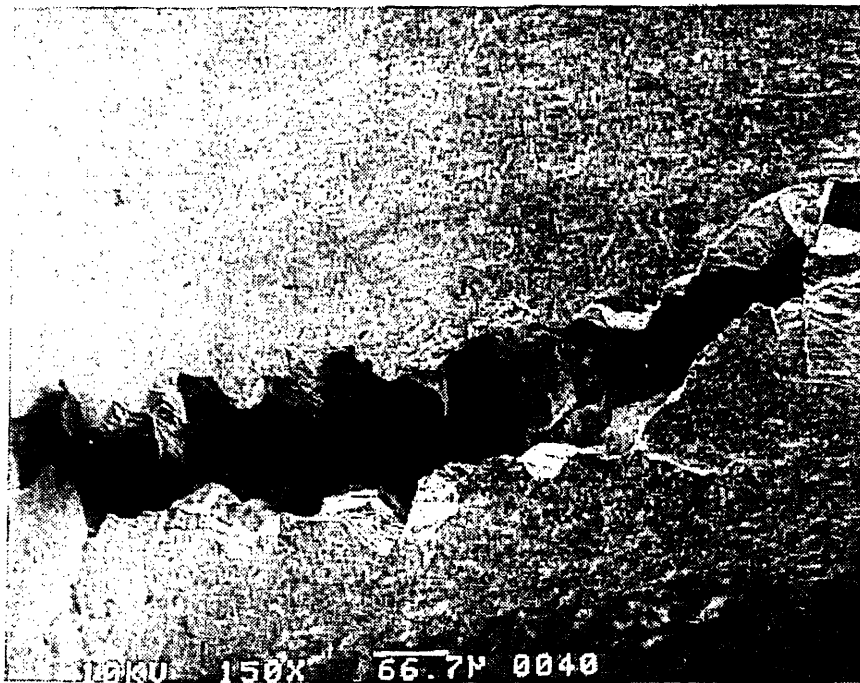


Figure 5.44. High magnification image of the large crack in upper left side of Figure 5.43.

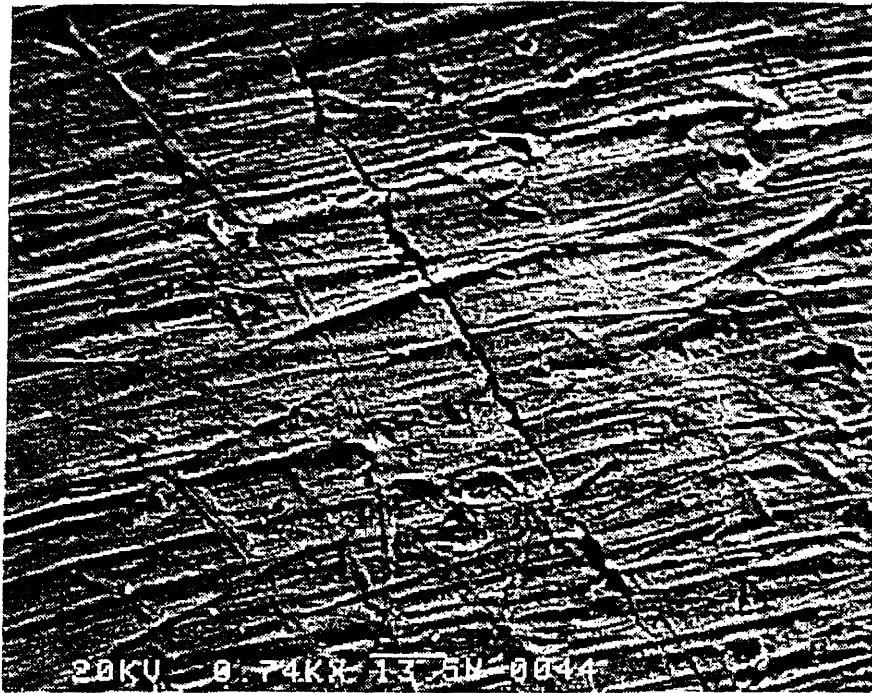


Figure 5.45. One of several small cracks found on the side of specimen 2003, furnace sensitized alloy 304, away from the fracture surface.



Figure 5.46. High magnification of a small crack found on the side of specimen 2003, furnace sensitized alloy 304, away from the fracture surface.



Figure 5.47. Fracture surface of specimen 80, alloy 304 irradiated to $0.8 \times 10^{21} \text{ cm}^{-2}$ ($E > 1 \text{ MeV}$). A small intergranular surface was found in the bottom edge of the fracture surface. The reduction in area was 65%.

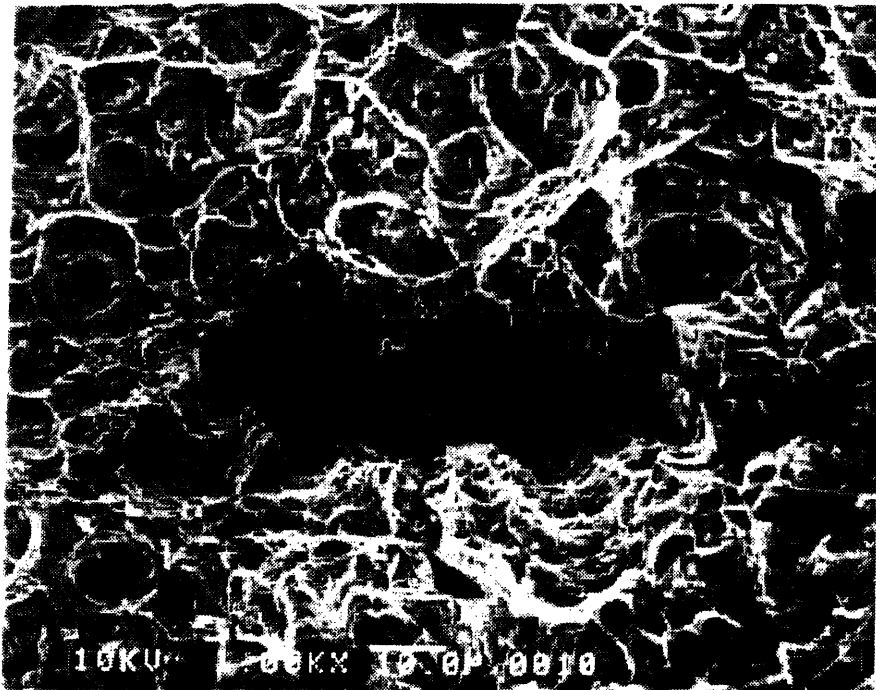


Figure 5.48. A higher magnification image of the ductile fracture surface of specimen 80, alloy 304 irradiated to $0.8 \times 10^{21} \text{ cm}^{-2}$ ($E > 1 \text{ MeV}$).



Figure 5.49. The top left quadrant of specimen 80's (alloy 304 irradiated to $0.8 \times 10^{21} \text{ cm}^{-2}$ ($E > 1 \text{ MeV}$)) fracture surface.



Figure 5.50. The bottom left quadrant of specimen 80's (alloy 304 irradiated to $0.8 \times 10^{21} \text{ cm}^{-2}$ ($E > 1 \text{ MeV}$)) fracture surface. The intergranular surface is seen in the bottom of the image.



Figure 5.51. The top right quadrant of specimen 80's (alloy 304 irradiated to $0.8 \times 10^{21} \text{ cm}^{-2}$ ($E > 1 \text{ MeV}$)) fracture surface.



Figure 5.52. The bottom right quadrant of specimen 80's (alloy 304 irradiated to $0.8 \times 10^{21} \text{ cm}^{-2}$ ($E > 1 \text{ MeV}$)) fracture surface.

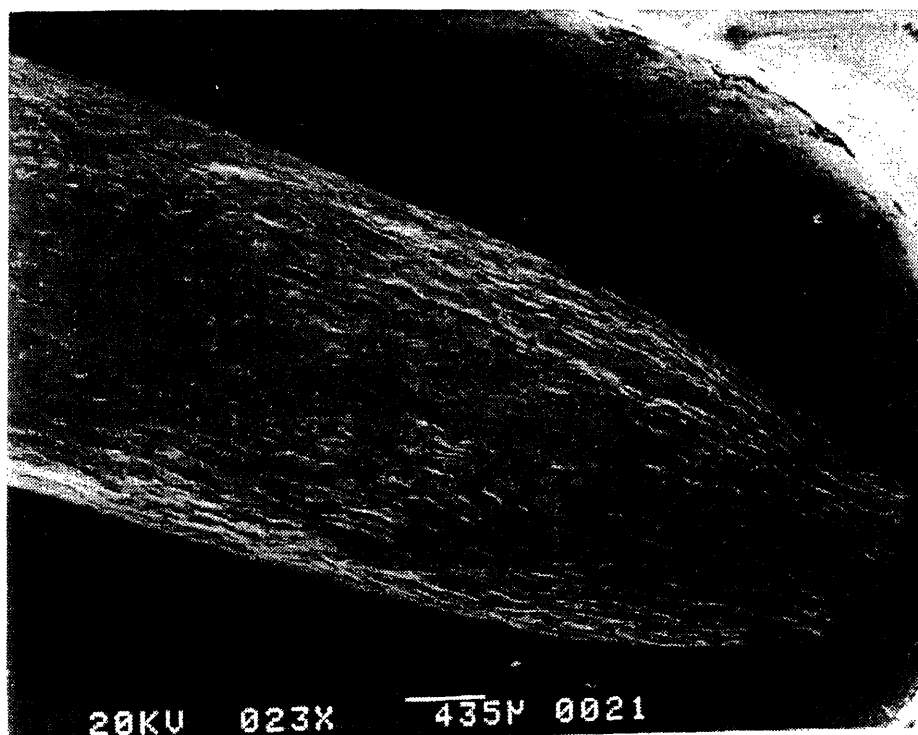


Figure 5.53. Side view of the fracture surface of specimen 80 (alloy 304 irradiated to $0.8 \times 10^{21} \text{ cm}^{-2}$ ($E > 1 \text{ MeV}$)).



Figure 5.54. Typical blunted cracks found on the side of specimen 80 (alloy 304 irradiated to $0.8 \times 10^{21} \text{ cm}^{-2}$ ($E > 1 \text{ MeV}$)) away from the fracture surface. The arrow indicates the tensile direction.



Figure 5.55. High magnification image of the blunted crack shown in Figure 5.52. Note the small cracks emanating from the corners of the blunted crack. The arrow indicates the tensile direction.



Figure 5.56. Image of side of specimen 80 (alloy 304 irradiated to $0.8 \times 10^{21} \text{ cm}^{-2}$ ($E > 1 \text{ MeV}$)) away from the fracture surface showing slip bands, and small intergranular, transgranular and blunted cracks. The arrow indicates the tensile direction.

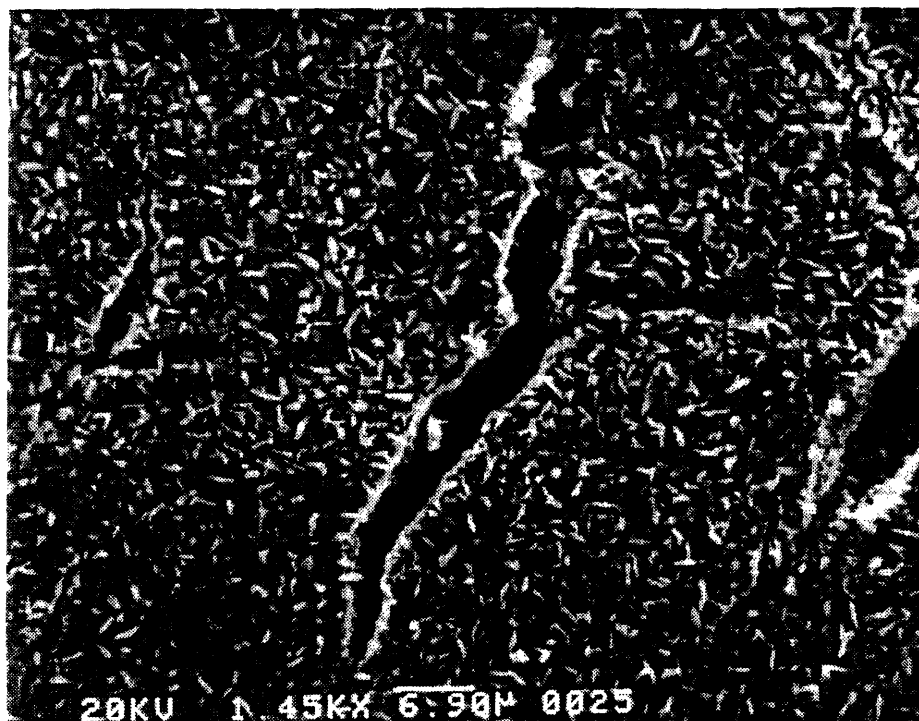


Figure 5.57. Magnified image of transgranular cracks on the side of specimen 80 (alloy 304 irradiated to $0.8 \times 10^{21} \text{ cm}^{-2}$ ($E > 1 \text{ MeV}$)). The arrow indicates the tensile direction.

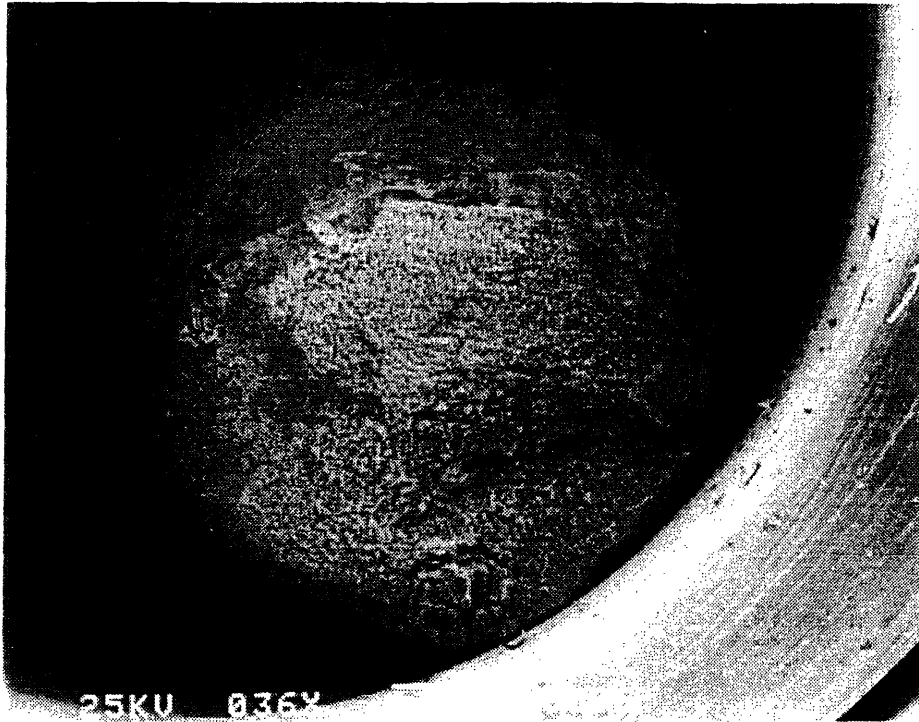


Figure 5.58. Fracture surface of specimen 82 (alloy 304 irradiated to $0.8 \times 10^{21} \text{ cm}^{-2}$ ($E > 1 \text{ MeV}$)). 9% of the fracture surface was found to be intergranular. The reduction in area was 60%.

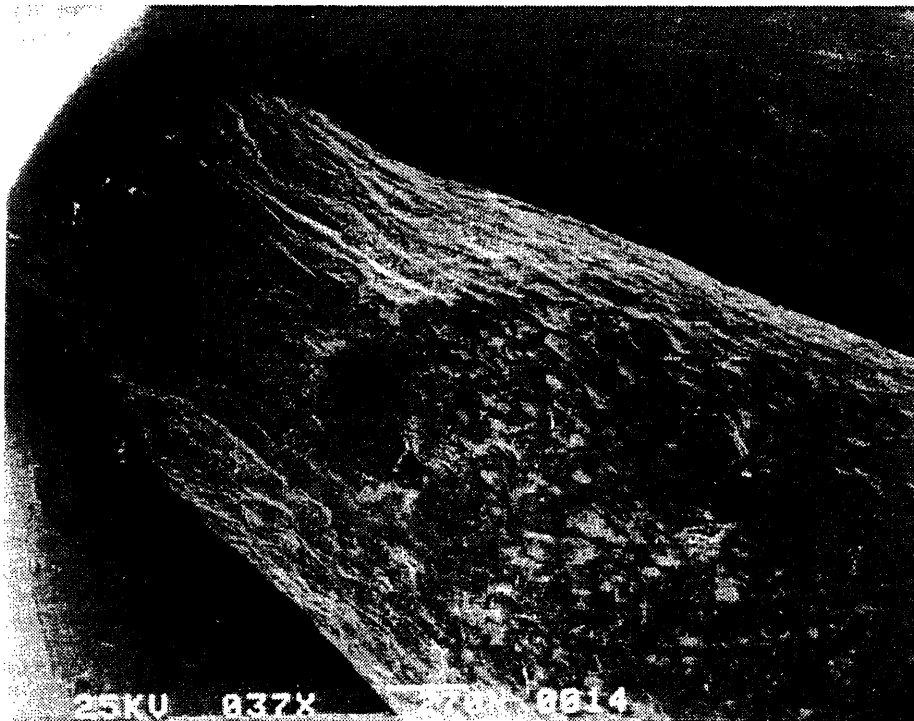


Figure 5.59. Side view of specimen 82's (alloy 304 irradiated to $0.8 \times 10^{21} \text{ cm}^{-2}$ ($E > 1 \text{ MeV}$)) fracture surface showing reduction in diameter and large blunted cracks.

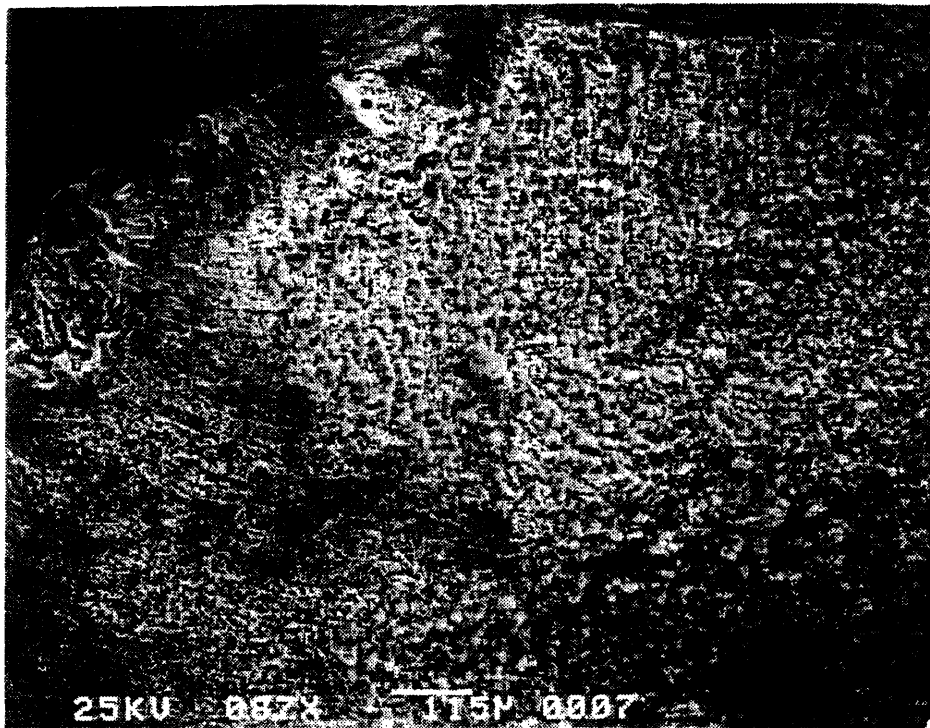


Figure 5.60. Top left quadrant of specimen 82's (alloy 304 irradiated to $0.8 \times 10^{21} \text{ cm}^{-2}$ ($E > 1 \text{ MeV}$)) fracture surface. Intergranular and transgranular surfaces are seen on the left side of this image.

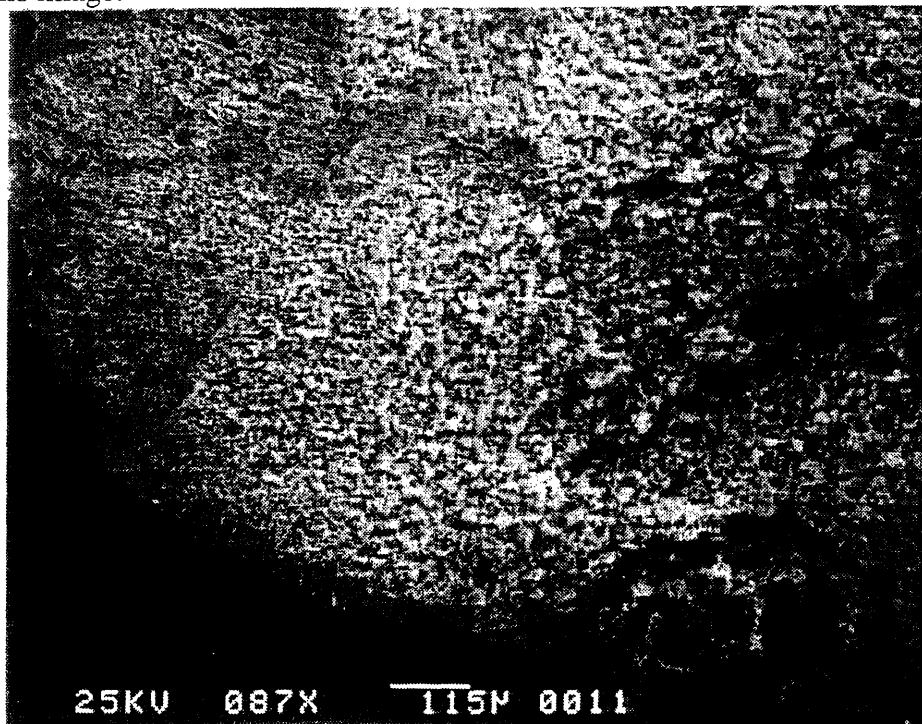


Figure 5.61. Bottom left quadrant of specimen 82's (alloy 304 irradiated to $0.8 \times 10^{21} \text{ cm}^{-2}$ ($E > 1 \text{ MeV}$)) fracture surface. An intergranular surface is seen at the bottom right corner of this image.

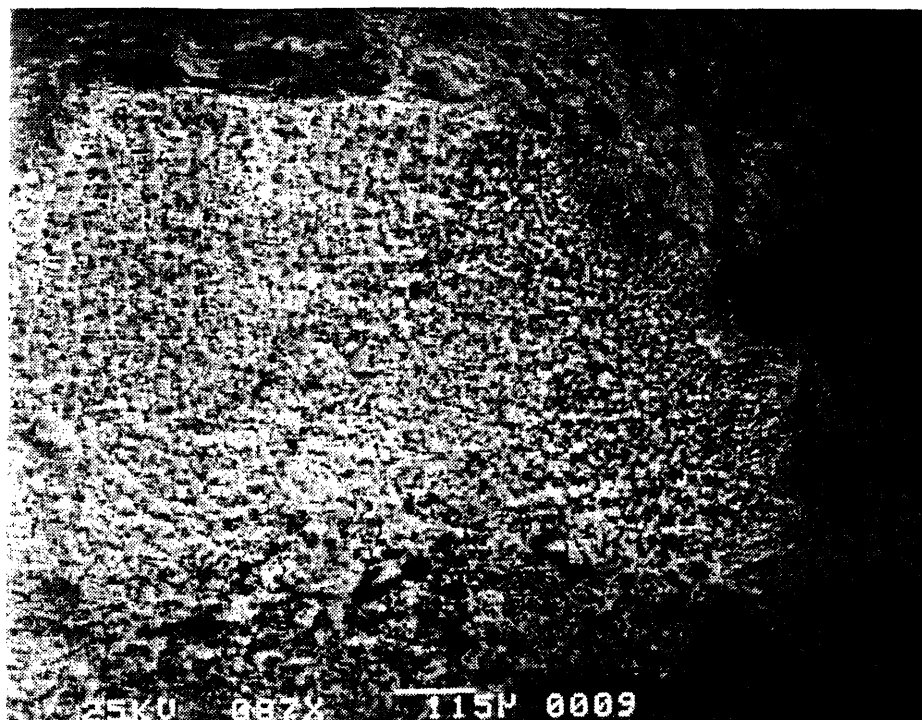


Figure 5.62. Top right quadrant of specimen 82's (alloy 304 irradiated to $0.8 \times 10^{21} \text{ cm}^{-2}$ ($E > 1 \text{ MeV}$)) fracture surface.



Figure 5.63 Bottom right quadrant of specimen 82's (alloy 304 irradiated to $0.8 \times 10^{21} \text{ cm}^{-2}$ ($E > 1 \text{ MeV}$)) fracture surface.

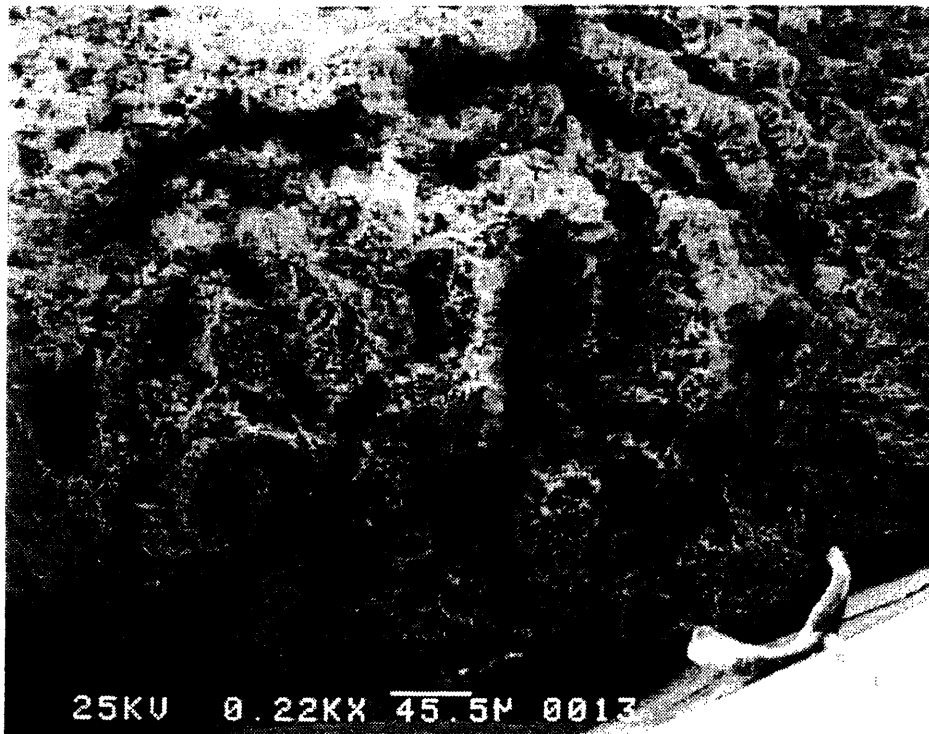


Figure 5.64. A magnified image of the intergranular surface seen in Figure 5.59.



Figure 5.65. Side view of the intergranular surface seen in Figure 5.62. Note the slip bands to the side of the intergranular surface, but no slip bands in line with the intergranular surface.

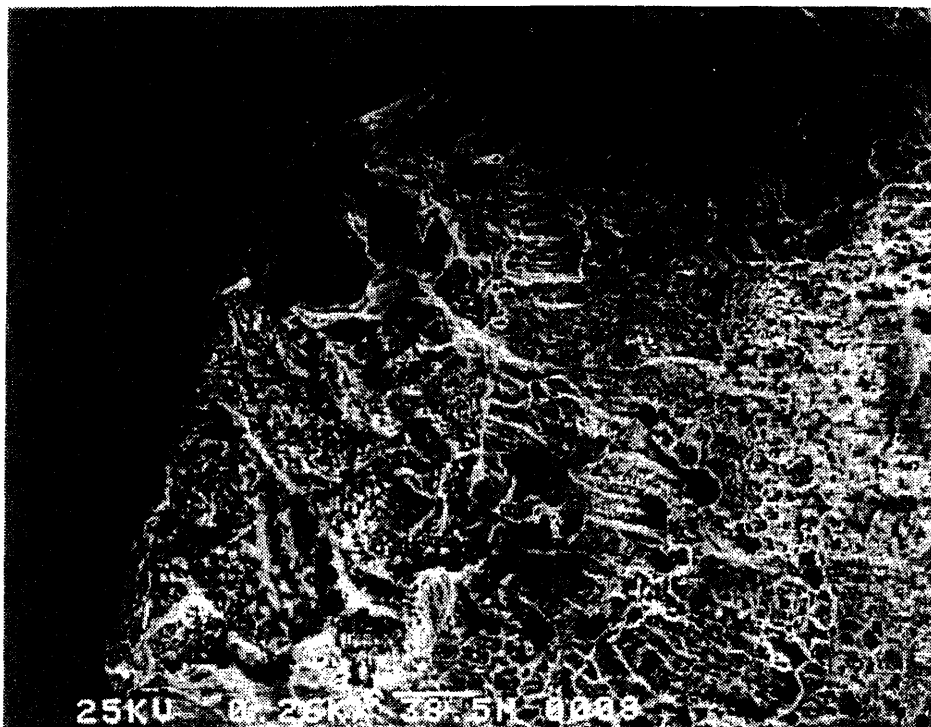


Figure 5.66. Magnified view of the intergranular surface seen in Figure 5.58. The intergranular surface becomes transgranular and finally ductile.

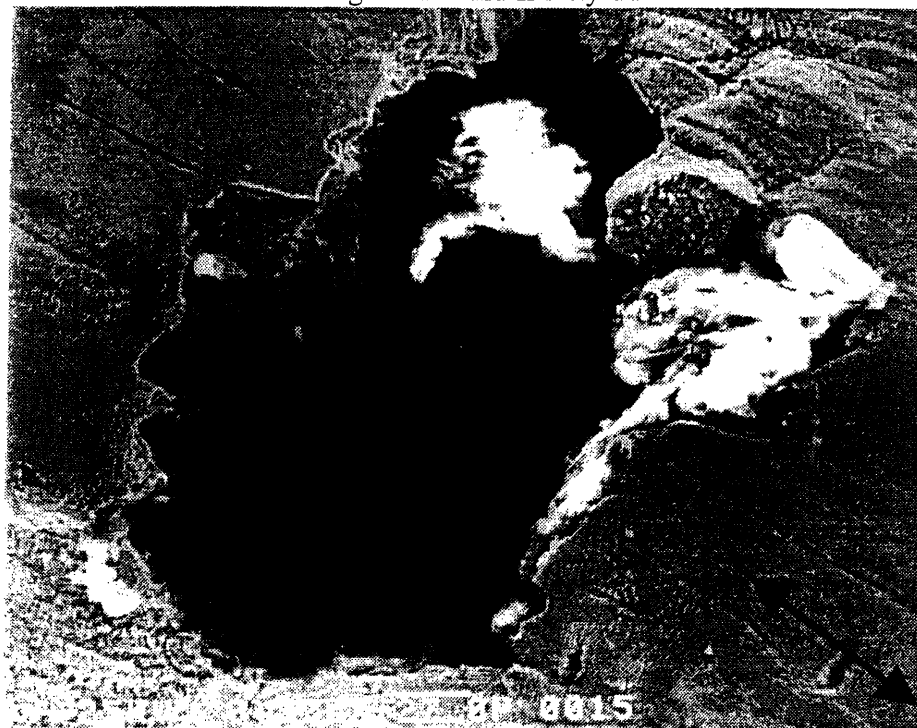


Figure 5.67. A large crack on the side of specimen 82 (alloy 304 irradiated to $0.8 \times 10^{21} \text{ cm}^{-2}$ ($E > 1 \text{ MeV}$)) which became blunted. This crack is seen in the lower right side of the specimen's side in Figure 5.57.



Figure 5.68. Cracks in the side of specimen 82 (alloy 304 irradiated to $0.8 \times 10^{21} \text{ cm}^{-2}$ ($E > 1 \text{ MeV}$)). The arrow indicates the tensile direction.



Figure 5.69. Intergranular, transgranular and blunted cracks on the side of specimen 80 (alloy 304 irradiated to $0.8 \times 10^{21} \text{ cm}^{-2}$ ($E > 1 \text{ MeV}$)). The arrow indicates the tensile direction.



Figure 5.70. Transgranular cracks emanating from the corner of a blunted crack of specimen 82 (alloy 304 irradiated to $0.8 \times 10^{21} \text{ cm}^{-2}$ ($E > 1 \text{ MeV}$)). The arrow indicates the tensile direction.



Figure 5.71. Cracks at what appears to be a grain triple point in specimen 82 (alloy 304 irradiated to $0.8 \times 10^{21} \text{ cm}^{-2}$ ($E > 1 \text{ MeV}$)). The arrow indicates the tensile direction.

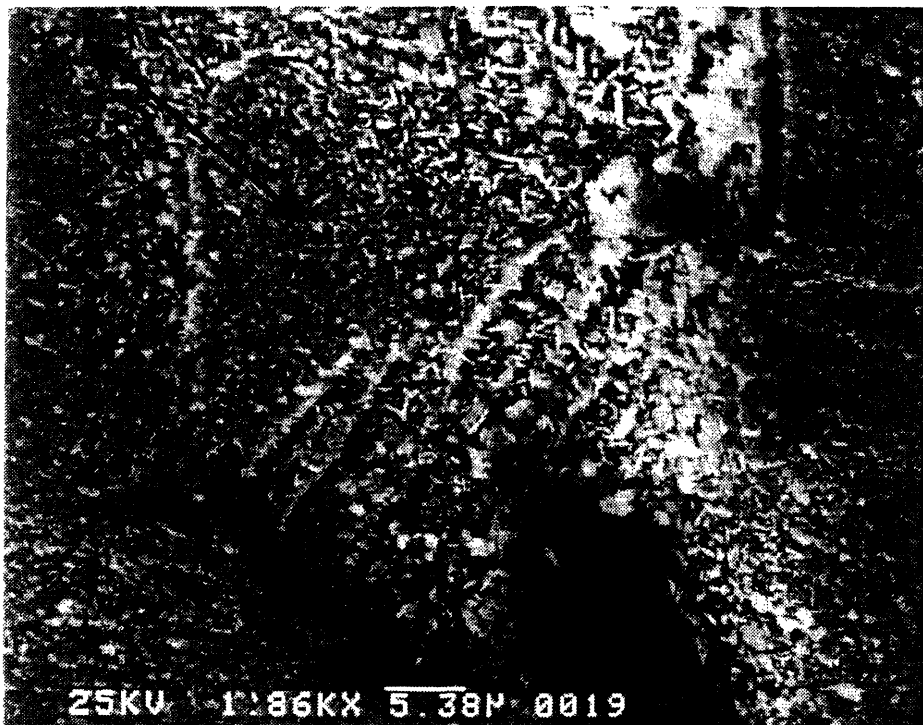


Figure 5.72. Transgranular cracks in the side of specimen 82 (alloy 304 irradiated to $0.8 \times 10^{21} \text{ cm}^{-2}$ ($E > 1 \text{ MeV}$)). The arrow indicates the tensile direction.

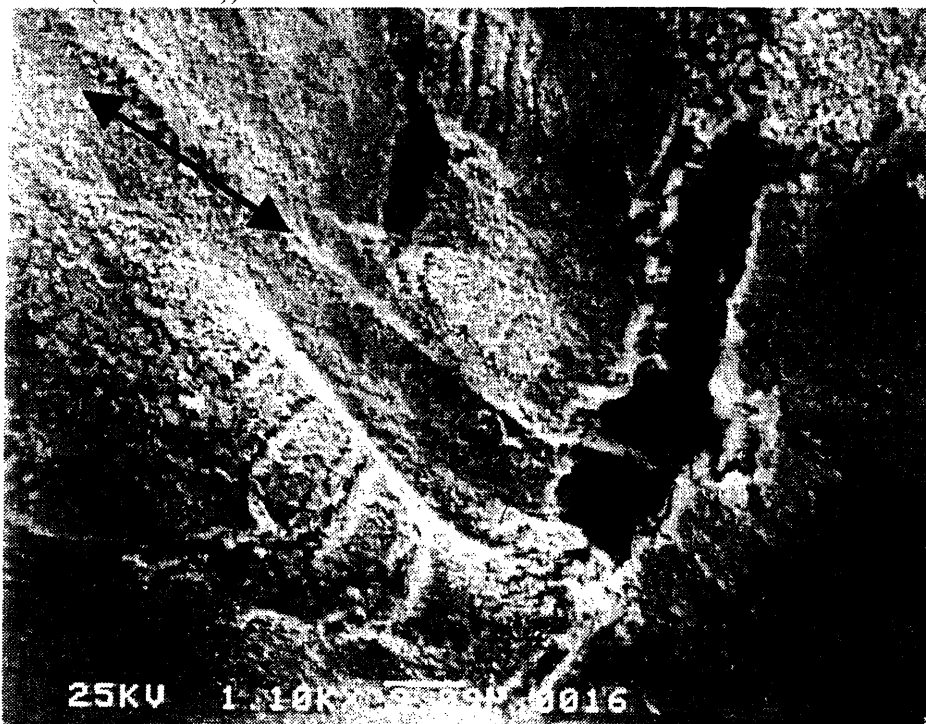


Figure 5.73. Cracks and blunted cracks in the side of specimen 82 (alloy 304 irradiated to $0.8 \times 10^{21} \text{ cm}^{-2}$ ($E > 1 \text{ MeV}$)). The arrow indicates the tensile direction.

5.3.4. Discussion

The main loop water chemistry was shown to be controllable within the desired limits. In-core ECP measurements (section 5.2.) showed how fast neutron and gamma radiation and measured exit water chemistry relate to in-core ECP. It was seen that for letdown water dissolved oxygen concentration greater than about 50 ppb, ECP of stainless steel in-core is greater than 0.000 VSHE for the reactor either at full power or shutdown. This was also seen to be monitorable by the in-core platinum electrode. During in-core ECP mapping the potential of platinum vs ground (which was stainless steel in electrical contact with titanium and therefore similar to that measured in the SSRT rig) while testing using NWC was -50 to -120 mV for the reactor at 4.5 MW and 0 to +70 mV for the reactor shutdown. The potentials on both the platinum and ground are mixed potentials and each change with respect to the SHE scale with reactor power. The potential of platinum with respect to SHE decreases by 10mV when the reactor power increases from zero to 4.5 MW which is much less than the increase in potential of stainless steel (70 mV). Because the positive terminal of the high impedance voltmeter is connected to platinum, an increase in stainless steel potential registers as a decrease in measured potential.

Loop exit water conductivity was higher than desired. Conductivity was intended to be less than 0.2 $\mu\text{S}/\text{cm}$, the lowest conductivity reached during in-core SSRT testing was 0.6 $\mu\text{S}/\text{cm}$. Lower water conductivities (about 0.05 $\mu\text{S}/\text{cm}$ lower) were seen during periods when the reactor was shutdown, but conductivity returned to higher values when the reactor returned to power operation. The cause for this is not clear. On-line HPLC shows a proportional increase in all measurable species (Cl^- , SO_4^{2-} , NO_3^- and CrO_4^{2-}) during the conductivity transient, but the conductivity imparted to the water by these constituents for the concentrations measured is less than the total water conductivity. Increasing the charging rate had no effect on conductivity. Increasing the loop water

volume replenishment rate should decrease the loop exit conductivity if the conductivity source were within the high pressure volume of the water system. Moreover, conductivity was noted to decrease during periods when the facility was operated at HWC (after specimen fracture, but before reactor shutdown), transition metal ions and CrO_4^{2-} and HCrO_4^- were suspected at first. Inductively coupled plasma atomic emission spectroscopy (ICP-AES) analysis of loop exit water samples, however, showed that Fe, Cr and Ni concentrations were all less than 5 ppb and thus not sufficient for the observed conductivities.

Organic contamination is presently considered to be the most likely cause for the higher than desired loop exit water conductivity. Organic species become oxidized in high temperature water to carbonic acid and other ionic species. This would explain why loop exit water conductivity decreases when the aqueous environment is changed from an oxidizing one (NWC) to a reducing one (HWC). It would also explain why increasing the charging rate had no effect since the source of organic contaminants could be the demineralizers, or tubing and tanks used in the low pressure water systems. This being the case, increasing the charging rate would increase the rate at which organics, or contaminants, were added to the main loop. Increasing the charging rate does not, however, increase the loop exit water conductivity. This could be due to the organic oxidation reaction rate being saturated for the existing environmental condition. Radiation from the nuclear reactor would increase the oxidation rate of organic contaminants. This could explain the change in conductivity with reactor power. An ultra-violet sterilizer is used in the facility's clean-up system upstream of the ion exchanger.

Ionic species of organic origin mostly take the form of carbonate. In general, increasing water conductivity increases material cracking susceptibility. However, the impacts on material cracking caused by increased Cl^- and SO_4^{2-} concentrations are

significantly higher than those due to increased concentrations of other ionic species including carbonates. This is reflected in the BWR water chemistry guidelines which now lists action levels for Cl^- and SO_4^{2-} concentrations in addition to conductivity. The concentration of both Cl^- and SO_4^{2-} in loop exit water during in-core tensile testing was less than action level 2 [12].

Efforts are presently underway to verify that organic contamination is the source of the higher than desired loop exit water conductivity, and in lowering the total oxidizable carbon (TOC) to levels which result in little increase in conductivity. A new ion exchange resin has been received and is ready for implementation. This resin is designed specifically to reduce organic contamination without reduction in purification capability.

Figures 5.28. through 5.32. show that the facility can produce and reproduce the desired mechanical loading conditions. Strain rates less than $4 \times 10^{-7} \text{s}^{-1}$ are present during initial elastic loading of the specimen. The typical strain rate during elastic loading is 1×10^{-7} to $2 \times 10^{-7} \text{s}^{-1}$ and is acceptable. The only detriment of using this slow strain rate during initial specimen loading is the time required to reach yield and subsequently the end of test. Initial loading extended the testing of specimens 80 and 82 by 36 hours. This time could have been reduced by increasing the load placed on the specimen prior to initiation of the test, or controlling the strain rate by manual adjustment of cross head displacement rate during elastic loading. If it becomes required to expedite the testing of specimens one or both of these methods could be easily employed. Strain rates up to $1 \times 10^{-6} \text{s}^{-1}$ are acceptable, and therefore the increase in specimen strain rate for strains higher than the ultimate tensile stress (UTS) is also not problematic.

Specimen 2003 was shown to be highly susceptible to intergranular SCC (IGSCC) by the high percentage of the fracture surface being intergranular (97%) and additional large and small cracks found on the specimen side away from the fracture surface. The

large cracks were shown to be intergranular. This is in good agreement with the results of the double loop EPR test performed on a cut off piece of the specimen following the sensitization heat treatment. The measured EPR ratio was 16.5%. Double loop EPR testing is used in non-destructive evaluation of a material to determine the extent to which it is sensitized to IGSCC. Materials with EPR ratios greater than 6 are generally considered sensitized.

SSRT testing of a thermally sensitized specimen was used to verify that the facility would be able to reproduce an intergranular fracture surface on a material specimen known to be susceptible to intergranular cracking. Requirements for IGSCC SSRT testing are similar to the requirements for IASCC testing. Both are cracking phenomena known to occur in the high water temperature oxidizing environment that is present in the in-core and recirculation systems of a BWR operating under NWC. More is known about IGSCC than IASCC, however. Austenitic stainless steels become susceptible to IGSCC through a thermal treatment at 550°C to 850°C for a given period of time. At these temperatures metal carbides rich in chromium nucleate and grow along grain boundaries which reduces the chromium concentration in the metal along the grain boundary. RIS resulting in grain boundary chromium depletion is expected to play a significant role in metallurgical aspects of IASCC susceptibility. IGSCC SSRT testing utilizes strain rates similar to those used for IASCC SSRT testing. Strain rates used for the testing of IGSCC susceptibility can be as high as $2 \times 10^{-6} \text{ s}^{-1}$, however, strain rates used for IASCC SSRT testing do not normally exceed $5 \times 10^{-7} \text{ s}^{-1}$.

Trace intergranular cracking was found on the fracture surface of the pre-irradiated specimens (3% for specimen 80 and 9% for specimen 82). These specimens were irradiated to a fluence of $0.8 \times 10^{21} \text{ cm}^{-2}$ ($E > 1 \text{ MeV}$) which is within a fluence range where intergranular cracking is not always seen. A review of applicable literature indicates that these specimens could be expected to show between 0% and 40% IGSCC

on the fracture surface. Jacobs finds a fluence threshold of about $0.5 \times 10^{21} \text{cm}^{-2}$ for IASCC susceptibility [9], but Kodama finds a fluence threshold of about $2 \times 10^{21} \text{cm}^{-2}$ [10]. Bruemmer correlates the onset of IASCC susceptibility with yield stress rather than a threshold fluence, with IASCC susceptibility beginning at a yield stress of 400 to 600 MPa [11]. Specimens 80 and 82 had yield stresses of 500 MPa each, again placing them in the center of the threshold region.

The intergranular part of specimen 80's fracture surface shown in Figure 5.64 and the bottom of Figure 5.58 can be shown to have existed before the specimen necked significantly. Note in Figure 5.58 that little reduction in area occurred around the intergranular surface. Moreover, in Figure 5.65 the area beneath the intergranular surface is free of slip bands implying that limited strain occurred in that area.

Cracks and slip bands such as those seen in Figures 5.56 and 5.65. were seen during SEM analyses conducted on the sides of the specimen. These were not seen during a similar examination of the thermally sensitized specimen, number 2003. Slip bands in irradiated austenitic stainless steels have been seen before. Bruemmer explains that these result from dislocation channeling [11]. Figure 5.57. shows parallel cracks that appear to result from slip bands and cross slip caused by dislocation channeling.

Figures 5.56, 5.57, 5.70, 5.71, 5.72, and 5.73 show closely spaced small cracks and slip bands aligned normal to the stressed direction. These cracks and slip bands were spaced about 1 to 20 μm apart and appeared to be either transgranular or intergranular. From the numerous cracks on the sides of the specimen it is clear that crack initiation occurs readily, but because of the small fraction of IGSCC fracture surface and evidence of blunted cracks, it is concluded crack propagation beyond a critical size proceeds with difficulty.

There is evidence of both transgranular and intergranular cracks on the side of the specimen remote from the fracture surface. These are competing modes. In materials exposed to a higher fast neutron fluence or strained at a lower strain rate intergranular fracture could become increasingly prominent. In addition, dislocation channeling may be easier in materials under a fast neutron flux due to the presence of high concentrations of vacancies and interstitials. Further investigations of these aspects are required.

5.4. References

- [1] Boerigter, S. T., "An Investigation of Neutron-Irradiation Induced Segregation in Austenitic Stainless Steels", Sc.D. Thesis, MIT, Cambridge, MA, 1992.
- [2] Vergara Aimone, J. A., "The Development of a Facility for the Evaluation of Environmentally Assisted Cracking of In-Core Structural Materials in Light Water Reactors", Ph.D. Thesis, MIT, Cambridge, MA, 1992.
- [3] Indig, M. E., Nelson, J. L., Corrosion, Vol. 47, pg. 202-209, 1991.
- [4] NWT Corporation, Corrosion Potential Measurement Source Book, EPRI NP-7142, Electric Power Research Institute, Palo Alto, CA, 1991.
- [5] Bertuch, A., Macdonald, D. D., Pang, J., Kriksunov, L., Arioka, K., "Modeling the Corrosion Behavior of the Heat Transport Circuits of Light Water Nuclear Reactors", in the Proceedings of the Sixth International Symposium on Environmental Degradation of Materials in Nuclear Power Systems, ANS, San Diego, CA, August, 1993.
- [6] Indig, M. E., Goldstein, J. S., Jarvis, A. J., Pathania, R., "Electrochemical Response to Hydrogen Water Chemistry at the J. A. Fitzpatrick BWR", in the Proceedings of the Sixth International Symposium on Environmental Degradation of Materials in Nuclear Power Systems, ANS, San Diego, CA, August, 1993.
- [7] Indig, M. E., GE. Co., Vallecitos Nuclear Center, Pleasanton, CA, personal communication.
- [8] Lin, C. C., and Smith, F. R., Electrochemical Potential Measurements Under Simulated BWR Chemistry Conditions, EPRI NP-6732, Electric Power Research Institute, Palo Alto, CA, 1990.

- [9] Jacobs, A. J., Hale, D. A., and Siegler, M., Unpublished Data, GE Nuclear Energy, San Jose, CA, January, 1986.
- [10] Kodama, M., Nishimura, S., Morisawa, J., Suzuki, S., Shima, S., and Yamamoto, M., "Effects of Fluence and Dissolved Oxygen on IASCC on Austenitic Stainless Steel", in the Proceedings of the Fifth International Symposium on Environmental Degradation of Materials in Nuclear Power Systems, ANS, Monterey, CA, August, 1991.
- [11] Bruemmer, S. M., Cole, J. I., Brimhall, J. L., Carter, R. D., and Was, G. S., "Radiation Hardening Effects on Localized Deformation and Stress Corrosion Cracking of Stainless Steels", in the Proceedings of the Sixth International Symposium on Environmental Degradation of Materials in Nuclear Power Systems, ANS, San Diego, CA, August, 1993.
- [12] Wood, C. J., ed. BWR Water Chemistry Guidelines-1993 Revision, Normal and Hydrogen Water Chemistry, EPRI TR-103515, Electric Power Research Institute, Palo Alto, CA, 1994.

6. CONCLUSIONS

A comprehensive understanding of irradiation effects on IASCC susceptibility is required for the continued safe and economical operation of light water power reactors. The unique in-core slow strain rate testing facility described in this thesis can contribute to this understanding by providing data which is not otherwise obtainable. The facility positions a mechanical property test specimen in the center of the MIT nuclear reactor core and can be used to test material specimens in an environment very similar to the environment present in the in-core sections of commercial nuclear power reactors. Measurements have been made on the effects of fast neutron and gamma fluxes on stainless steel ECP in the in-core facility. In-core tensile tests have begun. Forthcoming results will be used to benchmark an IASCC sensitivity model.

6.1. Conclusions from In-Core ECP Measurements

In-core ECP measurements have been made before. Previous tests have placed radiation qualified electrodes, similar to the ones used in this experiment, in local power range monitor (LPRM) tubes in BWR's. In-core ECP measurements discussed in this paper consist of the first attempts made to study in-core stainless steel ECP with the ability to vary parameters such as fast neutron and gamma radiation (by varying reactor power and electrode position), temperature, flow rate and chemistry. These tests were performed for two reasons. The first was to learn the effects of varying parameters on stainless steel ECP in the in-core sections of the facility. This was important because the ability to monitor and control the ECP of the stainless steel specimen during SSRT testing was required. Testing also provided information which can be used to benchmark radiolysis and ECP models. These models can be valuable to the nuclear power industry, however, verifying these models is a difficult task. This testing facility provides a testing platform which is easier to model than large, complex BWR commercial nuclear reactors.

Conclusions from in-core ECP mapping are as follows:

- 1) Stainless steel ECP in the position of the SSRT specimen is measured to be 150 mVSHE with the reactor operating at 4.5 MW, and 130 mVSHE with the reactor shutdown. These values are repeatable when loop exit water dissolved oxygen concentration is between 100 and 500 ppb. The letdown reference autoclave also provides indication that the main loop environment is sufficiently oxidizing. The ECP of stainless steel measured in the reference autoclave is always less than the ECP of stainless steel in the center of the reactor core where the SSRT specimen is located.
- 2) One of the radiation qualified Ag/AgCl electrodes did not accurately measure ECPs during HWC operations with the reactor operating at power. ECP measurements were accurate when operating in NWC and when operating in HWC with the reactor shutdown. The ECP measured by the platinum electrodes were consistent during HWC operations.
- 3) Hydrogen in excess of 100 ppb reduces the ECP of stainless steel throughout the facility below -230 mVSHE, the threshold ECP for IGSCC and possibly IASCC.
- 4) During NWC operation the potential measured between the in-core platinum electrode and ground corresponding to stainless steel ECP of 150 mVSHE with the reactor operating a 4.5 MW was -70mV.

6.2. Conclusions from In-Core SSRT Testing

The present work has shown that the facility is capable of loading a mechanical property test specimen in tension in the MIT nuclear reactor core using a slow constant extension rate in environmental conditions similar to those present in in-core commercial BWR reactors. It has been able to reproduce the target oxidizing environment in four consecutive in-core tests. It has caused a thermally sensitized specimen to fail by 97%

IGSCC as verified by SEM analysis. Two irradiated specimens were tested in-core. Both specimens displayed a small percentage IGSCC fracture surface which is expected due to the fast neutron fluence to which it was exposed. Both specimens displayed slip bands, and transgranular, intergranular and blunted cracks on their sides remote from the fracture surface. The slip bands are the result of a deformation mechanism seen only in irradiated materials, dislocation channeling. These slip bands appear to provide crack initiation sites for both intergranular and transgranular cracks. Crack propagation by this mechanism may also be possible. From the numerous cracks on the sides of the specimen it is clear that crack initiation occurs readily, but because of the small fraction of IGSCC fracture surface and evidence of blunted cracks, it is concluded that crack propagation beyond a critical size proceeds with difficulty.

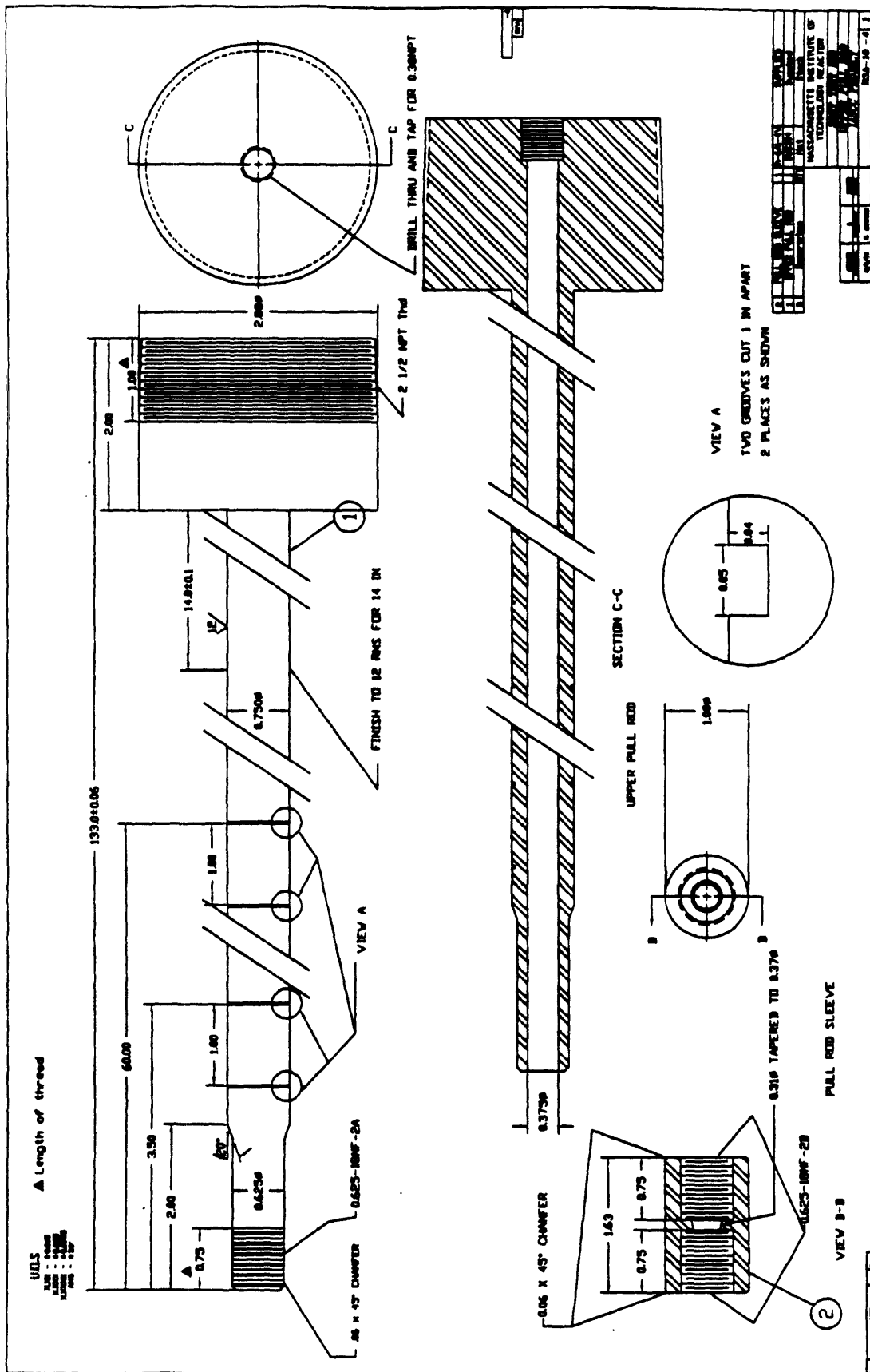
6.3. Recommendations for Future Work

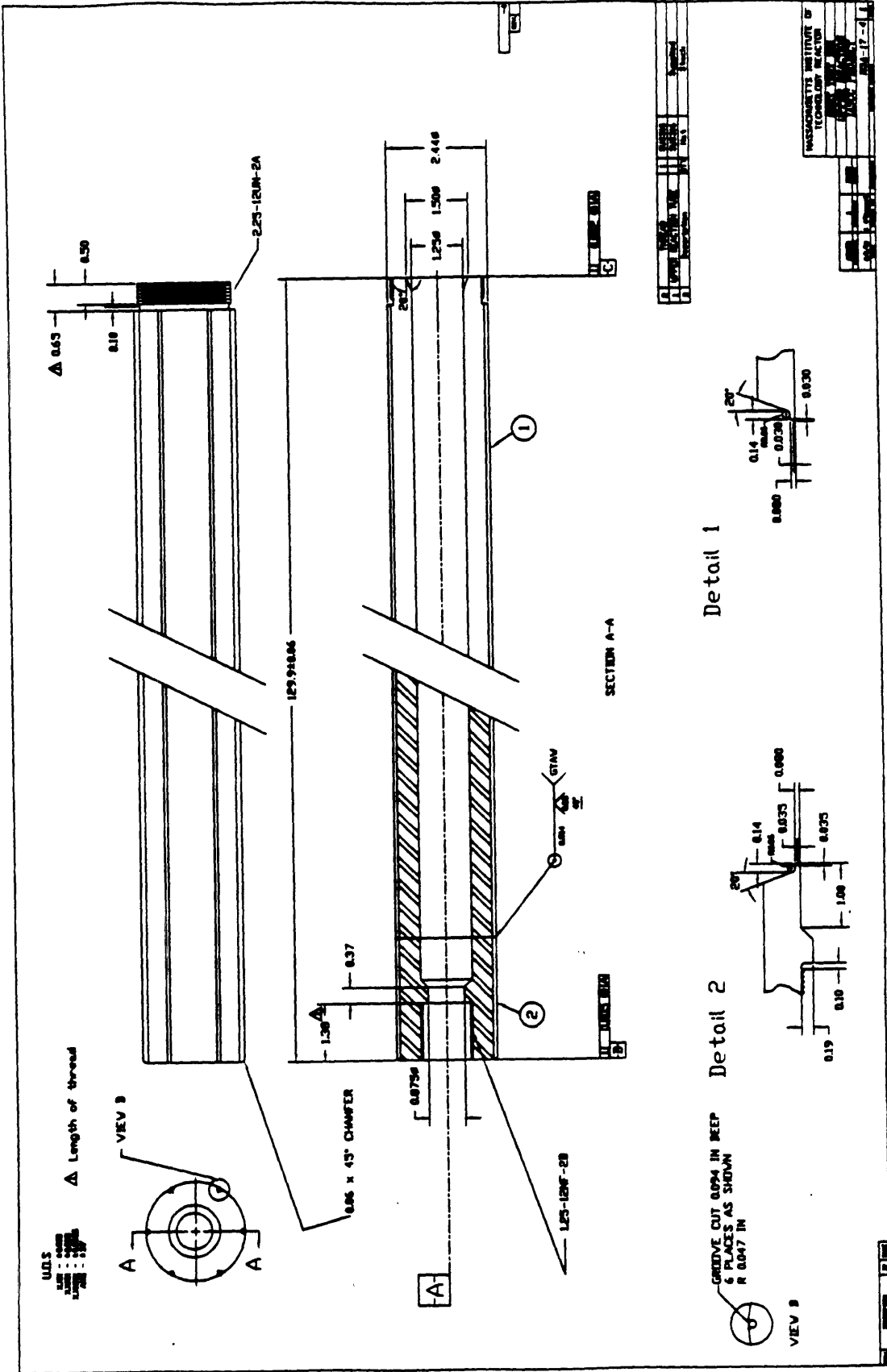
I strongly urge that testing of irradiated specimens in-core continue. A comprehensive test plan should be developed which could be used to study a variety of materials under varying environmental conditions and strain rates. Constant load tests should also be considered. Performing multiple tests using similar testing conditions is important to collect statistically significant data. Zero flux testing should be included so that the non-persistent effects of irradiation on cracking can be studied.

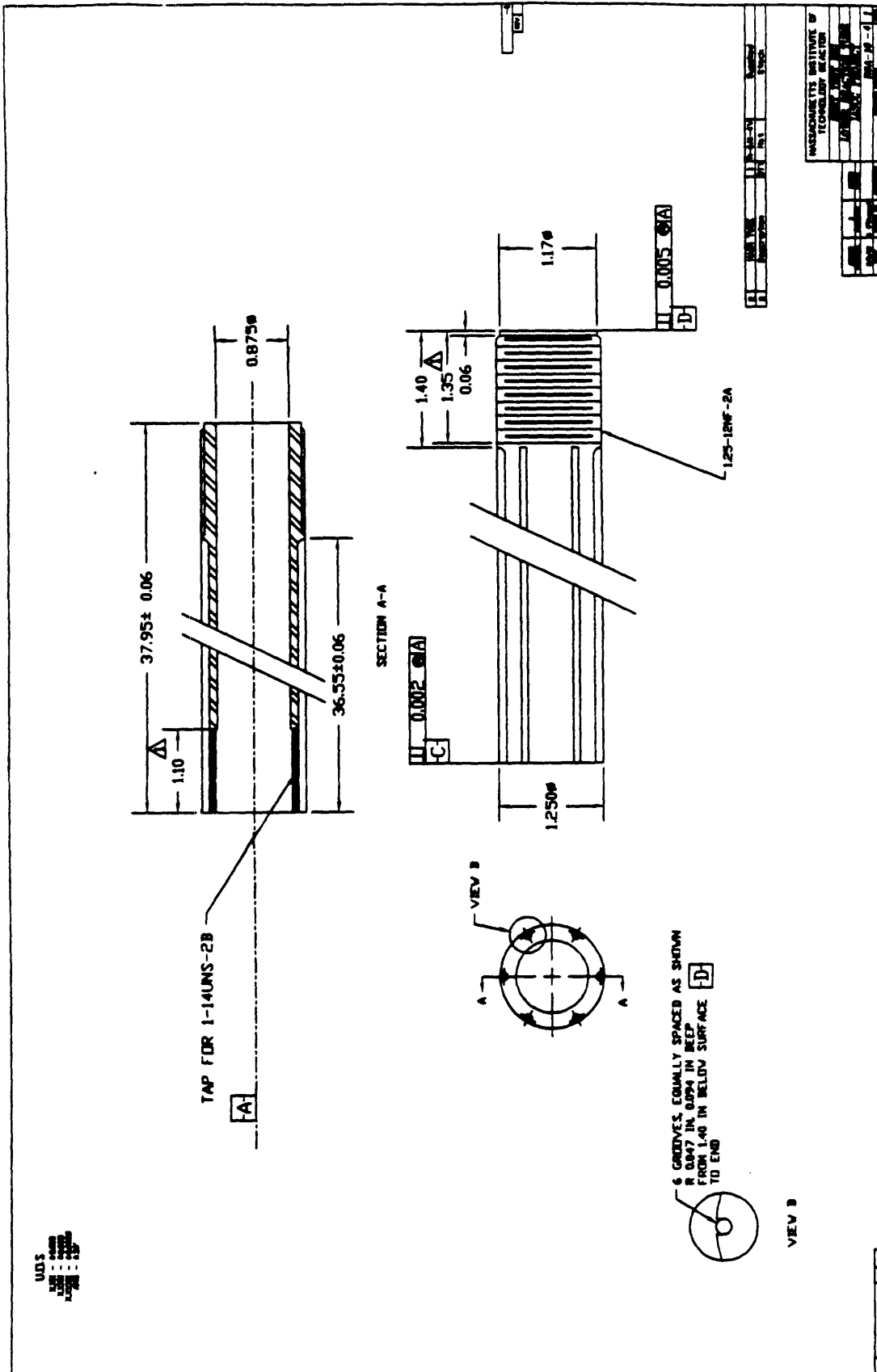
When it becomes necessary to build the next generation in-core SSRT facility some improvements could increase its worth. The implementation of a device with which the specimen's strain could be measured and strain rate controlled should be seriously considered. Radiation hardened LVDTs and displacement sensors utilizing eddy currents exist in commercially available packages. While radiation qualified LVDTs are large and would require complex remote handling during specimen changing, use of the smaller eddy current displacement transducer could be relatively easy. Sensors such as these are currently used in cores of commercial nuclear reactors to monitor fuel

rod position and vibration. Both of these techniques would provide strain measurement in real time through specimen failure. Further development of the DCPD technique should continue. When used in concert with other strain measurement devices, DCPD can be used to monitor crack initiation and growth rate. The DCPD strain characteristics developed in this work would be used to cancel out effects of strain of the DCPD signal.

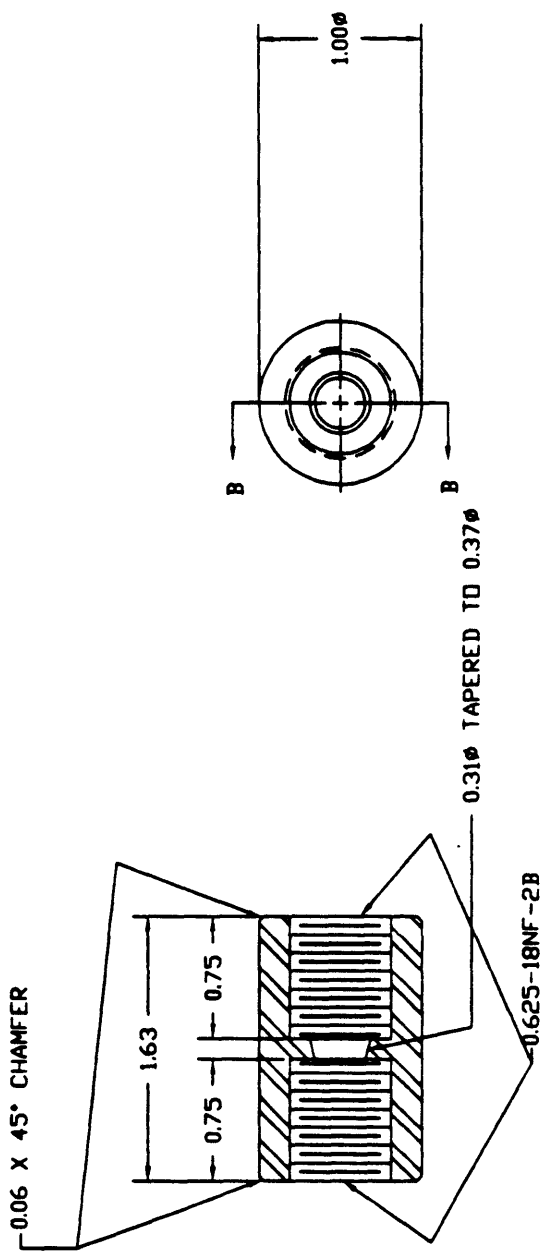
APPENDIX A. DETAILED DRAWINGS







U.O.S
 .XXX - .0015
 .XXXX - .0005
 .XXXXX - .00005
 ANG - 2.30°



VIEW B-B

DO NOT SCALE DRAWING

REV -3

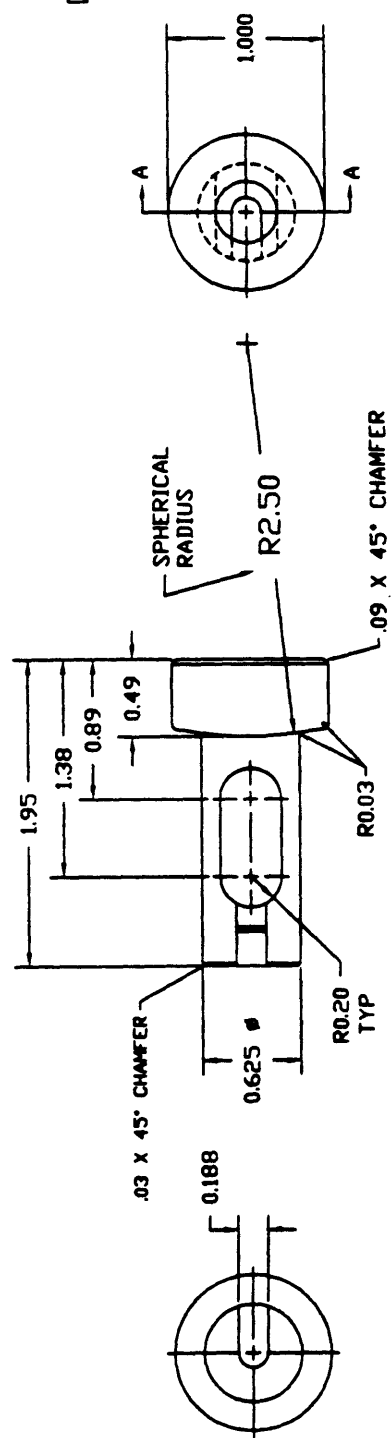
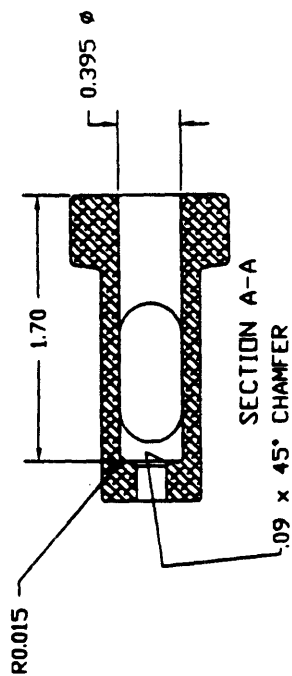
MASSACHUSETTS INSTITUTE OF
 TECHNOLOGY REACTOR
 SSRT TEST RIG
 PULL ROD SLEEVE
 IASCC PROJECT

DESIGN	DATE
CHECKED	DATE
APPROVED	DATE
BY	DATE

REV. DESCRIPTION BY DATE

R3A-24-3

U.D.S
XXX - .0015
XXX - .0005
XXX - .0005
ANG - 30'



REV -3

DO NOT SCALE THIS DRAWING

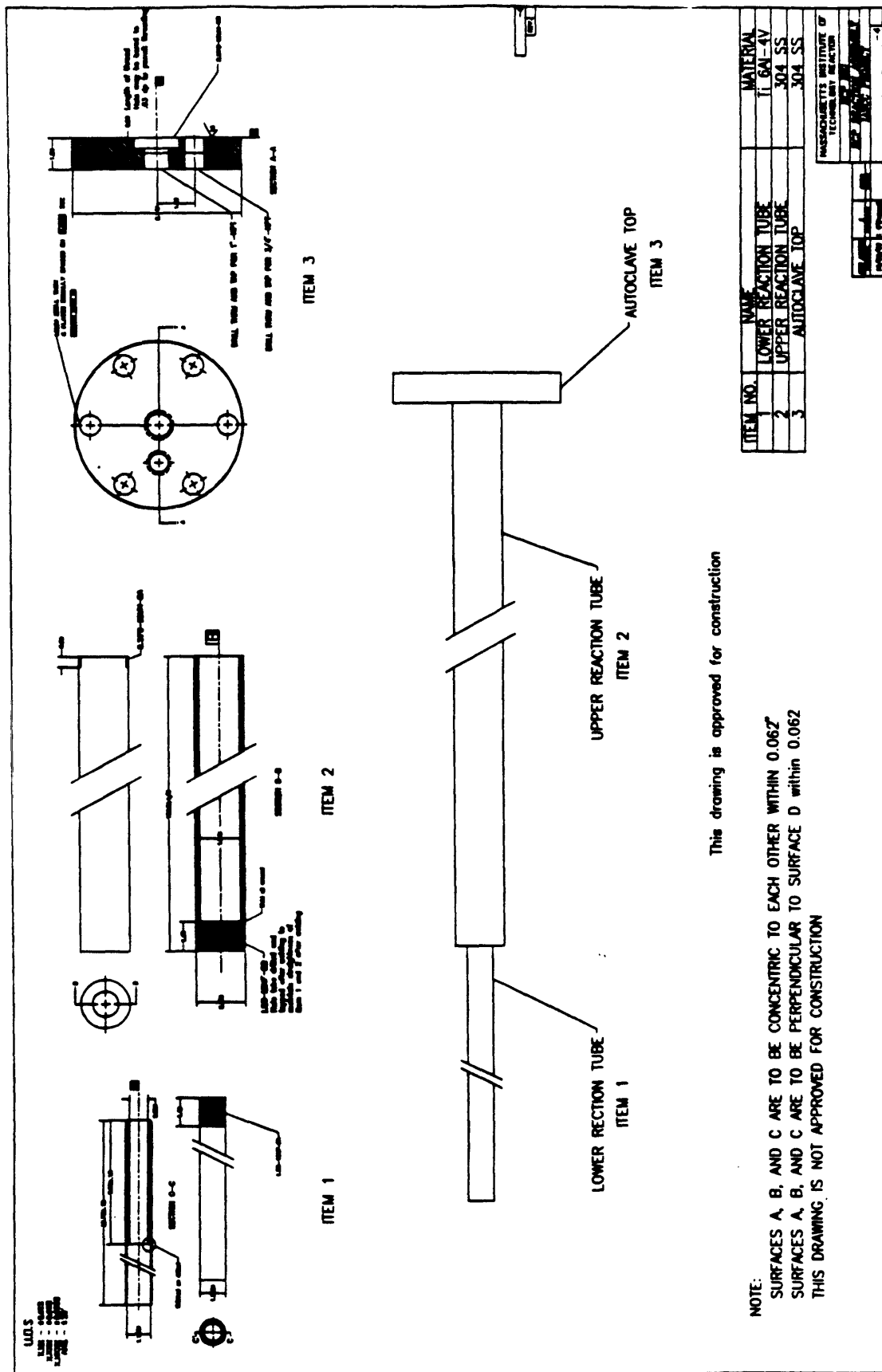
MASSACHUSETTS INSTITUTE OF TECHNOLOGY REACTOR
SSRT TEST RIG
LOWER GRIP
LASCC PROJECT
RJA-23-3

DATE	BY	CHKD
9/26/58	J. P. ...	J. P. ...
REV	DESCRIPTION	DATE

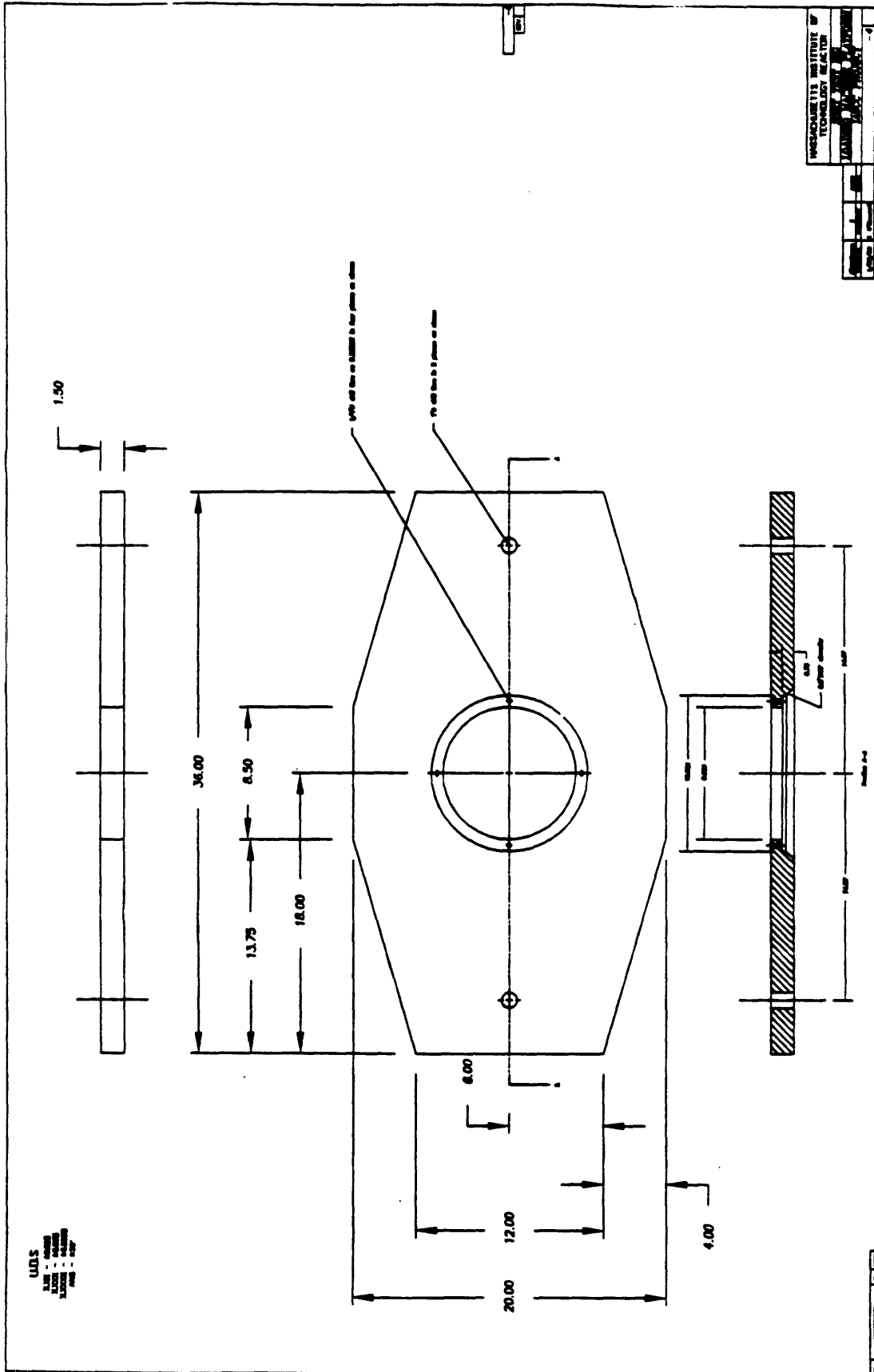
REV DESCRIPTION BY DATE

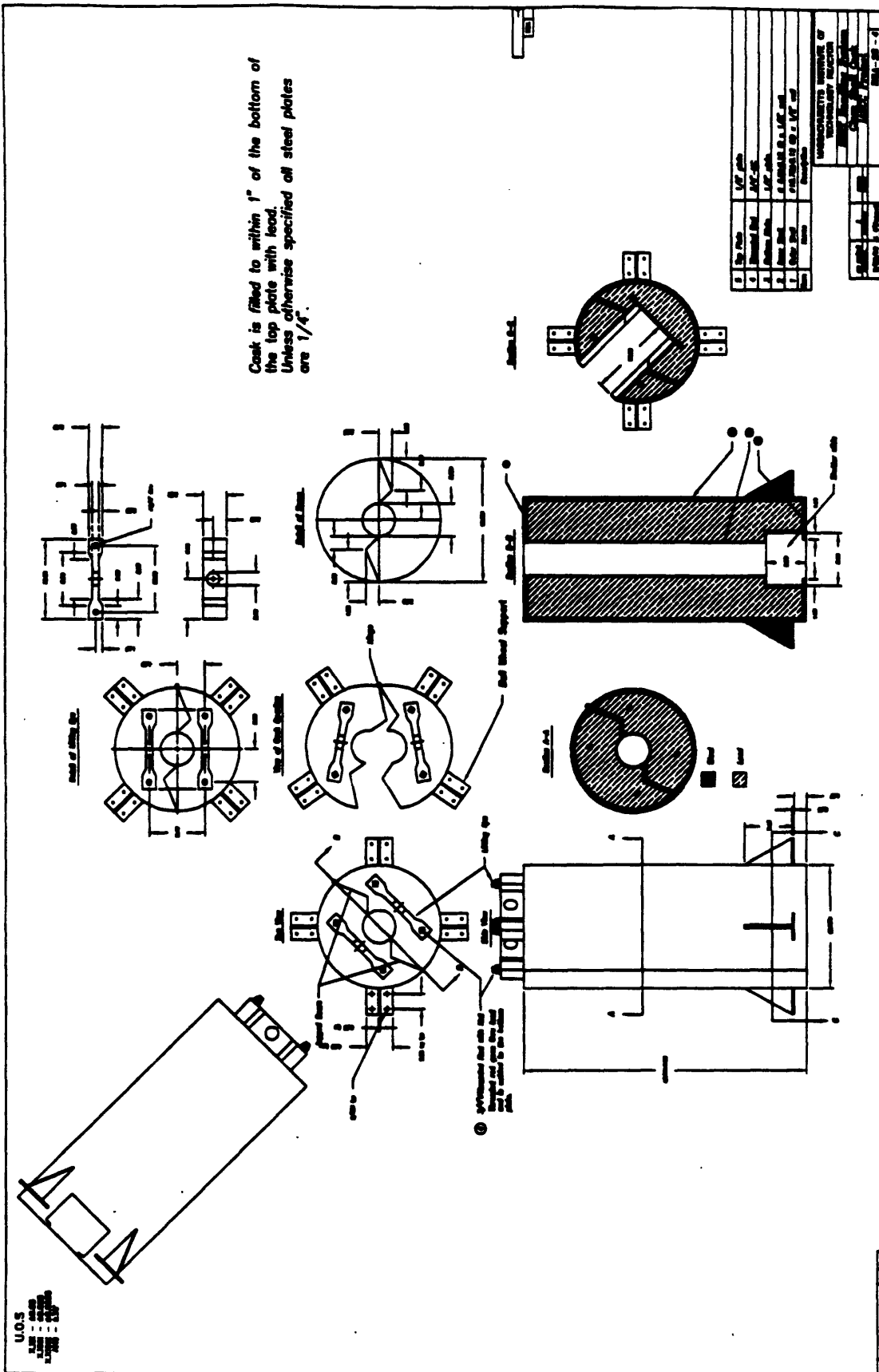
PROJECT	1-141MS-2A
DATE	10/1/58
DESIGNER	W. J. ...
CHECKER	...
APPROVER	...
SCALE	...
QUANTITY	...
REVISIONS	...

U.S.S.
 1/2" - 20
 1/4" - 28
 3/8" - 32
 1/2" - 36
 3/4" - 44
 1" - 48
 1 1/4" - 54
 1 1/2" - 60
 2" - 72
 2 1/2" - 84
 3" - 96
 3 1/2" - 108
 4" - 114
 4 1/2" - 120
 5" - 126
 5 1/2" - 132
 6" - 138
 6 1/2" - 144
 7" - 150
 7 1/2" - 156
 8" - 162
 8 1/2" - 168
 9" - 174
 9 1/2" - 180
 10" - 186
 10 1/2" - 192
 11" - 198
 11 1/2" - 204
 12" - 210
 12 1/2" - 216
 13" - 222
 13 1/2" - 228
 14" - 234
 14 1/2" - 240
 15" - 246
 15 1/2" - 252
 16" - 258
 16 1/2" - 264
 17" - 270
 17 1/2" - 276
 18" - 282
 18 1/2" - 288
 19" - 294
 19 1/2" - 300
 20" - 306
 20 1/2" - 312
 21" - 318
 21 1/2" - 324
 22" - 330
 22 1/2" - 336
 23" - 342
 23 1/2" - 348
 24" - 354
 24 1/2" - 360
 25" - 366
 25 1/2" - 372
 26" - 378
 26 1/2" - 384
 27" - 390
 27 1/2" - 396
 28" - 402
 28 1/2" - 408
 29" - 414
 29 1/2" - 420
 30" - 426
 30 1/2" - 432
 31" - 438
 31 1/2" - 444
 32" - 450
 32 1/2" - 456
 33" - 462
 33 1/2" - 468
 34" - 474
 34 1/2" - 480
 35" - 486
 35 1/2" - 492
 36" - 498
 36 1/2" - 504
 37" - 510
 37 1/2" - 516
 38" - 522
 38 1/2" - 528
 39" - 534
 39 1/2" - 540
 40" - 546
 40 1/2" - 552
 41" - 558
 41 1/2" - 564
 42" - 570
 42 1/2" - 576
 43" - 582
 43 1/2" - 588
 44" - 594
 44 1/2" - 600
 45" - 606
 45 1/2" - 612
 46" - 618
 46 1/2" - 624
 47" - 630
 47 1/2" - 636
 48" - 642
 48 1/2" - 648
 49" - 654
 49 1/2" - 660
 50" - 666
 50 1/2" - 672
 51" - 678
 51 1/2" - 684
 52" - 690
 52 1/2" - 696
 53" - 702
 53 1/2" - 708
 54" - 714
 54 1/2" - 720
 55" - 726
 55 1/2" - 732
 56" - 738
 56 1/2" - 744
 57" - 750
 57 1/2" - 756
 58" - 762
 58 1/2" - 768
 59" - 774
 59 1/2" - 780
 60" - 786
 60 1/2" - 792
 61" - 798
 61 1/2" - 804
 62" - 810
 62 1/2" - 816
 63" - 822
 63 1/2" - 828
 64" - 834
 64 1/2" - 840
 65" - 846
 65 1/2" - 852
 66" - 858
 66 1/2" - 864
 67" - 870
 67 1/2" - 876
 68" - 882
 68 1/2" - 888
 69" - 894
 69 1/2" - 900
 70" - 906
 70 1/2" - 912
 71" - 918
 71 1/2" - 924
 72" - 930
 72 1/2" - 936
 73" - 942
 73 1/2" - 948
 74" - 954
 74 1/2" - 960
 75" - 966
 75 1/2" - 972
 76" - 978
 76 1/2" - 984
 77" - 990
 77 1/2" - 996
 78" - 1002
 78 1/2" - 1008
 79" - 1014
 79 1/2" - 1020
 80" - 1026
 80 1/2" - 1032
 81" - 1038
 81 1/2" - 1044
 82" - 1050
 82 1/2" - 1056
 83" - 1062
 83 1/2" - 1068
 84" - 1074
 84 1/2" - 1080
 85" - 1086
 85 1/2" - 1092
 86" - 1098
 86 1/2" - 1104
 87" - 1110
 87 1/2" - 1116
 88" - 1122
 88 1/2" - 1128
 89" - 1134
 89 1/2" - 1140
 90" - 1146
 90 1/2" - 1152
 91" - 1158
 91 1/2" - 1164
 92" - 1170
 92 1/2" - 1176
 93" - 1182
 93 1/2" - 1188
 94" - 1194
 94 1/2" - 1200
 95" - 1206
 95 1/2" - 1212
 96" - 1218
 96 1/2" - 1224
 97" - 1230
 97 1/2" - 1236
 98" - 1242
 98 1/2" - 1248
 99" - 1254
 99 1/2" - 1260
 100" - 1266
 100 1/2" - 1272
 101" - 1278
 101 1/2" - 1284
 102" - 1290
 102 1/2" - 1296
 103" - 1302
 103 1/2" - 1308
 104" - 1314
 104 1/2" - 1320
 105" - 1326
 105 1/2" - 1332
 106" - 1338
 106 1/2" - 1344
 107" - 1350
 107 1/2" - 1356
 108" - 1362
 108 1/2" - 1368
 109" - 1374
 109 1/2" - 1380
 110" - 1386
 110 1/2" - 1392
 111" - 1398
 111 1/2" - 1404
 112" - 1410
 112 1/2" - 1416
 113" - 1422
 113 1/2" - 1428
 114" - 1434
 114 1/2" - 1440
 115" - 1446
 115 1/2" - 1452
 116" - 1458
 116 1/2" - 1464
 117" - 1470
 117 1/2" - 1476
 118" - 1482
 118 1/2" - 1488
 119" - 1494
 119 1/2" - 1500
 120" - 1506
 120 1/2" - 1512
 121" - 1518
 121 1/2" - 1524
 122" - 1530
 122 1/2" - 1536
 123" - 1542
 123 1/2" - 1548
 124" - 1554
 124 1/2" - 1560
 125" - 1566
 125 1/2" - 1572
 126" - 1578
 126 1/2" - 1584
 127" - 1590
 127 1/2" - 1596
 128" - 1602
 128 1/2" - 1608
 129" - 1614
 129 1/2" - 1620
 130" - 1626
 130 1/2" - 1632
 131" - 1638
 131 1/2" - 1644
 132" - 1650
 132 1/2" - 1656
 133" - 1662
 133 1/2" - 1668
 134" - 1674
 134 1/2" - 1680
 135" - 1686
 135 1/2" - 1692
 136" - 1698
 136 1/2" - 1704
 137" - 1710
 137 1/2" - 1716
 138" - 1722
 138 1/2" - 1728
 139" - 1734
 139 1/2" - 1740
 140" - 1746
 140 1/2" - 1752
 141" - 1758
 141 1/2" - 1764
 142" - 1770
 142 1/2" - 1776
 143" - 1782
 143 1/2" - 1788
 144" - 1794
 144 1/2" - 1800
 145" - 1806
 145 1/2" - 1812
 146" - 1818
 146 1/2" - 1824
 147" - 1830
 147 1/2" - 1836
 148" - 1842
 148 1/2" - 1848
 149" - 1854
 149 1/2" - 1860
 150" - 1866
 150 1/2" - 1872
 151" - 1878
 151 1/2" - 1884
 152" - 1890
 152 1/2" - 1896
 153" - 1902
 153 1/2" - 1908
 154" - 1914
 154 1/2" - 1920
 155" - 1926
 155 1/2" - 1932
 156" - 1938
 156 1/2" - 1944
 157" - 1950
 157 1/2" - 1956
 158" - 1962
 158 1/2" - 1968
 159" - 1974
 159 1/2" - 1980
 160" - 1986
 160 1/2" - 1992
 161" - 1998
 161 1/2" - 2004
 162" - 2010
 162 1/2" - 2016
 163" - 2022
 163 1/2" - 2028
 164" - 2034
 164 1/2" - 2040
 165" - 2046
 165 1/2" - 2052
 166" - 2058
 166 1/2" - 2064
 167" - 2070
 167 1/2" - 2076
 168" - 2082
 168 1/2" - 2088
 169" - 2094
 169 1/2" - 2100
 170" - 2106
 170 1/2" - 2112
 171" - 2118
 171 1/2" - 2124
 172" - 2130
 172 1/2" - 2136
 173" - 2142
 173 1/2" - 2148
 174" - 2154
 174 1/2" - 2160
 175" - 2166
 175 1/2" - 2172
 176" - 2178
 176 1/2" - 2184
 177" - 2190
 177 1/2" - 2196
 178" - 2202
 178 1/2" - 2208
 179" - 2214
 179 1/2" - 2220
 180" - 2226
 180 1/2" - 2232
 181" - 2238
 181 1/2" - 2244
 182" - 2250
 182 1/2" - 2256
 183" - 2262
 183 1/2" - 2268
 184" - 2274
 184 1/2" - 2280
 185" - 2286
 185 1/2" - 2292
 186" - 2298
 186 1/2" - 2304
 187" - 2310
 187 1/2" - 2316
 188" - 2322
 188 1/2" - 2328
 189" - 2334
 189 1/2" - 2340
 190" - 2346
 190 1/2" - 2352
 191" - 2358
 191 1/2" - 2364
 192" - 2370
 192 1/2" - 2376
 193" - 2382
 193 1/2" - 2388
 194" - 2394
 194 1/2" - 2400
 195" - 2406
 195 1/2" - 2412
 196" - 2418
 196 1/2" - 2424
 197" - 2430
 197 1/2" - 2436
 198" - 2442
 198 1/2" - 2448
 199" - 2454
 199 1/2" - 2460
 200" - 2466
 200 1/2" - 2472
 201" - 2478
 201 1/2" - 2484
 202" - 2490
 202 1/2" - 2496
 203" - 2502
 203 1/2" - 2508
 204" - 2514
 204 1/2" - 2520
 205" - 2526
 205 1/2" - 2532
 206" - 2538
 206 1/2" - 2544
 207" - 2550
 207 1/2" - 2556
 208" - 2562
 208 1/2" - 2568
 209" - 2574
 209 1/2" - 2580
 210" - 2586
 210 1/2" - 2592
 211" - 2598
 211 1/2" - 2604
 212" - 2610
 212 1/2" - 2616
 213" - 2622
 213 1/2" - 2628
 214" - 2634
 214 1/2" - 2640
 215" - 2646
 215 1/2" - 2652
 216" - 2658
 216 1/2" - 2664
 217" - 2670
 217 1/2" - 2676
 218" - 2682
 218 1/2" - 2688
 219" - 2694
 219 1/2" - 2700
 220" - 2706
 220 1/2" - 2712
 221" - 2718
 221 1/2" - 2724
 222" - 2730
 222 1/2" - 2736
 223" - 2742
 223 1/2" - 2748
 224" - 2754
 224 1/2" - 2760
 225" - 2766
 225 1/2" - 2772
 226" - 2778
 226 1/2" - 2784
 227" - 2790
 227 1/2" - 2796
 228" - 2802
 228 1/2" - 2808
 229" - 2814
 229 1/2" - 2820
 230" - 2826
 230 1/2" - 2832
 231" - 2838
 231 1/2" - 2844
 232" - 2850
 232 1/2" - 2856
 233" - 2862
 233 1/2" - 2868
 234" - 2874
 234 1/2" - 2880
 235" - 2886
 235 1/2" - 2892
 236" - 2898
 236 1/2" - 2904
 237" - 2910
 237 1/2" - 2916
 238" - 2922
 238 1/2" - 2928
 239" - 2934
 239 1/2" - 2940
 240" - 2946
 240 1/2" - 2952
 241" - 2958
 241 1/2" - 2964
 242" - 2970
 242 1/2" - 2976
 243" - 2982
 243 1/2" - 2988
 244" - 2994
 244 1/2" - 3000
 245" - 3006
 245 1/2" - 3012
 246" - 3018
 246 1/2" - 3024
 247" - 3030
 247 1/2" - 3036
 248" - 3042
 248 1/2" - 3048
 249" - 3054
 249 1/2" - 3060
 250" - 3066
 250 1/2" - 3072
 251" - 3078
 251 1/2" - 3084
 252" - 3090
 252 1/2" - 3096
 253" - 3102
 253 1/2" - 3108
 254" - 3114
 254 1/2" - 3120
 255" - 3126
 255 1/2" - 3132
 256" - 3138
 256 1/2" - 3144
 257" - 3150
 257 1/2" - 3156
 258" - 3162
 258 1/2" - 3168
 259" - 3174
 259 1/2" - 3180
 260" - 3186
 260 1/2" - 3192
 261" - 3198
 261 1/2" - 3204
 262" - 3210
 262 1/2" - 3216
 263" - 3222
 263 1/2" - 3228
 264" - 3234
 264 1/2" - 3240
 265" - 3246
 265 1/2" - 3252
 266" - 3258
 266 1/2" - 3264
 267" - 3270
 267 1/2" - 3276
 268" - 3282
 268 1/2" - 3288
 269" - 3294
 269 1/2" - 3300
 270" - 3306
 270 1/2" - 3312
 271" - 3318
 271 1/2" - 3324
 272" - 3330
 272 1/2" - 3336
 273" - 3342
 273 1/2" - 3348
 274" - 3354
 274 1/2" - 3360
 275" - 3366
 275 1/2" - 3372
 276" - 3378
 276 1/2" - 3384
 277" - 3390
 277 1/2" - 3396
 278" - 3402
 278 1/2" - 3408
 279" - 3414
 279 1/2" - 3420
 280" - 3426
 280 1/2" - 3432
 281" - 3438
 281 1/2" - 3444
 282" - 3450
 282 1/2" - 3456
 283" - 3462
 283 1/2" - 3468
 284" - 3474
 284 1/2" - 3480
 285" - 3486
 285 1/2" - 3492
 286" - 3498
 286 1/2" - 3504
 287" - 3510
 287 1/2" - 3516
 288" - 3522
 288 1/2" - 3528
 289" - 3534
 289 1/2" - 3540
 290" - 3546
 290 1/2" - 3552
 291" - 3558
 291 1/2" - 3564
 292" - 3570
 292 1/2" - 3576
 293" - 3582
 293 1/2" - 3588
 294" - 3594
 294 1/2" - 3600
 295" - 3606
 295 1/2" - 3612
 296" - 3618
 296 1/2" - 3624
 297" - 3630
 297 1/2" - 3636
 298" - 3642
 298 1/2" - 3648
 299" - 3654
 299 1/2" - 3660
 300" - 3666
 300 1/2" - 3672
 301" - 3678
 301 1/2" - 3684
 302" - 3690
 302 1/2" - 3696
 303" - 3702
 303 1/2" - 3708
 304" - 3714
 304 1/2" - 3720
 305" - 3726
 305 1/2" - 3732
 306" - 3738
 306 1/2" - 3744
 307" - 3750
 307 1/2" - 3756
 308" - 3762
 308 1/2" - 3768
 309" - 3774
 309 1/2" - 3780
 310" - 3786
 310 1/2" - 3792
 311" - 3798
 311 1/2" - 3804
 312" - 3810
 312 1/2" - 3816
 313" - 3822
 313 1/2" - 3828
 314" - 3834
 314 1/2" - 3840
 315" - 3846
 315 1/2" - 3852
 316" - 3858
 316 1/2" - 3864
 317" - 3870
 317 1/2" - 3876
 318" - 3882
 318 1/2" - 3888
 319" - 3894
 319 1/2" - 3900
 320" - 3906
 320 1/2" - 3912
 321" - 3918
 321 1/2" - 3924
 322" - 3930
 322 1/2" - 3936
 323" - 3942
 323 1/2" - 3948
 324" - 3954
 324 1/2" - 3960
 325" - 3966
 325 1/2" - 3972
 326" - 3978
 326 1/2" - 3984
 327" - 3990
 327 1/2" - 3996
 328" - 4002
 328 1/2" - 4008
 329" - 4014
 329 1/2" - 4020
 330" - 4026
 330 1/2" - 4032
 331" - 4038
 331 1/2" - 4044
 332" - 4050
 332 1/2" - 4056
 333" - 4062
 333 1/2" - 4068
 334" - 4074
 334 1/2" - 4080
 335" - 4086
 335 1/2" - 4092
 336" - 4098
 336 1/2" - 4104
 337" - 4110
 337 1/2" - 4116
 338" - 4122
 338 1/2" - 4128
 339" - 4134
 339 1/2" - 4140
 340" - 4146
 340 1/2" - 4152
 341" - 4158
 341 1/2" - 4164
 342" - 4170
 342 1/2" - 4176
 343" - 4182
 343 1/2" - 4188
 344" - 4194
 344 1/2" - 4200
 345" - 4206
 345 1/2" - 4212
 346" - 4218
 346 1/2" - 4224
 347" - 4230
 347 1/2" - 4236
 348" - 4242
 348 1/2" - 4248
 349" - 4254
 349 1/2" - 4260
 350" - 4266
 350 1/2" - 4272
 351" - 4278
 351 1/2" - 4284
 352" - 4290
 352 1/2" - 4296
 353" - 4302
 353 1/2" - 4308
 354" - 4314
 354 1/2" - 4320
 355" - 4326
 355 1/2" - 4332
 356" - 4338
 356 1/2" - 4344
 357" - 4350
 357 1/2" - 4356
 358" - 4362
 358 1/2" - 4368
 359" - 4374
 359 1/2" - 4380
 360" - 4386
 360 1/2" - 4392
 361" - 4398
 361 1/2" - 4404
 362" - 4410
 362 1/2" - 4416
 363" - 4422
 363 1/2" - 4428
 364" - 4434
 364 1/2" - 4440
 365" - 4446
 365 1/2" -



This drawing is approved for construction





B.3. ECP Rig Worth

1cc water is equal to 1mbeta is equal to 0.786X10 ⁻³ %dK/K			
WORTH OF WATER VOLUME IN CT			
worth per cc	0.000786		
total volume (in ³)	15.15922807		
total water volume (cc)	248.4152405		
total worth (%dK/K)	0.195254379		
		Volume within CT	25.33888896
		ID	1.42
		L	16
WORTH OF THIMBLE/CT GAP			
worth per cc	0.000786		
total volume (in ³)	8.46252873	Volume of Reaction Tube	3.73065
total water volume (cc)	138.6759999	OD-1	1.25
total worth (%dK/K)	0.108999336	ID-1	1.125
		L-1	16
		Volume of Electrode CLUSTER	6.449010893
volume within thimble (in³)			
ID	58.44848625		
L	1.75	Volume of cluster bottom	0.407691124
	24.3	Volume of Both Shrouds	0.70250278
volume of CT (in³)			
OD	36.29407031	Volume of Cluster Middle	4.14465399
Length of tube	1.625	Volume of Cluster Top	0.554878624
Length of end	17	Volume of Threaded Rod	0.183984375
	0.5	Volume of Electrodes	0.4553
volume of Al slug (in³)			
OD	13.69188721	Volume of Ti Slug	0
Length of slug	1.6875	OD-1	1.32
	6.125	ID-1	0.2
		L-1	5.87
		OD-2	1
		ID-2	0.2
		L-2	0.63

B.4. Fluid Flow Characteristics of the Main Loop

Head (ft)	ΔP (psi)	flow rate (cc/min)	flow rate (gpm)	viscosity (in ² /s)
29.59593126	13.022	45235.53	11.95	0.00
Tubing			Heater Tubes	
Re	510199.959		Re	324571.65
Length (ft)	20.000		Length (ft)	6.50
ID (in)	0.584		ID (in)	0.46
velocity (in/s)	171.843		velocity (in/s)	139.09
friction factor	0.012		friction factor	0.01
head (ft)	15.589		head (ft)	4.73
UCT-URT			LCT-LRT	
Re	83053.044		Re	157499.25
Length (ft)	11.300		Length (ft)	2.71
Hyd D (in)	3.588		Hyd D (in)	1.89
velocity (in/s)	4.554		velocity (in/s)	16.38
friction factor	0.019		friction factor	0.02
head (ft)	0.002		head (ft)	0.01
LRT-LPR			URT-UPR	
Re	276048.660		Re	204396.66
Length (ft)	3.210		Length (ft)	10.88
Hyd D (in)	1.079		Hyd D (in)	1.46
velocity (in/s)	50.306		velocity (in/s)	27.58
friction factor	0.014		friction factor	0.01
head (ft)	0.135		head (ft)	0.11
Rig U-Turn			Elbow (2)	
Le/D	60.000		Le/D	60.00
velocity (in/s)	33.341		velocity (in/s)	171.84
friction factor	0.020		friction factor	0.01
Head (ft)	0.145		Head (ft)	2.28
Rig In			Rig Out	
Le/D	90.000		Le/D	90.00
velocity (in/s)	88.198		velocity (in/s)	99.71
friction factor	0.015		friction factor	0.01
Head (ft)	1.158		Head (ft)	1.30
Heater Y (2)			90° Bend (4)	
Le/D	40.000		Le/D	80.00
velocity (in/s)	139.092		velocity (in/s)	171.84
friction factor	0.013		friction factor	0.01
Head (ft)	1.113		Head (ft)	3.03

B.6. Main Loop Radiation Levels-SSRT Rig

Activity in (dps/ml)	
time in-core (s)	0.3228
lambda (s ⁻¹)	0.097605634
f (s ⁻¹ cm ⁻²)	1.82E+13
Nfs/lambda (per ml)	846735959.6
activity out (dps/ml)	2563348.092
time out of core (s)	6.9326
activity back in (dps/ml)	1302979.331
Activity in (dps/ml)	1302979.331
time in-core (s)	0.3228
lambda (s ⁻¹)	0.097605634
f (s ⁻¹ cm ⁻²)	1.82E+13
Nfs/lambda (per ml)	846735959.6
activity out (dps/ml)	3825914.318
time out of core (s)	6.9326
activity back in (dps/ml)	1944756.272
Activity in (dps/ml)	1944756.272
time in-core (s)	0.3228
lambda (s ⁻¹)	0.097605634
f (s ⁻¹ cm ⁻²)	1.82E+13
Nfs/lambda (per ml)	846735959.6
activity out (dps/ml)	4447785.955
time out of core (s)	6.9326
activity back in (dps/ml)	2260860.781
Activity in (dps/ml)	2260860.781
time in-core (s)	0.3228
lambda (s ⁻¹)	0.097605634
f (s ⁻¹ cm ⁻²)	1.82E+13
Nfs/lambda (per ml)	846735959.6
activity out (dps/ml)	4754086.192
time out of core (s)	6.9326
activity back in (dps/ml)	2416556.716
Activity in (dps/ml)	2416556.716
time in-core (s)	0.3228
lambda (s ⁻¹)	0.097605634
f (s ⁻¹ cm ⁻²)	1.82E+13
Nfs/lambda (per ml)	846735959.6
activity out (dps/ml)	4904953.073
time out of core (s)	6.9326
activity back in (dps/ml)	2493244.088
Activity in (dps/ml)	2493244.088
time in-core (s)	0.3228
lambda (s ⁻¹)	0.097605634
f (s ⁻¹ cm ⁻²)	1.82E+13
Nfs/lambda (per ml)	846735959.6
activity out (dps/ml)	4979261.916
time out of core (s)	6.9326
activity back in (dps/ml)	2531016.127
activity at top (dps/ml)	4096243.781
activity at top (Ci/ml)	0.000110709
area of tube (cm ²)	1.727280158
activity per length (Ci/cm)	0.000191226
length of loop (cm)	609.6
volume of loop (ml)	1052.949985
Activity of loop (Ci)	0.116571347
Dose Rate at 1 m (mR/hr)	116.5713466
thickness of shield (in)	2
Dose Rate at 1 m (mR/hr)	12.12002801

B.7. Main Loop Radiation Levels-ECP Rig

Activity in (dps/ml)	0
time in-core (s)	0.3228
lambda (s ⁻¹)	0.097605634
f (s ⁻¹ cm ⁻²)	1.82E+13
Nfs/lambda (per ml)	846735959.6
activity out (dps/ml)	2563348.092
time out of core (s)	14.0642
activity back in (dps/ml)	649578.9453
Activity in (dps/ml)	649578.9453
time in-core (s)	0.3228
lambda (s ⁻¹)	0.097605634
f (s ⁻¹ cm ⁻²)	1.82E+13
Nfs/lambda (per ml)	846735959.6
activity out (dps/ml)	3192779.748
time out of core (s)	14.0642
activity back in (dps/ml)	809083.4434
Activity in (dps/ml)	809083.4434
time in-core (s)	0.3228
lambda (s ⁻¹)	0.097605634
f (s ⁻¹ cm ⁻²)	1.82E+13
Nfs/lambda (per ml)	846735959.6
activity out (dps/ml)	3347337.067
time out of core (s)	14.0642
activity back in (dps/ml)	848249.8682
Activity in (dps/ml)	848249.8682
time in-core (s)	0.3228
lambda (s ⁻¹)	0.097605634
f (s ⁻¹ cm ⁻²)	1.82E+13
Nfs/lambda (per ml)	846735959.6
activity out (dps/ml)	3385288.709
time out of core (s)	14.0642
activity back in (dps/ml)	857867.2072
Activity in (dps/ml)	857867.2072
time in-core (s)	0.3228
lambda (s ⁻¹)	0.097605634
f (s ⁻¹ cm ⁻²)	1.82E+13
Nfs/lambda (per ml)	846735959.6
activity out (dps/ml)	3394607.757
time out of core (s)	14.0642
activity back in (dps/ml)	860228.7506
Activity in (dps/ml)	860228.7506
time in-core (s)	0.3228
lambda (s ⁻¹)	0.097605634
f (s ⁻¹ cm ⁻²)	1.82E+13
Nfs/lambda (per ml)	846735959.6
activity out (dps/ml)	3396896.055
time out of core (s)	14.0642
activity back in (dps/ml)	860808.6289
activity at top (dps/ml)	1698698.024
activity at top (Ci/ml)	4.59108E-05
area of tube (cm ²)	1.727280158
activity per length (Ci/cm)	7.93007E-05
length of loop (cm)	609.6
volume of loop (ml)	1052.949985
Activity of loop (Ci)	0.048341731
Dose Rate at 1 m (mR/hr)	48.34173131
thickness of shield (in)	2
Dose Rate at 1 m (mR/hr)	5.026133388

APPENDIX C. OPERATING INSTRUCTIONS

This appendix lists and describes the steps necessary to safely operate the facility. It is intended to be used as a guideline for experimenters in facility operation and as a training aid for experimenters new to the facility; it is not intended to replace any operating procedure which has been previously approved by the reactor safeguards committee or the MITR-II Technical Specifications.

Each instruction consists of three parts; a section which describes the condition that the facility should be in prior to beginning the operation, the *Initial Conditions*, a section which lists things to be aware of while performing the operation, *Precautions*, and a list of steps needed to be completed in the order that they should be completed in, *Instructions*.

C.1. Facility Startup Operations

C.1.1. Specimen Loading onto Load Train Grips

Initial Conditions

- a) The load train is supported by the bracket above hot cell number 2.
- b) The specimen to be tested is cleaned and in hot cell number 2.
- c) Two experimenters present.

Precautions

a) The specimen is very fragile, any scratch made on the surface of the specimen during handling with the manipulators could seriously impact the test. Try as much as possible to handle the specimen with its button or shoulder section, avoid the narrow gauge section.

b. If polishing of the pull rod is required when replacing the dynamic seal take care not to spread contamination.

c. Do not drop the pull rod if the pull rod's threaded top is removed for dynamic seal replacement. It will be difficult to retrieve if it falls into the autoclave top.

Instructions

a. On the hot cell top check that the pull rod in the area where the dynamic seal is used is smooth by lifting the pull rod from the autoclave top about 12 inches. Experience shows that the Rulon backing collar can leave hard deposits on the pull rod which affects sealing. If hard deposits are found on the pull rod clean the surface of the pull rod, with a clean rag and deionized water, and try to rub the deposit off the pull rod. If this doesn't work 600 grit emery paper will, be careful not to spread contamination and clean the surface with de-ionized water and a clean rag when deposits are removed and before lowering the pull rod.

b. On the hot cell top inspect the pull rod's dynamic seal by loosening the autoclave top gland nut and pulling the pull rod and gland nut up together. This should expose the red Rulon backing collar, the beige split backing ring, and finally the beige dynamic seal. If the bottom edge of the dynamic sealing ring appears rounded significantly more than a new seal it needs to be replaced, experience shows that one ring will work satisfactorily for multiple tests, but it is best to replace it between each test. To replace the seal remove the pull rod's threaded top, the autoclave top gland nut, rulon backing collar, split backing ring, and used dynamic seal. Place the new dynamic sealing ring on the pull rod, open side down, followed by the split backing ring, Rulon backing collar, and gland nut. Put the pull rod's threaded top onto the top of the pull rod. While supporting the pull rod through the center of the hole in the autoclave top and the gland nut push the dynamic sealing ring into the autoclave top. When the dynamic seal is

inside the autoclave top below the chamfered section, the split backing rings and Rulon collar can be pushed into the autoclave top and the gland nut threaded on. Lower the pull rod so that the pull rod's threaded top rests on the gland nut.

c. If the DCPD system is to be utilized, loosen the two Conax feed-throughs for the test specimen DCPD wires to allow the wires to move. If the wires are to be reused, pull them down with the manipulators so that their end is near the welding fixture in the hot cell. If they are to be replaced, remove the old wires and install new ones, then pull the wires with the manipulators so that their end is near the welding fixture in the hot cell. Place the lower grip on the welding fixture table and thread both DCPD wires through the bottom hole in the lower grip and then through the eye which has the slot machined through to the hole in the lower grip's top. Place the test specimen into the welding fixture and clamp it down. Slide the end of one of the wires through one of the grooves so that it goes under the test specimen, pressurize the appropriate air cylinder to clamp the wire to the specimen with the welding probe, and weld the wire to the specimen using the welding machine and foot-switch. Repeat for the other wire, and loosen the clamp holding the specimen to the welding fixture.

d. Place the specimen to be tested onto the grip machined into the bottom end of the pull rod. Pick the specimen up by its button head or shoulder section, try to avoid touching the gauge section.

e. Place the lower grip onto the bottom button of the test specimen.

f. On the hot cell top, lift the pull rod to seat the lower grip into the lower grip holder. Have someone in front of the hot cell verify that the specimen is seated properly in both grips as it is raised into the reaction tube. When the lower grip mates with the lower grip holder insert the pull rod collar between the pull rod's threaded top and gland nut, loosen the pull rod's threaded top nut to allow the collar to fit between it and the

gland nut, then tighten it so that the lower grip remains in positive contact with the lower grip holder. Secure the collar in place with a tie-wrap.

g. Insert the nickel wire into the lower grip holder so that it will support the lower grip holder and lower half of the specimen after the specimen breaks.

h. Pull the DCPD wires tight and tighten the Conax feed-throughs finger tight.

C.1.2. Assembling the Facility in its In-Core Test Position

Initial Conditions

a. The reactor is shutdown, lid and test plug are rotated into position for in-core IASCC testing.

b. The dummy element is installed into core position B3, the thin walls of the dummy element are facing the A-ring.

c. Permission for transfer is granted by MITR-II Reactor Operations Office and Reactor Radiation Protection Office.

d. The thimble/autoclave is supported by the bracket next to hot cell number 1 with its in-core sections in the shielded clam shell cask on the containment building floor. The upper flange is connected to the lifting beam's inner most position using 3/8" eye bolts and a 10" longX1/4" sling. The clam shell cask is connected to the middle lifting position of the lifting beam using 10' longX5/8" slings.

e. The load train is supported by the bracket over hot cell number 2 and a test specimen is loaded into the grips of the load train as described in section 5.1.1.

f. The charging tank is full and pressurized to about 5 psi with He gas. The clean up system is operating with the UV sterilizer on. MUV-6 is selected to the charging tank.

The charging pump and main loop recirculation pumps are off. The charging tank bubbling system is operating. The charging tank vent can be closed or throttled open.

g. The heater control cabinet control power is off.

h. This procedure requires at minimum 2 experimenters, an experienced crane operator, and 2 reactor operators (one on the reactor top, one in the control room). The reactor operators are not required after the load train is in-core. The crane operator is not required after the loading machine is in place.

Precautions

a. To prevent potential damage to the MITR reactor core, the thimble is to be inserted into the in-core dummy element using springs and a hand hoist.

b. Because of the potential for high radiation levels near the rig and reactor top, the experimenter should check with RRPO before proceeding with each step in the procedure.

c. Before moving the load train from the hot cell ensure that the collar has the lower grip in positive contact with the lower grip holder. If the collar is not properly positioned the specimen's button ends may slip out of the grips.

d. Take care when moving the lead doughnut to and from the reactor top lid. Avoid damaging the fragile aluminum tube protruding from the outside of the upper flange.

Instructions

a. Using the three ton crane and appropriate rigging remove the large reactor top lid access plug for viewing the insertion of the thimble/autoclave into the dummy fuel element. Lift the reactor top cask plate, clean it, and place it onto the reactor top lid using the markings on the lid as a guide. Insert the white Teflon seal onto the step in the test plug if it is not already installed.

b. Using the 3 ton crane and lifting beam, lift the thimble/autoclave and clam shell cask over the reactor top decking over a clean piece of brown paper. Using a vacuum cleaner, remove any dirt on the bottom, sides, and top of the cask. Lift the cask onto the reactor top cask plate over the hole in the test plug. Secure the cask in place using the wheel chocks. Open the cask's shutter half way. Have the operator in the control room clear the containment building floor of any unnecessary personnel and open the inside door of the airlock. With all personnel clear of the reactor top area, lower the thimble/autoclave until the upper flange is about 8 feet above the top of the reactor lid. Open the clam shell cask, lock the cask open, and keep the cask from rolling using wheel chocks. Position the rig collar, red side up, about the rig on the step in the test plug, and lower the rig onto the collar so that the collar supports the weight of the thimble/autoclave. Disconnect the rigging from the upper flange and carefully lift the open clam shell cask to the BTF area and remove the rigging from the lifting beam.

c. Connect the hand hoist to the hook of the 3 ton crane and the hook of the hand hoist to the lifting beam. Hang the two springs from the middle lifting positions on the lifting beam. Position the 3 ton crane so that its hook is directly over the rig's upper flange and connect the upper flange to the bottom of the two springs; lift the thimble/containment with the 3 ton crane and remove the collar from the reactor top lid. Using the 3 ton crane and watching the bottom of the thimble through the viewing port,

lower the thimble/autoclave to the top of the dummy element. Continue lowering the thimble/autoclave into the dummy element with the hand hoist until the thimble collar makes contact with the Teflon seal on the step in the test plug; the thimble collar supports the weight of the thimble/autoclave. Remove the rigging from the upper flange, move the 3 ton crane hook away from the reactor top and remove the lifting beam and hand hoist.

d. Remove the reactor top lid cask plate from the reactor top lid. Replace the viewing plug in the top lid.

e. Rotate the upper flange so the markings on the upper flange and test plug line up. The 1/8" aluminum tube protruding from the upper flange points towards the cat walk.

f. Lift the lead doughnut, clean it, and place it on the reactor top lid around the upper flange. Lift the cask support plate onto the lead doughnut and support bricks.

g. Clean the open clam shell cask with a clean rag and/or the vacuum cleaner. Lift the cask with the 3 ton crane and lifting beam to the top of hot cell number 2 about the rig. Remove the plastic sleeving and any shielding around the load train, unlock the cask allowing it to close, close it around the rig and secure it closed with the two hasps. Lower the hook so that the bottom of the lifting beam is 2 inches from the top of the pull rod. Connect the autoclave top to the inner most positions of the lifting beam using 3/8" lifting eyebolts and the 22" long 1/4" sling. Notify the control room operator to remove any unnecessary personnel from the containment building floor and open the inside door of the airlock. With all personnel clear of the top of the hot cells, lift the load train from the support bracket taking care not to scrape the rig on the bracket. When the in-core sections of the load train are within the cask shut and lock shut the cask's shutter.

h. Remove the used O-ring in the upper autoclave, clean the flange surface with a clean rag and acetone. Install a new O-ring in the upper autoclave.

i. Lift the load train and cask from the hot cell top to the reactor top lid and lower the cask onto the lid plate over the upper flange without lowering the rig. Notify the control room operator to clear the reactor floor of unnecessary personnel and open the inside door of the airlock. Open the shutter half-way and clear personnel from the reactor top area. Lower the load train into the autoclave until the autoclave top is about 8 feet above the top of the reactor top, open and lock open the clam shell cask using wheel chocks to keep the cask from rolling. Position the IASCC collar about the load train, red side up, so that neither side of the collar contacts the sealing surface of the upper autoclave or autoclave top and lower the load train onto the collar. Disconnect the rigging from the autoclave top and lift the opened clam shell cask to the BTU and disconnect the cask's rigging from the lifting beam.

j. Bring the 3 ton crane and lifting beam so the hook is directly over the autoclave top, connect the autoclave top to the lifting beam and lift the load train a few inches. Remove the collar from the reactor top and lower the load train until the bottom of the autoclave top is within an inch of the upper flange. Rotate the autoclave top so that the marks on the autoclave top and upper flange line up. Clean two autoclave top bolts and place them in two holes on opposite sides of the autoclave top. Use these to find the final rotational position for the autoclave top. Lower the load train, tighten the two bolts and torque them to 125 ft-lbs.

k. Clean and lubricate the remaining bolts with high temperature lubrication and tighten them and torque them to 125 ft-lbs. Remove the original two bolts, lubricate them and torque them to 125 ft-lbs. Torque all bolts in 50 ft-lb increments to 275 ft-lbs.

l. Connect the three CO₂ lines to the upper flange and turn on the system by opening the valves on the two CO₂ tanks, opening the valve at the inlet to the lower pressure regulator and at the exit of the humidity sensor and throttling open the outlet side flow control valve so that the flow meter reads about 20 when pressure reaches 15 psi.

m. Place four 1/4" aluminum shims between the bottom of the upper flange and the test plug. Because the test plug is not level use additional thin shims on two of the 1/2" shims (I use the cask wheel chocks for this purpose). These shims support the weight of the rig and loading machine. Lift the Instron loading machine from the containment building floor to the reactor top using the outer most lifting position on the lifting beam and the 3 ton crane. Slowly lower the loading machine and handle it so that the hole in the lower plate comes safely over the pull rod, instrumentation wires and cooling jackets. When the lower plate is beneath the fittings but still above the autoclave top bolts, position the plate so that it is centered with respect to the autoclave top and continue to lower it past the top bolts. The chamfer in the under side of the bottom plate will center the plate on the upper flange. Use the four 5/16" bolts and washers to position the loading machine plate over the upper flange. Ensure that all of the weight of the loading machine goes onto the upper flange by keeping the loading machine's four feet in the air until the loading machine is bolted to the upper flange. Lower the loading machine so that its weight is supported by the upper flange. Tighten all four bolts so that the loading machine is locked to the upper flange, lower the four feet so that the loading machine doesn't fall over, and disconnect the loading machine from the crane. Connect the four straps between the loading machine top and lid hold down bolts for loading machine security.

n. Connect the three cables from the Instron frame interface box to the Instron loading machine and turn on the system. With the manual control panel lower the load cell to meet with the pull rod top, connect the pull rod to the load cell and remove the collar. On the loading machine control panel set the maximum load to 100 lbs, set action to transfer and hold, then in position control have the Instron move up at a rate of 0.1 inches per minute. This moves the loading machine up until the specimen is seated, places a 100 lb load on the specimen and holds that load until it receives further orders. With 100 lbs on the specimen check that the position is -0.7 to -0.5 inches, this verifies

that the specimen is loaded in the grips properly. If the specimen is not loaded in the grips properly, remove the loading machine and load train as described in section 5.2.2.

o. Isolate the pressurizer and chemistry rack from the main loop by closing the charging pump outlet valve, pressurizer isolation valve and MUV-5. Place a small bucket and plastic bag under one of the two capped off connections and remove the cap, taking care to collect the contaminated main loop water. Connect the main loop to the autoclave top using the prepared spool piece and 3/4" flare fittings. Repeat for the other connection. Open the pressurizer isolation valve and MUV-5. Check for leaks at the newly made fittings and autoclave top seals.

p. Open or check open the charging pump suction and discharge valves, back pressure regulator, letdown line filter isolation valves, and reference autoclave isolation or bypass valves and turn on the charging pump. Check for leaks. Pressurize the loop at a charging rate of about 600 cc/min to 1750 psi in 250 psi increments checking for leaks along the way. When pressure is greater than 250 psi start the main loop recirc pump.

q. Connect the auxiliary cooling water lines to the autoclave top cooling jackets and cooling coil. Check the valve line up for cooling water flow to the NRHX, main loop recirc pump, and autoclave top and turn on the auxiliary cooling water pump in the Sensor project's chemistry control rack. Check for leaks.

r. Stack lead bricks and plates to provide shielding for personnel from the high energy gamma radiation that will come from the main loop piping and autoclave top when the reactor is at power.

s. Connect the instrumentation wires to the proper terminals in the gray terminal box. Connect the two thermocouples from the autoclave top to the receptacle on the heater casing. Turn on the data acquisition system and Instron control computer and start the two programs.

t. Energize the heater control power. Verify the five temperatures monitored by the heater control cabinet read about room temperature. Verify the temperatures monitored by the black box on the chemistry control rack read properly. Verify the data acquisition is reading expected values for all parameters monitored. Verify that all alarms in the control room are clear and pressure and temperature indication in the control room read properly. The loop low temperature trip may need resetting for heater startup.

u. Use the 1%O₂/He gas mix to the charging tank through the gas addition flow meter to ensure that the main loop water remains oxidizing during loop heatup as described in section 5.3.4.

v. Place the main loop heater controller in manual control and set heater power to 75%. Select phase A on the ammeter and energize the main heater to begin heatup. Monitor heater current on all three phases, check that current is equal for all phases and not more than 30 amps.

w. Place the pressurizer heater controller in manual control and set heater power to 50%. Turn on the ammeter and energize the pressurizer heater to begin pressurizer heatup. Monitor heater current and check that current is not more than 25 amps.

x. Monitor the pressurizer and main loop temperatures continually. When the pressurizer reaches about 550°F place it in automatic control with a setpoint of 565°F. Watch it for a while to make sure that it has positive control. Do not let the heater lead bath temperature as read by the indicator on the heater cabinet exceed 700°F. Reduce heater power if necessary to allow the loop to continue to heat up while keeping the lead temperature below 700°F. When loop temperature reaches 535°F, lead bath temperature is about 650°F, and heater power is set to 30%, place the main loop heater controller into

automatic control with a set point of 535°F. Watch it for a while to make sure that it has positive control. Reset the low temperature trip to 500°F.

y. The reactor can be brought critical anytime after lead is stacked and the loop is being heated. The reactor should raise power to 4.5 MW in 0.5 MW steps in ten minute intervals.

z. After the reactor is at full power and steady state chemistry is attained, replace the He tank with the He/O₂ mix tank and slowly decrease the O₂ concentration in the charging tank by slowing O₂ flow rate into the charging tank and/or increasing charging tank vent rate. The final O₂ concentration in the charging tank should be 200 ppb. This can be controlled by varying the charging tank pressure (coarse adjust) and vent rate (fine adjust).

C.1.3. Tensile Test Startup

Initial Conditions

a. The facility is operating as described in section 5.1.2. The main loop is at 535°F, 1750 psi. The loading machine control and data acquisition programs are running. Letdown water chemistry is within acceptable limits to begin SSRT testing.

b. This procedure requires one experimenter.

Precautions

a. Do nothing that would vary system pressure after the tensile test has started if at all possible. System pressure affects the load on the test specimen, although the rig is pressure compensated, it is not perfect. During out of core testing, while performing a tensile test the loading machine tripped off on high load when the charging rate was

increased. Operations which could affect system pressure include: varying charging rate, bypassing the reference autoclave, and bypassing the letdown line filter.

b. Limit the rate of performing any operation which could cause a temperature transient. The load train is nearly 15 feet long, varying the temperature could cause uneven thermal expansion/contraction of the pull rod and reaction tube resulting in a strain rate higher or lower than expected. Experience with out of core and in-core temperature transients is that varying the system pressure by as much as 10°F while the test specimen is loaded at a stress less than the yield stress with the loading machine in position control caused no measurable change in load. This indicates that the pull rod and reaction tube have similar thermal expansion/contraction properties buffering effects on specimen strain. Operations which affect system temperature include varying reactor power and changing heater controller mode between manual and automatic.

c. Check the pressure in the He/O₂ mix gas tank often until the rate at which it is emptying is verified. Should the tank empty during a test chemistry control could be lost. When tank pressure gets low, replace it by placing a new tank beside the old one and remove its cap. Quickly shut the valve on top of the old tank, remove the regulator taking care not to change the pressure supplied to the reactor top, attach it to the new tank, and open the valve on top of the new tank. If the tank empties as indicated by negative pressure at the charging tank pressure gauge, close the valve at the outlet of the pressure regulator on the charging tank before changing the tanks. If this valve is not shut prior to removing the regulator on the He/O₂ gas mix tank charging tank water could drain to the containment building floor.

d. Monitor charging tank level during a test. It shouldn't vary at all during a test although it does vary significantly during main loop heatup and cool down. If the level appears to decrease in excess of the water accounted for by sampling a slow water leak could be present, an further investigation is warranted. All water is potentially

contaminated and should be accounted for. Don't add water to the charging tank during a test unless the situation requires that it be filled immediately. Adding even very pure water to the charging tank adds O₂ and CO₂ to the tank which impacts charging tank and eventually main loop water chemistry.

Instructions

a. Step through the loading machine control program on the HP computer on the reactor containment building floor which leads to starting the tensile test. This program is designed to start a test with the facility in almost any condition. It will set limits and vary control modes during the test setup automatically. Once the test has commenced verify that the loading machine is in position control by checking the green light beside the "POSITION" print on the left hand side of the loading machine control panel and the word "RUNNING" are lit in green on the lower left hand side of the same panel.

C.2. Facility Shutdown Operations

C.2.1. Securing From a Tensile Test

Initial Conditions

a. A tensile test has been running, the loading machine control program is running, the loading machine is in position control and the green "RUNNING" words are lit on the loading machine control panel.

b. The main loop is pressurized at 1750 psi and heated to 535°F.

c. The data acquisition system is operating.

d. The specimen has fractured as indicated by load displayed on the Instron control panel being 0 ± 20 lbs and not increasing or the specimen is not broken and the project team wants the test secured.

- e. This procedure requires one experimenter.

Precautions

- a. Don't attempt to remove main loop fittings until main loop temperature is less than 130°F.
- b. Don't depressurize the main loop unless the main loop recirc pump is off.
- c. Don't cool down the main loop until the reactor is shutdown.

Instructions

- a. Begin shutting down the reactor. Steps b through d may be performed with the reactor operating.
- b. On the loading machine control computer press the function button corresponding to the command "FRONT PANEL CONTROL".
- c. On the loading machine control panel verify that the red light corresponding to remote control on the bottom center of the panel is not lit. Press the button labeled "WAVEFORM" for position control on the inclined section of the panel. The lower display should read, "Ramp Rate is 0.000 in/hr". Press 1 on the numeric key pad then press "ENTER". This increases the ramp rate to 1 in/hr. If the specimen is not yet broken it will break within 15 to 30 minutes as indicated by load dropping to 0. If it is broken, indicated load should remain about 0.
- d. When the specimen is confirmed broken, stop the function generator by pressing the "HOLD" button on the lower left hand side of the loading machine control panel.

e. Warn the reactor operators in the control room that they are about to receive alarms, then de-energize the main loop and pressurizer heaters by going over to the heater control cabinet and turning off control power. It takes about 4 hours for the main loop to cool below 200°F and about 8 hours for the pressurizer to cool to below 200°F.

C.2.2. Disassembling the Entire Testing Facility From the Reactor Top

Initial Conditions

- a. The reactor is shutdown.
- b. The main loop and pressurizer are cooled to below 130°F as described in section 5.2.1.
- c. The loading machine is in position control and the function generator is turned off as described in section 5.2.1.
- d. permission for rig removal from the reactor core is given by Reactor Operations Office and Reactor Radiation Protection Office.
- e. This procedure requires at minimum 2 experimenters, an experienced crane operator, and 2 reactor operators (one on the reactor top, one in the control room). The reactor and crane operators are not required after both sections of the rig have been removed from the reactor.

Precautions

- a. Do not depressurize the main loop before turning the main loop Recirc pump off.
- b. Use plastic bags to contain the contaminated water that will leak from the main loop when loosening the fittings on the main loop. To minimize the amount of water that

leaks do not loosen any fittings unless the charging tank and pressurizer are isolated from the loop.

c. To prevent potential damage to the MITR reactor core, the thimble is to be removed from the in-core dummy element using springs and a hand hoist.

d. Because of the potential for high radiation levels near the rig and reactor top, the experimenter should check with RRPO before proceeding with each step in the procedure.

e. Take care when moving the lead doughnut to and from the reactor top lid. Avoid damaging the fragile aluminum tube protruding from the outside of the upper flange.

Instructions

a. Remove the stacked lead from the top of the autoclave, loading machine, and reactor top lid. Stack the plates and bricks neatly on the heater casing.

b. Disconnect the auxiliary cooling water lines to the autoclave top, roll the line up and store them neatly beside the main loop heater casing. Turn off the auxiliary cooling water pump if it doesn't need to be on.

c. Disconnect the DCPD and ECP instrumentation wires connected in the gray terminal box. Unplug the thermocouple connection on the heater controller. Roll all the cables up neatly using tie-wraps near the autoclave top.

d. Place the collar between the autoclave top gland nut and the pull rod's threaded top around the pull rod to support the pull rod during transport to the hot cell. Secure it into position with a tie-wrap and disconnect the pull rod from the load cell.

e. Turn off the main loop Recirc pump then the charging pump and depressurize the main loop by opening the back pressure regulator fully.

f. Isolate the pressurizer from the main loop by closing the pressurizer isolation valve.

g. Isolate the charging tank by closing the charging pump outlet isolation valve and MUV-5. Change the position of MUV-6 to read the charging tank. Switch charging tank pressurization tank to pure He from He/O₂ mix, and adjust charging tank vent rate as desired.

h. Tape a bag around the lowest main loop fitting between the heater casing and the reactor top lid to catch the contaminated water that will leak when the fitting is opened. Open the fitting carefully, then completely, keeping the bag under both ends. Loosen the flare fitting at the highest point on the autoclave top, this will drain all the water from the lower fitting. Remove the spool piece between the autoclave top and the fitting first opened, drain the water in it into the bag and store the spool piece in a large clean plastic bag. Remove the second spool piece, drain it into the same bag of water, and store it in the same bag that the other spool piece is stored in. Tie the bag and place the bag neatly on the platform. Cap the second fitting on the main loop. Loosen both main loop elbow fittings on the autoclave top so they can rotate.

i. Put the lifting beam on the hook of the three ton crane and attach the loading machine to the outer most lifting position of the lifting beam. Remove the 5/16" screws locking the loading machine to the upper flange and store them in a clean plastic bag, store them in a drawer in the reactor top area. Remove the three loading machine power cables from the loading machine, roll them up and hang them neatly from their support bracket between the reactor top and BTF areas. Remove the four support straps from the loading machine lifting eyes and the reactor top lid hold down bolts and store them in a

clean plastic bag on the heater casing. Lift the loading machine over the autoclave top taking care not to bump or break fittings on the autoclave top. Wipe the loading machine down with clean rags and Versene taking care not to spread contamination. Move it to its storage position on the reactor containment building floor. Cover it with plastic and mark it with a contaminated material sign. Remove the shims between the upper flange and lid test plug.

j. Mark the position of the upper flange and the reactor top and the autoclave top. This should be done between each test because the markings fade each time the rig is heated. Remove the autoclave top bolts, clean them and store them in a clean plastic bag on the heater casing. Turn off the CO₂ system by shutting the low pressure regulator inlet isolation valve, the humidity sensor outlet isolation valve, and the flow control valve. Disconnect the three CO₂ lines from the upper flange, roll them up neatly and store them beside the reactor top.

k. Using the three ton crane and appropriate rigging, lift the lead doughnut over the autoclave top and set it down about the upper flange taking care not to bump the doughnut into the small aluminum tube protruding from the upper flange. Lift the reactor top cask support plate onto the doughnut and supports so that it lines up with the markings on the reactor top lid. Using 3/8" lifting eyebolts and the 22"X1/4" slings lift the load train so that the autoclave top is about 8 feet above the reactor top lid. Position the collar about the load train, red side up, so that neither side of the collar comes into contact with the sealing surface of the upper flange or bottom of the autoclave top. Lower the load train onto the collar so that the collar supports the weight of the load train. Disconnect the load train from the lifting beam.

l. Clean the clam shell cask using clean rags and a vacuum cleaner. Lock the cask open and the shutter halfway out. Using the 3 ton crane and the middle lifting position on the lifting beam lift the cask onto the cask support plate about the load train. Use wheel

chocks to keep the cask from rolling. Connect the load train to the innermost position of the lifting beam and lift the load train up several inches. Remove the collar from the top lid. Remove the wheel chocks from the cask rollers and roll the cask closed around the reaction tube and lock the cask shut using the hasps. Have the control room operator clear the building floor of unnecessary personnel and lock the airlock. With all personnel clear of the reactor lid area, lift the load train into the cask. Allow five minutes for the rig to drip dry, then close the shutter. Lift the cask and load train to hot cell number 2. Ball up a clean rag and stuff it partially into the autoclave to keep dirt out of the autoclave.

m. Secure a couple of rags on the end of the hot cell support bracket to protect the autoclave top sealing surface. Remove the railings on the front of hot cell number 2. Lift the cask and load train to the hot cell top, hasp side to the containment wall. Position the cask and load train so that the load train is directly over the front hole in the hot cell taking care not to scrape the sides of the load train on the support bracket. Open the shutter half-way, clear the hot cell top area of personnel and lower the load train so that the autoclave top supports the weight of the load train on the support bracket. Open and lock open the cask and lift it to the reactor top lid area and clean it. Tie the autoclave top to the bracket so that it doesn't fall if jarred, and cover the exposed sections of the load train with plastic sleeving.

n. Lift the cask support plate and lead doughnut from around the upper flange, taking care not to bump the lead doughnut into the small aluminum tube protruding out of the upper flange.

o. Lift the large viewing plug from the top lid. Lift the cask support plate to the top lid around the upper flange and position it using the markings on the lid.

p. Connect the two springs to the inner most lifting position on the lifting beam, the beam to the hook on the hand hoist and the hand hoist to the hook on the 3 ton crane.

Connect the bottom of the springs to the upper flange using 3/8" eyebolts. While watching the thimble through the viewing port and the springs, lift the thimble with the hand hoist until the thimble is clear of the dummy element. Continue lifting the thimble/autoclave with the 3 ton crane until the upper flange is about 8 feet above the reactor top lid. Position the collar around the thimble, red side up, and lower the thimble/autoclave so that the collar supports its weight. Disconnect the upper flange from the springs and remove the hand hoist and springs from the lifting beam and 3 ton crane.

q. Lift the opened cask to the cask support plate on the top lid about the thimble/autoclave. Use wheel chocks to keep the cask from rolling. Connect the upper flange to the inner most lifting position on the lifting beam and lift it a few inches. Remove the collar from the reactor top. Remove the wheel chocks and close the cask using the hasps. Have the operator in the control room clear the reactor floor area of unnecessary personnel and open the inside door of the airlock. With the top lid clear of all personnel lift the thimble/autoclave into the cask. Wait 5 minutes for the thimble to drip dry, then close the shutter and lift the thimble/autoclave and cask to its storage position beside hot cell number 1.

r. When the upper flange is resting on its the support bracket, lock the support bracket and disconnect the lifting beam from the 3 ton crane.

s. Remove the Teflon gasket on the step in the test plug, put it into a clean plastic bag and store it on the reactor top.

C.2.3. Removal of the Fractured Test Specimen

Initial Conditions

- a. The load train is supported by the bracket over hot cell number 2.
- b. This procedure takes at least one experimenter, two is preferred.

Precautions

- a. Try not to let either half of the test specimen drop. It could damage the fracture surface and even roll into a location where it could be difficult to retrieve.

Instructions

- a. Place one manipulator on the bottom of the lower grip holder. This will keep the lower grip and bottom half of the specimen from falling. Use the other manipulator to remove the titanium dowel in the lower grip holder place it in a safe location of the welding fixture table. Slowly lower the manipulator from the lower grip holder, grasp the lower grip and specimen with the other manipulator. Place them down in a safe location on the welding fixture table.
- b. Remove the pull rod collar and lower the pull rod so that the pull rod's threaded top sits on the gland nut.
- c. Remove the top half of the test specimen from the upper grip.
- d. Place each half in individual labeled test tubes in the test tube holder in the hot cell.

C.3. Other Facility Operations

This section describes procedures not yet discussed that are not intuitively obvious.

C.3.1. Removal of The Load Train to the Hot Cell for Specimen Replacement and Immediate Re-Testing.

Initial Conditions

- a. The reactor is shutdown.
- b. The main loop and pressurizer are cooled to below 130°F as described in section 5.2.1.
- c. The loading machine is in position control and the function generator is turned off as described in section 5.2.1.
- d. permission for rig removal from the reactor core is given by Reactor Operations Office and Reactor Radiation Protection Office.
- e. Permission for transfer is granted by MITR-II Reactor Operations Office and Reactor Radiation Protection Office.
- f. This procedure requires at minimum 2 experimenters, an experienced crane operator, and 2 reactor operators (one on the reactor top, one in the control room).

Precautions

- a. Do not depressurize the main loop before turning the main loop Recirc pump off first.

b. Use a plastic bag to contain the contaminated water that will leak from the main loop when you loosen the fittings on the main loop. To minimize the amount of water that leaks, do not loosen any fittings on the main loop unless the charging tank and pressurizer are isolated from the loop.

c. To prevent potential damage to the MITR reactor core, the thimble is to be removed from the in-core dummy element using springs and a hand hoist.

d. Because of the potential for high radiation levels near the rig, the experimenter should check with RRPO before proceeding with each successive step in the procedure.

e. Take care when moving the lead doughnut to and from the reactor top lid. Avoid the small fragile aluminum tube protruding from the outside of the upper flange.

Instructions

a. follow instruction steps a. through k. of section 5.2.2.

b. perform sections 5.2.3. and 5.1.1. completely.

c. follow instruction steps g. through z. of section 5.1.2.

d. perform sections 5.1.3. completely.

C.3.2. Removing Dissolved Gases From the Charging Tank by Venting the Charging Tank.

Initial Conditions

a. The charging tank clean up system is on with CUV-1, CUV-2, CUV-3, CUV-5 open and CUV-7 throttled open. MUV-6 is selected to either the letdown or charging tank.

b. The charging tank is pressurized to about 5 psi with either pure He or He/O₂ mix and there exist dissolved gases in the charging tank whose concentration should be minimized (e.g. H₂ and O₂ during at reactor power operation or CO₂ and excess O₂ during loop startup or after charging tank filling).

Precautions

a. Take care when operating the vent line throttle valve. A very small change in position varies the flow rate significantly. Observe the bubbling rate in the vent line discharge bottle for an indication of vent rate. After changing the vent rate watch the bubbling rate in the vent line discharge bottle and the bottom of the charging tank for about a minute since varying the vent rate in turn affects the charging tank pressure which takes some time to equilibrate. The vent rate is most effective when the bubbling rate in the charging tank from both the discharge of the bubbling pump and the outlet of the low pressure regulator are equal. Vent rates higher than this are to be avoided since there is little chemistry control.

Instructions

a. While watching the bubbling rate in the vent line discharge bottle, open the vent line throttle valve a very small amount.

b. Watch the bubbling rates in the charging tank and vent line discharge bottle for a minute or two until they reach their steady value.

C.3.3. Adding Water to the Charging Tank

Initial Conditions

a. The charging tank clean up system is on with CUV-1, CUV-2, and CUV-3 open. The charging tank may be filled through MUV-4 and MUV-5 instead of MUV-2

and MUV-3 if required, but having the filling water enter the charging tank through MUV-2 and MUV-3 has the water pass through the demineralizer, UV sterilizer, and organic filter which is preferred.

b. The charging tank level is lower than it should be for facility startup, to replenish water due to numerous samples including on-line ion chromatography, or a water system leak.

Precautions

a. Filling the charging tank during in-core testing should be avoided because the filling water is aerated and therefore increases charging tank conductivity and O₂ levels for a short period.

b. As the charging tank is filling, watch the charging tank pressure. As the level increases so does the charging tank pressure, vent the charging tank pressure as it goes over 6 psi through the recombiner blowdown valve until pressure reaches about 5 psi. The charging tank has an over-pressure relief valve set at 10 psi, but this feature shouldn't be tested.

Instructions

a. Rinse and fill a clean poly bottle with demineralized water and bring it to the chemistry control rack.

b. Place the end of the filling line in the poly bottle, open CUV-6, then shut CUV-1.

c. Watch the charging tank level, the level in the poly bottle, and charging tank pressure. When the charging tank pressure exceeds 6 psi lower the pressure by opening the recombiner blowdown valve until pressure reaches about 5 psi.

d. When the poly bottle level empties or the charging tank fills open MUV-1 then shut MUV-6.

C.3.4. Adding Additional Gas to the Charging Tank

Initial Conditions

- a. The charging tank clean up and bubbling systems are operating.
- b. The situation requires additional O₂ or H₂ in the charging tank.

Precautions

a. Follow all precautions described in the safety manual when working with hydrogen or oxygen gas.

Instructions

- a. Check shut or shut the three valves in the gas addition line.
- b. Attach the appropriate regulator to the gas tank of the gas to be added to the charging tank.
- c. Attach the regulator to the nylon line to the inlet of the gas addition flow meter and pressurize the line to 10 psi.
- d. Remove the line from the inlet to the flow meter, allow gas to purge the line of unwanted gas, and reconnect the line to the inlet to the flow meter.
- e. Open the isolation ball valve and throttle valve down stream of the flow meter.
- f. Open the throttle valve on the flow meter to allow the gas to enter the charging tank at the desired rate.

APPENDIX D. RESULTS FROM IN-CORE ECP MEASUREMENTS

Figure D.1. Raw position 1 data for Ag/AgCl electrodes in the top, bottom clusters and reference autoclave.

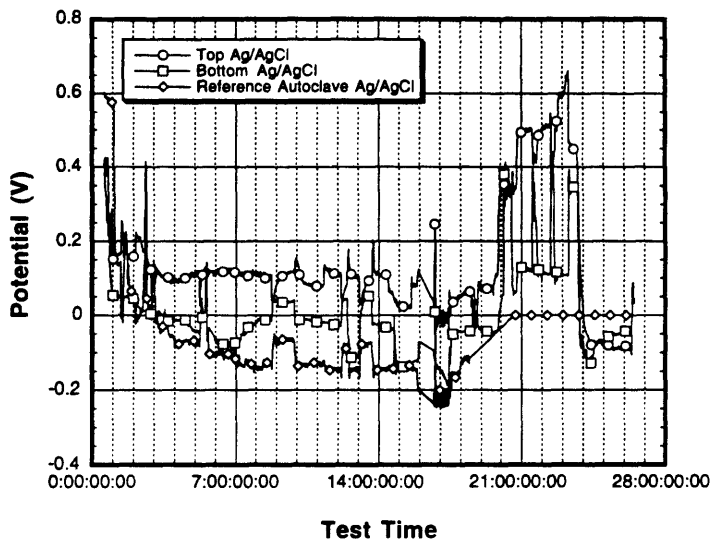


Figure D.2. Raw position 1 data for platinum electrodes in the top and bottom clusters and reference autoclave.

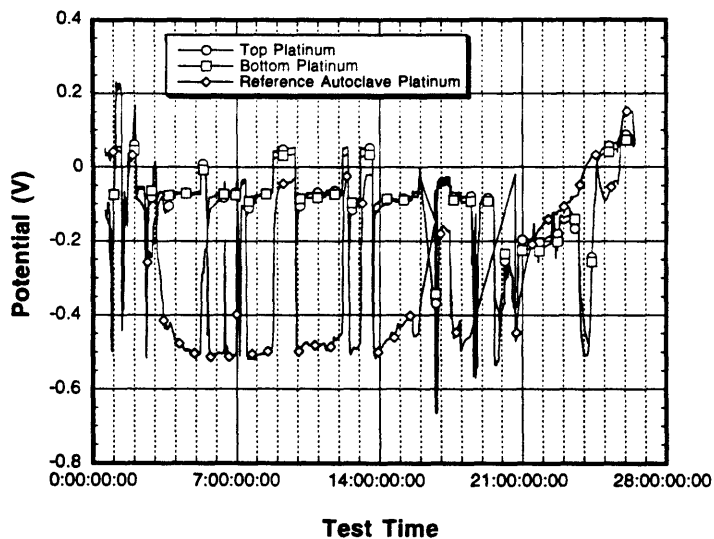


Figure D.3. Raw position 1 data for stainless steel electrodes in the top and bottom clusters and reference autoclave.

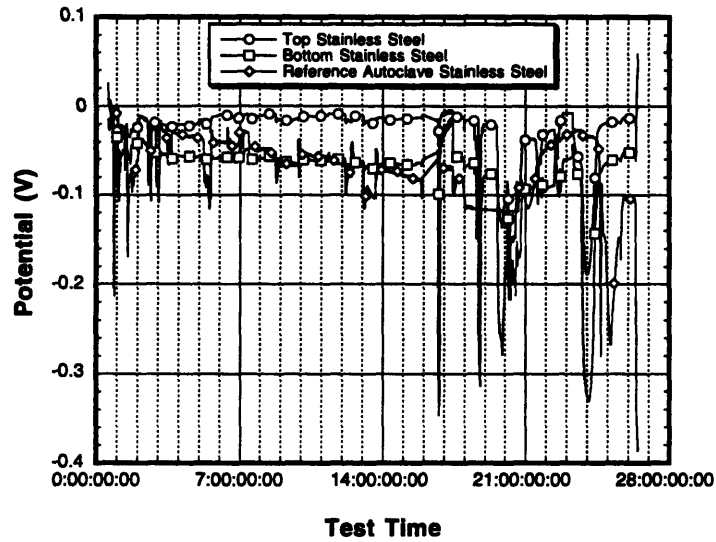


Figure D.4. Raw position 1 data for letdown line dissolved oxygen and hydrogen.

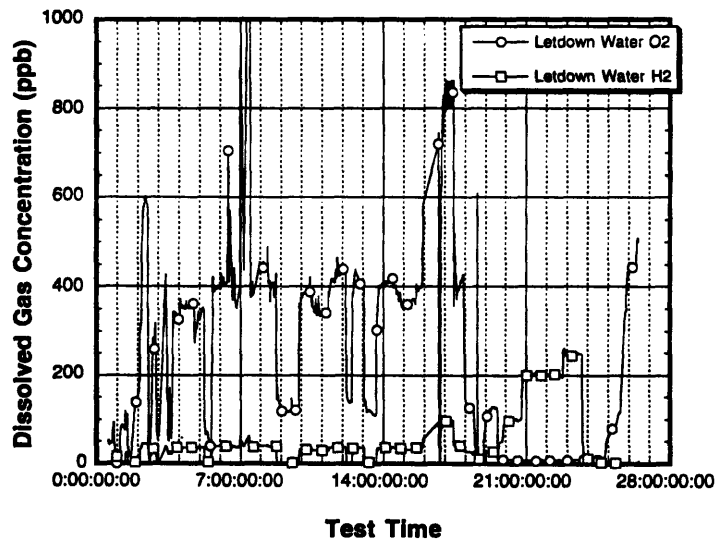


Figure D.5. Raw position 1 data for temperature.

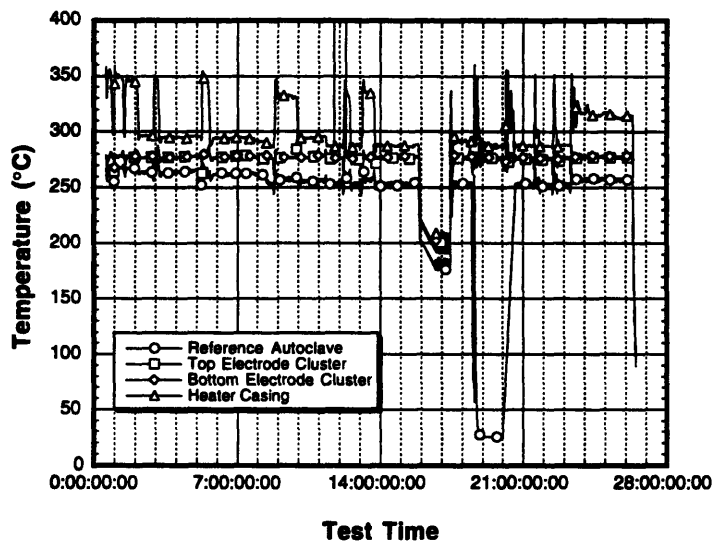


Figure D.6. Raw position 2 data for Ag/AgCl electrodes in the top and bottom clusters and reference autoclave.

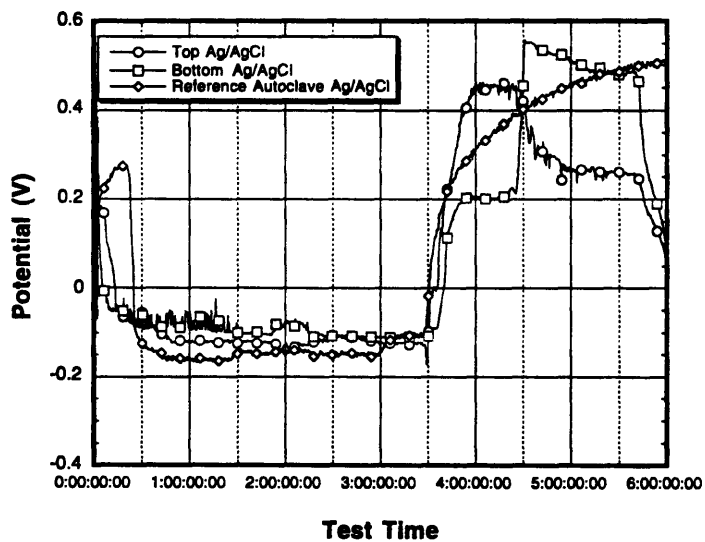


Figure D.7. Raw position 2 data for platinum electrodes in the top and bottom clusters and reference autoclave.

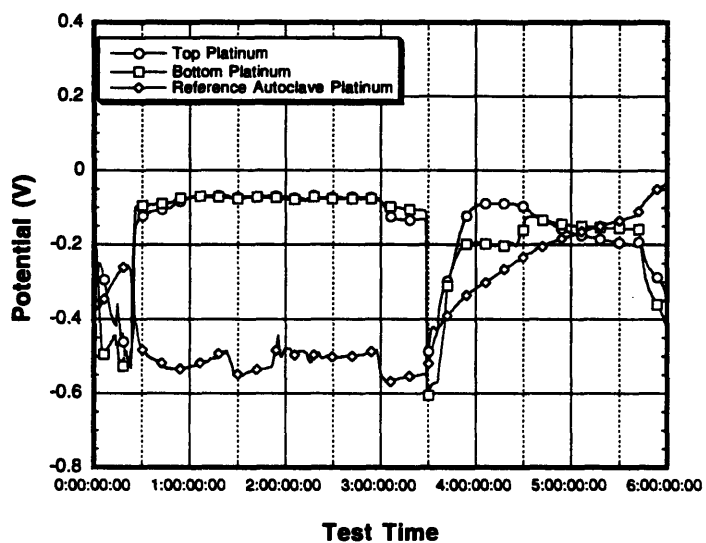


Figure D.8. Raw position 2 data for stainless steel electrodes in the top and bottom clusters and reference autoclave.

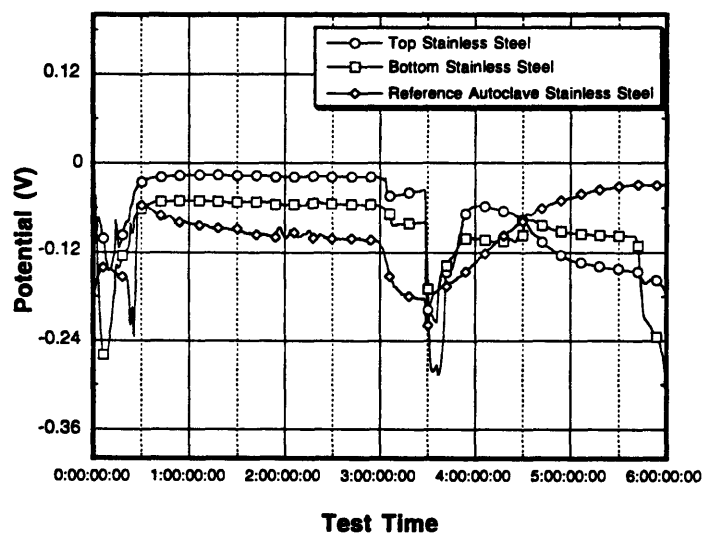


Figure D.9. Letdown oxygen and hydrogen concentration during in-core testing in position 2.

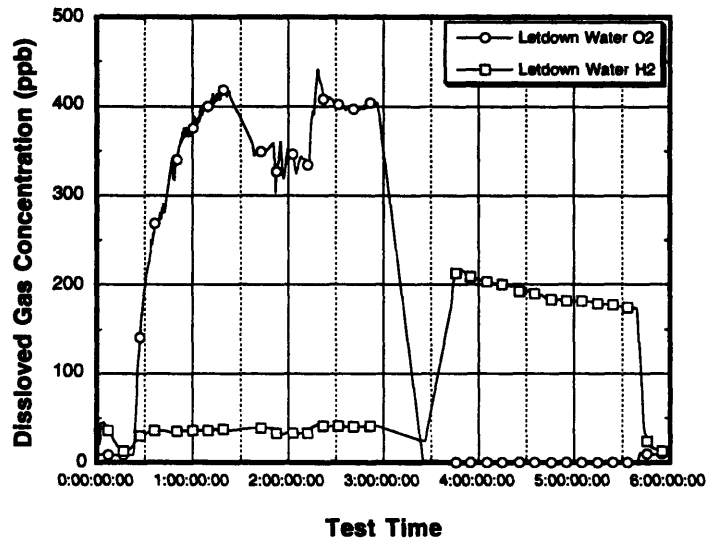
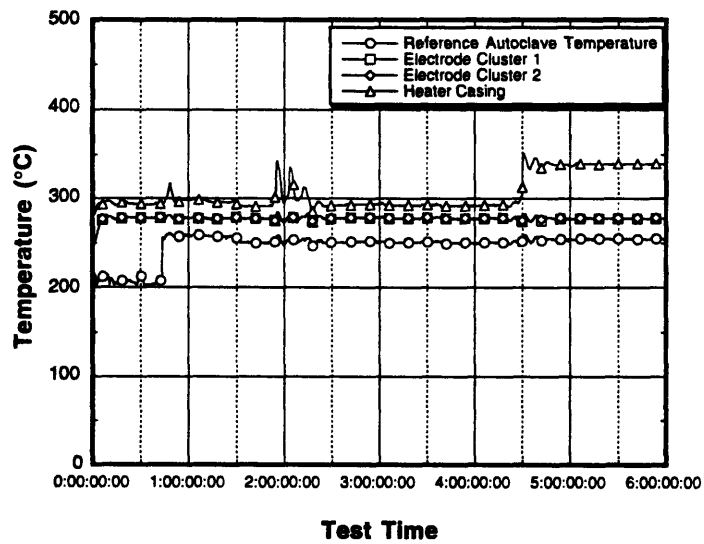


Figure D.10. Temperatures during in-core testing in position 2.



APPENDIX E. MECHANICAL PROPERTIES TEST TEST OF SPECIMEN 80.

Specimen 80 was irradiated to $0.8 \times 10^{21} \text{ cm}^{-2}$ alloy 304. The slow extension rate test was halted at 16% due to main loop recirculation pump failure. The specimen was subsequently loaded to failure using a fast extension rate. The results from this test are presented here.

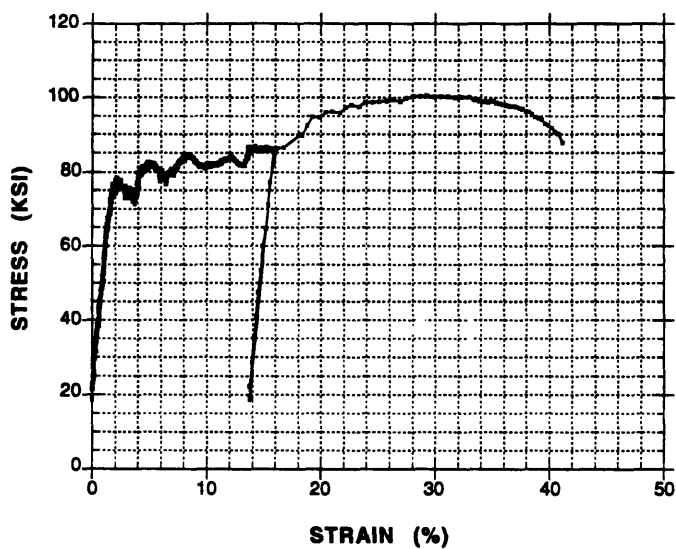


Figure E.1. Mechanical property test of specimen 80, alloy 304 irradiated to $0.8 \times 10^{21} \text{ cm}^{-2}$ ($E > 1 \text{ MeV}$).